

# Precast Bent System for High Seismic Regions

*Laboratory Tests of Column-to-Footing Socket Connections*

**Publication No. FHWA-HIF-13-039**

**June 2013**

***HIGHWAYS FOR LIFE***

*Accelerating Innovation for the American Driving Experience.*



*Photo courtesy of the Precast/Prestressed Concrete Institute*



U.S. Department of Transportation  
**Federal Highway Administration**

## **Notice**

This document is disseminated under the sponsorship of the U.S. Department of Transportation in the interest of information exchange. The U.S. Government assumes no liability for the use of the information contained in this document. This report does not constitute a standard, specification, or regulation.

The U.S. Government does not endorse products or manufacturers. Trademarks or manufacturers' names appear in this report only because they are considered essential to the objective of the document.

## **Quality Assurance Statement**

The Federal Highway Administration (FHWA) provides high-quality information to serve Government, industry, and the public in a manner that promotes public understanding. Standards and policies are used to ensure and maximize the quality, objectivity, utility, and integrity of its information. FHWA periodically reviews quality issues and adjusts its programs and processes to ensure continuous quality improvement

**Technical Report Documentation Page**

1. Report No. FHWA-HIF-13-039	2. Government Accession No. N/A	3. Recipient's Catalog No. N/A	
4. Title and Subtitle PRECAST BENT SYSTEM FOR HIGH SEISMIC REGIONS – LABORATORY TESTS OF COLUMN-TO-FOOTING SOCKET CONNECTIONS		5. Report Date June 2013	
		6. Performing Organization Code	
7. Author(s) Olafur S. Haraldsson <sup>1</sup> , Todd M. Janes <sup>1</sup> , Marc O. Eberhard <sup>1</sup> , and John F. Stanton <sup>1</sup>		8. Performing Organization Report No.	
9. Performing Organization Name and Address BergerABAM, Inc. 33301 Ninth Ave South, Suite 300 Federal Way, WA 98003  <sup>1</sup> University of Washington, Seattle, WA		10. Work Unit No.	
		11. Contract or Grant No. DTFH61-09-G-00005	
12. Sponsoring Agency Name and Address Federal Highway Administration Highways for LIFE Program Office 1200 New Jersey Avenue, SE Washington, DC 20590		13. Type of Report and Period Covered Final Report	
		14. Sponsoring Agency Code	
15. Supplementary Notes This is a companion report to the final project report, <i>Precast Bent System for High Seismic Regions</i> (FHWA-HIF-13-037).			
16. Abstract This report provides detailed information from the laboratory investigation of three precast column-to-spread footing large-scale tests, including descriptions of the specimen design, testing, data reduction, and conclusions regarding the use of the connection with the precast bent system.  The tests provide data regarding the performance of the precast column-to-spread footing connection. The results indicate that the connection, when used with a precast column, is sufficiently strong to support the factored design gravity loads and to resist plastic hinging in the column above the footing. The behavior is emulative of cast-in-place performance. However, the precast column also provides an improved load path for lateral force transfer to the footing, owing to the elimination of outwardly hooked column longitudinal reinforcement. Additionally, the connection performance is adequate without reinforcement passing from the footing into the column, thus simplifying construction.			
17. Key Words Bridges, earthquakes, accelerated bridge construction, precast bent, connections, spread footing foundations, prefabricated bridge elements and systems		18. Distribution Statement No restrictions. This document is available to the public through the National Technical Information Service, Springfield, VA 22161.	
9. Security Classif. (of this report) Unclassified	20. Security Classif. (of this page) Unclassified	21. No. of Pages 184	22. Price

## PREFACE

This report provides technical information from the laboratory testing of three precast column-to-spread footing specimens. These tests were conducted to support the development of a precast bent system for use in high seismic regions.

This report consists of seven chapters.

Chapter 1 provides background and overview material, including the spread footing socket connection concept and the research objective and scope.

Chapter 2 covers the design of the test specimens.

Chapter 3 provides a description of the test setup, instrumentation, and the method of control of the testing process.

Chapter 4 provides definition of the damage states that were observed and an overview of the damage progression that occurred during testing.

Chapter 5 provides the measured response of the three specimens, including material strengths, force and moment vs. displacement plots, curvature distributions, displacement histories, and strain histories. Strain histories are provided for all the principal reinforcement types. Also included are the results of the post-seismic tests of the axial capacity of the foundation.

Chapter 6 covers the analysis of the observed and recorded data, and it provides treatment of various modes of potential failure and how the test results compared relative to those failure modes.

Chapter 7 provides a summary, conclusions, and recommendations.

Appendixes are included to report more detailed information that may be useful in understanding the response of the specimens and the progression of damage.

## SI\* (MODERN METRIC) CONVERSION FACTORS

### APPROXIMATE CONVERSIONS TO SI UNITS

Symbol	When You Know	Multiply By	To Find	Symbol
<b>LENGTH</b>				
in	inches	25.4	millimeters	mm
ft	feet	0.305	meters	m
yd	yards	0.914	meters	m
mi	miles	1.61	kilometers	km
<b>AREA</b>				
in <sup>2</sup>	square inches	645.2	square millimeters	mm <sup>2</sup>
ft <sup>2</sup>	square feet	0.093	square meters	m <sup>2</sup>
yd <sup>2</sup>	square yard	0.836	square meters	m <sup>2</sup>
ac	acres	0.405	hectares	ha
mi <sup>2</sup>	square miles	2.59	square kilometers	km <sup>2</sup>
<b>VOLUME</b>				
fl oz	fluid ounces	29.57	milliliters	mL
gal	gallons	3.785	liters	L
ft <sup>3</sup>	cubic feet	0.028	cubic meters	m <sup>3</sup>
yd <sup>3</sup>	cubic yards	0.765	cubic meters	m <sup>3</sup>
NOTE: volumes greater than 1000 L shall be shown in m <sup>3</sup>				
<b>MASS</b>				
oz	ounces	28.35	grams	g
lb	pounds	0.454	kilograms	kg
T	short tons (2000 lb)	0.907	megagrams (or "metric ton")	Mg (or "t")
<b>TEMPERATURE (exact degrees)</b>				
°F	Fahrenheit	5 (F-32)/9 or (F-32)/1.8	Celsius	°C
<b>ILLUMINATION</b>				
fc	foot-candles	10.76	lux	lx
fl	foot-Lamberts	3.426	candela/m <sup>2</sup>	cd/m <sup>2</sup>
<b>FORCE and PRESSURE or STRESS</b>				
lbf	poundforce	4.45	newtons	N
lbf/in <sup>2</sup>	poundforce per square inch	6.89	kilopascals	kPa
<b>APPROXIMATE CONVERSIONS FROM SI UNITS</b>				
Symbol	When You Know	Multiply By	To Find	Symbol
<b>LENGTH</b>				
mm	millimeters	0.039	inches	in
m	meters	3.28	feet	ft
m	meters	1.09	yards	yd
km	kilometers	0.621	miles	mi
<b>AREA</b>				
mm <sup>2</sup>	square millimeters	0.0016	square inches	in <sup>2</sup>
m <sup>2</sup>	square meters	10.764	square feet	ft <sup>2</sup>
m <sup>2</sup>	square meters	1.195	square yards	yd <sup>2</sup>
ha	hectares	2.47	acres	ac
km <sup>2</sup>	square kilometers	0.386	square miles	mi <sup>2</sup>
<b>VOLUME</b>				
mL	milliliters	0.034	fluid ounces	fl oz
L	liters	0.264	gallons	gal
m <sup>3</sup>	cubic meters	35.314	cubic feet	ft <sup>3</sup>
m <sup>3</sup>	cubic meters	1.307	cubic yards	yd <sup>3</sup>
<b>MASS</b>				
g	grams	0.035	ounces	oz
kg	kilograms	2.202	pounds	lb
Mg (or "t")	megagrams (or "metric ton")	1.103	short tons (2000 lb)	T
<b>TEMPERATURE (exact degrees)</b>				
°C	Celsius	1.8C+32	Fahrenheit	°F
<b>ILLUMINATION</b>				
lx	lux	0.0929	foot-candles	fc
cd/m <sup>2</sup>	candela/m <sup>2</sup>	0.2919	foot-Lamberts	fl
<b>FORCE and PRESSURE or STRESS</b>				
N	newtons	0.225	poundforce	lbf
kPa	kilopascals	0.145	poundforce per square inch	lbf/in <sup>2</sup>

\*SI is the symbol for the International System of Units. Appropriate rounding should be made to comply with Section 4 of ASTM E380. (Revised March 2003)



## TABLE OF CONTENTS

<b>CHAPTER 1. INTRODUCTION.....</b>	<b>1</b>
Need for Rapid Construction.....	1
Socket Connection Concept .....	2
Objectives and Scope .....	4
<b>CHAPTER 2. DESIGN OF TEST SPECIMENS .....</b>	<b>7</b>
Design of Prototype and Test Columns.....	8
Design of Prototype and Test Specimen Column-to-Footing Connection.....	10
Specimens SF-1 and SF-2 .....	10
Specimen SF-3.....	13
<b>CHAPTER 3. EXPERIMENTAL PROGRAM.....</b>	<b>17</b>
Loading Setup.....	17
Instrumentation.....	18
Testing Protocol .....	22
<b>CHAPTER 4. DAMAGE PROGRESSION .....</b>	<b>25</b>
Definitions of Damage States.....	25
Preliminary Test Cycles .....	25
Factored Axial-Load Tests .....	25
Lateral-Load Tests (up to yielding).....	27
Lateral-Load Tests (after yielding).....	29
Axial-Load Testing to Collapse .....	33
<b>CHAPTER 5. MEASURED RESPONSE.....</b>	<b>35</b>
Material Properties .....	35
Concrete Strength .....	35
Grout Strength .....	36
Reinforcement .....	36
Friction Correction .....	37
Moment-Drift Response .....	38
Effective Force .....	42
Distribution of Column Curvature .....	44
Column Splice .....	46
Strains in Column Longitudinal Bars.....	50
Strain Profiles along the Height of Specimen .....	50
Strain Histories for Bars near Splice .....	52
Column Longitudinal Bar Strain Histories in Footing .....	53
Footing Strain Corrections .....	57
Strains in Bottom Mat of Footing Reinforcement.....	58

Strains in Bottom Bars in the North-South Direction (Loading Direction) .....	59
Implication of the Effective Width.....	61
Strains in Bottom Bars in the East-West Direction .....	62
Strains in Diagonal Bars.....	64
Strains in Footing Ties .....	66
Axial Load-Response .....	69
Factored Axial Loading.....	69
Ultimate Axial-Load Capacities .....	70
<b>CHAPTER 6. ANALYSIS OF MEASURED RESPONSE.....</b>	<b>73</b>
Footing Overturning.....	73
Footing Response .....	76
Footing Flexural Strength.....	76
Footing One-Way Shear Strength .....	77
Combined Punching Shear and Moment Transfer .....	78
Footing Punching Shear Strength.....	80
Footing Shear-Friction Strength.....	82
Footing Joint Shear.....	84
Column Response.....	87
Column Axial-Load Capacity.....	87
Column Flexural Strength .....	88
Column Shear Strength.....	90
Column Splice in Specimens SF-1 and SF-2 .....	92
Damage Progression Models.....	93
Effective Stiffness Model.....	94
Normalized Moment-Drift Response .....	94
Strength Degradation.....	96
Energy Dissipation .....	96
<b>CHAPTER 7. SUMMARY AND CONCLUSIONS .....</b>	<b>101</b>
Summary 101	
System Concept.....	101
Design of Test Specimens .....	101
Experimental Testing.....	102
Experimental Analysis.....	103
Conclusions .....	104
Recommendations .....	105
<b>REFERENCES.....</b>	<b>107</b>
<b>APPENDIX A: SPECIMEN CONSTRUCTION DRAWINGS .....</b>	<b>109</b>
Specimen SF-1 .....	109
Specimen SF-2 .....	113
Specimen SF-3 .....	117

<b>APPENDIX B: MATERIAL TESTS .....</b>	<b>123</b>
Concrete Strength .....	123
Grout Strength .....	126
Reinforcement .....	127
Stress-Strain Plots for Specimens SF-1 and SF-2 .....	129
Stress-Strain Plots for Specimen SF-3 .....	132
Corrugated Metal Ducts .....	134
 <b>APPENDIX C: DAMAGE PROGRESSION .....</b>	 <b>135</b>
Specimen SF-1 .....	135
Specimen SF-2 .....	139
Specimen SF-3 .....	143
 <b>APPENDIX D: CONSTRUCTION SEQUENCE .....</b>	 <b>153</b>
Specimen Construction Sequence .....	153
 <b>APPENDIX E: DESIGN CONCEPTS.....</b>	 <b>159</b>
Columns with Projecting Bars.....	159
Columns without Projecting Bars.....	161
Socket Columns.....	161
Long Struts .....	163
Short Struts .....	165



## LIST OF FIGURES

Figure 1. Diagram. Rapid construction sequence. ....	2
Figure 2. Diagram. Strut-and-tie models for (a) bent out bars and (b) headed bars. ....	3
Figure 3. Photo. Earlier form of the socket connection used by the City of Redmond over Washington State SR 520, as originally used. ....	4
Figure 4. Diagram. Precast column elevation for specimens SF-1 and SF-2. ....	9
Figure 5. Diagram. Specimen SF-1 footing steel arrangement.....	11
Figure 6. Diagrams. Spread footing cross section for (a) SF-1 and (b) SF-2 (section A-4). ....	12
Figure 7. Graph. Final criteria design space for specimen SF-3.....	13
Figure 8. Diagram. Specimen SF-3 footing steel arrangement.....	15
Figure 9. Diagram. Specimen SF-3 spread footing cross-section (section A-5). ....	16
Figure 10. Diagram. Specimen SF-3 longitudinal section (section A-7).....	16
Figure 11. Diagram. Test setup.....	17
Figure 12. Diagram. Locations of external instruments. ....	19
Figure 13. Diagram. Locations of strain gauges in the three specimens. ....	20
Figure 14. Diagram. Locations of strain gauges in the three specimens' cast-in-place footings. ....	21
Figure 15. Graph. Lateral loading displacement history.....	23
Figure 16. Chart. Comparison of specimens' drift ratios for the major damage states. ....	28
Figure 17. Diagram. Column vertical bar naming convention. ....	28
Figure 18. Photos. Test specimens after a cycle of maximum drift ratio of 4.28 percent. ....	29
Figure 19. Photo. Specimen SF-1 longitudinal bars fractured after one cycle to 10.65 percent drift ratio. ....	30
Figure 20. Photo. Specimen SF-3 footing failure. ....	31
Figure 21. Photo. Damage on top of footing after test.....	32
Figure 22. Diagram. Punching shear profile in the north-south direction (loading direction). ....	32
Figure 23. Photos. Specimens at the end of the test program. ....	33
Figure 24. Equation. Coefficient of friction.....	38
Figure 25. Equation. Calculation of the moment at the base of the column.....	38
Figure 26. Diagram. Displacements and forces on test specimen used in figure 25. ....	39
Figure 27. Graph. Specimen SF-1 moment-drift response. ....	39
Figure 28. Graph. Specimen SF-2 moment-drift response. ....	40
Figure 29. Graph. Specimen SF-3 moment-drift response. ....	40

Figure 30. Equation. Effective lateral force.....	42
Figure 31. Graph. Specimen SF-1 effective force-displacement response.....	42
Figure 32. Graph. Specimen SF-2 effective force-displacement response.....	43
Figure 33. Graph. Specimen SF-3 effective force-displacement response.....	43
Figure 34. Equation. Calculating the average curvature.....	44
Figure 35. Graph. Specimen SF-1 average column curvature.....	45
Figure 36. Graph. Specimen SF-2 average column curvature.....	45
Figure 37. Graph. Specimen SF-3 average column curvature.....	46
Figure 38. Photo. Crack opening measurement pot.....	47
Figure 39. Graph. Specimen SF-1 splice interface opening.....	48
Figure 40. Graph. Specimen SF-2 splice interface opening.....	48
Figure 41. Graph. Strain profiles in S-SW bar in specimen SF-1.....	51
Figure 42. Graph. Strain profiles in S-SW bar in specimen SF-2.....	51
Figure 43. Graph. Strain profiles in S-SW bar in specimen SF-3.....	52
Figure 44. Graphs. Strain-drift relationship 2 inches below the column splice interface.....	53
Figure 45. Graphs. Strains in N-NE bars in specimens SF-1 and SF-2 at various heights below the interface.....	54
Figure 46. Graphs. Strains in S-SW bars in specimen SF-1 and SF-2 at various heights below the interface.....	55
Figure 47. Graphs. Strains in N-NE and S-SW bars in Specimen SF-3 at various locations below the interface.....	56
Figure 48. Graph. Thermal effects in strain gauges.....	58
Figure 49. Graph. Specimen SF-1 strain profiles in bottom mat of the footing.....	59
Figure 50. Graph. Specimen SF-2 strain profiles in bottom mat of the footing.....	60
Figure 51. Graph. Specimen SF-3 strain profiles in bottom of the footing.....	60
Figure 52. Graph. Specimen SF-1 transverse strains in bottom mat of the footing.....	63
Figure 53. Graph. Specimen SF-2 transverse strains in bottom mat of the footing.....	63
Figure 54. Graph. Specimen SF-3 transverse strains in bottom mat of the footing.....	64
Figure 55. Graph. Specimen SF-1 strains in diagonal steel in footing.....	65
Figure 56. Graph. Specimen SF-2 strains in diagonal steel in footing.....	65
Figure 57. Graph. Specimen SF-3 strains in diagonal steel in footing.....	66
Figure 58. Graph. Specimen SF-1 strains in ties.....	67
Figure 59. Graph. Specimen SF-2 strains in ties.....	68

Figure 60. Graph. Specimen SF-3 strains in ties. ....	68
Figure 61. Graph. Column vertical displacement vs. cumulative column drift. ....	70
Figure 62. Graph. Axial response of specimens SF-1 and SF-2. ....	71
Figure 63. Photo. Specimen SF-2 after axial load of 817 kips. ....	71
Figure 64. Diagram. Support conditions. ....	74
Figure 65. Equation. Shear stress demand. ....	79
Figure 66. Equation. Nominal shear capacity. ....	79
Figure 67. Equation. Nominal punching shear capacity including transverse steel. ....	81
Figure 68. Equation. Nominal punching shear capacity excluding transverse steel. ....	81
Figure 69. Equation. Nominal shear friction resistance. ....	82
Figure 70. Equation. Maximum principal compressive stress. ....	84
Figure 71. Equation. Maximum principal tensile stress. ....	84
Figure 72. Equation. Principal tensile stress. ....	84
Figure 73. Equation. Principal compressive stress. ....	85
Figure 74. Diagrams. Strut and tie models for bent-out bars (left) and headed bars (right). ....	86
Figure 75. Photo. Joint region of specimen SF-3 after failure. ....	87
Figure 76. Equation. Nominal axial-load capacity of the column. ....	87
Figure 77. Graph. Moment-curvature model. <sup>(15)</sup> ....	89
Figure 78. Equation. Plastic overstrength shear demand. ....	90
Figure 79. Equation. Nominal shear resistance. ....	91
Figure 80. Equation. Component of total shear resistance due to concrete strength. ....	91
Figure 81. Equation. Concrete shear resistance. ....	91
Figure 82. Equation. Contribution of total shear resistance due to transverse steel strength. ....	91
Figure 83. Equation. Analytical plastic hinge length. ....	92
Figure 84. Equation. Damage model for spalling. ....	93
Figure 85. Equation. Damage model for bar buckling. ....	93
Figure 86. Equation. Damage model for bar fracture. ....	93
Figure 87. Equation. Effective modulus of rigidity. ....	94
Figure 88. Graphs. Normalized equivalent moment-drift response. ....	95
Figure 89. Graph. Comparison of effective force vs. drift. ....	96
Figure 90. Equation. Energy dissipation. ....	97
Figure 91. Graphs. Calculated energy dissipation per cycle (top), and calculated cumulative energy dissipation (bottom). ....	97

Figure 92. Graph. Equivalent viscous damping calculated per cycle. ....	98
Figure 93. Equation. Equivalent viscous damping. ....	98
Figure 94. Graph. Equivalent viscous damping vs. drift. ....	99
Figure 95. Photos. Specimen SF-1 (left) and specimen SF-2 (right). ....	102
Figure 96. Diagram. Specimen SF-1 column elevation and sections. ....	109
Figure 97. Diagram. Specimen SF-1 top mat plan view. ....	110
Figure 98. Diagram. Specimen SF-1 bottom mat plan view. ....	111
Figure 99. Diagram. Specimen SF-1 sections. ....	112
Figure 100. Diagram. Specimen SF-2 column elevation and sections. ....	113
Figure 101. Diagram. Specimen SF-2 top mat plan view. ....	114
Figure 102. Diagram. Specimen SF-2 bottom mat plan view. ....	115
Figure 103. Diagram. Specimen SF-2 sections. ....	116
Figure 104. Diagram. Specimen SF-3 column sections. ....	117
Figure 105. Diagram. Specimen SF-3 column elevation. ....	118
Figure 106. Diagram. Specimen SF-3 bottom mat plan view. ....	119
Figure 107. Diagram. Specimen SF-3 footing sections A7 and A6. ....	120
Figure 108. Diagram. Specimen SF-3 footing sections A5 and B5. ....	121
Figure 109. Equation. Calculating yield strain. ....	128
Figure 110. Graph. Specimens SF-1/SF-2 stress-strain curves for No. 6 bars. ....	129
Figure 111. Graph. Specimens SF-1/SF-2 stress-strain curve for No. 5 bar. ....	129
Figure 112. Graph. Specimens SF-1/SF-2 stress-strain curve for No. 4 bar. ....	130
Figure 113. Graph. Specimens SF-1/SF-2 stress-strain curves for No. 3 bar. ....	130
Figure 114. Graph. Specimens SF-1/SF-2 stress-strain curves for stirrups (2-gauge wire). ....	131
Figure 115. Graph. Specimens SF-1/SF-2 stress-strain curves for spiral reinforcement (3-gauge wire). ....	131
Figure 116. Graph. Specimen SF-3 stress-strain curve for No. 7 bar. ....	132
Figure 117. Graph. Specimen SF-3 stress-strain curve for No. 6 bar. ....	132
Figure 118. Graph. Specimen SF-3 stress-strain curve for No. 5 bar. ....	133
Figure 119. Graph. Specimen SF-3 stress-strain curve for No. 4 bar. ....	133
Figure 120. Graph. Specimen SF-3 stress-strain curve for No. 3 bar. ....	134
Figure 121. Photo. Corrugated metal duct used in test specimens. ....	134
Figure 122. Photo. Specimen SF-1 flexural cracks after cycle 4-1 (+1.00/-1.00 target drift ratio). ....	135

Figure 123. Photo. Specimen SF-1: first significant spalling at cycle 6-2 (+2.48/-2.48 target drift ratio).....	135
Figure 124. Photo. Specimen SF-1: plastic hinge became more pronounced in subsequent cycles. Photo taken during cycle 8-1 (+4.28/-4.28 target drift ratio).....	136
Figure 125. Photo. Specimen SF-1: first noticeable bar buckling was the N-NW bar in cycle 9-2 (+7.40/-7.40 target drift ratio).....	136
Figure 126. Photo. Specimen SF-1: N-NE bar fractured first when the column was loaded to peak in cycle 10-2 (+10.65/-10.65 target drift ratio). ....	137
Figure 127. Photo. Specimen SF-1: damage after the cyclic testing. ....	137
Figure 128. Photo. Specimen SF-1: no damage to the footing was observed after the cyclic testing.....	138
Figure 129. Photo. Specimen SF-1: damage the end of testing. The column crushed after application of vertical load of 842 kips.....	138
Figure 130. Photo. Specimen SF-2: flexural cracks after cycle 3-2 (+0.83/-0.83 target drift ratio). ....	139
Figure 131. Photo. Specimen SF-2: first significant spalling at cycle 7-1 (+2.97/-2.97 target drift ratio).....	139
Figure 132. Photo. Specimen SF-2: the column fully spalled after cycle 8-1 (+4.28/-4.28 target drift ratio). ....	140
Figure 133. Photo. Specimen SF-2: first noticeable bar buckling was the N-NW bar in cycle 9-3 (+7.40/-7.40 target drift ratio).....	140
Figure 134. Photo. Specimen SF-2: N-NW bar fractured first when the column was being loaded to peak in cycle 10-2 (+10.65/-10.65 target drift ratio). ....	141
Figure 135. Photo. Specimen SF-2: damage after the cyclic testing. ....	141
Figure 136. Photo. Specimen SF-2: no damage to the footing was observed after the cyclic testing.....	142
Figure 137. Photo. Specimen SF-2: damage the end of testing. The column crushed after application of vertical load of 819.5 kips.....	142
Figure 138. Photo. Specimen SF-3: significant horizontal crack in cycle 3-1 (+0.69/-0.69 target drift ratio).....	143
Figure 139. Photo. Specimen SF-3: separation at column-footing interface in cycle 5-3 (+1.72/-1.72 target drift ratio).....	143
Figure 140. Photo. Specimen SF-3: first diagonal cracking in cycle 6-1 (+2.06/-2.06 target drift ratio).....	144
Figure 141. Photo. Specimen SF-3: first column spalling in cycle 6-2 (+2.48/-2.48 target drift ratio).....	144
Figure 142. Photo. Specimen SF-3: radial footing crack propagation in cycle 6-2 (+2.48/-2.48 target drift ratio).....	145

Figure 143. Photo. Specimen SF-3: large horizontal crack in cycle 6-2 (+2.48/-2.48 target drift ratio).....	145
Figure 144. Photo. Specimen SF-3: large column flexural cracks occurring in cycle 7-2 (+3.57/-3.57 target drift ratio).....	146
Figure 145. Photo. Specimen SF-3: full column spalling in cycle 9-1 (+6.16/-6.16 target drift ratio).....	146
Figure 146. Photo. Specimen SF-3: first footing spalling in cycle 9-2 (+7.40/-7.40 target drift ratio).....	147
Figure 147. Photo. Specimen SF-3: transverse steel exposed in cycle 9-3 (+7.40/-7.40 target drift ratio).....	147
Figure 148. Photo. Specimen SF-3: first exposure of longitudinal reinforcement in cycle 9-3 (+7.40/-7.40 target drift ratio).....	148
Figure 149. Photo. Specimen SF-3: fracture of transverse reinforcement in cycle 10-1 (+8.87/-8.87 target drift ratio).....	148
Figure 150. Photo. Specimen SF-3: major footing spalling occurring in cycle 10-1 (+8.87/-8.87 target drift ratio).....	149
Figure 151. Photo. Specimen SF-3: major cracks in the concrete core in cycle 10-2 (+10.65/-10.65 target drift ratio).....	149
Figure 152. Photo. Specimen SF-3: condition of specimen just before last cycle. ....	150
Figure 153. Photo. Specimen SF-3: column after punching through in last cycle (cycle 10-3, +10.65/-10.65 target drift ratio). ....	150
Figure 154. Photo. Specimen SF-3: column after punching though in last cycle (cycle 10-3, +10.65/-10.65 target drift ratio). ....	151
Figure 155. Photo. Column segments for specimens SF-1 and SF-2 were match-tied at a bridge construction site in the City of Redmond. ....	153
Figure 156. Photo. Roughened surface of octagonal, bottom portion of column.....	154
Figure 157. Photo. Specimens SF-1 and SF-2, column segments formed and ready to be cast. ....	154
Figure 158. Photo. Specimen SF-3, column formed and ready to be cast.....	155
Figure 159. Photo. Specimen SF-1 footing ready to be cast.....	156
Figure 160. Photo. Specimen SF-3 footing formwork and reinforcement. ....	156
Figure 161. Photo. Specimen SF-3 column inserted into footing that is ready to cast.....	157
Figure 162. Photo. Specimen SF-3: finishing the footing surface.....	157
Figure 163. Diagram. Column detail with projecting bars. ....	160
Figure 164. Diagram. Socket column concept.....	163
Figure 165. Diagram. Long struts concept.....	164
Figure 166. Diagram. Short struts concept. ....	166

## LIST OF TABLES

Table 1. Strain gauge types used in the specimens.....	22
Table 2. Target displacement history.....	24
Table 3. Damage state description.....	26
Table 4. Damage milestones for all three specimens.....	27
Table 5. Average concrete strength on test day.....	35
Table 6. Average grout strength on test day.....	36
Table 7. Measured mild reinforcement properties.....	37
Table 8. Moments and drift ratios at maximum and 80 percent of maximum resistance.....	41
Table 9. Effective force and displacement at maximum and 80 percent of maximum resistance.....	44
Table 10. Axial load and strains across and near splice interfaces.....	49
Table 11. Axial load combinations on the test specimens.....	69
Table 12. External forces, displacements, and estimated reactions.....	75
Table 13. Footing flexural capacities and demands.....	76
Table 14. Footing one-way strength capacities and demands.....	78
Table 15. Combined punching shear and moment transfer capacities and demands.....	79
Table 16. Punching shear capacities and demands.....	80
Table 17. Footing shear-friction capacities and demands.....	84
Table 18. Footing joint shear stress capacities and demands.....	85
Table 19. Column axial-load capacities and demands.....	88
Table 20. Column flexural capacities and demands.....	90
Table 21. Column shear capacities and demands.....	91
Table 22. Comparison of damage model predictions and observed occurrences.....	93
Table 23. Comparison of model prediction and measured effective modulus of rigidity.....	94
Table 24. Summary of ratios of footing demands to calculated capacities.....	103
Table 25. Slump and air content test results.....	123
Table 26. Concrete compressive strengths up to 28 days.....	124
Table 27. Concrete compressive strengths on test day.....	125
Table 28. Concrete split cylinder strengths on test day. <sup>1</sup> .....	126
Table 29. Grout cube strength on test day.....	127
Table 30. Measured mild reinforcement properties.....	128



## LIST OF ABBREVIATIONS AND ACRONYMS

AASHTO	American Association of State Highway and Transportation Officials
ABC	Accelerated Bridge Construction
ACI	American Concrete Institute
ASCE	American Society of Civil Engineers
BDM	Bridge Design Manual
Caltrans	California Department of Transportation
CCC	Compression-compression-compression
DL	Dead load
HSS	Hollow structural section
LL	Live load
LRFD	Load and Resistance Factor Design
LVDT	Linear variable differential transformer
MEF	Maximum effective force
NEHRP	National Earthquake Hazards Reduction Program
o.c.	On center
o.d.	Outside diameter
OT	Overturning
PEER	Pacific Earthquake Engineering Research
PTFE	Polytetrafluoroethylene
SDC	Seismic Design Criteria
WSDOT	Washington State Department of Transportation



## CHAPTER 1. INTRODUCTION

### NEED FOR RAPID CONSTRUCTION

Numerous bridges in the United States are either functionally or structurally obsolete.<sup>(1)</sup> The replacement of these bridges and the construction of new ones will create the need for extensive bridge construction in the near future. If these bridges are built using conventional cast-in-place methods, this construction will exacerbate traffic congestion, which is already a costly problem, especially in urban areas.

New structural systems and construction methods are needed to reduce the time spent on-site. One solution for reducing construction-related delays is to precast structural elements off-site and then assemble them rapidly once they arrive on-site. This approach also has other benefits, such as improved worker safety and construction quality.

However, the use of precast components poses potential problems in seismic regions, where the connections need to accommodate inelastic deformations without loss of strength. To make fabrication and transportation easier, connections are typically made at beam-to-column and column-to-footing interfaces. During an earthquake, these interfaces are also the locations that experience the largest moments and inelastic deformation reversals. Designing connections for both ease of construction and seismic resistance is a daunting challenge.

Precast concrete has been used successfully for bridge substructures in non-seismic regions.<sup>(2,3)</sup> At the University of Washington, research on accelerated bridge construction (ABC) has focused on the development of precast concrete bridge substructures for seismic regions.<sup>(4,5)</sup> Hieber et al. performed numerical studies on two types of bridge piers made of precast elements and subjected to ground motions.<sup>(6)</sup> Wacker et al. developed displacement-based and force-based design procedures for precast systems.<sup>(5)</sup>

Pang et al. developed a “large-bar” column-to-cap beam connection.<sup>(7,8)</sup> In this connection, projecting column bars are grouted into ducts in the cap beam using only a small number of bars to facilitate fit-up on-site. The small number of bars means that each one must be large and, according to typical code provisions, such bars may require development lengths longer than those available in the cap beam. Tests on the pull-out strength of bars grouted in ducts showed that even No. 18 bars can be developed properly within the depth of a typical cap beam.<sup>(9,10)</sup> Cyclic tests on column-to-beam connections demonstrated that the seismic performance of the large-bar precast subassembly was essentially identical to that of a typical cast-in-place connection.<sup>(7)</sup> Cohagen et al. tested a similar connection that contained unbonded post-tensioning to improve the re-centering characteristics of the column after the ground motions stops.<sup>(11)</sup> Those tests showed that the post-tensioned tendon improves the re-centering for peak drifts greater than about 2 percent and offers an opportunity for improving the seismic performance of the bridge bents.

After the column-to-cap beam connection was developed, the research team turned their attention to the column-to-foundation connection. The grouted bar system used for the cap-beam connection can be used there, but it is more difficult to construct, so other concepts were investigated.

Three socket columns in spread footings were tested in two stages in the University of Washington Structural Research Laboratory. Haraldsson constructed two socket specimens.<sup>(12)</sup> In the first, the reinforcement was detailed to comply with current codes and design practice. In the second, the amount of secondary reinforcement, such as ties, was reduced below the prescriptive minimum, which made the connection easier to construct. Janes tested a third specimen with a thinner footing to better understand the failure behavior and limitations of the connection.<sup>(13)</sup> This report describes the development, testing and measured performance of these three socket connections.

## SOCKET CONNECTION CONCEPT

The new socket connection concept is shown in figure 1. It is suitable for use with spread footings. The column is precast with a roughened outer surface at the bottom of the column that will be embedded in the cast-in-place footing. Once the footing has been excavated, the column is brought to site, plumbed, leveled, and braced. Top and bottom footing reinforcement is then placed around the column, and the footing is cast. The final step is to connect the column to the cap beam by casting the footing. In comparison with conventional cast-in-place construction, the primary advantage of this system is construction speed; a footing and column can be built in little more time than is needed to cast the footing alone.

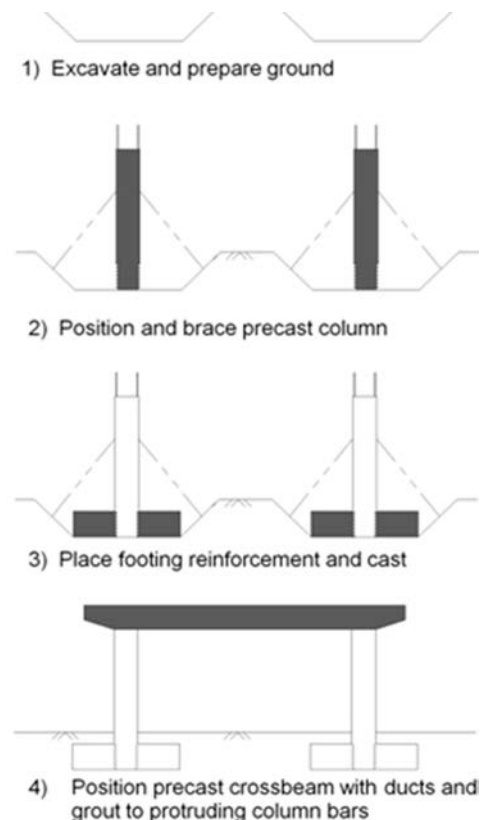


Figure 1. Diagram. Rapid construction sequence.

The structural details of the connection were developed at the University of Washington with extensive help from the Washington State Department of Transportation (WSDOT), Berger/ABAM Engineers, Tri-State Construction, Concrete Technology Corporation, and others in the construction industry.

The structural details differ from those of a conventional, cast-in-place system in two ways. First, no bars pass from the footing into the column, so the only resistance to vertical load comes from shear friction across the interface between the precast column and the cast-in-place footing. That interface is intentionally roughened to facilitate this load transfer. Second, the longitudinal column bars are not bent out at the bottom, but instead, they achieve their anchorage by headed anchors. This choice simplifies transportation and handling, and it reduces the hazard posed by protruding bars. The configuration also provides a much simpler and more direct flow of internal forces than is possible with bent-out bars. The transfer of internal forces is illustrated by the strut-and-tie model shown in figure 2. Figure 2a shows that, with conventional bent-out bars, the force in the diagonal strut must be transferred to the vertical bar by bond around the curved region of the bar. That mode of transfer is relatively weak, and a diagonal crack forms in the footing when the bond fails. By contrast, the headed bar shown in figure 2b achieves the load transfer very effectively at a compression-compression-compression (CCC) node.

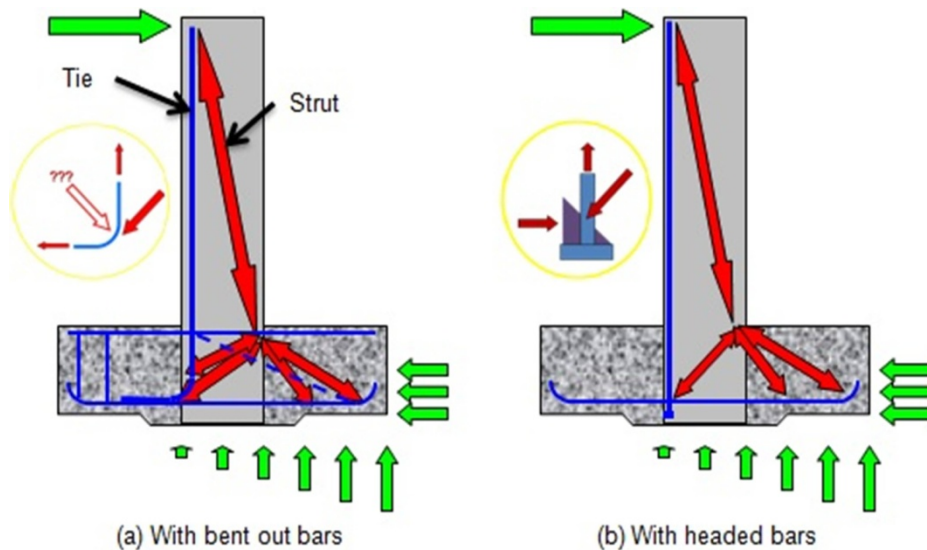


Figure 2. Diagram. Strut-and-tie models for (a) bent out bars and (b) headed bars.

A preliminary version of the socket connection was deployed as part of a bridge over SR520 in Washington State (see figure 3).



Figure 3. Photo. Earlier form of the socket connection used by the City of Redmond over Washington State SR 520, as originally used.

## **OBJECTIVES AND SCOPE**

The goal of the research was to evaluate the seismic and gravity load performance of a socket column-to-foundation connection proposed for a precast bent system with spread footings. The connection concept is to precast the column with an intentionally roughened surface in the region that will be eventually embedded in the cast-in-place footing.

The global question to be resolved is whether the proposed column-to-footing connection can transfer moments from the column to footing under cyclic lateral loading, such as imposed by an earthquake, while resisting large vertical loads that might be caused by a combination of gravity and seismic loadings.

The specific questions to be addressed by this research are primarily structural:

- Does the precast column need to be designed such that the bottom layer of footing reinforcement passes through or under the column? It would be more convenient to place these reinforcing bars outside of the column footprint.
- Is shear friction steel needed between the precast column and the surrounding cast-in-place footing? Such friction steel would typically be placed with form savers where the bars are screwed into the column base, which would slow down construction. If shear friction steel is needed at all, it would be more convenient to place the bars diagonally around the column so that they provide a normal force across the interface between the precast and cast-in-place elements without crossing it.
- If the diagonal bars that trim the space around the column can be used to replace shear-friction steel across the interface, can the amount required be reduced greatly? It would be even more convenient if only a few diagonal bars were needed.

- By using headed bars at the base of the precast column, is it possible to place fewer ties in the footing than are required by current bridge specifications? Placing ties footings can be time-consuming.

Two scaled (42 percent) cantilever test specimens (SF-1 and SF-2) were constructed to answer these questions. One was designed according to current design specifications—the 2009 American Association of State Highway and Transportation Officials (AASHTO) *LRFD [Load and Resistance Factor Design] Bridge Design Specifications* (referred to hereinafter as AASHTO LRFD), the 2009 *AASHTO Guide Specification for LRFD Seismic Bridge Design* (AASHTO Seismic Guide Specifications), the 2006 *Caltrans Seismic Design Criteria* (Caltrans SDC), and the 2008 *WSDOT Bridge Design Manual* (BDM). (See references 14, 15, 16, and 17.) The other was a simpler, less conservative version that is easier to construct.

As discussed in chapters 4 and 5, the results of these tests showed that the socket connection performed exceptionally well. The damage and deformation were concentrated in the columns, while the footings remained unscathed. The simpler, less conservative specimen (SF-2) performed as well as the specimen designed to the current specifications (SF-1).

Since neither specimen failed in the connection region, further investigation was needed to determine how and when the footing could fail. This could only be done by testing a column with a footing thinner than tested previously, in which the footing depth had been approximately equal to the column diameter. A footing thinner than the column diameter is relatively unusual, but it may be necessary for large columns, in which very deep footings would lead to overheating while the footing concrete cures. A third test was conducted on a column-to-footing specimen with a thin footing, identified as specimen SF-3. The third specimen was designed to address the following questions:

- How far can the footing depth be reduced before failure occurs in the connection zone of the footing rather than the column?
- What is the failure mode for the footing?
- Footing failure by combined punching shear and moment transfer is currently not recognized in the AASHTO LRFD. (Such failure is recognized in American Concrete Institute [ACI] 318 for slabs around columns).<sup>(18)</sup> Could this type of failure occur in a spread footing?

Chapter 2 describes the development of the test specimens and describes the proposed connection in detail. Chapter 3 describes the experimental program. The subsequent two chapters evaluate the performance of the proposed connection by considering the damage progression (chapter 4) and measured response (chapter 5). Chapter 6 provides an analysis of test results, and finally, chapter 7 summarizes the report findings and gives recommendations for future research.



## CHAPTER 2. DESIGN OF TEST SPECIMENS

Three cantilever column specimens with footings were designed, constructed, and tested as part of this research. All three specimens had identical 20-inch-diameter, 60-inch-long precast columns, resulting in a span-to-depth ratio of 3. Each column was embedded in a cast-in-place footing (90 inches long and 68 inches wide). This geometry represented, at 42 percent scaling, a 48-inch-diameter column embedded in an 18-foot by 18-foot cast-in-place footing. Those dimensions were the ones used in a prototype bridge constructed by WSDOT shortly after completion of the testing. The prototype bridge was designed in parallel with the development and testing of the socket concept.

The specified nominal material strengths for the test specimens were the same as for the prototype bridge. The concrete strength specified was 4 ksi for both the columns and the footings, and all reinforcement conformed to ASTM A706. Expected material strengths were used in the design, in accordance with the AASHTO Seismic Guide Specifications. The construction drawings for the three specimens are provided in appendix A.

Specimens SF-1 and SF-2 were nearly identical. For scheduling reasons, both had to be built at the same time, so the reductions in reinforcement used in specimen SF-2 had to be based on estimates, rather than knowledge of the performance of specimen SF-1.

- The cast-in-place footings had the same geometry (22.5 inches deep, 90 inches long, and 68 inches wide).
- Both columns were segmental and included a splice 20 inches above the footing surface. At this location, it was expected that the yield moment would develop at the same time as the ultimate moment would develop at the column-to-footing interface. These moments were calculated for the smallest axial load expected for the prototype column on site, which corresponded to the unfactored dead load and included the effects of overturning. The scaled down axial load was 87.5 kips.

SF-1 and SF-2 differed only in the column-to-footing connection details, including:

- The presence (SF-1) or absence (SF-2) of a slot at the base of the embedded column to permit some of the footing steel to be placed directly under the column.
- The amount of diagonal reinforcement in the footing surrounding the column was less in specimen SF-2.
- The amount of transverse reinforcement within the footing was reduced 50 percent in specimen SF-2.

The design of specimen SF-3 was influenced by the test results of specimens SF-1 and SF-2. In the first two tests, the failure occurred in the columns, so specimen SF-3 was designed to fail in the footing. The specimen had the same column design as specimens SF-1 and SF-2, in which the expected moment strength was 3,100 kip-in. However, the footing depth in SF-3 was reduced to half of the column depth (10 inches). Reinforcement in the footing was placed in strategic locations to suppress one-way shear failure but allow for a combined punching shear and moment transfer failure mechanism to occur.

## DESIGN OF PROTOTYPE AND TEST COLUMNS

The test specimen dimensions and reinforcement were scaled (42 percent) from a bridge over Interstate 5 (US 12) designed by WSDOT. This bridge was designed according to the AASHTO LRFD, the AASHTO Seismic Guide Specifications, the WSDOT BDM, and the Caltrans Seismic Design Criteria (SDC). (See references 14, 15, 16, and 17.) The AASHTO Seismic Guide Specifications were based on the Caltrans SDC, but the 2009 edition omits some reinforcement steel as footing ties. These ties are expected to be included in the next edition of the AASHTO Seismic Guide Specifications. For those details, the Caltrans criteria were used in the project.

The prototype columns were constructed of precast concrete with three segments (top, base and middle). Segmental construction was not necessarily economical in this case, but WSDOT wanted to use this project to test its feasibility in future projects in which it would be necessary. Both the top and base segments had a longitudinal reinforcement ratio,  $\rho_l$ , of 1.0 percent (8 No. 14 bars) and a transverse reinforcement ratio,  $\rho_s$ , of 0.76 percent (No. 5 spiral at 4-inch pitch). In the prototype, the top segments had projecting bars that were to be grouted into ducts in the cap beam. This top segment was not modeled in the laboratory for this project, because it had already been tested.<sup>(8)</sup>

The bottom part of the base segment that was embedded in the cast-in-place footing was intentionally roughened with a saw-tooth detail similar to the one required by the WSDOT BDM for the ends of prestressed girders. Shear-friction design of the socket was calculated according to the AASHTO LRFD. The longitudinal bars for the base segment were terminated with mechanical anchors at their bottom ends, instead of the more conventional detail of bending the longitudinal bars outwards into the foundation.

In the prototype, the middle segments had 16 No. 10 bars lap-spliced at both ends to steel ducts and confined by No. 5 spiral at 4-inch pitch. All reinforcement conformed to ASTM A706. Prescribed ducts conformed to ASTM A653 and were 30 inches tall and had an outside diameter (o.d.) of 4 inches.

For the prototype, the locations of the splices were determined by plastic-hinge length calculations performed using procedures found in the AASHTO Seismic Guide Specifications. AASHTO Seismic Guide Specifications article 4.11.7 requires that heavier lateral confinement reinforcement be provided over the plastic-hinge region length,  $L_{pr}$ . The length is to be taken as the larger of:

- 1.5 times the gross-section column diameter (72 inches).
- The location where 75 percent of the overstrength moment occurs (30 inches).
- The analytical plastic-hinge length calculated using equation 4.11.6-1 in the AASHTO Seismic Guide Specifications (35 inches).

The location of the splice for the prototype bridge was controlled by 1.5 times the cross-sectional diameter, which corresponded to 6 feet above the footing-column interface.

Specimens SF-1 and SF-2 were constructed segmentally, similar to the prototype. The longitudinal reinforcement for the scaled-down precast base segment of the column consisted of

eight No. 6 bars and had projecting bars to be grouted in ducts in the middle segment. However, the transverse reinforcement ratio was increased slightly to 0.88 percent to be consistent with previous tests done at the University of Washington.<sup>(8,11)</sup> The transverse reinforcement consisted of 3-gauge (0.244-inch-diameter) smooth spiral at a pitch of 1.25 inches. The diameters of the steel ducts were scaled down from the prototype 4 inches to 1.67 inches, but the duct length of 15 inches was controlled by the splice length requirements between the ducts and longitudinal bars in the specimen's top segments. The splice length was evaluated using the procedure described in article 12.2.3 in ACI 318-08, rather than the AASHTO LRFD, because ACI's procedure resulted in a more conservative development length than that of the AASHTO LRFD. In both procedures, a reduction factor based on the presence of the column spiral confinement was used, and an amplification "top steel" factor was used because the precast columns were to be cast horizontally. (The size of the test precast columns would have allowed them to be cast vertically, but that was not true for the prototype columns.) In the test specimen, a shear key was added in the joint between column segments, even though the horizontal shear could theoretically be fully resisted by the longitudinal reinforcement crossing the interface between the segments. Figure 4 shows an elevation for specimens SF-1 and SF-2.

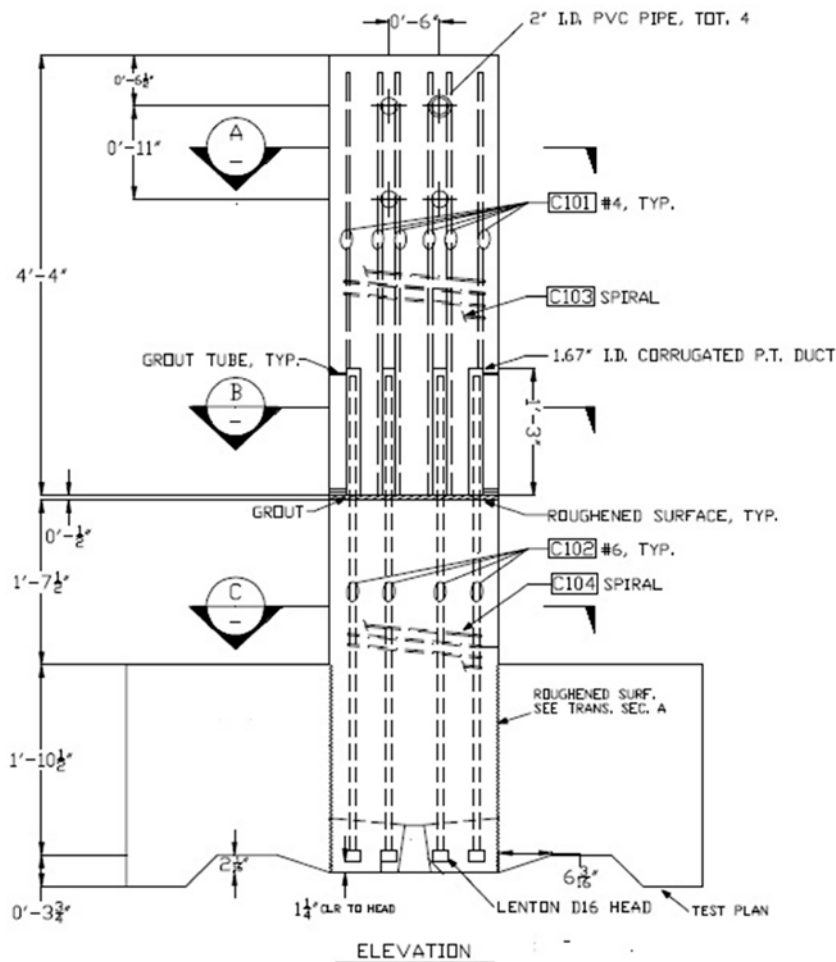


Figure 4. Diagram. Precast column elevation for specimens SF-1 and SF-2.

To better understand the performance of the splices near the yield moment, the splice locations in SF-1 and SF-2 were located less conservatively than would be required by the AASHTO Seismic Guide Specifications. Namely, the splices were located such that the first yield moment ( $M_y = 1,861$  kip-in.) was expected to develop at the splice at the same time the overstrength moment ( $M_{po} = 2,792$  kip-in.) was reached at the interface (assuming an axial load of 87.5 kips, the smallest unfactored axial load in the scaled-down column). That moment was calculated to occur 20 inches above the footing surface, which was less than 1.5 times the specimen column diameter.

The column in specimen SF-3 did not consist of two segments like the previous two specimens, but rather, it was cast as one piece and had the same reinforcement detail as the bottom segments in specimens SF-1 and SF-2.

The dimensions of the roughened surface at the column base (that was going to be embedded in the cast-in-place footing) were scaled down to 42 percent of those of the prototype.

The moment-curvature program XTRACT was used to analyze the test specimens. Steel and concrete were modeled according to the AASHTO Seismic Guide Specifications, and the confined concrete was modeled using Mander's confined concrete model.<sup>(19)</sup>

## **DESIGN OF PROTOTYPE AND TEST SPECIMEN COLUMN-TO-FOOTING CONNECTION**

### **Specimens SF-1 and SF-2**

The prototype spread footing was designed according to the AASHTO LRFD, the AASHTO Seismic Guide Specifications, the WSDOT BDM, and the Caltrans SDC. Elevations of the spread footing for SF-1 and SF-2 are provided in figure 4. The detailed drawings of these two specimens are provided in appendix A.

Stability against overturning and one-way shear determined the footing's dimensions. The AASHTO Seismic Guide Specifications require that the resultant reaction forces be located within the center two-thirds of the base, if no live load were present, which resulted in a footing length and width of 18 feet. The one-way shear stress demand was kept limited to  $2\sqrt{f'_c}$  (psi) by keeping the depth at 4.5 feet. Minimum transverse reinforcement was provided using No. 5 bars at 12 inches within the effective width, as required by the Caltrans SDC. Top and bottom flexural steel were determined by minimum steel requirements and resulted in No. 8 bars at 12 inches on center (o.c.) and No. 11 bars at 12 inches o.c., respectively, in each principal direction. Diagonal bars, 12 No. 10, were placed horizontally around the column, to provide confinement of the region around the column which would lead to normal force and corresponding shear friction resistance across the interface between the precast and cast-in-place elements. They are shown in figures 5 and 6, marked as F115. The diagonal bars were concentrated into three sets at the bottom and one at the top. The diagonal reinforcing steel used was equal to the amount needed if the cohesive component of the shear friction force defined by the AASHTO LRFD was ignored completely. An additional four No. 8 diagonal bars were provided on the top mat for trimming purposes.

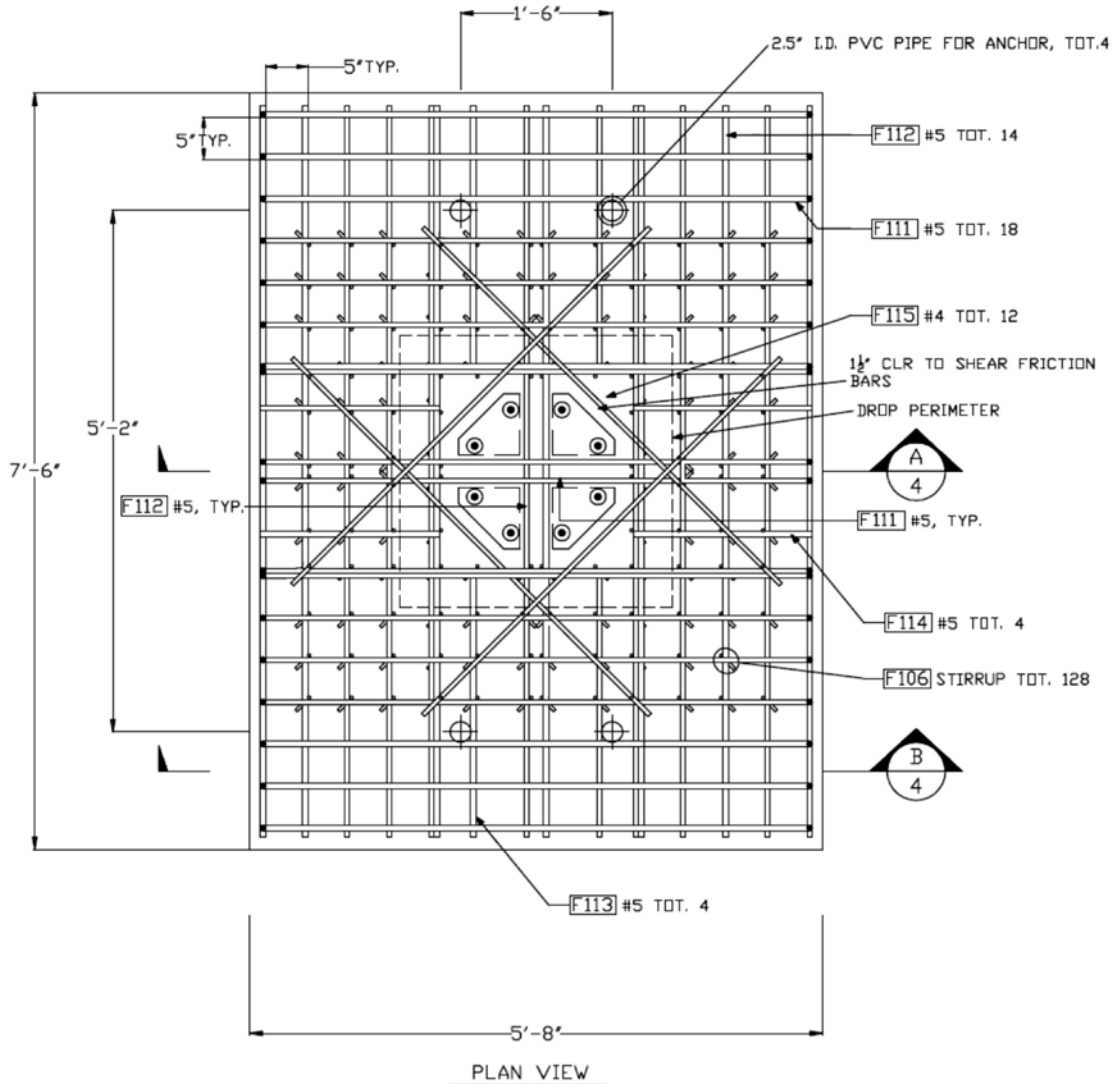
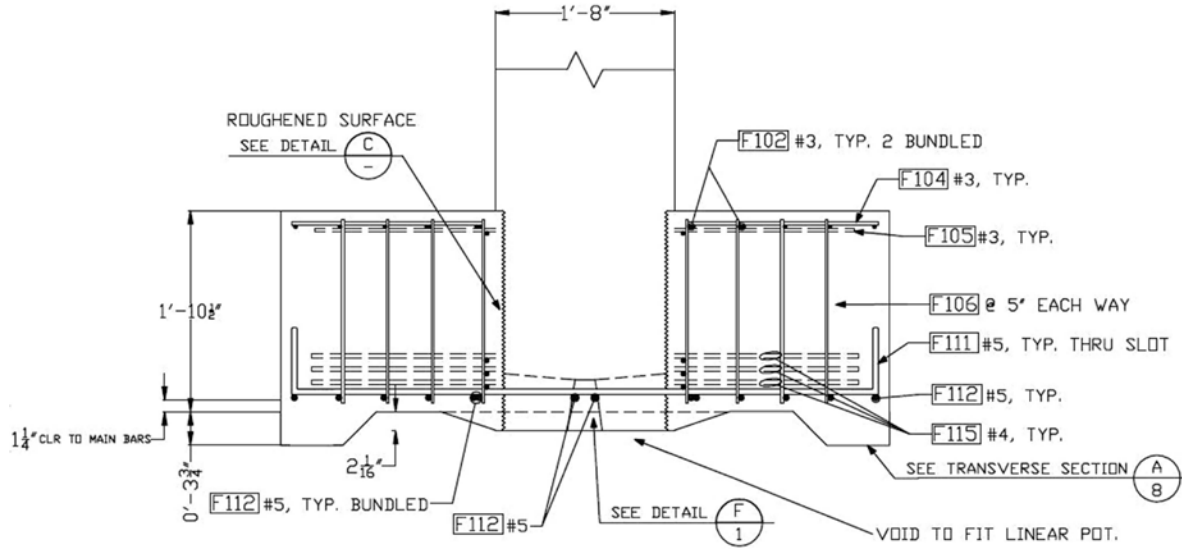


Figure 5. Diagram. Specimen SF-1 footing steel arrangement.

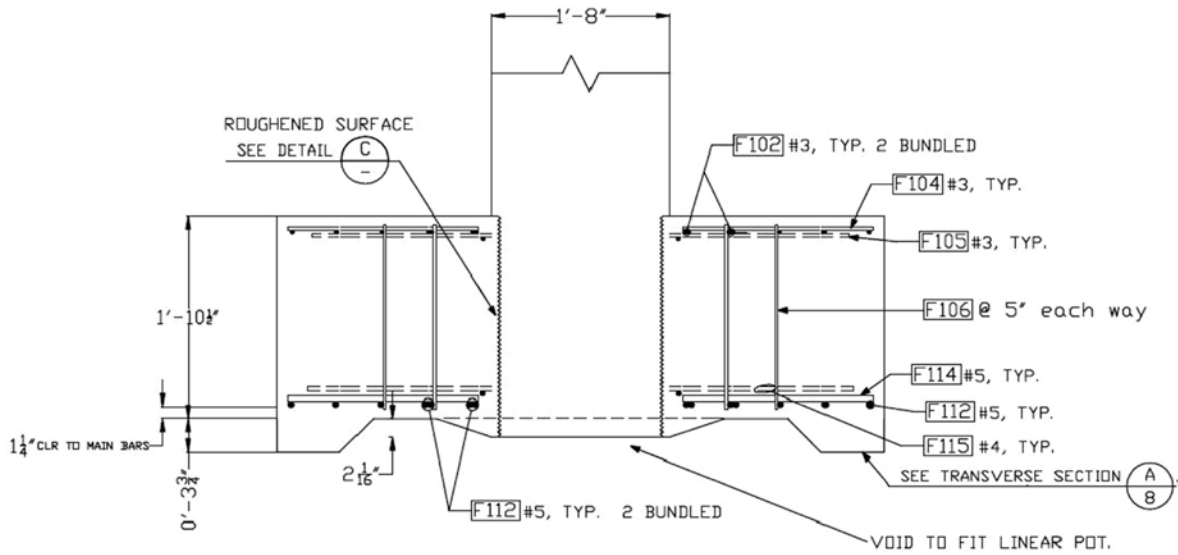
The design of SF-1 was the more conservative.<sup>(12)</sup> SF-1 had slots under the column to allow some bars of the bottom mat (No. 5 at 5 inches o.c.) reinforcement to go through the base of the column, which ensured a direct engagement between the compressive strut from the column and the tension steel in the footing. The scaled-down top mat consisted of No. 3 bars at 5 inches o.c. Diagonal shear friction bars placed around the column were 12 No. 4 in the bottom and 4 No. 3 in the top. Caltrans's requirement of transverse reinforcement was met with 3-gauge ties at 5-inch spacing within the effective width of the footing. The total number of stirrups was therefore 128 in specimen SF-1.

Specimen SF-2 was a simplified version of specimen SF-1. One difference was that the slots at the base of the columns were removed to simplify the column formwork. Consequently, the bars could not go under the column, and instead, they were bundled with existing bars on either side of the column. Most of the diagonal shear friction steel was taken out, leaving only one set (four

bars) in each of the bottom and top mats. Ties were reduced by half and kept in the locations where they would most effectively engage with 45-degree compressive struts.



(a) SF-1 (Conservative)



(b) SF-2 (Simpler)

Figure 6. Diagrams. Spread footing cross section for (a) SF-1 and (b) SF-2 (section A-4).

### Specimen SF-3

The design of specimen SF-3 was based on the test results for specimens SF-1 and SF-2, in which nearly all of the damage was concentrated in the column, as opposed to the footing.<sup>(13)</sup> The footing in SF-3 was designed to be much thinner to increase the likelihood of footing damage.

To estimate the failure load and mode of the footing, a design space was created based on AASHTO code criteria. However, the demands were based on the columns strength calculated using expected material properties ( $f_y = 68$  ksi and  $f'_c = 5.2$  ksi), while the footing and connection capacities were based on nominal strengths, calculated with  $\phi$  factors according to the AASHTO LRFD and AASHTO Seismic Guide Specifications. The design space (displayed in figure 7 for specimen SF-3) shows combinations of the normalized column depth ( $h_{footing}/D_{column}$ ) and normalized footing length ( $L_{footing}/D_{column}$ ) that would lead to failure. Each curve in the figure corresponds to a particular failure mode. Combined shear and moment transfer was also added to the design space, where it is designated “ACI moment transfer.” Each curve is marked “above” or “below,” to indicate whether the design point on the graph should lie above or below the curve.

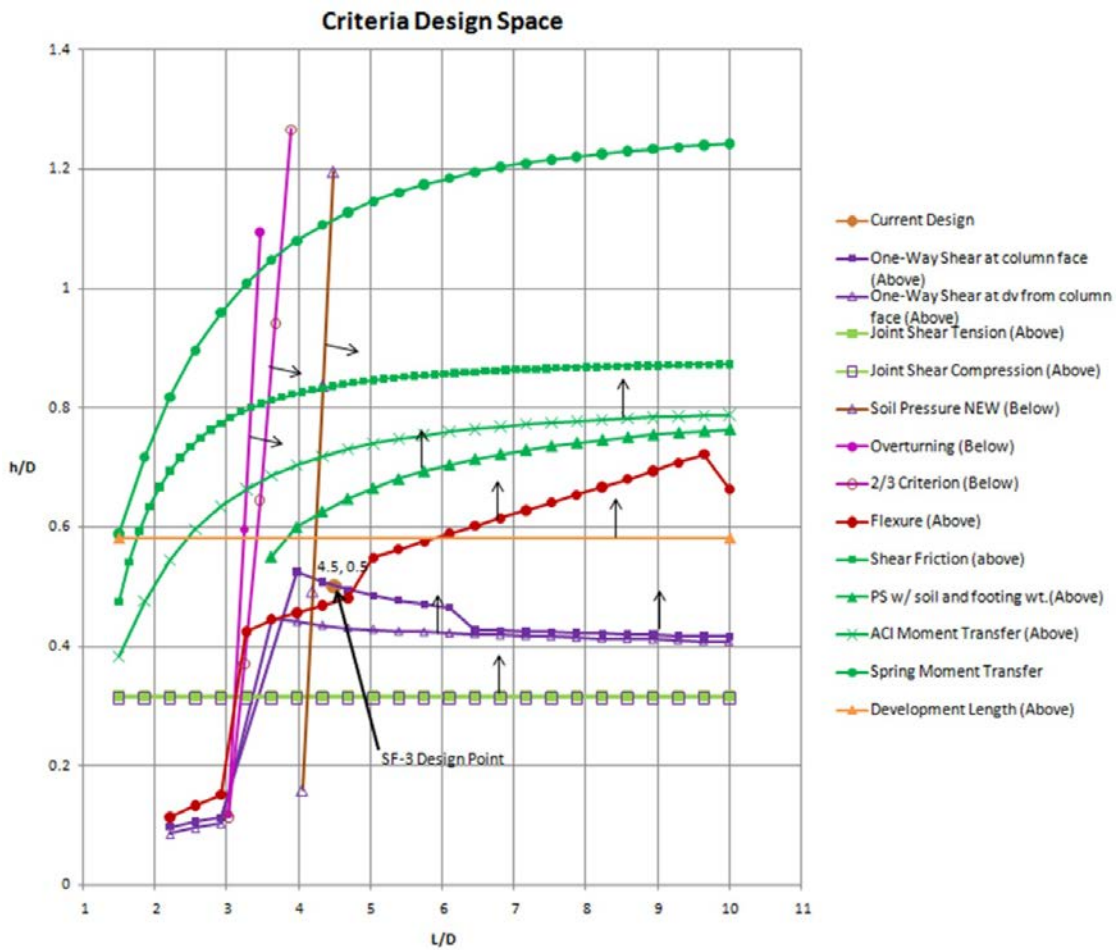


Figure 7. Graph. Final criteria design space for specimen SF-3.

The  $L_{footing}/D_{column}$  ratio of the footing was determined by overturning considerations to be 4.5. Then, the design space showed that the critical failure modes were one-way shear, and the ACI combined punching shear and moment transfer mechanism (shown as the green line with “x” marks). Note that the design space also shows a potential shear friction failure and a column longitudinal bar development failure. These criteria are not relevant in the design of specimen SF-3. First, the shear friction curve corresponds to shear friction resistance provided by the cohesive component alone and ignores the benefits of any shear friction steel. In fact, shear friction steel was provided. Second, the longitudinal bar development curve does not account for the fact that the column bars were terminated with mechanical anchors.

To suppress the one-way beam shear but allow combined punching shear and moment transfer to occur, shear reinforcement needed to be placed in strategic locations. Transverse reinforcement was placed outside the nominal conical failure surface for punching shear (extending  $d$  from the column faces in all directions) but within the beam shear failure planes (consisting of lines located  $d$  from the “compression” and “tension” faces of the column). Since the column portion embedded in the footing was octagonal, the failure plane was predicted to be closer in shape to that of an octagon, and is shown in figure 8 as the perimeter marked “punching shear critical perimeter.” Placement of the shear reinforcement was also limited by the effective shear width defined in the AASHTO Seismic Guide Specifications, which is shown in figure 8 as the effective width boundary.

The result of this design procedure was a footing depth that was half the column diameter. Unlike specimens SF-1 and SF-2, the bottom flexural reinforcement of specimen SF-3 was not controlled by minimum requirements. Strength considerations resulted in No. 7 bars at 2.5 inches o.c. in which the first four lines of steel on either side of the column were bundled. Minimum steel was placed in the top mat, and instead of distributing those bars along the specimen’s width, fewer and larger bars were used and were placed near the column to hold up the ties. Since the tie steel was designed to suppress the one-way shear failure mechanism, it exceeded the Caltrans SDC minimum requirement of  $2\sqrt{f'_c}$  (psi) stress capacity and resulted in a stress of about  $5\sqrt{f'_c}$  (psi) (area of steel within the effective width,  $b_{eff}$ , 40 inches). The 2 to 1 ratio of column diameter to footing depth, along with suppression of beam shear, predicted that the footing would fail in combined punching shear and moment transfer. Figures 9 and 10 show sections through the footing.

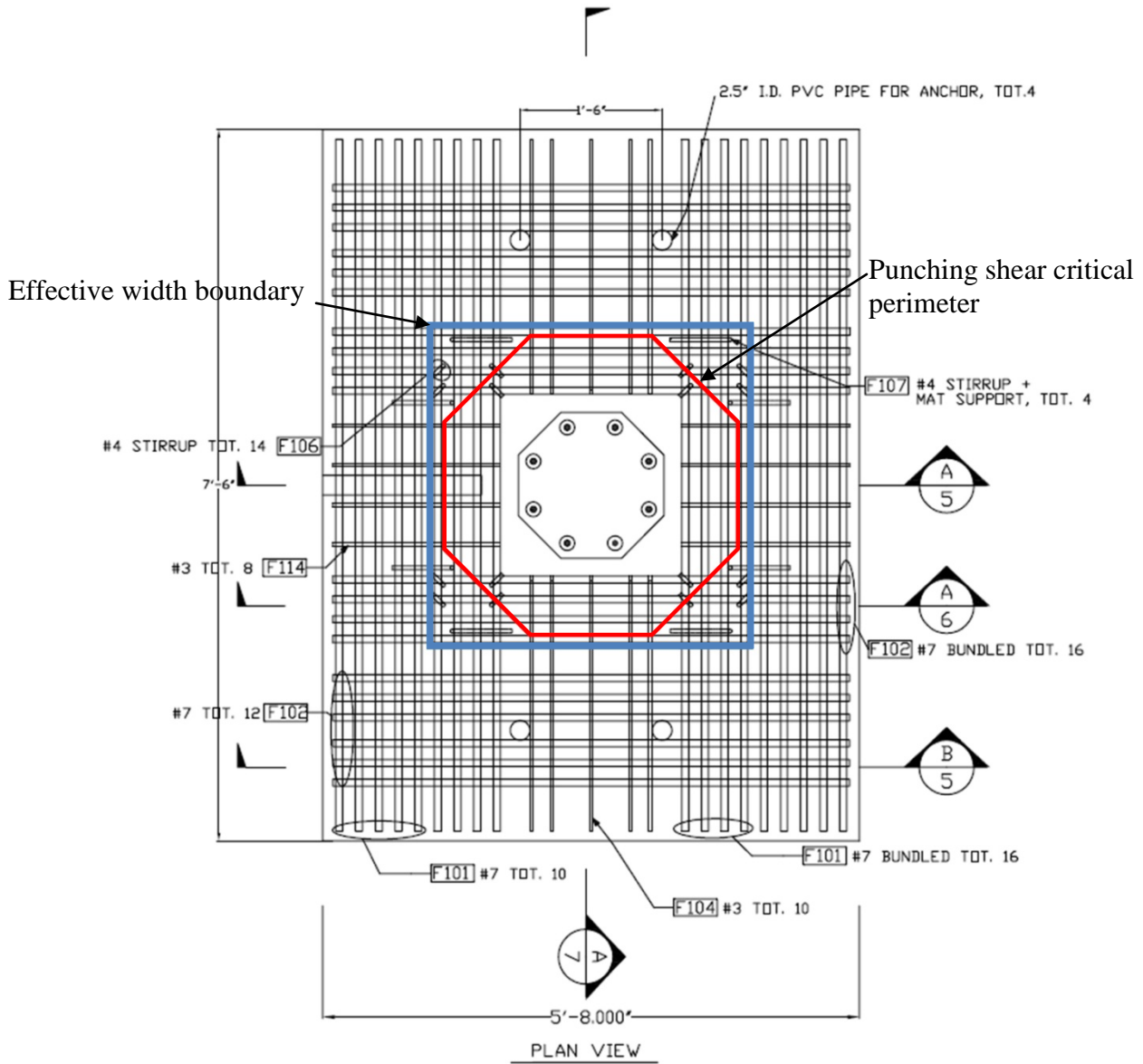


Figure 8. Diagram. Specimen SF-3 footing steel arrangement.

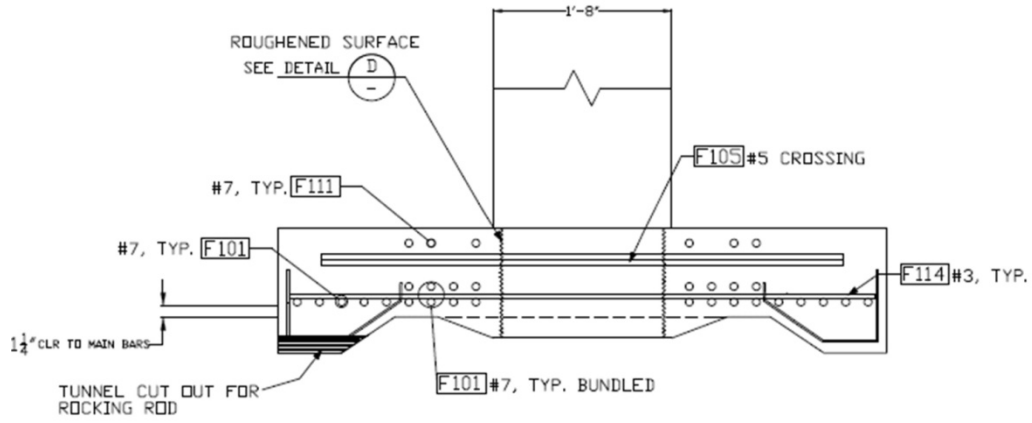


Figure 9. Diagram. Specimen SF-3 spread footing cross-section (section A-5).

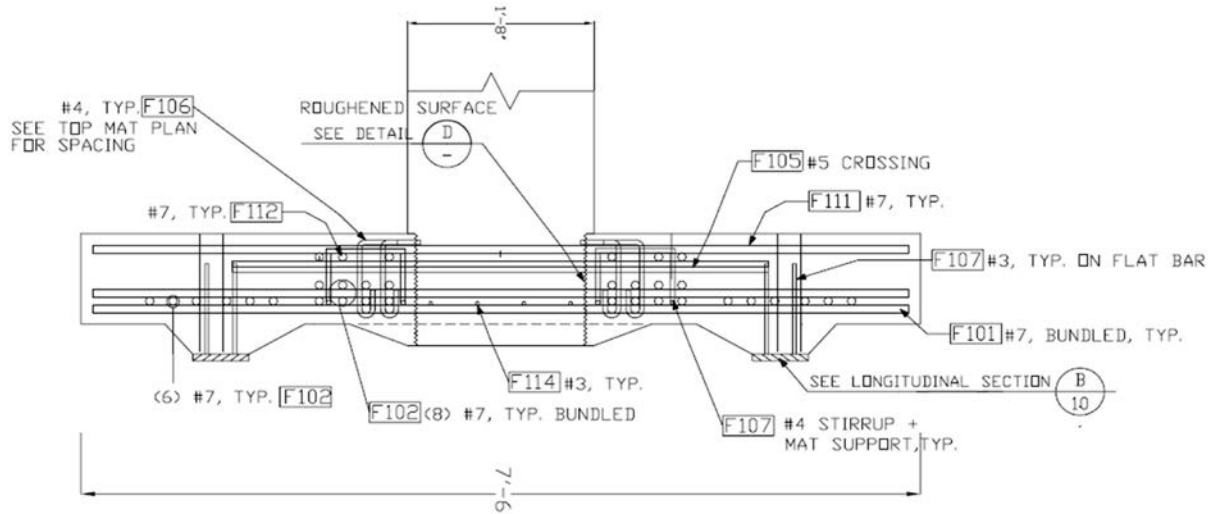


Figure 10. Diagram. Specimen SF-3 longitudinal section (section A-7).

## CHAPTER 3. EXPERIMENTAL PROGRAM

### LOADING SETUP

The three specimens were tested using the self-reacting loading assembly shown in figure 11. The specimen was placed in the loading assembly, leveled with shims, and attached to the underlying footing with Hydrostone. To prevent possible overturning, four threaded 1.25-inch-diameter Williams bars were placed in plastic tubes through the footing and threaded into nuts cast into the underlying concrete block. The top nuts on these bolts were left with a clearance of 1/16 inches to prevent them from providing resisting forces until the base started to overturn. This gap was introduced because the specimen had been designed to simulate a spread footing in the field, in which no such holding down force could exist. The bolts were used only as a backup system to prevent overturning in the event that the column proved unexpectedly strong, and the lateral strength was controlled by overturning rather than the strength in one of the structural components.

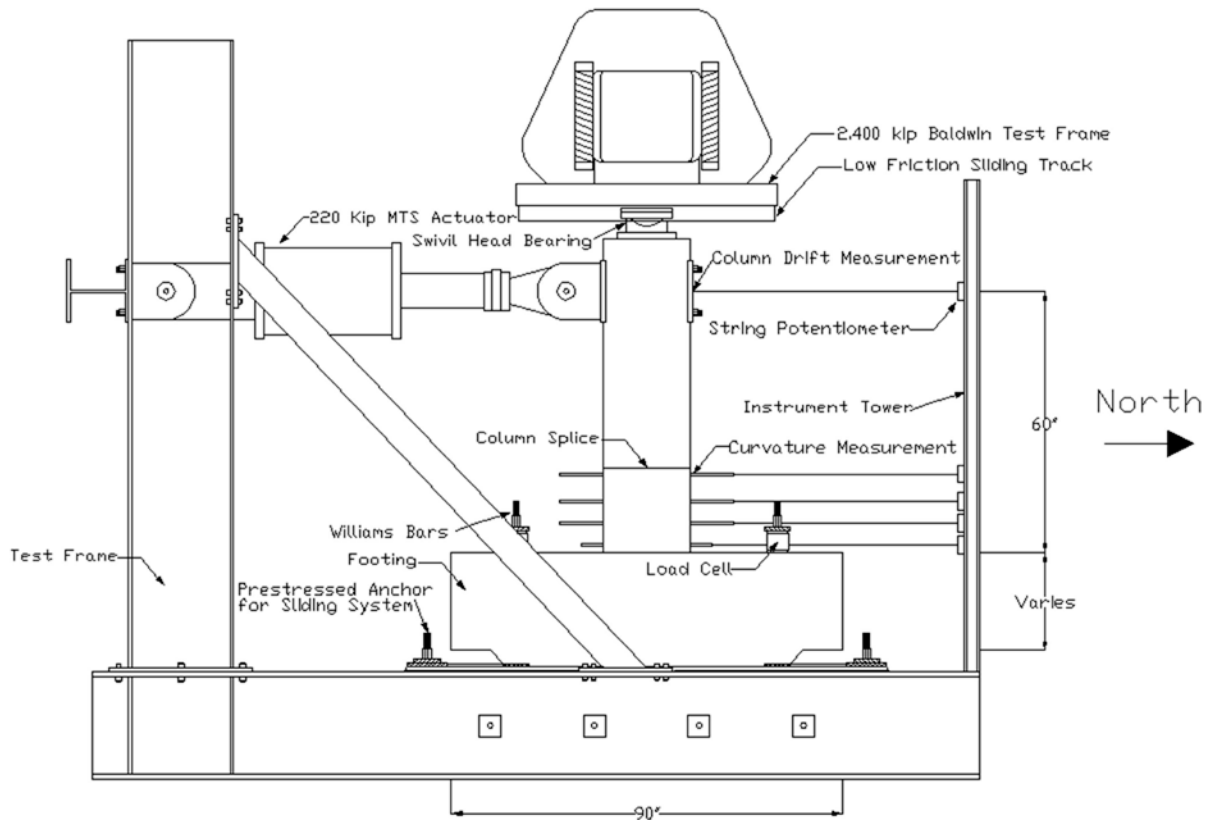


Figure 11. Diagram. Test setup.

The horizontal loads were applied to the column with a servo-controlled actuator with a capacity of 220 kips. The other end of the actuator was attached to a steel frame with two vertical W24x94 beams, which were stiffened on each side with a diagonal HSS 6x6x3/8. Reactions were provided by a large concrete base on which the footing rested. The axial force on the column was provided by the laboratory's 2.4-million-lb Baldwin Universal Testing Machine.

The force was transferred through a spherical bearing that slid against the Baldwin head, guided by a channel. To minimize the friction across this interface, stainless steel plates were placed in the channel and sheets of greased polytetrafluoroethylene (PTFE) were glued to the top and the sides of the bearing.

## **INSTRUMENTATION**

The response of the specimen was monitored with load and displacement transducers on the exterior of the column and the footing, and by internal strain gauges. The strain gauges were applied to selected vertical bars and spiral turns in the column, and to flexural bars, diagonal shear friction bars, and vertical stirrups in the footing.

Load cells in the Baldwin Universal Testing Machine and the MTS actuator captured the vertical and horizontal loads applied to the specimen. Load cells were also placed between the top surface of the footing and the upper nuts on the Williams bars to detect any forces that restrained overturning.

As shown in figure 12, a total of 25 linear potentiometers were used to capture deformations of the specimens. Potentiometers No. 1 to 8 were used to determine relative rotations of the column at various heights by measuring relative displacements of aluminum flat-bars that were mounted on threaded rods protruding from the columns. These rods were located 1.75, 6.75, 11.75, and 18 inches above the footing surface.

A linear variable differential transformer (LVDT) built into the actuator monitored its displacements, but these displacements are not reported here, because those measurements included both the column displacement and the displacement of the steel reaction frame. Instead, five string potentiometers (No. 9 to 13) measured horizontal displacements of the column relative to an independent, unloaded, instrumentation reference frame. The first four of them were attached to the threaded curvature rods, and the fifth one was attached at the point where the horizontal load was applied.

Two potentiometers (No. 14 and 15) were to measure potential opening of the column splice. Eight potentiometers (No. 16 to 23) were used to measure any uplift and slip of the specimen and the testing rig. One LVDT (No. 24) was used to measure any vertical slip between column and footing, and another (No. 25) measured deflections of the steel reaction beam where the actuator was attached. Four inclinometers (No. 26 to 29) were placed at 10, 18, 30, and 40 inches up the east side of the column, and they measured the angle of the column at those heights.

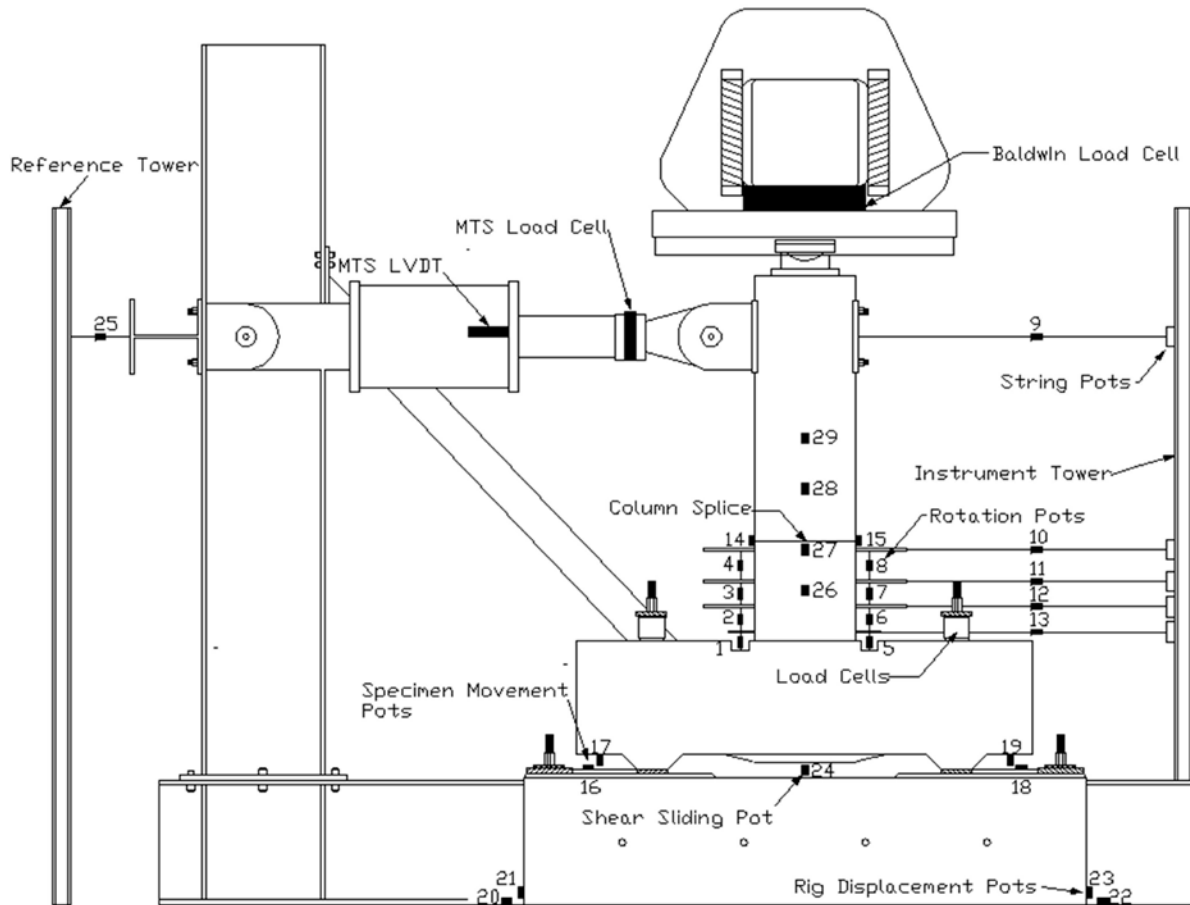
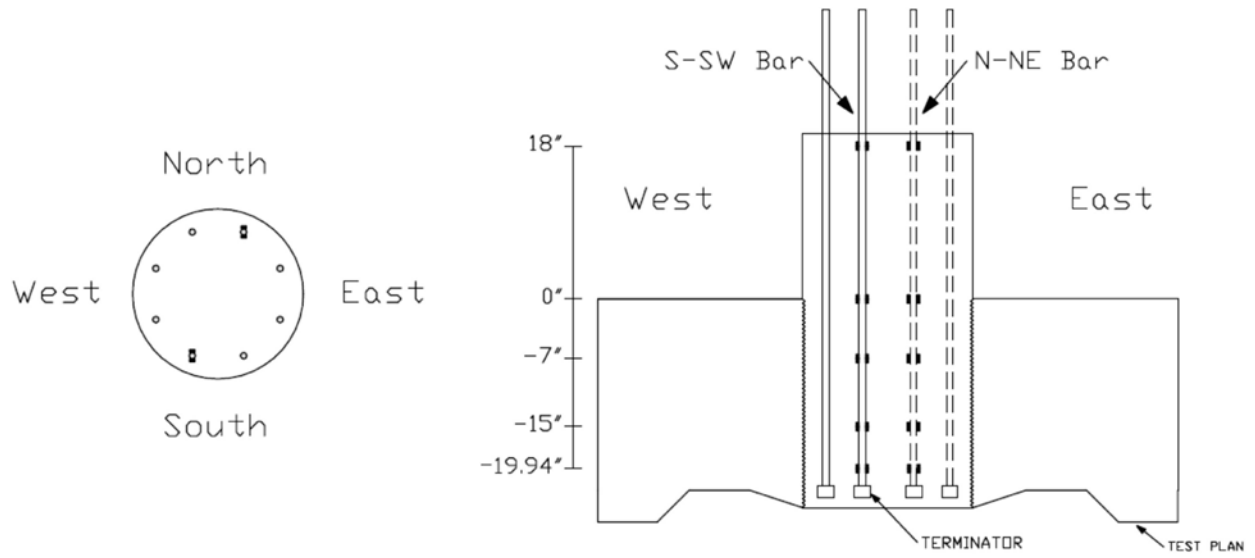
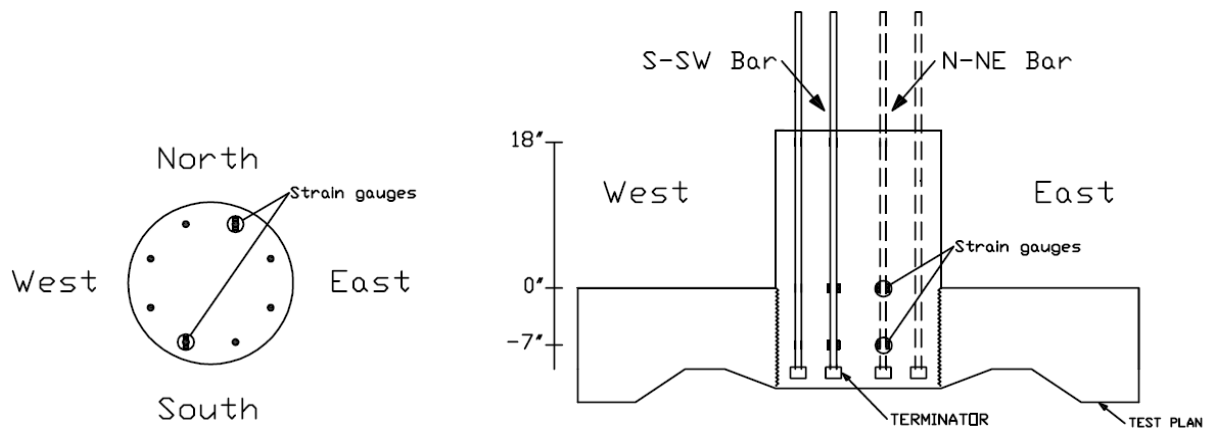


Figure 12. Diagram. Locations of external instruments.

As shown in figures 13 and 14, key reinforcing bars were strain gauged. All gauges were supplied by Texas Instruments. YFLA-5-5L strain gauges were used with some exceptions because of stock availability, in which case FLA-5-3LT gauges were used. Table 1 summarizes the quantity of strain gauges, the types used in the specimens, and their location.

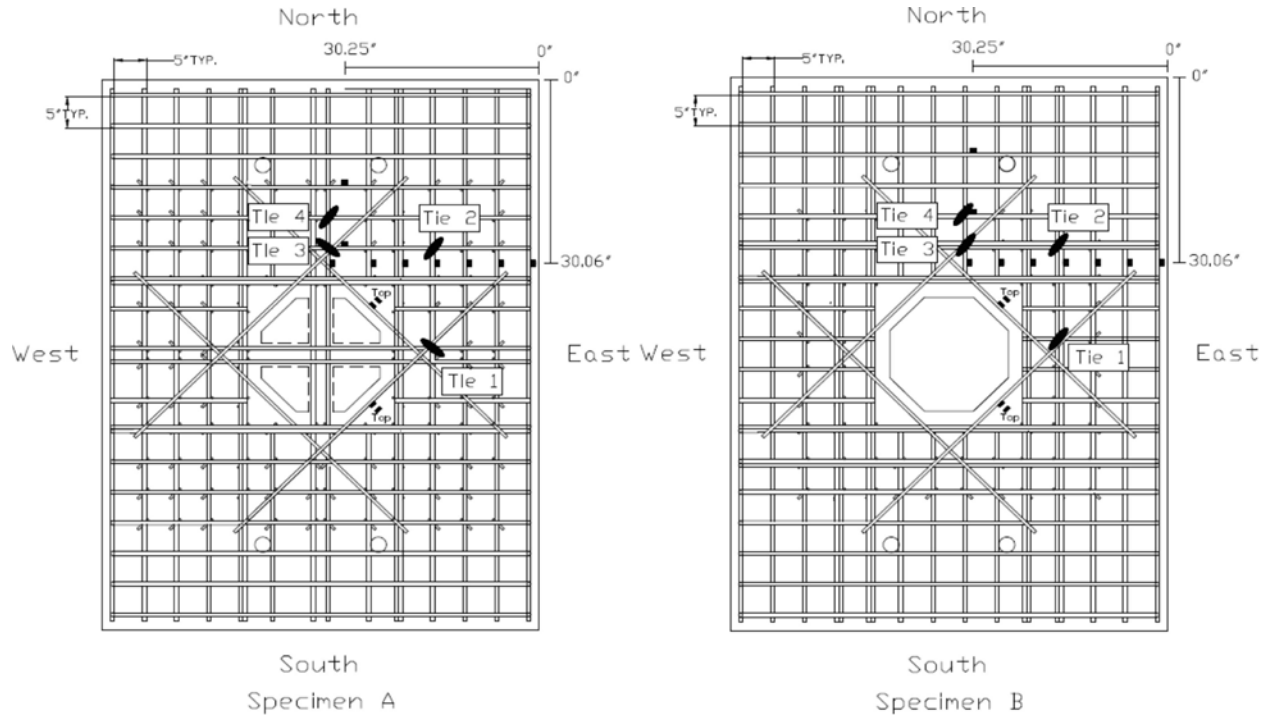


**(a) Location of gauges in specimens SF-1 and SF-2**

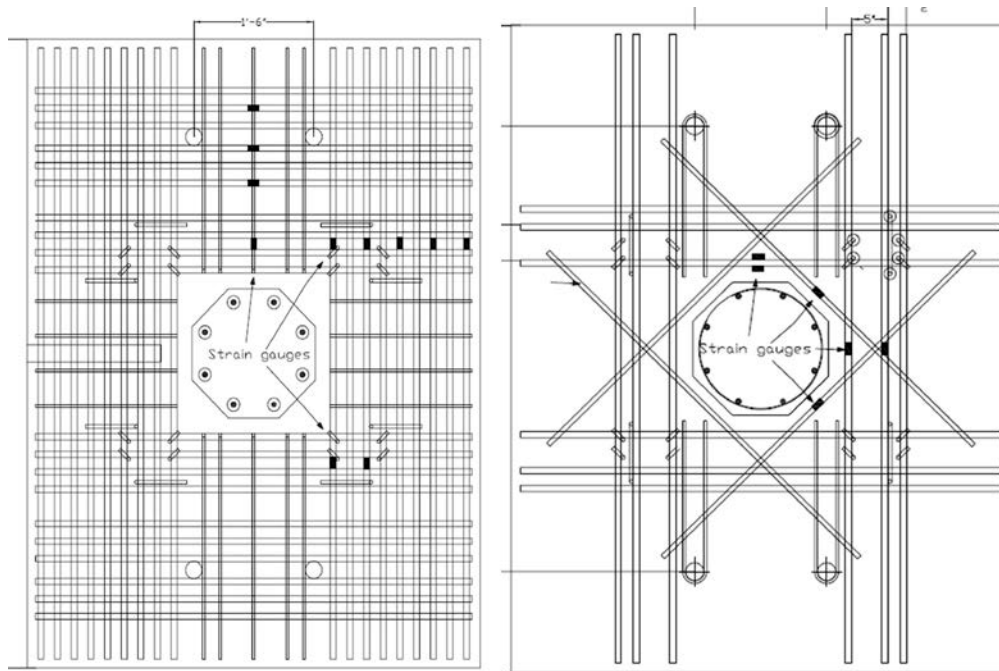


**(b) Location of gauges in Specimen SF-3**

Figure 13. Diagram. Locations of strain gauges in the three specimens.



**(a) Location of gauges in specimens SF-1 and SF-2**



**(b) Location of gauges in Specimens SF-3**

Figure 14. Diagram. Locations of strain gauges in the three specimens' cast-in-place footings.

Table 1. Strain gauge types used in the specimens.

Location	Type	Quantity of each in SF-1	Quantity of each in SF-2	Quantity of each in SF-3
Precast Column	YFLA/FLA	24/0	24/0	8/0
Cast-in-place Footing	YFLA/FLA	10/7	13/4	23/0
Total		41	41	31

The two column bars (N-NE and S-SW, see the nomenclature for the bars in figure 13) that were expected to experience the largest strains were equipped with strain gauges. Specimens SF-1 and SF-2 each bar had 10 gauges, placed in pairs at 5 locations. Three pairs of gauges were placed below the top surface of the footing to check the development of the bars and the effectiveness of the bar terminators. The other two were located at the footing surface to determine the peak bar strain and 18 inches above the surface to check development near the precast column splice. Specimen SF-3 had a shallower foundation and no column splice; therefore, each bar had only four gauges placed in pairs at the footing surface and near the bar terminators.

Selected bars in the footing were strain gauged as well. Because the footing was symmetric about two axes, gauges were placed only on half of the north side bottom bars, half of the diagonal bars, and selected footing ties.

Data were recorded with sampling rate of 0.2 seconds using LabVIEW from National Instruments.

## TESTING PROTOCOL

All three specimens were tested following the same testing protocol. In the first stage of testing, the column was subjected to pure axial load. The target load of 240 kips consisted of the scaled-down factored dead and live loads, according to the AASHTO LRFD. The specified load rate was 8 kips per second. Once the target load was reached, it was held for 5 minutes, and the connection was inspected visually.

The axial load was then reduced to an unfactored dead load value of 159 kips, and the specimen was subjected to displacement-controlled cycles. The same displacement history was applied as in previous research on rapid construction.<sup>(8,11)</sup> This load history is a modification of the loading history for precast structural walls recommended in the National Earthquake Hazards Reduction Program (NEHRP).<sup>(20)</sup>

The target displacement history is provided in figure 15 and table 2. The history consisted of sets of four cycles in which the peak amplitude was 1.2A, 1.4A, 1.4A, and 0.33A respectively, where A is the peak amplitude from the previous cycle set. The small amplitude cycle was intended to evaluate the residual small-displacement stiffness in the column after the set's peak amplitude. In

all cycles, the actuator moved from zero displacement to the peak cycle displacement in 20 seconds.

In this report, the positive and negative peak displacements within a cycle are referred to as “peak” and “valley.” Positive displacements occurred when the actuator was in tension, pulling towards the south in the laboratory.

After cyclic testing of SF-1 and SF-2, the columns were loaded again with pure axial load until the column failed. This post-test axial loading was not performed for SF-3, because it was damaged too much during the lateral-load testing.

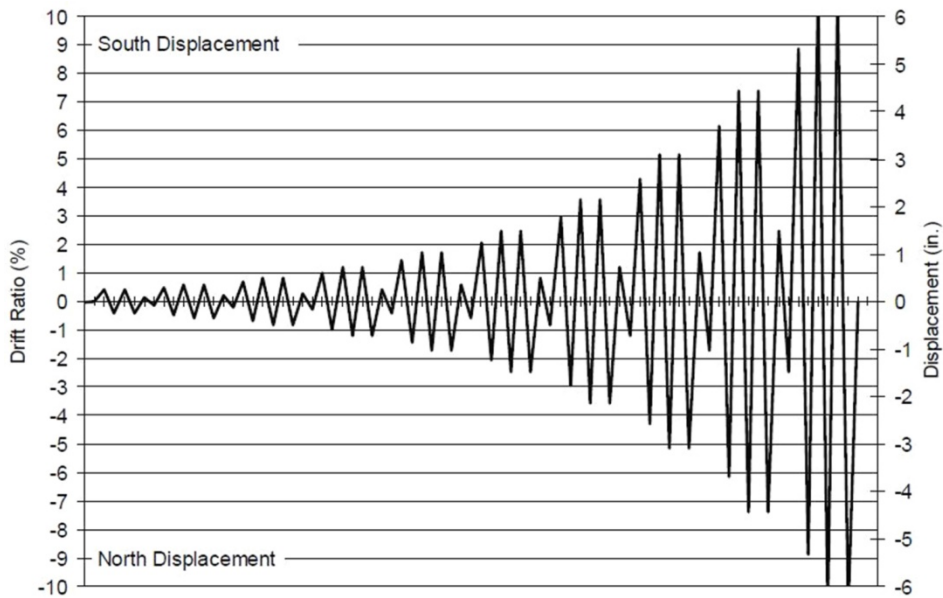


Figure 15. Graph. Lateral loading displacement history.

Table 2. Target displacement history.

Set	Cycle	Drift Ratio (%)	Displ. (in.)
<b>1</b>	1	±0.33	±0.20
	2	±0.40	±0.24
	3	±0.40	±0.24
	4	±0.13	±0.08
<b>2</b>	1	±0.48	±0.29
	2	±0.58	±0.35
	3	±0.58	±0.35
	4	±0.19	±0.12
<b>3</b>	1	±0.69	±0.41
	2	±0.83	±0.50
	3	±0.83	±0.50
	4	±0.28	±0.17
<b>4</b>	1	±1.00	±0.60
	2	±1.19	±0.72
	3	±1.19	±0.72
	4	±0.40	±0.24
<b>5</b>	1	±1.43	±0.86
	2	±1.72	±1.03
	3	±1.72	±1.03
	4	±0.57	±0.34

Set	Cycle	Drift Ratio (%)	Displ. (in.)
<b>6</b>	1	±2.06	±1.24
	2	±2.48	±1.49
	3	±2.48	±1.49
	4	±0.83	±0.50
<b>7</b>	1	±2.97	±1.78
	2	±3.57	±2.14
	3	±3.57	±2.14
	4	±1.19	±0.71
<b>8</b>	1	±4.28	±2.57
	2	±5.14	±3.08
	3	±5.14	±3.08
	4	±1.71	±1.03
<b>9</b>	1	±6.16	±3.70
	2	±7.40	±4.44
	3	±7.40	±4.44
	4	±2.47	±1.48
<b>10</b>	1	±8.87	±5.32
	2	±10.65	±6.39
	3	±10.65	±6.39
	4	±3.55	±2.13

## **CHAPTER 4. DAMAGE PROGRESSION**

Damage progression during the test was recorded in detail with sketches, crack measurements, photography, video, and notes of observations. This chapter defines the damage states and summarizes the damage progression for all three specimens. Additional images of the observed damage can be found in appendix C.

### **DEFINITIONS OF DAMAGE STATES**

The performance of the subassemblies was followed carefully to identify key damage states, as defined for the University of Washington Pacific Earthquake Engineering Research (PEER) Center Structural Performance Database.<sup>(21)</sup> This approach facilitated comparison of damage progression among specimens. The key damage states are defined in table 3.

### **PRELIMINARY TEST CYCLES**

Small-deformation test cycles were imposed on all three specimens to verify the functioning of the instrumentation. The columns were loaded axially with 90 kips and then cycled laterally to drift ratios of  $\pm 0.05$  percent (0.03-inch displacement at actuator level). Only hairline cracks were detected during these preliminary cycles, and all of these cracks closed upon unloading.

### **FACTORED AXIAL-LOAD TESTS**

Before any lateral deformations were imposed on specimen SF-1, it was subjected to a vertical load of 918 kips. This load corresponded to 3.8 times the scaled maximum factored dead load plus live load ( $1.25DL+1.75LL$ ) for the column. Deformations were not measured during this test, but the column and footing were inspected for damage. None was detected.

On the days that lateral loads were applied, the first two specimens (SF-1 and SF-2) were subjected to a vertical load of 240 kips, which corresponded to a scaled-down maximum factored dead load plus live load ( $1.25DL+1.75LL$ ). The specimens were loaded at an average rate of 8 kips/sec, and the maximum load was held constant for about 5 minutes. Specimens SF-1 and SF-2 withstood this level of axial load without forming any new cracks.

Specimen SF-3, with a thinner footing, was loaded axially with a load of 342 kips, corresponding to 1.4 times the factored load. No damage was observed to the column or to the footing at this level of axial load, demonstrating that the capacity of the shallower spread footing exceeded 140 percent of the factored axial design load.

Table 3. Damage state description.

<b>Damage Event</b>	<b>Description</b>
<b>First significant horizontal crack</b>	Crack width $\geq 0.02$ inches
<b>First significant diagonal crack</b>	Diagonal crack extends 1/4 of column diameter. Crack width $\geq 0.02$ inches
<b>First open residual crack</b>	Residual crack width $\geq 0.01$ inches
<b>First yield of longitudinal reinforcement</b>	First strain gauge that reaches yield strain (SF-1 & SF-2: 0.00212; SF-3: 0.00204)
<b>First yield of transverse reinforcement</b>	First strain gauge that reaches yield strain (0.00204)
<b>First spalling in footing</b>	Observed spalling on surface
<b>First spalling in column</b>	Observed flaking, minor spalling
<b>Significant spalling in column</b>	Spalled height $\geq 1/4$ of column diameter
<b>Fully spalled</b>	Spalling height no longer increases with increasing deformation
<b>Exposure of longitudinal reinforcement</b>	First observation of column longitudinal reinforcement.
<b>Buckling of longitudinal reinforcement</b>	First observation of column longitudinal bar buckling.
<b>Large cracks in concrete core</b>	Crack width $\geq 0.08$ inches
<b>Fracture of transverse reinforcement</b>	Observation or sound
<b>Fracture of longitudinal reinforcement</b>	Observation or sound
<b>Loss of axial capacity</b>	Instability of member

## LATERAL-LOAD TESTS (UP TO YIELDING)

For the lateral-load tests, the axial load was reduced to 159 kips, which corresponded to the scaled-down, unfactored dead load plus the influence of overturning on the subassembly. The displacement history consisted of sets of four cycles. In general, the cyclic loading was paused at peak displacements (both at “peaks,” or positive drifts, and “valleys,” or negative drifts) in the first two cycles of each cycle set to observe and record cracks. Between cycles, at zero displacement, residual crack widths were measured for selected cracks. Subsequent cycles in each set were imposed continuously during which the testing was not stopped to mark or record cracks. All three specimens were subjected to 39 cycles of deformation. Table 4 lists the cycle and drift ratio at which each specimen reached each damage state defined in table 3.

Table 4. Damage milestones for all three specimens.

Damage Event	Specimen SF-1			Specimen SF-2			Specimen SF-3		
	Set	Cycle	Drift (%)	Set	Cycle	Drift (%)	Set	Cycle	Drift (%)
First significant horizontal crack	4	1	0.69	3	2	0.56	3	1	0.49
First significant diagonal crack	6	1	1.68/-1.80	6	1	1.74	6	1	1.71
First open residual crack	6	1	1.68/-1.80	4	3	0.88/-0.95	5	1	1.13/-1.23
First yield of longitudinal reinforcement	3	2	0.55	3	2	0.47	3	1	-0.51
First yield of transverse reinforcement	8	2	-4.63	9	1	-4.93	8	2	-4.77
First spalling in footing	N/A	N/A	N/A	N/A	N/A	N/A	9	2	7.11/-6.92
First spalling in column	5	1	1.07/-1.21	5	1	1.10/-1.19	5	3	1.41/-1.49
Significant spalling in column	6	2	-2.25	7	1	2.64	6	2	2.13/-2.21
Full spalling in column	9	3	7.08/-6.90	8	1	3.98	9	1	5.84/-5.76
Exposure of longitudinal reinforcement	9	1	-5.68	9	2	-6.85	9	3	7.15/-6.93
Buckling of longitudinal reinforcement	9	2	7.09/-6.88	9	3	7.19/-6.88	9	3	7.15/-6.93
Large cracks in concrete core	10	2	10.61	10	2	-9.95	10	2	10.58/-9.97
Fracture of transverse reinforcement	9	2	-6.88	10	1	-8.29	10	1	8.72
Fracture of longitudinal reinforcement	10	2	10.61	10	2	10.65	N/A	N/A	N/A
Loss of axial capacity	N/A	N/A	N/A	N/A	N/A	N/A	10	3	10.7

As shown in figure 16, the damage progression was similar for all specimens. Horizontal hairline cracks were observed on both sides of the columns during the first cycle. In subsequent cycles, the cracks propagated and widened, but they closed after each cycle. The first significant horizontal crack (crack width of at least 0.02 inches) for specimen SF-1 was observed at a drift

ratio of 0.69 percent, which slightly exceeded the drift ratios for this state for SF-2 (0.56 percent) and SF-3 (0.49 percent).

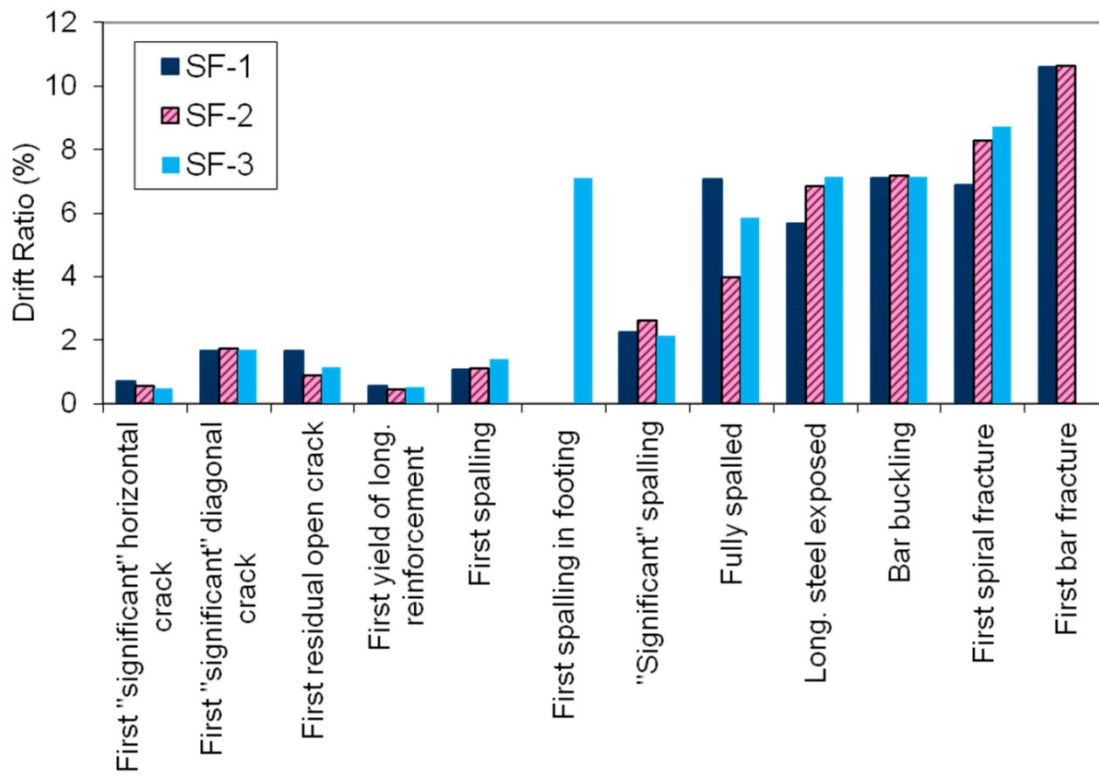


Figure 16. Chart. Comparison of specimens' drift ratios for the major damage states.

The nomenclature for identifying the longitudinal bars is shown in figure 17. First yield in the column longitudinal bars was detected at the level of the column-to-footing interface. It occurred at nearly the same drift for all three specimens. The S-SW bar in specimen SF-1 yielded at 0.55 percent drift, the N-NE bar in specimen SF-2 yielded at +0.47 percent drift, and the S-SW bar in specimen SF-3 yielded at a drift ratio of -0.51 percent (valley in cycle 3-2).

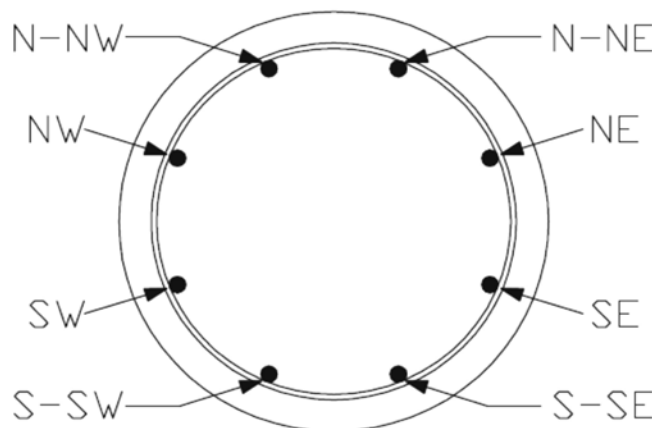


Figure 17. Diagram. Column vertical bar naming convention.

## LATERAL-LOAD TESTS (AFTER YIELDING)

As the specimens were cycled, a horizontal crack formed at interface between the precast column and the cast-in-place footing. The first open residual crack was observed in specimen SF-1 at a drift ratio of 1.7 percent, which greatly exceeded the corresponding drift ratio for specimen SF-2 (+0.88/-0.95 percent drift) and specimen SF-3 (1.13/-1.23 percent drift). The reason for these differences in behavior is unknown.

The spalling patterns among the three specimens were similar but not identical. Minor spalling first appeared in specimens SF-1 and SF-2 at drift ratios of approximately 1.1-1.2 percent. Specimen SF-3 reached this level of damage slightly later, at a drift ratio of 1.4 percent. All three specimens reached the level of “significant spalling” (spalled height  $\geq 1/4$  of column diameter) at about 2.2 to 2.6 percent drift. The fully spalled state (above which point spalling no longer progressed) varied both in terms of drift ratio and extent of spalling. This state was reached for specimens SF-1, SF-2, and SF-3 at drift ratios of 7 percent, 4 percent, and 6 percent, respectively. The spalling in SF-1 and SF-2 extended over the bottom 10 to 12 inches, whereas in SF-3, the spalling extended up only to a height of 7 inches (to the top of the second curvature rod). Figure 18 compares spalling of the three columns at a drift ratio of 4.28 percent (cycle 8-1).

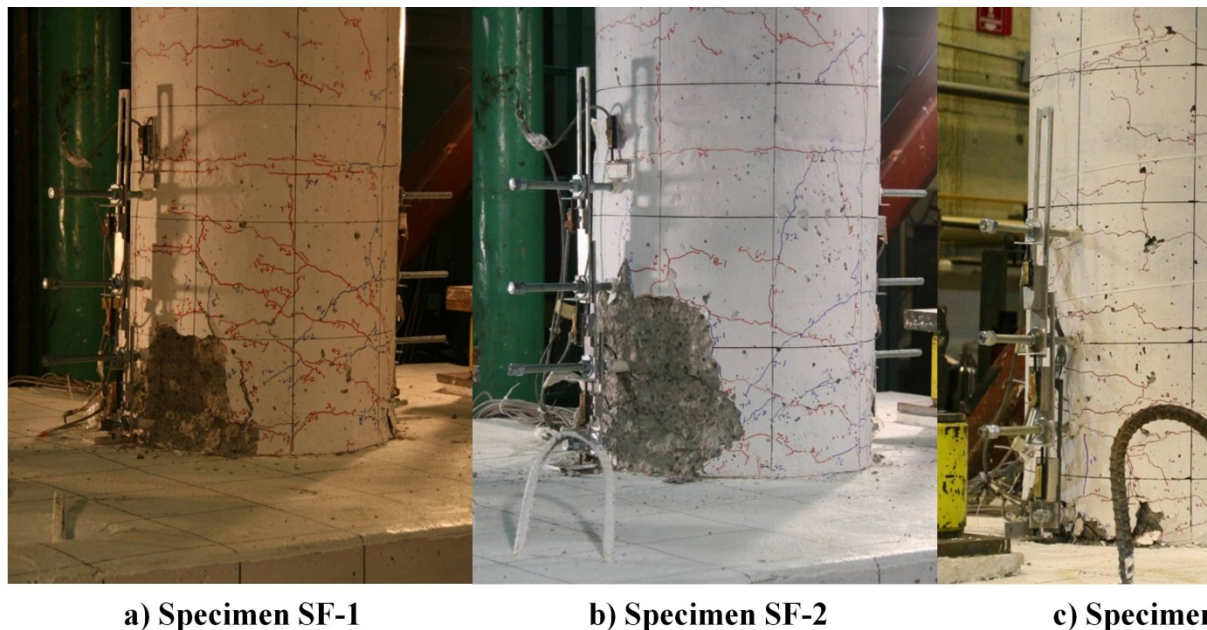


Figure 18. Photos. Test specimens after a cycle of maximum drift ratio of 4.28 percent.

Spiral yielding occurred late in the tests and was associated with the longitudinal bars necking on the north side of the columns (N-NW and N-NE bars). The spiral yielded in cycle set 8 for both specimens SF-1 and SF-3 (cycle 8-2, maximum drift ratio = 5.14 percent). In specimen SF-2, the spiral yielded in cycle set 9 (cycle 9-1, maximum drift ratio = 6.16 percent). In all cases, the yielding occurred after the peak displacement as the specimen was pushed to the valley (SF-1: -4.63 percent drift, SF-2: -4.93 percent drift, SF-3: -4.77 percent drift).

As spalling in the column increased, the longitudinal bars became visible. Bar buckling became visible in all specimens at approximately 7 percent drift (cycle set 9). The spirals fractured at approximately the same time, apparently as a result of buckling of the longitudinal bars.

In subsequent cycles, those bars at extreme tension and compression (N-NE, N-NW, S-SW, and S-SE) underwent alternating axial shortening and elongation, and cyclic bending and straightening. This behavior induced large cyclic strains, which caused them to fracture a few cycles after the spirals failed in both specimens SF-1 and SF-2. In both columns, the first longitudinal bar fractured going south to peak in cycle 10-2 (maximum drift ratio = 10.65 percent). In specimen SF-1, a total of three bars fractured, and in specimen SF-2, four bars fractured. The condition of the bars in specimen SF-1 is shown in figure 19. No bars fractured in specimen SF-3.



Figure 19. Photo. Specimen SF-1 longitudinal bars fractured after one cycle to 10.65 percent drift ratio.

No vertical interface crack between the roughened surface of the precast column and cast-in-place footing was noticed throughout testing of specimens SF-1 and SF-2.

Spalling in the footing was not observed in specimens SF-1 and SF-2. Cracks in the SF-1 and SF-2 footings were few, occurred only on the sides, and remained at the hairline level throughout the tests.

Footing damage and cracking was more significant in specimen SF-3. Cracks in the sides of the footing were first observed at 0.30 percent drift. No additional damage was observed until 0.89 percent drift, in which small cracks propagating out radially on the surface of the footing from the column-footing interface were noted. This radial cracking continued to propagate in cycles 6-1 and 6-2. In the first two cycles in set 7, new radial cracking on the NE and SW sides of the

column was noted along with continued propagation of the existing footing cracking. Spalling of the footing did not occur until set 9 at 7 percent drifts, in which approximately the top 1/8<sup>th</sup> inch of the footing lifted up. This spalling increased during the following cycles. In cycle 10-1 (8.72 percent drift), major spalling of the top of the footing had occurred in specimen SF-3. Then, during cycle 10-3 (maximum drift ratio = 10.65 percent), as the column was returning from peak, the column punched completely through the footing at 10.7 percent drift. Just before the column punched through, a piece approximately 8 inches by 14 inches by 1.5 inches thick (N-S by E-W) on the north side of the footing lifted up and spalled off.

Since the octagonal section in the connection region was smaller than the column, some of the load was likely taken by this bearing surface. When enough spalling occurred in the column, no resistance could be provided by this bearing surface, and the stress in the connection increased, leading to failure. The last cycle, during which the footing failed, can be seen in figure 20.



Figure 20. Photo. Specimen SF-3 footing failure.

Based upon inspection of the SF-3 footing after the test, spalling on the bottom of the footing had occurred as well. Measurements were taken after the test to obtain a profile of the failure plane in the footing (figures 21 and 22).



Figure 21. Photo. Damage on top of footing after test.

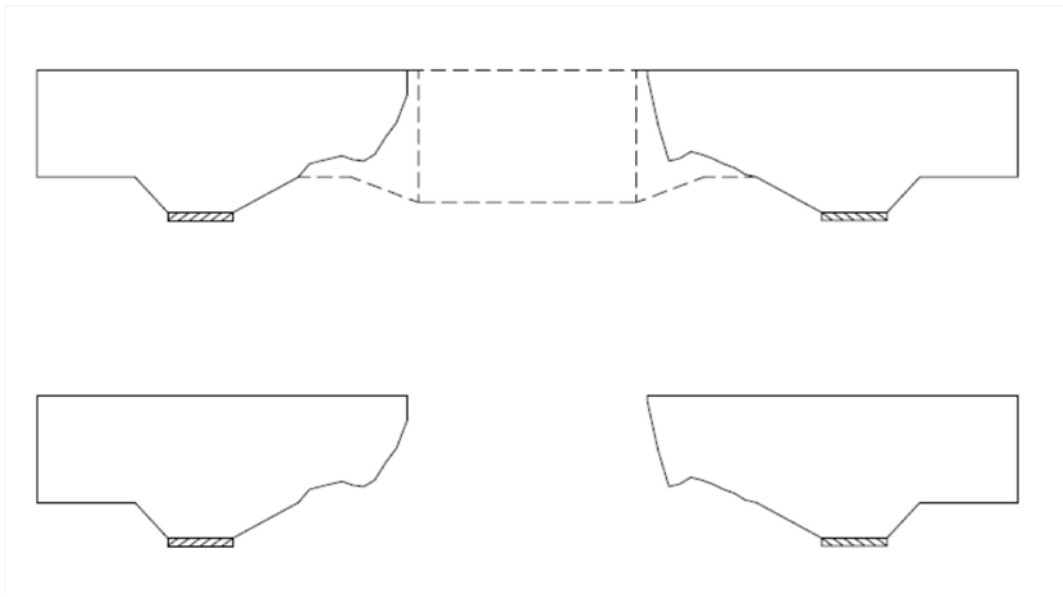


Figure 22. Diagram. Punching shear profile in the north-south direction (loading direction).

## AXIAL-LOAD TESTING TO COLLAPSE

After the cyclic lateral loading was complete, the instruments mounted on the columns of specimens SF-1 and SF-2 were removed, and pure axial load was applied until some element failed and the load started to drop. In both specimens, failure occurred by crushing of the concrete in the plastic hinge region. Specimen SF-1 sustained a maximum axial load of 842 kips, and specimen SF-2 sustained a maximum axial load of 819.5 kips. Both of these values corresponded to about 3.5 times the factored axial load of 240 kips.

This aspect of the test was not performed on specimen SF-3, since the column had already punched through the spread footing during cyclic testing. Figure 23 shows the damage state of the three specimens at the end of the test program.



a) Specimen SF-1

b) Specimen SF-2

c) Specimen SF-3

Figure 23. Photos. Specimens at the end of the test program.



## CHAPTER 5. MEASURED RESPONSE

This chapter documents the responses measured by instruments mounted on and within the test specimens.

### MATERIAL PROPERTIES

Material tests for the concrete and reinforcement used in the test specimens were conducted in the University of Washington Structural Research Laboratory. The specified 28-day concrete strength for both the columns and the footings was 4 ksi, and the reinforcement conformed to ASTM A706, with the exception that smooth wires conforming to ASTM A82 were used where a direct scaling resulted in a deformed bar smaller than No. 3. A detailed description of the concrete mix and the material test results are presented in appendix B.

#### Concrete Strength

Specimens SF-1 and SF-2 had segmental precast columns. The column segments were fabricated off campus at a construction site in the City of Redmond, they were cast on the same day, and they were delivered 1 week later to the University of Washington Structural Research Laboratory. In the laboratory the columns were embedded in cast-in-place spread footings. Specimen SF-3 was built entirely in the Structural Research Laboratory.

For both the precast column and cast-in-place footing pours, concrete test cylinders were prepared (4-inch by 8-inch cylinders for SF-1 and SF-2, and 6-inch by 12-inch cylinders for SF-3). For specimens SF-1 and SF-2, the cylinders were kept adjacent to the corresponding element, whereas the cylinders for specimen SF-3 were stored in a fog room. Cylinders were tested in pairs at 7 days, 28 days, and on the test days for specimens SF-1 and SF-2. Column concrete strength tests at 7 days were not performed because of a shortage of test cylinders. Cylinders for specimen SF-3 were tested at 7 days, 14, days, 21 days, 28 days, and on the test day. Table 5 summarizes the average concrete strength for both the precast columns and cast-in-place footings on the test day.

Table 5. Average concrete strength on test day.

Specimen	Column Concrete		Footing Concrete	
	Strength (psi)	Days	Strength (psi)	Days
SF-1	4,995	113	6,505	91
SF-2	5,496	129	6,764	107
SF-3	7,935	120	7,905	113

## Grout Strength

The grout used was an unsanded, silica fume, commercially available product, which is designed to be used as a flowable grout. The grout was mixed in a high-speed shear mixer, and water was added according to the manufacturer's instructions. The grouting operations for the precast column interfaces for specimens SF-1 and SF-2 were performed on the same day. During this operation, four standard 2-inch by 2-inch test cubes were taken, and two cubes were tested on each subassembly's test day. The ducts were grouted four days later, at which time, an additional four test cubes were prepared. Table 6 summarizes the average grout strength measured from those tests. The table shows that the grout strength used in the ducts of specimen SF-2 was noticeably lower than the strength in other locations. This is attributed to the fact that one cube was mishandled before the compression test. If that cube is excluded from the average, the grout properties for SF-1 and SF-2 were nearly identical.

Table 6. Average grout strength on test day.

Specimen	Interface Grout		Grout in Ducts	
	Strength (psi)	Days	Strength (psi)	Days
SF-1	13,075	60	12,500	56
SF-2	13,025	77	11,175	73

## Reinforcement

Tension tests were performed on No. 7, No. 6, No. 5, No. 4, and No. 3 mild reinforcing bars, as well as 2-gauge and 3-gauge wires. Load and strain were recorded using a LabView data acquisition system. Stress was calculated using the nominal bar areas. A laser extensometer was used to measure bar elongation over a gauge length of 1 inch for specimens SF-1 and SF-2. For specimen SF-3, elongations during the tension tests were monitored with an 8-inch gauge length mechanical extensometer.

Test coupons had definite yield plateaus for all of the bars except the wires and the No. 3 bars in specimens SF-1 and SF-2. In these tests, the strain hardening of the bars was measured. In specimen SF-3, the coupons were loaded until the steel began to yield and the load dropped. The extensometer was then removed to prevent damage to the equipment. The coupon was then loaded until failure, after which time the length was measured to obtain a strain at failure. Therefore, the line from yield to failure shown in the SF-3 plots does not represent a measured response. Instead, it is only there to provide a visual connection between the yield and failure point. To be consistent with previous tests, the yield strain was taken as 0.35 percent strain to avoid any subjectivity into the test results. Table 7 summarizes the average measured yield stress, ultimate stress, and nominal area of the reinforcement.

Table 7. Measured mild reinforcement properties.

Bar	$A_{nominal}$ (in <sup>2</sup> )	Specimens SF-1 and SF-2		Specimen SF-3		Use/Location
		$f_y$ (ksi)	$f_u$ (ksi)	$f_y$ (ksi)	$f_u$ (ksi)	
No. 7	0.60	N/A	N/A	66.2	95	SF-3/footing flexural reinforcement
No. 6	0.44	61.6	86.1	59.2	88.2	All/column longitudinal bars
No. 5	0.31	63.3	91.4	66.1	108	SF-1, SF-2/footing flexural reinforcement SF-3/shear friction steel
No. 4	0.20	63.7	90.4	65.9	91.6	SF-1, SF-2/shear friction reinforcement SF-3/ties
No. 3	0.11	65.2	94.5	62.4	99.9	SF-1, SF-2/top footing flexural reinforcement
2 GA.	0.054	63.4	86.4	N/A	N/A	SF-1, SF-2/ties
3 GA.	0.047	59.4	73.6	N/A	N/A	All/column spiral

All A706 bars exceeded their minimum specified yield stress of 60 ksi except the No. 6 column bars in specimen SF-3. These bars had a yield stress of 59.2 ksi, only 1.3 percent below the specified value. In both the SF-1/SF-2 and SF-3 tension tests, the No. 6 column bars did not reach a yield stress of 68 ksi, which is the expected value that AASHTO Seismic Guide Specifications recommended to be used (for A706 reinforcement) in the calculation for the column overstrength moment. The wires did not meet the minimum specified yield stress of 70 ksi. This poor performance of the wires is attributed to the fact they had to be straightened out before tensile testing.

### FRICITION CORRECTION

The measured horizontal load was corrected using a friction model and the recommendations proposed by Brown.<sup>(22)</sup> This correction has been done previously in research at the University of Washington.<sup>(7)</sup> The test setup in the Baldwin Universal Testing Machine introduced a small friction force into the system by two mechanisms: rotation between the greased steel-to-steel spherical element in the swivel head bearing, and horizontal sliding between the bearing's top flat plate and the channel attached to the Baldwin head. The friction component in the channel was minimized by placing sheets of silicon-greased Teflon between the bearing and the smooth stainless steel plates in the channel. The model consists of a bilinear spring with a spring

stiffness,  $k$ , of 60 kips/in., and has a maximum friction force,  $F_{max,friction}$ , of  $\mu_{eff} \cdot P$ , where  $\mu_{eff}$  is the coefficient of friction and  $P$  is the target axial load. The coefficient of friction can be approximated as shown in figure 24.

$$\mu_{eff} = \mu_{flat} + \mu_{curved} \frac{R}{L_{total}}$$

Figure 24. Equation. Coefficient of friction.

In this equation,  $\mu_{flat}$  is the flat friction between the top swivel head bearing plate and the sliding channel,  $\mu_{curved}$  is the friction between greased steel-to-steel spherical element,  $R$  is the radius of spherical element, and  $L_{total}$  is the height between footing surface and top of bearing. When  $R \ll L_{total}$ , then  $\mu_{eff} \approx \mu_{flat}$ .

Brown's model was implemented assuming  $\mu_{eff} = 1.6$  percent. For an axial load of 159 kips, the corresponding maximum resistance in the sliding channel was 2.54 kips, which was about 5 percent of the maximum applied load in all tests.

### **MOMENT-DRIFT RESPONSE**

The moment at the base of the column was calculated using the equation in figure 25, for which the variables are illustrated in figure 26.

$$M = h_1 \cdot H + \Delta_1 \cdot \frac{h_2}{h_1} \cdot P$$

Figure 25. Equation. Calculation of the moment at the base of the column.

In this equation,  $M$  is the calculated base moment,  $h_1$  is the height from the top of the spread footing to the line of action of the lateral load,  $H$  is the corrected lateral load that takes into account both the friction force between the bearing and the sliding channel, and the greased steel-to-steel spherical element on bearing,  $\Delta_1$  is the lateral displacement where the lateral load,  $H$ , is applied,  $h_2$  is the height from the top of the spread footing to where the axial load, and  $P$  is the axial load applied by the Baldwin Universal Testing Machine.  $\Delta_2$  was not measured but estimated to be  $\Delta_1(h_2/h_1)$ .

Figures 27 to 29 show the responses of the three test specimens in terms of moment vs. drift ratio.

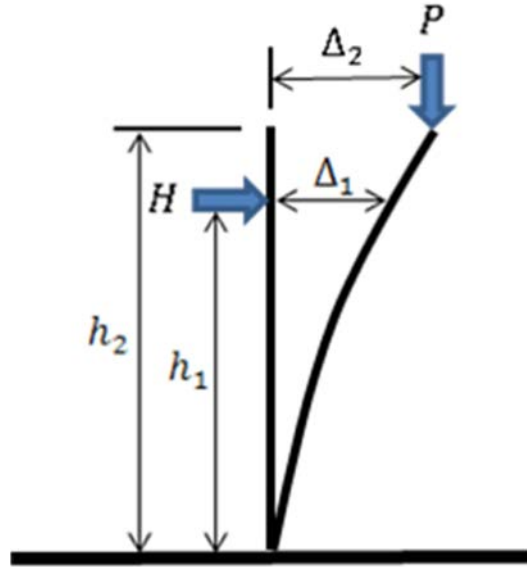


Figure 26. Diagram. Displacements and forces on test specimen used in figure 25.

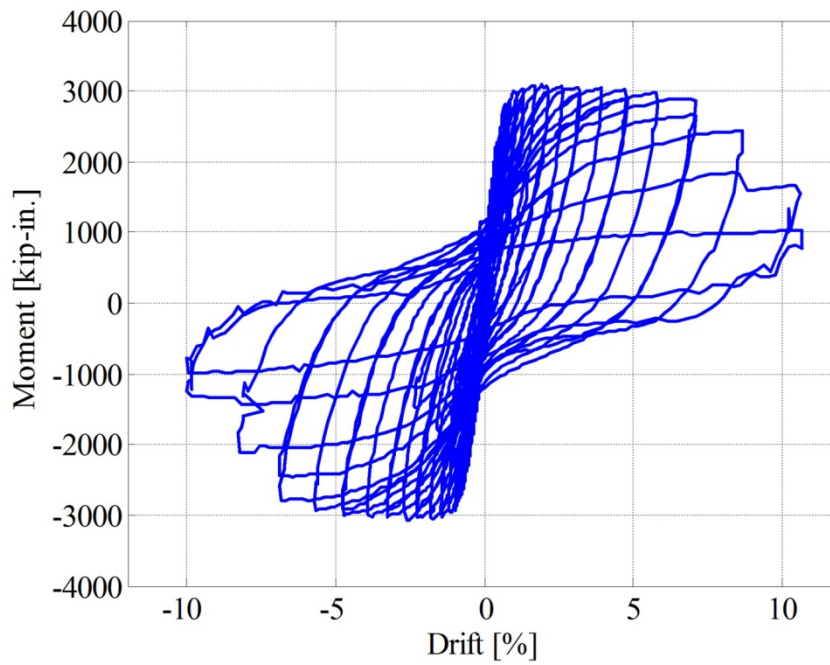


Figure 27. Graph. Specimen SF-1 moment-drift response.

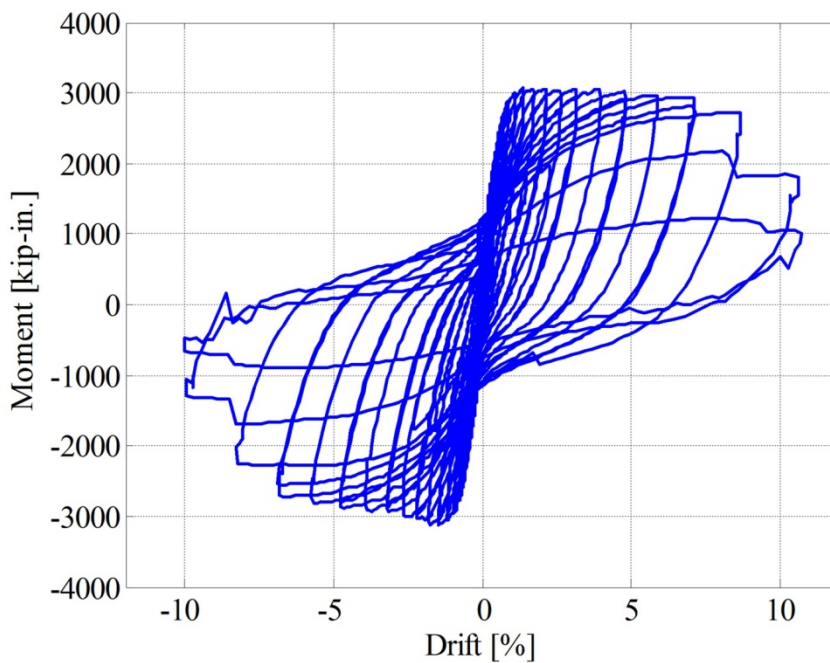


Figure 28. Graph. Specimen SF-2 moment-drift response.

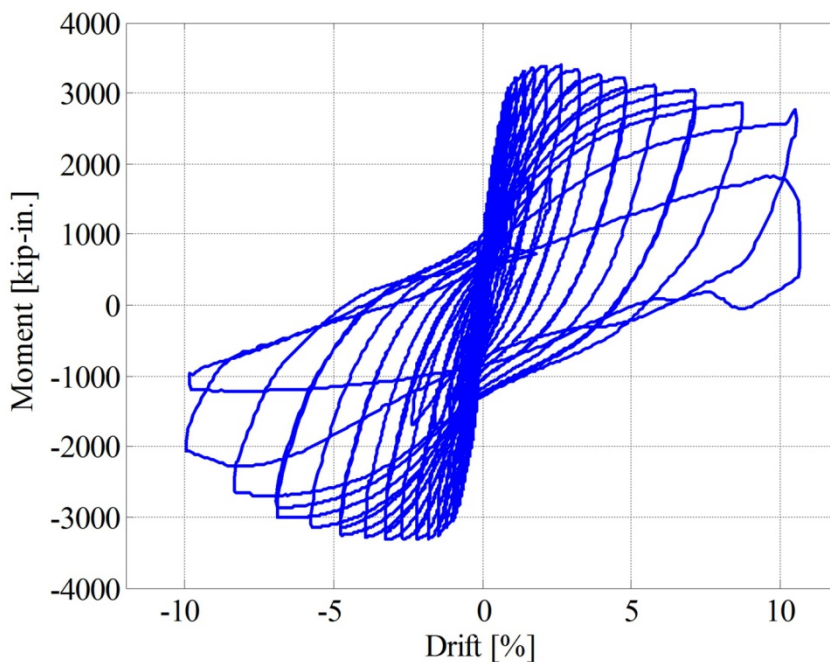


Figure 29. Graph. Specimen SF-3 moment-drift response.

All three specimens shared the same column geometry and reinforcing pattern. The measured responses of the three specimens were similar but not identical. The responses of both specimens SF-1 and SF-2 were stable to large drifts (at about 6 percent), at which point the lateral-load

resistance dropped rapidly. By contrast, the strength of specimen SF-3 decayed more gradually, starting at 2.5 percent.

As shown in table 8, the stiffnesses of the columns (measured at the force corresponding to first yield of the reinforcement) were similar for all the specimens. However, the columns were slightly stiffer in the south direction of loading for specimens SF-1 and SF-2, which was the direction in which they were first loaded.

The maximum base moments were approximately 3,100 kip-in. for both specimens SF-1 and SF-2. Specimen SF-3 was approximately 10 percent stronger than the other two specimens. Material tests showed that the column longitudinal bars had virtually the same yield and ultimate strength for all three specimens (see table 7). In contrast, the concrete cylinder tests showed that the concrete compressive strength was about 50 percent higher (table 5) for specimen SF-3 than for specimens SF-1 and SF-2.

Table 8. Moments and drift ratios at maximum and 80 percent of maximum resistance.

Points of Interest	Specimen SF-1		Specimen SF-2		Specimen SF-3	
	North Direction	South Direction	North Direction	South Direction	North Direction	South Direction
Secant Stiffness at Initial Yield (kip/in.)	108	114	116	132	132	126
Maximum Column Base Moment (kip-in.)	-3,073	3,091	-3,113	3,065	-3,315	3,392
Drift Ratio at Maximum Column Base Moment (percent)	-2.61	1.95	-1.45	1.38	-2.69	2.64
80 Percent of Maximum Column Base Moment (kip-in.)	-2,417	2,473	-2,490	2,452	-2,652	2,714
Drift Ratio at 80 percent of Maximum Base Column Moment (percent)	-6.79	7.09	-6.88	8.69	-8.26	10.5

As the columns were cycled, the longitudinal bars went through more inelastic strains and stress reversals. The definition of failure is often taken as the state at which the effective lateral load resistance measured drops below 80 percent of the maximum resistance obtained earlier in the test. In specimens SF-1 and SF-2, that state occurred at approximately 7 percent drift and corresponded to the onset of buckling of the longitudinal bars (+7.1 percent/-6.9 percent in SF-1 and +7.2 percent/-6.9 percent in SF-2). The 80 percent milestone occurred slightly later (at +8.7

percent) in specimen SF-2’s south direction. Ultimately, the bars fractured in specimens SF-1 (at +10.6 percent) and SF-2 (at +10.6 percent), at which point the lateral-load resistance of the columns decreased abruptly.

Specimen SF-3 maintained its strength above 80 percent of the maximum to a drift ratio 8.3 percent when being pushed in the north direction (“valley”) and 10.5 percent drift when pushed to the south (“peak”). The column bars did not fracture in specimen SF-3. Instead, the column punched through the footing before bar fracture.

**EFFECTIVE FORCE**

The effective force acting on the specimens was calculated by dividing the moment at the base of the column by the height from the top of the spread footing to the line of action of the lateral load. The equation in figure 25 is divided by  $h_1$  to give the equation shown in figure 30.

$$F_{eff} = H + P \cdot \frac{\Delta_1 h_2}{h_1^2}$$

Figure 30. Equation. Effective lateral force.

Figures 31 through 33 show similar plots to figures 27 through 29, but they are expressed in terms of the effective force and displacement.

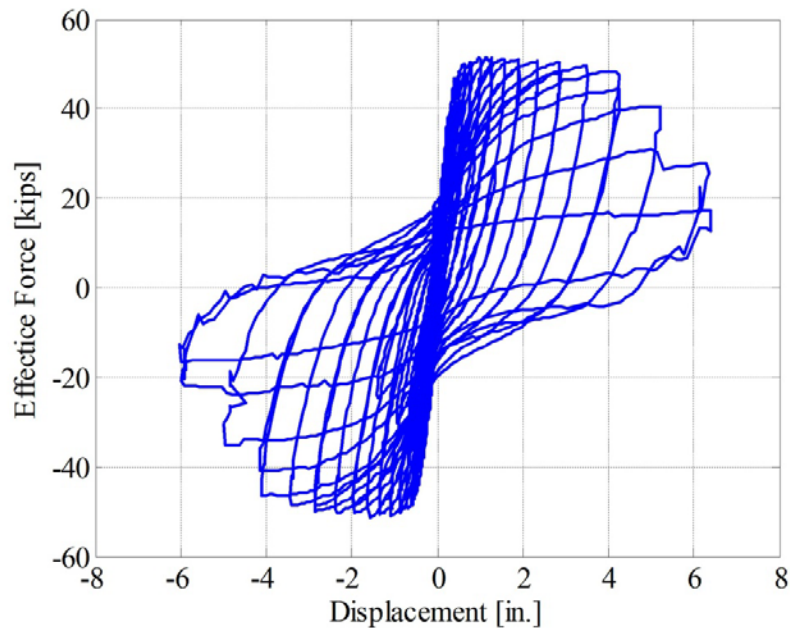


Figure 31. Graph. Specimen SF-1 effective force-displacement response.

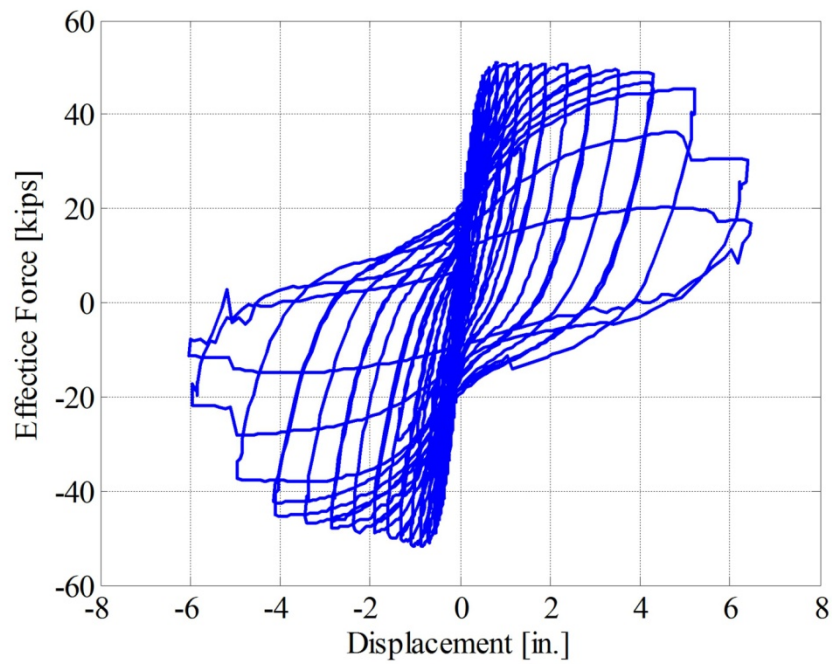


Figure 32. Graph. Specimen SF-2 effective force-displacement response.

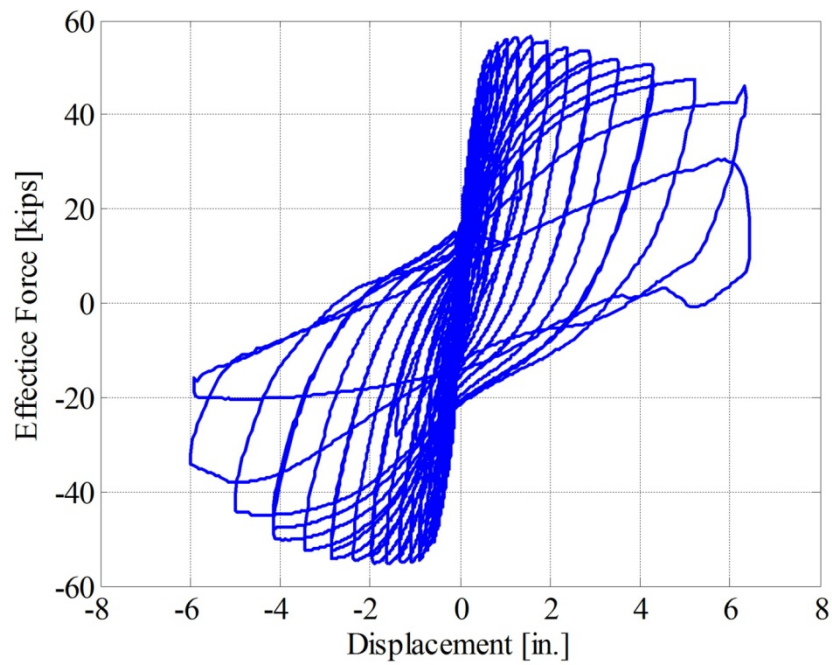


Figure 33. Graph. Specimen SF-3 effective force-displacement response.

Table 9 summarizes the maximum effective force (MEF) resistance, 80 percent of the maximum, and their corresponding displacements.

Table 9. Effective force and displacement at maximum and 80 percent of maximum resistance.

Points of Interest	Specimen SF-1		Specimen SF-2		Specimen SF-3	
	North Direction	South Direction	North Direction	South Direction	North Direction	South Direction
<b>MEF (kips)</b>	-51.2	51.5	-51.9	51.1	-55.3	56.5
<b>Displacement at MEF (in.)</b>	-1.57	1.17	-0.87	0.83	-1.61	1.58
<b>80 percent of MEF (kips)</b>	-40.3	41.2	-41.5	40.9	-44.2	45.2
<b>Displacement at 80 percent of MEF (in.)</b>	-4.07	4.25	-4.13	5.21	-3.57	6.33

## DISTRIBUTION OF COLUMN CURVATURE

Average column curvatures were determined from the column rotations at various heights. These were obtained from the relative displacements between the ends of threaded rods embedded horizontally in the column at about 2, 7, 12, and 18 inches above the footing surface. The average curvature within a column segment between rods is plotted at the midpoint of the segment. The curvatures were calculated using the equation in figure 34.

$$\varphi_i = \frac{\delta_{i,N} - \delta_{i,S}}{L_i} / H_i$$

Figure 34. Equation. Calculating the average curvature.

In this equation,  $\varphi_i$  is the calculated average curvature,  $\delta_i$  is the displacement of the curvature on one side (north or south) at particular height above the spread footing surface,  $L_i$  is the horizontal length between north and south potentiometers, and  $H_i$  is the initial vertical distance between the curvature rods.

Figures 35 to 37 show the average column curvature for selected drift ratios versus height above the spread footing surface.

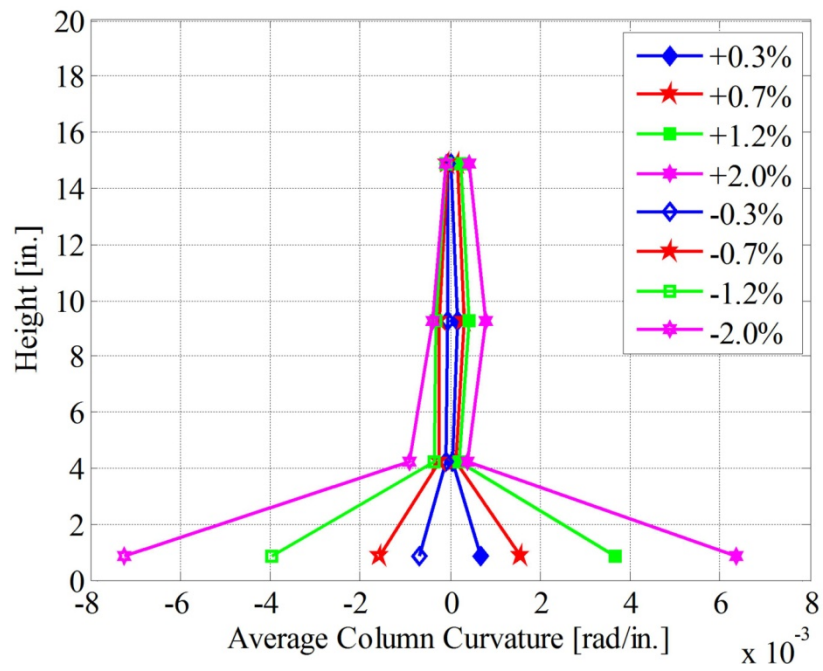


Figure 35. Graph. Specimen SF-1 average column curvature.

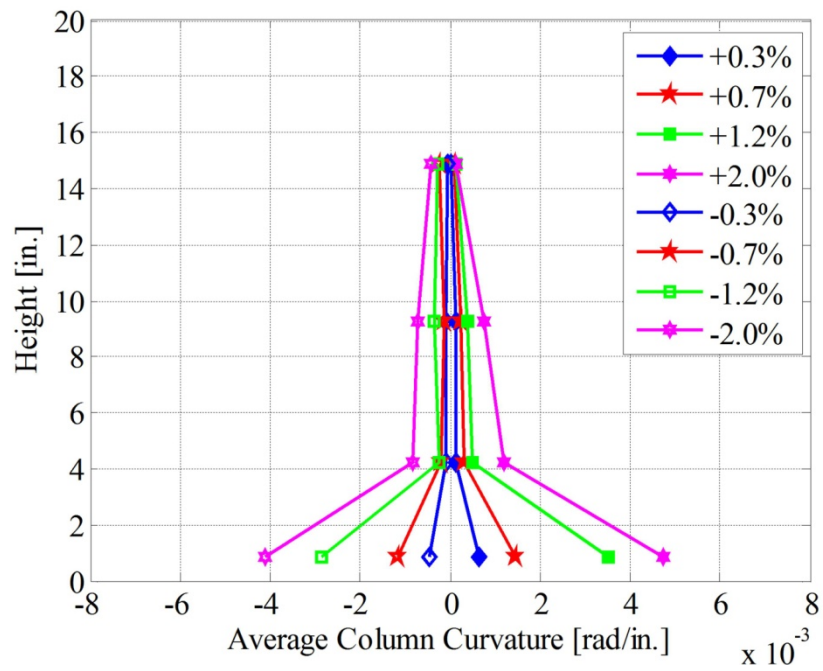


Figure 36. Graph. Specimen SF-2 average column curvature.

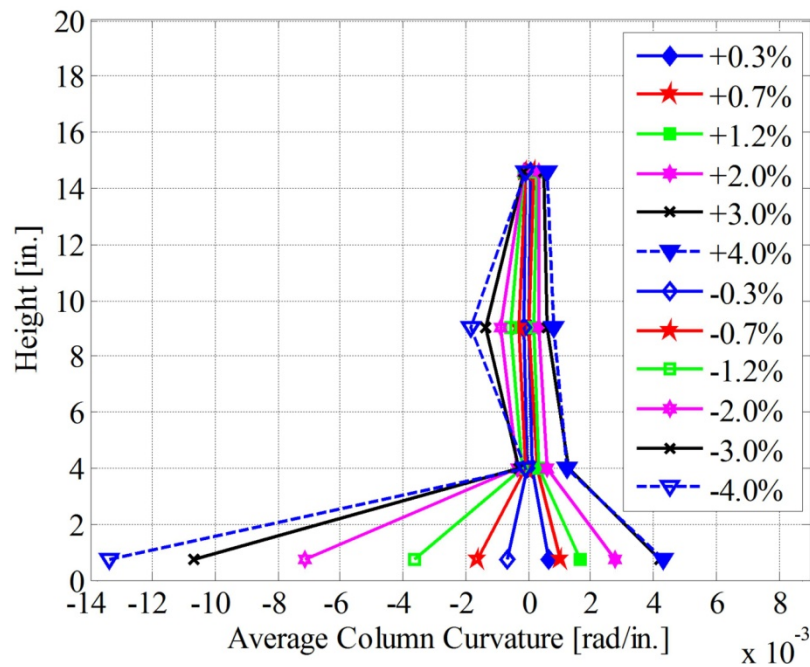


Figure 37. Graph. Specimen SF-3 average column curvature.

All potentiometers in specimens SF-1 and SF-2 worked well up to a drift ratio of 2 percent. At larger drifts some potentiometers measured only a small deformation, which suggests that the measurements were no longer accurate. At no time during the tests were potentiometers noted to lose contact in a way that might explain this behavior. This behavior was not observed for specimen SF-3, which was instrumented with new potentiometers. For SF-1 and SF-2, curvatures above a drift ratio of 2 percent are not reported in this report because of these discrepancies between potentiometers.

The curvature distribution was similar for all three specimens. The behavior of the column-to-foundation connection in all specimens was similar to that expected in cast-in-place construction; the deformation was concentrated at the base of the column. As expected, the distribution was super-linear, even though the moments were distributed linearly. This behavior reflects the fact that the response is non-linear in the plastic hinge region near the column base and essentially linear above that.

## COLUMN SPLICE

The precast columns for specimens SF-1 and SF-2 were constructed segmentally, whereas the column in specimen SF-3 was cast in a single piece. For the segmental columns, the column splice was located 20 inches above the spread footing surface. This location was where the moment was expected to just reach the yield moment,  $M_y$ , when the overstrength moment,  $M_{po}$ , was reached at the column base. This location was determined for the smallest axial load expected on the prototype connection, corresponding to a scaled-down value of 87.5 kips. The splice would have been closer to the footing with a higher axial load; about 18 inches for an axial load of 159 kips. For SF-1 and SF-2, one potentiometer was mounted on each side of the column

to monitor potential crack opening, as shown in figure 38. The measured splice interface openings are plotted in figures 39 and 40.



Figure 38. Photo. Crack opening measurement pot.

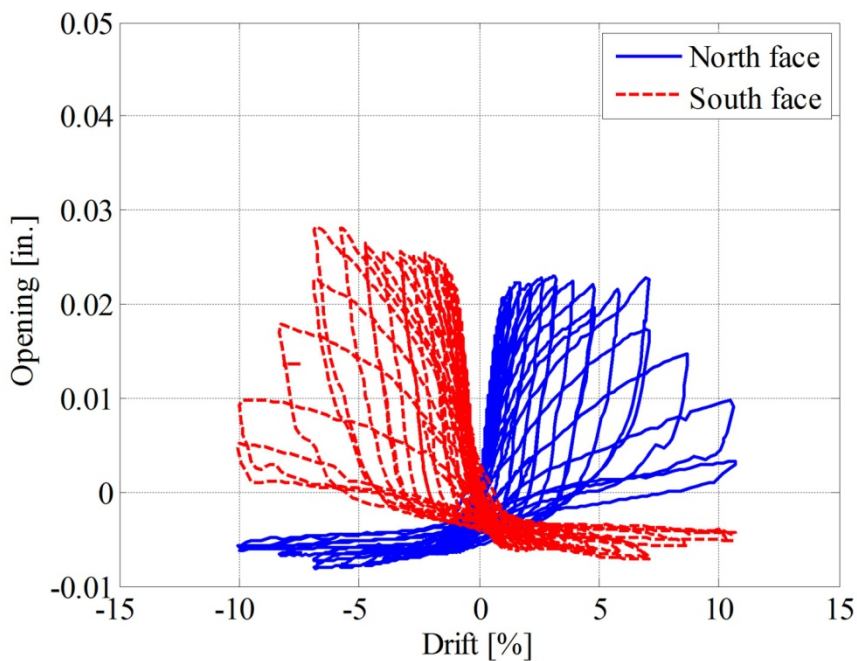


Figure 39. Graph. Specimen SF-1 splice interface opening.

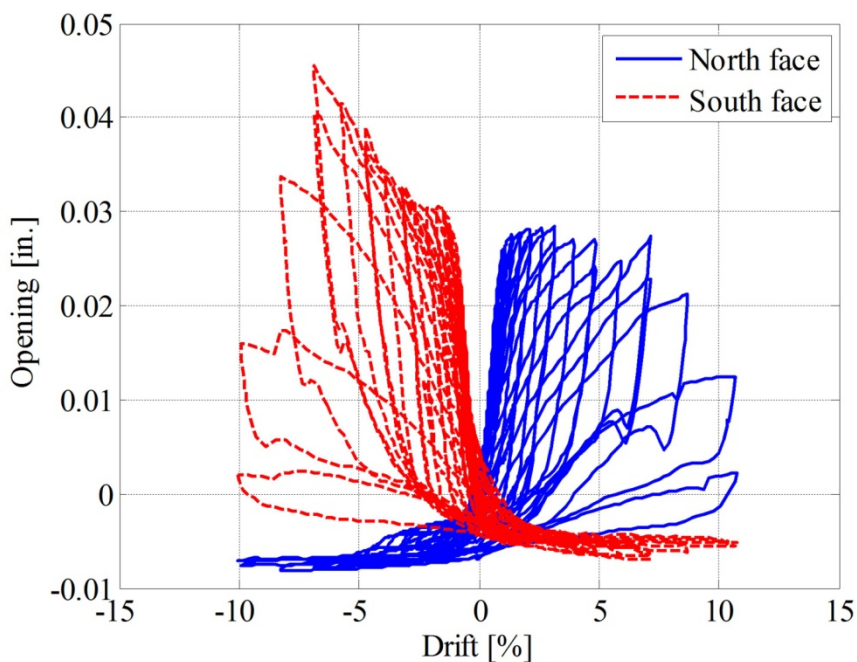


Figure 40. Graph. Specimen SF-2 splice interface opening.

When axial loads were applied to the specimens, the columns shortened. The recorded average shortening within the splice regions for SF-1 and SF-2 were recorded over a gauge length of 2.75 inches, which was the center-to-center distance to the aluminum plates mounted on the

specimens (see figure 38). The applied axial loads and the corresponding measured average axial strains are reported in table 10. For a load of about 159 kips, the measured average axial strains were about 0.001. Assuming that the elastic modulus can be approximated as  $57,000 \sqrt{f'_c}$ , the expected strains would be about 0.00012, differing by a factor of eight. For a load of about 240 kips, the measured axial strains ranged from 0.0011 to 0.0012, in comparison with the expected axial strains of about 0.00019. It is possible that the approximately ½-inch grout layer was more deformable than the concrete.

Table 10. Axial load and strains across and near splice interfaces.

Loading	Specimen SF-1		Specimen SF-2	
	1.0DL+1.0OT*	1.25DL+1.75LL	1.0DL+OT*	1.25DL+1.75LL
<b>Axial Load (kips)</b>	159.4	241.7	159.2	242.2
<b>Measured Axial Shortening (Averaged LVDTs) (in.)</b>	0.0030	0.0033	0.0025	0.0029
<b>Average Axial Strain</b>	0.0011	0.0012	0.00091	0.0011
<b>Calculated Axial Strain</b>	0.00013	0.00019	0.00012	0.00018
<b>Ratio of Measured/Calculated Axial Strain</b>	8.5	6.3	7.6	6.1
<b>Measured Average Axial Strain in Bars near Interface</b>	0.00027	0.00035	0.00029	0.00038
<b>Ratio of Measured/Calculated Axial Strain</b>	2.1	1.8	2.4	2.1

\*OT = overturning

For the lateral-load tests, the maximum extreme compressive strain calculated from the measured data was 0.002 on the north side of SF-2. In both tests, cracks appeared at the splice early, but they were small and closed after each cycle. The largest opening was 0.045 inches in SF-2 and corresponded to a rotation at the splice of about 0.24 percent. This value corresponded to about 2.1 percent of the total rotation at the location where lateral load was applied. There were no indications of damage at the interface between the column segments. At the end of cyclic testing, the maximum axial shortening measurements with these gauges were about 0.0028 inches for specimen SF-1 and 0.0052 inches for specimen SF-2, indicating that the splice interfaces had closed.

## **STRAINS IN COLUMN LONGITUDINAL BARS**

The longitudinal bars in the columns were gauged as described in chapter 3. In all specimens, symmetry of the column longitudinal bars was utilized; therefore, only the N-NE and S-SW longitudinal column bars were strain gauged. Gauges were attached on the bars in pairs at five locations in specimens SF-1 and SF-2:

- 18 inches above the spread footing surface.
- At the column-to-footing interface.
- 7 inches and 15 inches below the footing surface to verify reinforcement development length.
- 20 inches below the footing interface by the longitudinal terminators to estimate the extent to which the anchors were engaged.

Specimen SF-3 had a shallower spread footing than specimens SF-1 and SF-2 and did not have a column splice, so the strains in SF-3 were only monitored in two locations:

- At the column-to-footing interface.
- 7 inches below the footing surface.

### **Strain Profiles along the Height of Specimen**

The strain distributions over the height of the S-SW bar at various drift levels are shown for all three specimens in figures 41 to 43. In general, the reported strains for SF-1 and SF-2 at each location correspond to the average of the strain readings on each side of the bar at a particular location. Strains reported at the column-to-footing interface (0-inch height) in specimens SF-1 and SF-2 are from one gauge only because the data acquisition system capped the readings at a strain limit of 0.011. Similarly, the strain readings were not averaged for specimen SF-3, because the gauges facing the cover of the column did not produce reliable strain gauge readings. Strains are plotted up to 3 percent drift, and this drift is less than the maximum drifts reached by the specimens.

The strain measurements indicate that the bars at the interface yielded at a drift ratio of about 0.5 percent for all three specimens.

The strain profiles for specimen SF-1 and SF-2 were nearly identical. The strains were largest at the column-to-footing interface and decreased down into the spread footing and up in to the column, as expected. By contrast, specimen SF-3 showed much lower strains at the interface and significant post-yield strains at the bottom end, next to the terminators. First yield at the terminators occurred at 0.49 percent drift. Furthermore, gauges were placed on the bars in pairs, yet at some locations one gauge showed compression while the other showed tension.

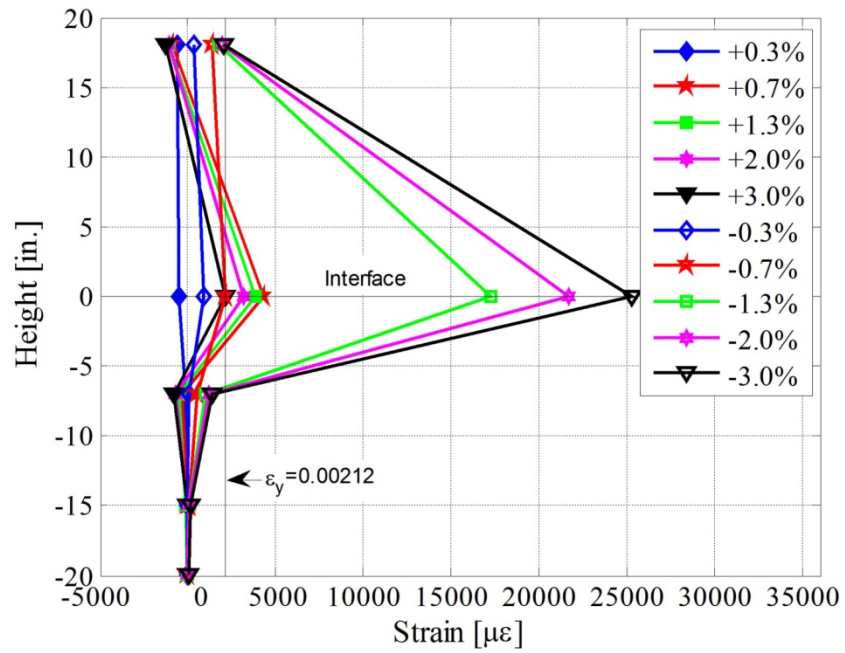


Figure 41. Graph. Strain profiles in S-SW bar in specimen SF-1.

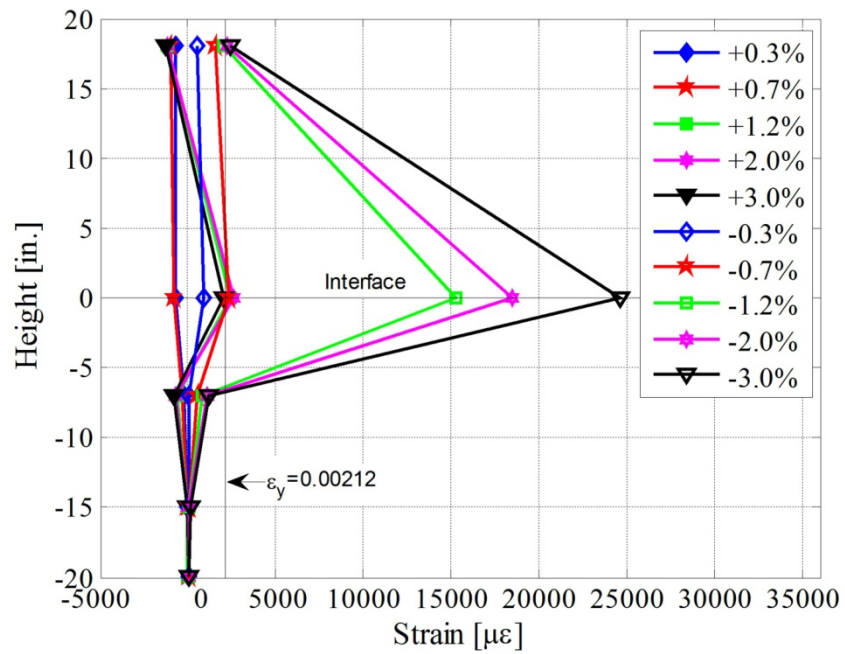


Figure 42. Graph. Strain profiles in S-SW bar in specimen SF-2.

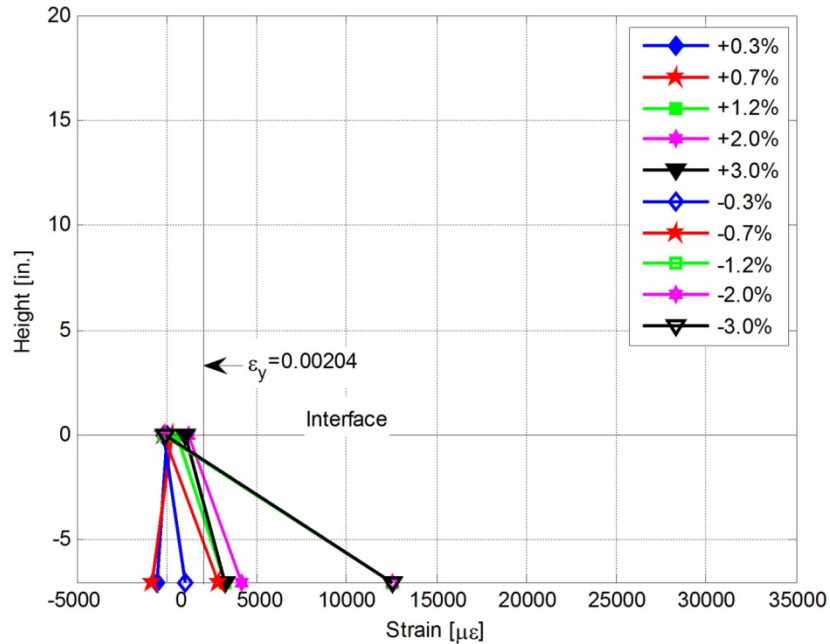


Figure 43. Graph. Strain profiles in S-SW bar in specimen SF-3.

These measured bar strains in specimen SF-3 are inconsistent with the observed behavior. The column was seen to undergo many cycles of inelastic bending deformations just above the interface before it finally failed by combined punching and moment transfer in the connection region. A possible explanation is that the gauges were mislabeled or connected wrongly to the data acquisition system. Results of individual strain gauges for all three specimens are reported in more detail in the section regarding the column longitudinal bar strain histories within the footing.

Residual strains became apparent at about 0.8 percent drift in the strain gauges at the column-to-footing interface. The S-SW bar in specimen SF-3 did not reach yielding at the interface throughout the test. After 2.4 percent drift for specimen SF-1, 2.6 percent drift for specimen SF-2, and 0.98 percent drift for specimen SF-3, strains began to exceed the reading capacity of the data acquisition system ( $25000\mu\epsilon$  for specimens SF-1 and SF-2, and  $12000\mu\epsilon$  for specimen SF-3). Maximum strains that the system was capable of reading ranged from  $\pm 0.011$  to  $\pm 0.025$ . Before the strain gauges had delaminated from the reinforcement, strains would be capped at these limits and the readings would be within the recording range again once strains were lower.

### Strain Histories for Bars near Splice

Figure 44 shows the strain histories for the strain gauges located 2 inches below the segment splice (18 inches above the spread footing). These gauges indicate that the gauged N-NE bars started to yield at 0.8 percent drift for specimen SF-1 and 1 percent drift for specimen SF-2. For the S-SE bars it was about 3.2 percent drift for SF-1 and 1.2 percent drift for SF-2.

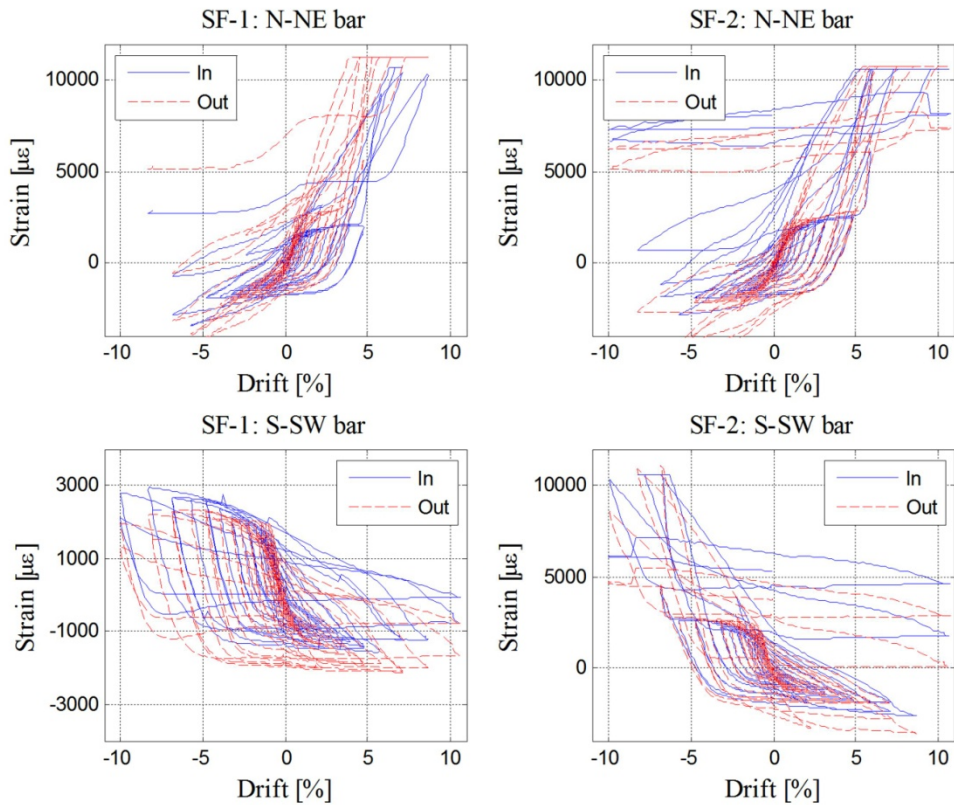


Figure 44. Graphs. Strain-drift relationship 2 inches below the column splice interface.

All bars except the S-SW bar in specimen SF-1 yielded considerably near the column splice once spalling developed. This difference was attributed to the fact that the full spall height on the south side for specimen SF-2 was 12 inches while it was 8 inches for SF-1. However, on the north side for both specimens, the full spall height was 12 inches. This suggests that the splice bars were yielding.

### Column Longitudinal Bar Strain Histories in Footing

Figures 45 through 47 show for all three specimens the strain-drift relationship at locations within the footing. In the figures, each strain gauge is plotted individually. The gauge marked “In” refers to the gauged facing towards the column core, and the one marked “Out” faced the column concrete cover. Strains were plotted until voltage spikes were detected frequently, at which point the gauges were deemed unreliable. Two strain gauges were damaged from the very beginning and therefore are not included in the plots.

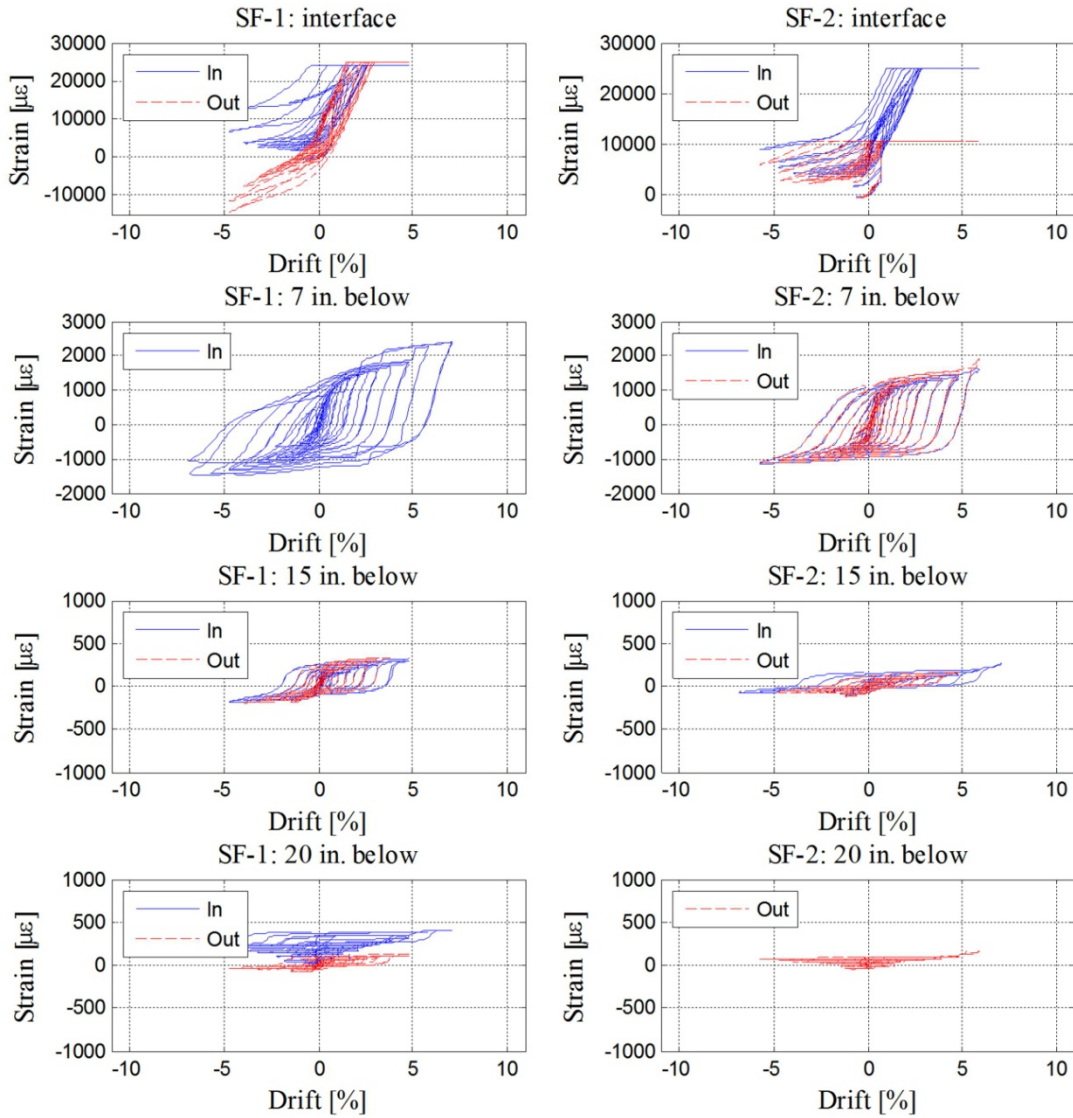


Figure 45. Graphs. Strains in N-NE bars in specimens SF-1 and SF-2 at various heights below the interface.

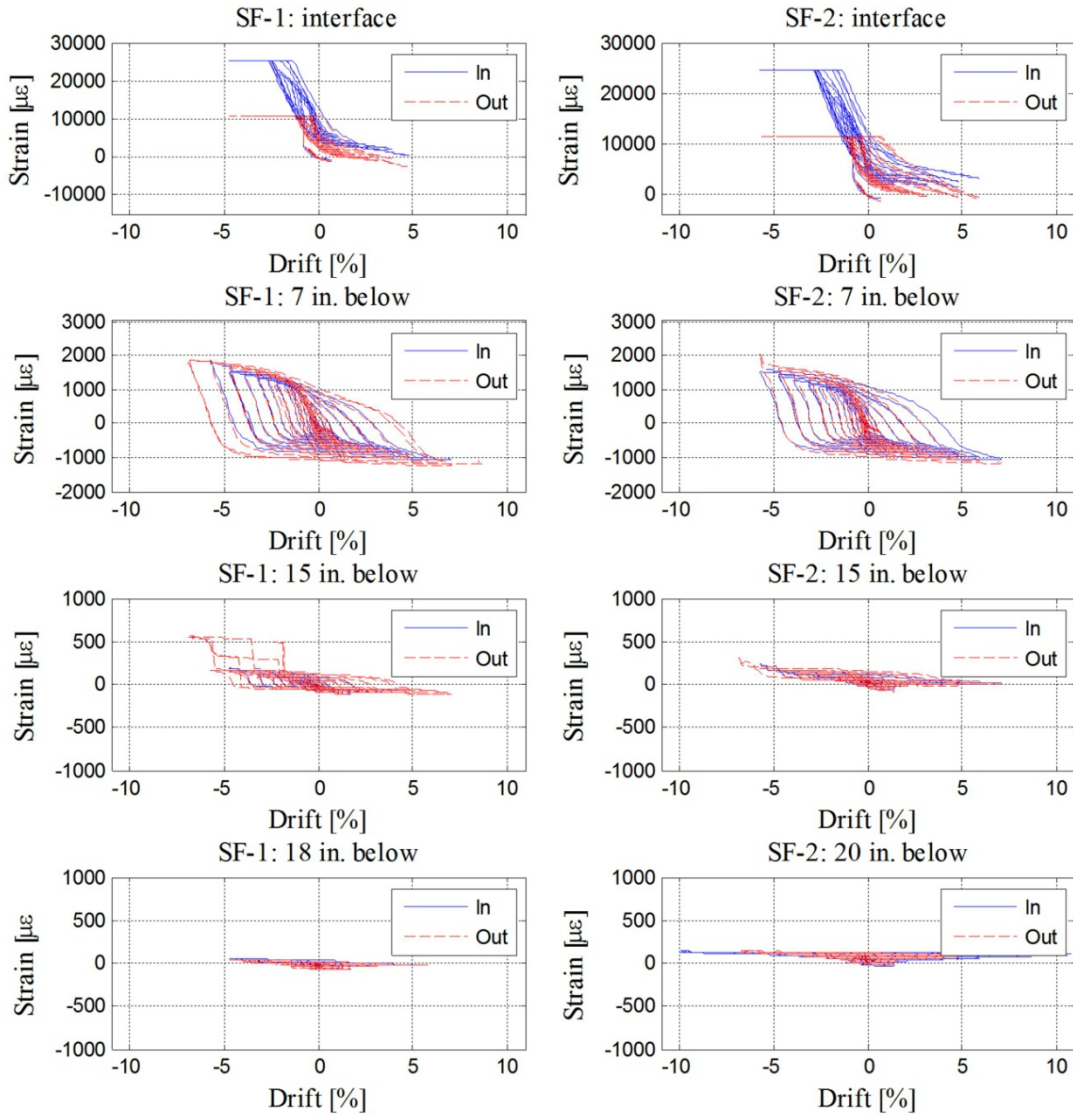


Figure 46. Graphs. Strains in S-SW bars in specimen SF-1 and SF-2 at various heights below the interface.

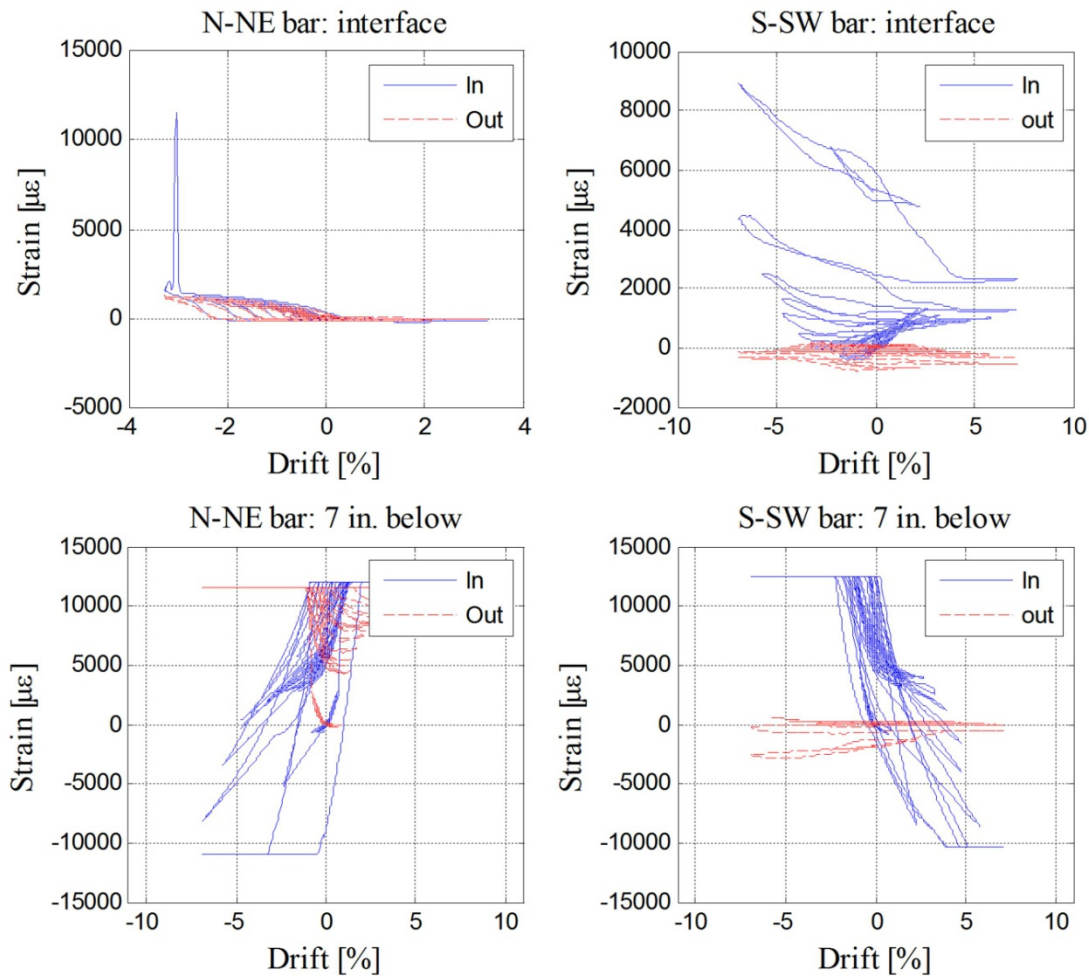


Figure 47. Graphs. Strains in N-NE and S-SW bars in Specimen SF-3 at various locations below the interface.

Strains recorded in specimens SF-1 and SF-2 were similar. Pairs of gauges were attached at the interface and at 7, 15, and 20 inches below it. The gauges at 20 inches were adjacent to the terminators. The N-NE bars and the S-SW bars showed strains of similar magnitudes, confirming that the overall behavior of the two specimens was similar, as shown by the load-displacement curves. The largest strains recorded were at the column-to-footing interface, as was expected. Furthermore, at the interface, the readings of the two individual gauges differed, especially at higher drifts, implying the presence of bending as well as tension. The pairs of strain gauges located below the column-to-footing interface gave almost identical readings, implying pure tension. At 7 inches below the interface the bars almost yielded, at 15 inches the peak stress was approximately 10 ksi, and by 20 inches the peak stress was approximately 3 ksi. (The highest strain, for the “inside” gauge of specimen SF-1, is higher than this, but its value is an outlier and is inconsistent with the “outside” gauge reading at that location.) The values suggest that the bars were fully anchored by that depth and that the mechanical anchors served as a secondary anchorage.

The strains in the N-NE and S-SW bars in specimen SF-3 are somewhat erratic and do not follow the pattern that was expected from the observed behavior in the test. In specimen SF-3 the column underwent inelastic cyclic bending before the connection region failed in combined punching shear and moment transfer. That inelastic bending implies larger strains at the interface and smaller strains near the mechanical anchors. At larger drifts, the strain was expected to increase at both locations.

The measured strains in specimen SF-3 display three trends. First, the strains at the interface are general smaller than those near the terminators, 7 inches below the interface. This trend implies negative bond stresses, which are thermodynamically impossible. Other explanations must therefore be sought, and mislabeling of the gauges is the most likely one. Second, most of the gauge pairs show large differences between the two readings, implying significant bending of the bar. Such bar bending is plausible, but no independent verification measurements were available to confirm it. Third, the bending appears to be more severe near the terminator than at the interface. This is the opposite of the trend seen in specimens SF-1 and SF-2, and is difficult to explain, except by gauge mislabeling.

It was therefore concluded that the gages were most likely mislabeled, in which case the data cannot be used.

## **FOOTING STRAIN CORRECTIONS**

Strains reported in the spread footings for specimens SF-1 and SF-2 are the mechanical strains derived from the measured strain values. The strains in the bottom mat were so small that they were affected strongly by thermal effects (see figure 48). This behaviour was not observed in specimen SF-3. In specimens SF-1 and SF-2 it was believed to have been caused by heat from the lights acting on the strain gauges lead wires. To determine the mechanical strain during cyclic testing, thermal strains needed to be accounted for. The mechanical strains were obtained by calculating the difference between the strain value measured at the peak of the cycle and the strain value when the moment in the column was zero. It was assumed that the change in thermal strain during that time (about 20 seconds) was negligible. The largest rate in thermal strain change occurred in specimen SF-1 between data counts 40681 and 41672 at an average rate of 0.083 microstrain/count. If this rate were applied to the period of loading (94 counts, going from “peak” to “valley”), it would imply a thermal strain change of 7.8 microstrain during that time. The calculated mechanical strain value was then added to the initial strain obtained when the specimen was loaded axially up to 159 kips before starting the cyclic test.

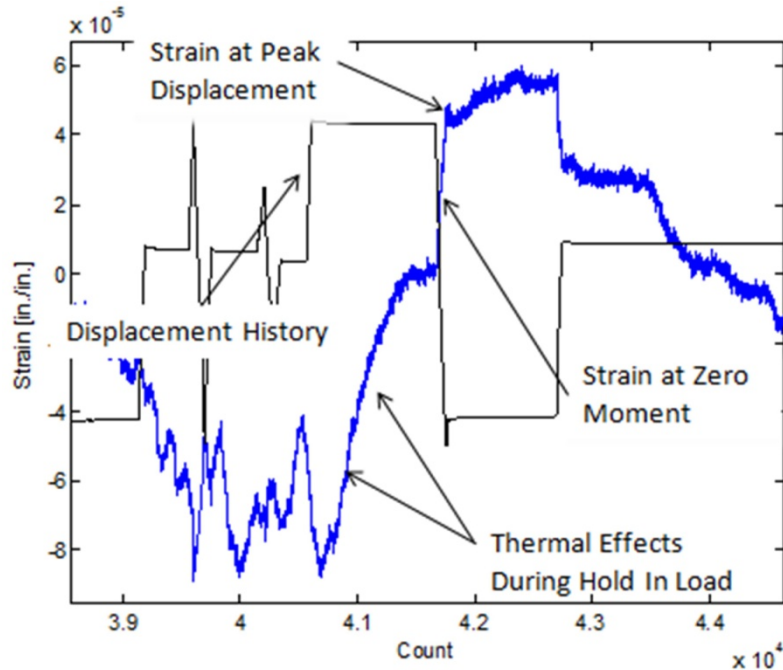


Figure 48. Graph. Thermal effects in strain gauges.

### STRAINS IN BOTTOM MAT OF FOOTING REINFORCEMENT

The configuration of the bars in the footing and the locations of strain the gauges were shown in figure 13. The columns in all three specimens were designed to have the same flexural strength. Specimens SF-1 and SF-2 had the same spread footing depth of 22.5 inches, so the total amount of flexural steel was also the same in both specimens. However, it was distributed differently because specimen SF-1 contained slots in the bottom of the column to allow some of the bottom mat bars to pass directly beneath the column. In contrast, specimen SF-2 contained no slots, so the bars had to be moved laterally to pass by the sides of the column, where they were bundled with other bars already existing there. In addition, to satisfy AASHTO LRFD minimum bar spacing requirements and to provide crack control reinforcement, additional steel, of the same size and spacing as in the main mat (5 inches center-to-center), was provided in line with the column. Those bars were short and terminated at the column face.

Specimen SF-3 had a much thinner footing than the other two specimens (half of the column depth); thus, a great deal of flexural steel was required. The bottom mat was arranged to be similar to specimen SF-2, but modifications were needed due to the high amount of steel congestion. For example, the reduced footing depth resulted in a smaller effective width in which a much greater amount of steel was required. The consequence was the use of larger bars (No. 7 instead of No. 5) bundled at a spacing of 2.5 inches. Steel was placed in line with the column to satisfy AASHTO LRFD requirements. It was the minimum permitted and was terminated at the column face.

### Strains in Bottom Bars in the North-South Direction (Loading Direction)

Longitudinal bars were gauged so that the distribution of strain across the footing could be determined. The northeast quadrant of the spread footings was equipped with gauges at a point 5.5 inches to the north of the column face, including some short bars. The gauges were placed on the side of the bar to minimize the effects of bending about a horizontal axis. They were all chosen to be on the east side of the footing because the response was expected to be symmetric in each principal direction. All strain gauges worked well except two—one located 17.5 inches away from column center in specimen SF-2 and the other located 27 inches away from the column center in specimen SF-3, which were damaged during casting. The bar strains at various drift levels are shown in figures 49 through 51.

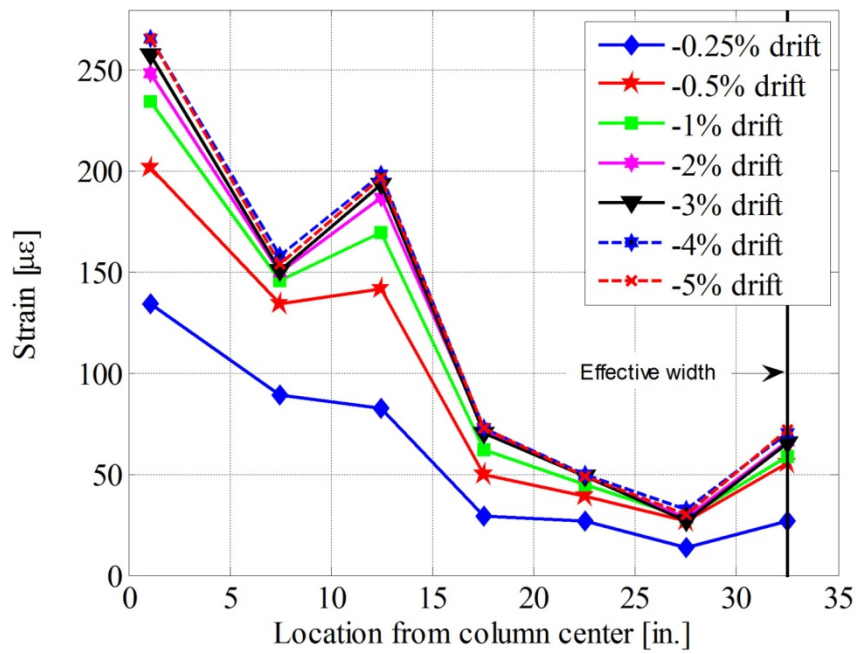


Figure 49. Graph. Specimen SF-1 strain profiles in bottom mat of the footing.

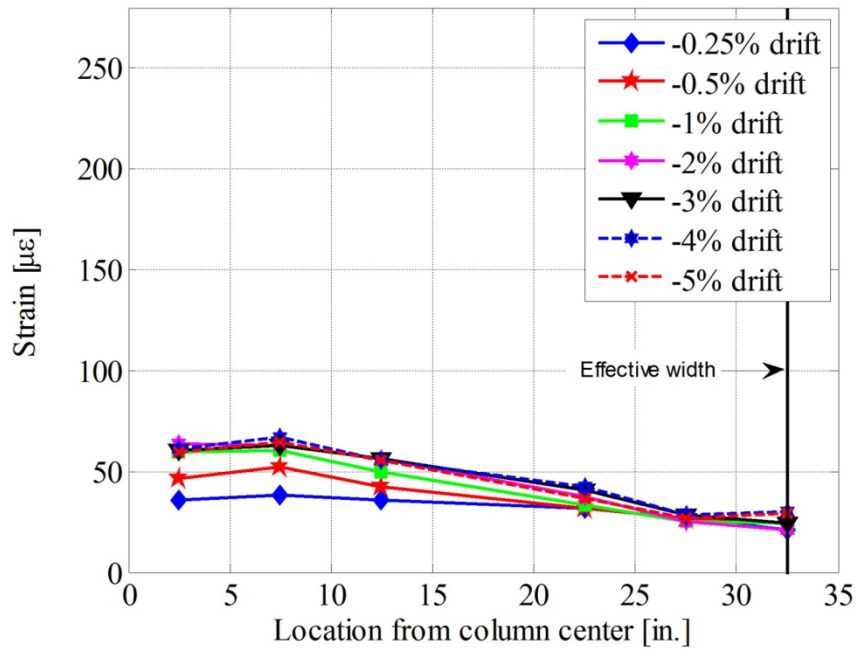


Figure 50. Graph. Specimen SF-2 strain profiles in bottom mat of the footing.

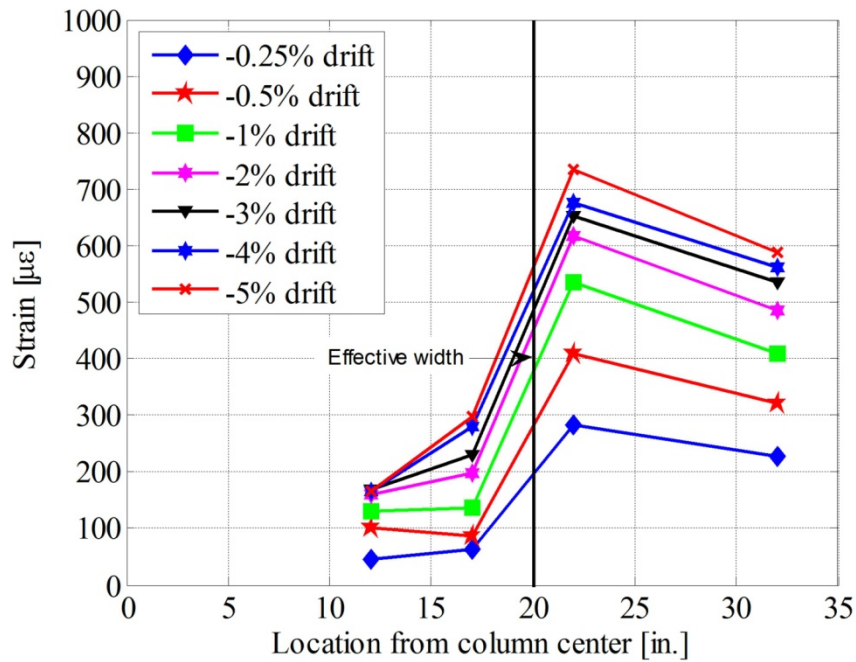


Figure 51. Graph. Specimen SF-3 strain profiles in bottom of the footing.

The distribution of strains in the footing differed. However, the strains in all three specimens shared the common feature that they increased with drift up to about 1 percent drift, after which they were approximately constant. This occurred because the column yielded initially at about 0.5 percent drift and the force was nearly constant after 1 percent drift. The strain measurements in specimens SF-1 and SF-2 must be regarded as less reliable than those in specimen SF-3 because of the need to correct for thermal effects. The peak strains remained low up to 5 percent drift. In all specimens, the first yield in the column longitudinal bars was detected at about 0.50 percent drift.

In specimen SF-1, the strains consistently decreased with distance from the centerline of the specimen, as might be expected. After yielding of the first longitudinal bar, the moment introduced in the footing was nearly constant and therefore resulted a identical footing strain profiles after 0.5 percent drift for specimens SF-1 and SF-2. The biggest strain recorded at 5 percent drift was  $0.12\varepsilon_y$  and was measured in the bars going through the slots. This strain value reflects the fact that the footing was essentially uncracked and remained elastic throughout the test. The lower strain in the bar 7.5 inches away from the column center is most likely due to the fact that it was a short bar that ended in front of the column. The strains increased in the set of bundled bars (12.5 inches away from center) and decreased rapidly in the remaining bars.

Strain profiles for specimen SF-2 did not have the two peaks that are present in the profiles for specimen SF-1. Recall that no bars passed beneath the column in specimen SF-2. The first two bars from the column center were short bars, and the following two were bundled. The strains in bars 7.5 inches and 12.5 inches away from the column center are three to four times smaller in specimen SF-2 than in specimen SF-1. This difference was already apparent during the application of the axial load. The strain profiles beyond one column diameter die out similarly in both specimens after that. The observation that the strains were all much less than the yield strain, and that the strains in short and long bars were almost the same, suggests that the concrete was not cracked and was carrying tension force.

The flexural reinforcement layout for specimen SF-3 was similar to the one in specimen SF-2, but the steel was heavier because the footing was shallower. In contrast to specimens SF-1 and SF-2, specimen SF-3's strain profiles consistently increased from the column center, and maximum strain was recorded outside the effective width, even though the all gauged bars were long ones. Strains increased constantly with drift ratio in specimen SF-3 which reflects the fact that the cracks were becoming more pronounced. At 5 percent drift, the maximum strain was about  $0.30\varepsilon_y$ .

### **Implication of the Effective Width**

The strain profiles shown in figures 49 to 51 allow the definition of the effective width to be evaluated. It is defined in the AASHTO Seismic Guide Specifications as the sum of the column diameter and two times the footing depth ( $b_{eff} = D_c + 2H_f$ ) and implies that only the bars inside it will experience significant tension strain and contribute to resisting the applied moment.<sup>(15)</sup> If the footing steel required for strength is more than the minimum, the concrete should be expected not to crack. Thus, it is reasonable to suppose that the definition of effective width is based on an uncracked section since specimens SF-1 and SF-2 did not display visible flexural cracks, and the low strains also suggest an uncracked condition. The evidence from their strains cannot be used

to evaluate the AASHTO equation for  $b_{eff}$ . However, despite the uncertainty caused by the need for thermal corrections, the strain profiles displayed the expected reduction in strain with distance from the column centerline.

In specimen SF-3, the concrete cracked and the steel strains were larger, although they never reached yield. Thus, they are appropriate for evaluating the definition of  $b_{eff}$ . However, they show that the largest strains were in the bars outside the effective width, which is the opposite of what would be expected. Furthermore, specimen SF-3 was the only one of the three in which the effective width was significantly less than the total width, so the strains were expected to be strongly and unambiguously concentrated inside the effective width. The reasons for the anomalous behavior are unknown.

### **Strains in Bottom Bars in the East-West Direction**

Strut-and-tie modeling suggests that compressive struts forming within the footing are more three dimensional in specimen SF-2 and specimen SF-3 than in specimen SF-1, which results in more tension in the transverse bars in the bottom mat.

In specimen SF-1, some of the longitudinal steel passed directly under the column, allowing the formation of a 2-D truss in the footing. In the other two specimens, no bars passed beneath the column, so any truss that formed would be necessarily 3-D and transverse bar forces would be necessary for equilibrium. Some transverse bars were gauged, as shown in figures 52 through 54, to evaluate the formation of such trusses.

Because the footing did not suffer visible flexural cracking in specimens SF-1 and SF-2, the bar strains were too small to permit a reliable evaluation. In each case they were approximately half the corresponding longitudinal bar strains, but they would be actually larger in specimen SF-2 than in specimen SF-1, contrary to what would occur if the expected truss had formed.

In specimen SF-3, the transverse bar strains implied a stress of approximately 10 ksi. This is large enough to confirm the existence of some 3-D behavior, but it is still only about one-quarter of the stress predicted by the truss model.

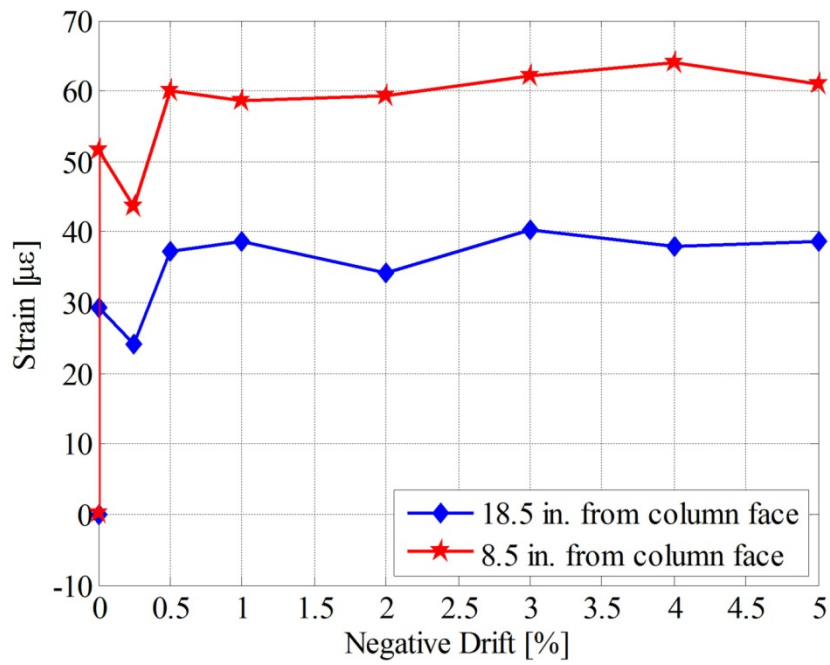


Figure 52. Graph. Specimen SF-1 transverse strains in bottom mat of the footing.

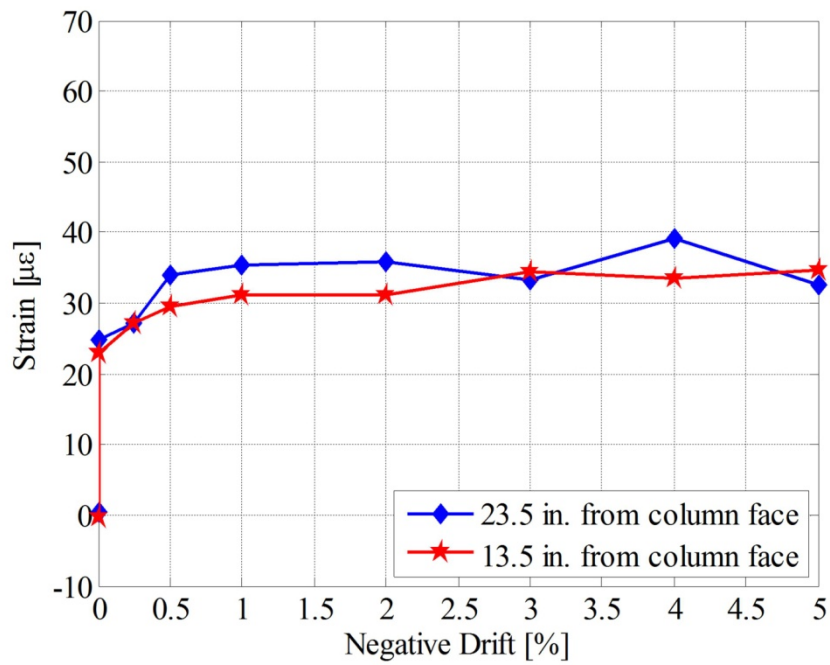


Figure 53. Graph. Specimen SF-2 transverse strains in bottom mat of the footing.

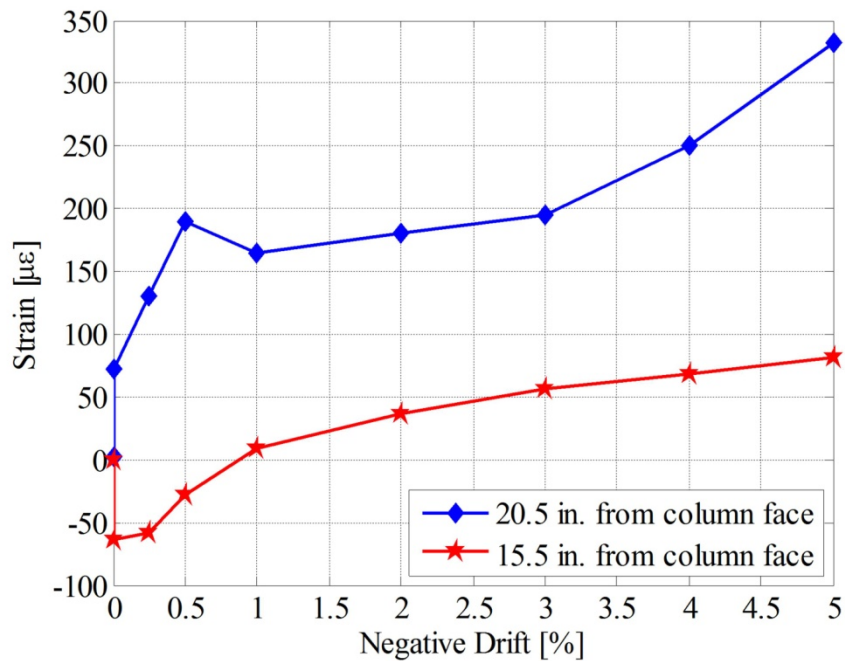


Figure 54. Graph. Specimen SF-3 transverse strains in bottom mat of the footing.

### STRAINS IN DIAGONAL BARS

Diagonal bars were placed in both the top and bottom mats to play a role similar to that of “shear friction” steel, which in other situations would cross the interface between the precast and cast-in-place elements. The total amount of diagonal steel in specimens SF-1 and SF-3 was equal to the amount needed if the cohesion component of the AASHTO LRFD article 5.8.4 equation (5.8.4.1-3) for shear friction was ignored between the precast column and the cast-in-place footing. The difference between the two (SF-1 and SF-3) was that the longitudinal footing steel in specimen SF-3, running north and south, was accounted for when determining shear friction resistance. The amount of steel was reduced in SF-2.

In all specimens, two diagonal bars in the bottom mat and two diagonal trim bars in the top mat were gauged as shown in figure 13. The strains in the south bottom steel in specimens SF-1 and SF-3, and north bottom steel in specimen SF-3 as well are not reported because the gauges were damaged during casting. The strains in the diagonal bars are plotted in figure 55 through 57.

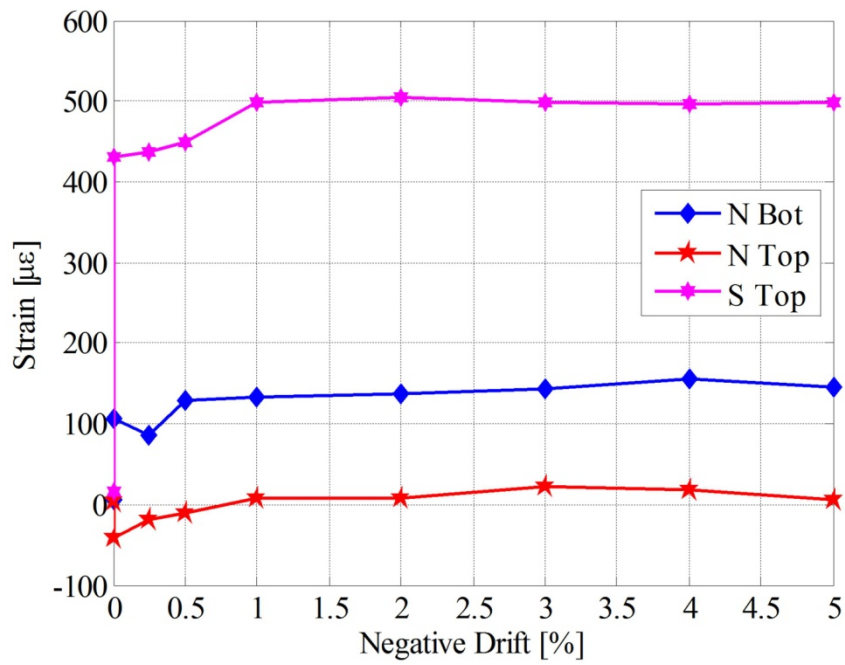


Figure 55. Graph. Specimen SF-1 strains in diagonal steel in footing.

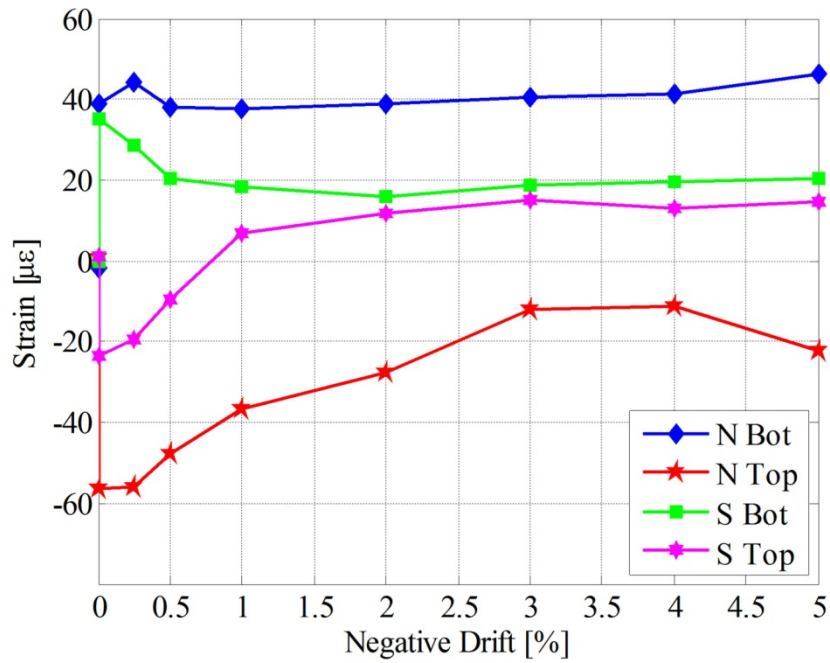


Figure 56. Graph. Specimen SF-2 strains in diagonal steel in footing.

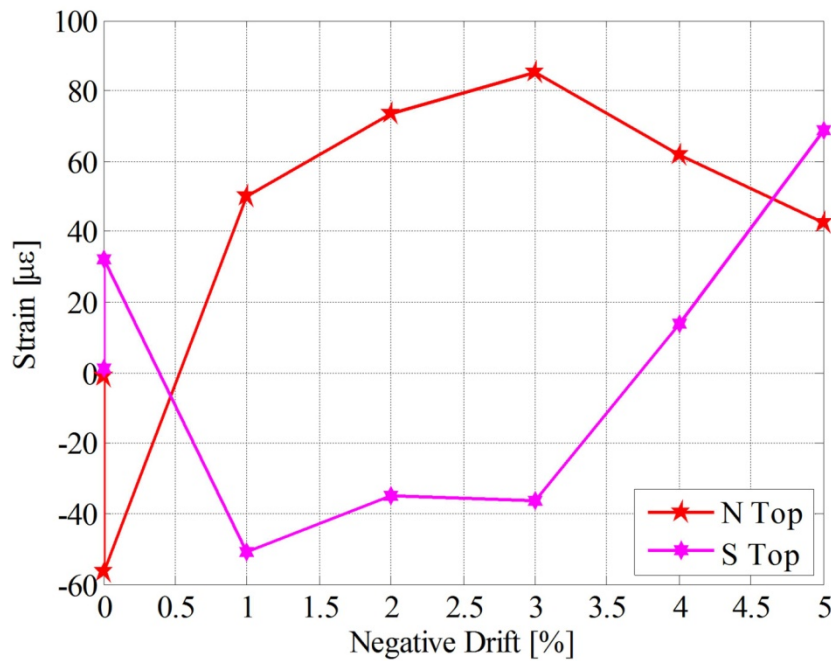


Figure 57. Graph. Specimen SF-3 strains in diagonal steel in footing.

Strains reported in specimens SF-1 and SF-2 are only the mechanical strains. The thermal strains were removed using the process described in the previous section on footing strain corrections. At 0 drift, the effect of only the axial load is noticeable. Each bar had one strain gauge on the side facing out from the column. When the column displaced northward in specimens SF-1 and SF-3 towards the gauges, the north-bottom gauges barely recorded any stress. However, strains increase for north-top and south-bottom bars as expected. The column was pushing out in those areas.

Overall, the strains measured in the diagonal steel were small. The maximum strain measured was in specimen SF-1 and it was about  $0.25\epsilon_y$ . However, the tension strains in the diagonal steel of specimens SF-2 and SF-3 were all less than 100 micro-strain, which corresponds to a stress of 3 ksi. The low strains in the steel, and the lack of cracking in the footings of specimens SF-1 and SF-2, imply that the shear-friction mechanism was never activated there. The column in specimen SF-3 punched through the footing, but the stresses in the bars were small enough that the diagonal steel contributed little to resisting the loads.

### STRAINS IN FOOTING TIES

Ties were provided in specimen SF-1 in accordance with the Caltrans recommendations and were reduced by half in specimen SF-2.<sup>(16)</sup> It is believed that the main reason for their existence is to permit a load path to exist in the footing when the column bars are bent outwards, as is commonly done in cast-in-place construction. However, this function was unnecessary here, because the column bars were straight and equipped with anchor heads. The ties, once in place, might serve any one of three functions: one-way “beam” shear resistance, two-way “punching” shear resistance, or joint shear resistance. For one-way shear, the footing depth was selected so

the concrete resistance alone would just suffice, because WSDOT expressed a strong preference for that approach. The joint shear resistance is closely related to the internal force path, so the required strength is likely to be very different when headed straight bars rather than bent-out bars are used in the column. Thus, the expectations for stress in the ties were unclear.

The ties in specimen SF-3 varied greatly from both specimen SF-1 and specimen SF-2. Unlike SF-1 and SF-2, the ties were not placed to follow Caltrans' recommendations. Ties in the footing were strategically placed such that the one-way shear failure mode would be suppressed without inhibiting failure by combined moment transfer and punching shear, since the goal of the test was to investigate strength in that failure mechanism. This meant that the ties needed to be placed within the effective width of the footing but outside of the punching shear plane.

Four ties were strain gauged in each of specimens SF-1 and SF-2. One tie was on the west side of the column, and the other three were on the north side. Because of the way that the ties were placed strategically in specimen SF-3, the ties were lumped together in four different corners. The six ties in the northeast quadrant of the footing were gauged.

Figures 58 through 60 show the measured strains in the ties for selected drift levels. Thermal stresses were accounted for in specimens SF-1 and SF-2 following the same process described earlier. The strains in specimens SF-1 and SF-2 measured in the ties were even smaller than those in the flexural and shear friction steel, and even with no thermal correction it never exceeded  $0.04\epsilon_y$  strain in tension. Many values were negative.

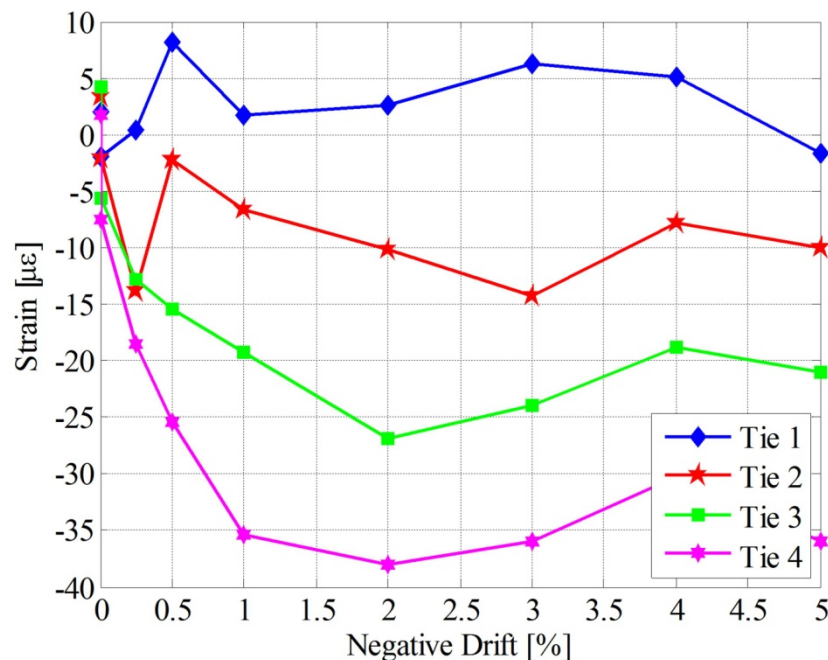


Figure 58. Graph. Specimen SF-1 strains in ties.

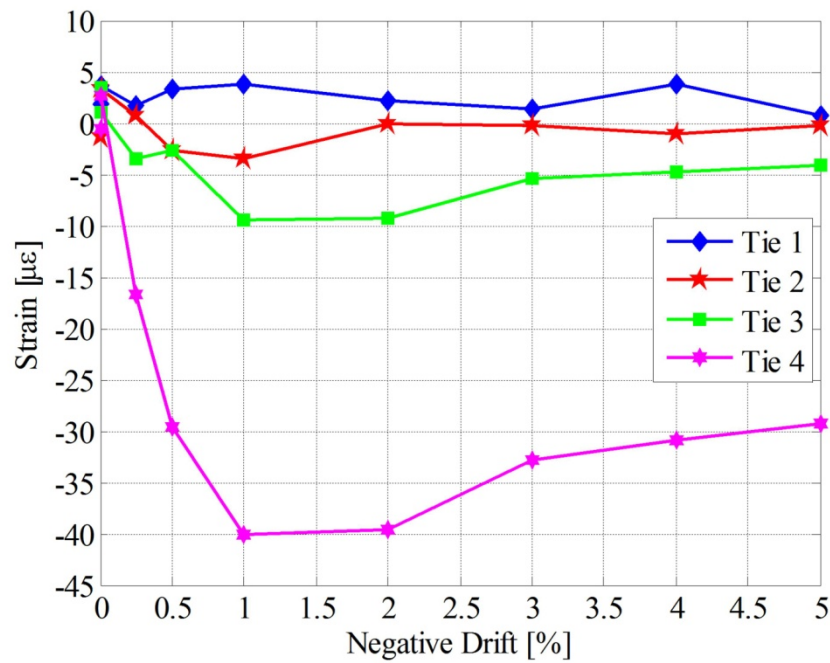


Figure 59. Graph. Specimen SF-2 strains in ties.

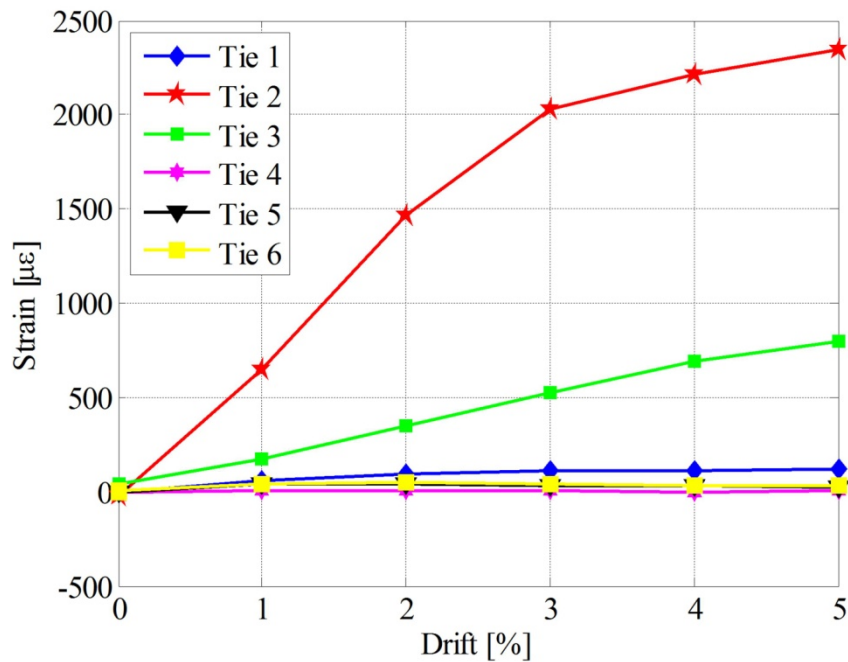


Figure 60. Graph. Specimen SF-3 strains in ties.

The vertical ties in specimen SF-3 had much higher strains than those in specimens SF-1 and SF-2. Tie No. 2 reached yielded at 3 percent drift, whereas in the other two specimens the maximum strain never exceeded 4 percent of yield strain. This difference was expected since the footing

was designed such that the ties would work to suppress the one-way shear. Although the gauged ties in specimen SF-3 were all within 1 foot of each other, it is likely that tie No. 2 was the tie closest to the punching shear failure plan, and therefore had the highest strain.

## AXIAL LOAD-RESPONSE

### Factored Axial Loading

The test specimens were loaded axially with three load combinations at three different times. Before cyclic testing, the columns were loaded with the biggest axial load expected on the socket connection scaled down from the prototype (1.25DL+1.75). After that, the axial load was reduced to the unfactored dead load plus overturning (1.0DL+1.0OT) while the cyclic lateral load was applied. After the lateral loading was complete, the column was subjected an “ultimate” axial load to failure. The last test was not conducted on specimen SF-3 because it had already failed by punching.

Specimens SF-1 and SF-2 successfully carried both of the first two load combinations throughout the tests. However, specimen SF-3 punched through the spread footing while being cycled, as was anticipated in the design. Table 11 summarizes the loading applied and the measured corresponding column vertical displacement. The socket shear stress is calculated assuming that the load is resisted uniformly with depth of the footing.

Table 11. Axial load combinations on the test specimens.

Specimen	Load combination	Axial Load (kips)	Measured Deflection under the Column (in.)	Socket Shear Stress (psi)
SF-1	1.25DL+1.75LL	241.7	0.022	175
	1.0DL+1.0OT*	159.4	0.014	116
	3.5(1.25DL+1.75LL)	842	0.082	611
	3.8(1.25DL+1.75LL)	918	N/A	666
SF-2	1.25DL+1.75LL	242.4	0.0086	176
	1.0DL+1.0OT*	159.2	0.0060	116
	3.4(1.25DL+1.75LL)	819.5	0.079	595
SF-3	1.25DL+1.75LL	240.8	0.056	393
	1.0DL+1.0OT*	159.2	0.031	260
	1.4(1.25DL+1.75LL)	342	0.068	559

\*OT = Overturning

Figure 61 shows column vertical displacement versus cumulative drift (P = 159 kips). Specimens SF-1 and SF-2 maintained the same vertical displacement throughout the test while specimen SF-3 gradually slid through the spread footing.

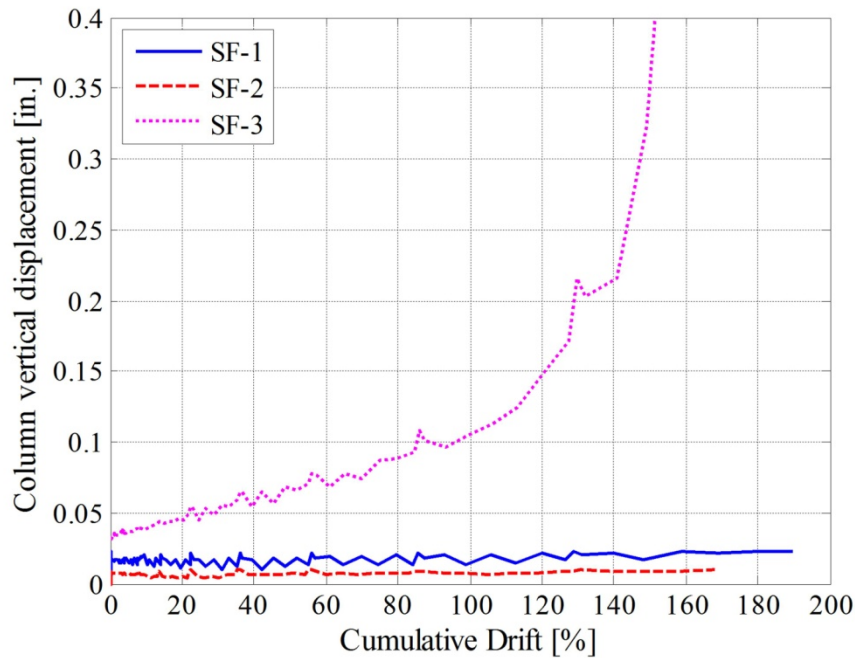


Figure 61. Graph. Column vertical displacement vs. cumulative column drift.

### Ultimate Axial-Load Capacities

Specimens SF-1 and SF-2 carried the full service axial dead load during the cyclic lateral loading. Subsequently, the column was loaded axially to induce between the precast column and the cast-in-place footing. In both cases, the column failed by crushing in the previously damaged plastic hinge region before any failure occurred in the column-to-footing connection region.

The axial load-deflection response is shown in figure 62. The load reached was about the scaled equivalent of  $3.5 P_u$ , where  $P_u$  is the factored axial load given by  $1.25DL+1.75LL$  in the prototype. The load was measured by a load cell in the Baldwin Universal Testing Machine, and the column vertical displacement was measured by the LVDT beneath the column. The potentiometer instrument itself was located just outside the column, and the motion was delivered to it by a lever mechanism that was treated as sacrificial in the event of the column slipping.

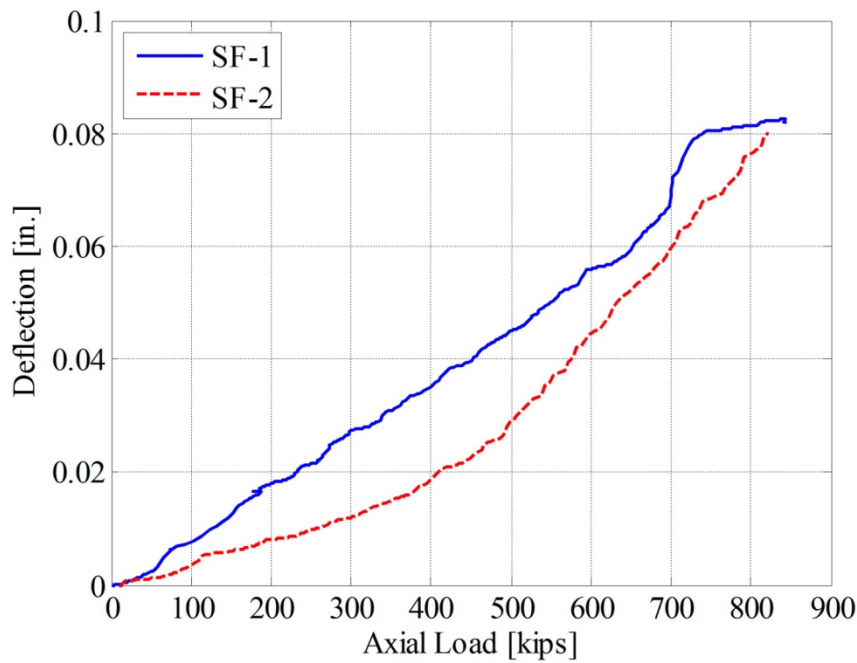


Figure 62. Graph. Axial response of specimens SF-1 and SF-2.

Both specimens responded similarly to the axial loading. Specimen SF-1 was loaded up to 842 kips, and specimen SF-2 was loaded up to 819.5 kips (see figure 63). No sliding failure was observed between the precast column and cast-in-place footing during this test. The shear friction capacity of the connection region was at least that large, and it may have been much higher. In the absence of damage due to moment transfer, such as occurred in specimen SF-3, the shear friction capacity of the deeper footing is clearly sufficient.



Figure 63. Photo. Specimen SF-2 after axial load of 817 kips.

Strain gauge measurements in the bottom mat showed strains greater than concrete cracking strain ( $\epsilon_{crack} \approx 135\mu$ ), but all were smaller than the yield strain of the reinforcement. The largest strain measured was  $0.51\epsilon_y$  and it was in specimen SF-1. The measurement was obtained from the bars going through the slots that allowed them to go under the column. In both specimens, strains in the bundled bars were approximately  $0.31\epsilon_y$ . There were no signs of permanent deformation or damage to either the specimen or the supporting hydrostone layer in the base. The deflections measured were attributed to the flexural and shear deformations of the footing.

## CHAPTER 6. ANALYSIS OF MEASURED RESPONSE

This chapter documents a comparison between the measured responses obtained through laboratory testing and results obtained using analytical models. The response measured in the experiments is denoted with the subscript “u” (e.g.,  $M_u$  – measured moment). The calculated quantities are denoted with subscripts as used in the AASHTO specifications (e.g.,  $V_n$  – nominal shear strength and  $M_n$  – nominal flexural strength).<sup>(14,15)</sup>

### FOOTING OVERTURNING

To protect against overturning of a spread footing, the AASHTO Seismic Guide Specifications requires that the footing be able to resist the overstrength moment of the column. This requirement is manifested in two specific limitations:

- The centroid of the pressure block under the footing must lie within the middle two-thirds of the footing. If, as is common, the pressure block is assumed to be triangular, this means that the footing may lift off the soil over no more than half of its width.
- The peak stress under the footing may not exceed the nominal bearing capacity, which was 75 ksf for the soil at the site.

The prototype footings were designed at the limit of these requirements. The prototype bridge bent consisted of four columns. The maximum axial load (1,157 kips, including structural and footing weights plus influence of overturning), the maximum moment (41,428 kip-in., including overstrength), and the maximum shear (345 kips) yielded an eccentricity of 4.3 ft. However, the minimum axial-load condition ( $P_{min}=737$  kips,  $M_{po} = 36,141$  kip-in,  $V_{po} = 301$  kips) resulted in an eccentricity of 5.9 ft, which led to a minimum footing size of 18 ft.

To accommodate seismic loading from any direction, the footing was square. The resulting peak soil pressure under the critical combined loading was only 9.2 ksf, which was much less than the nominal capacity of 75 ksf, soil pressure. The support conditions are illustrated in figure 64.

To replicate this situation as closely as possible in the laboratory, the three specimens were supported along two lines, each situated (at lab scale) at the same eccentricity as the centroid of the limiting soil pressure block in the field. That distance was 42 percent of 5.9 feet, or 30 inches. However, to make it possible to conduct axial-load tests with support from all four edges of the footing, support was also provided, in all specimens, along the sides of the footing, as shown in figure 64. Doing so created a pressure distribution that consisted of a distributed load (along the sides) and two line loads (at the ends).

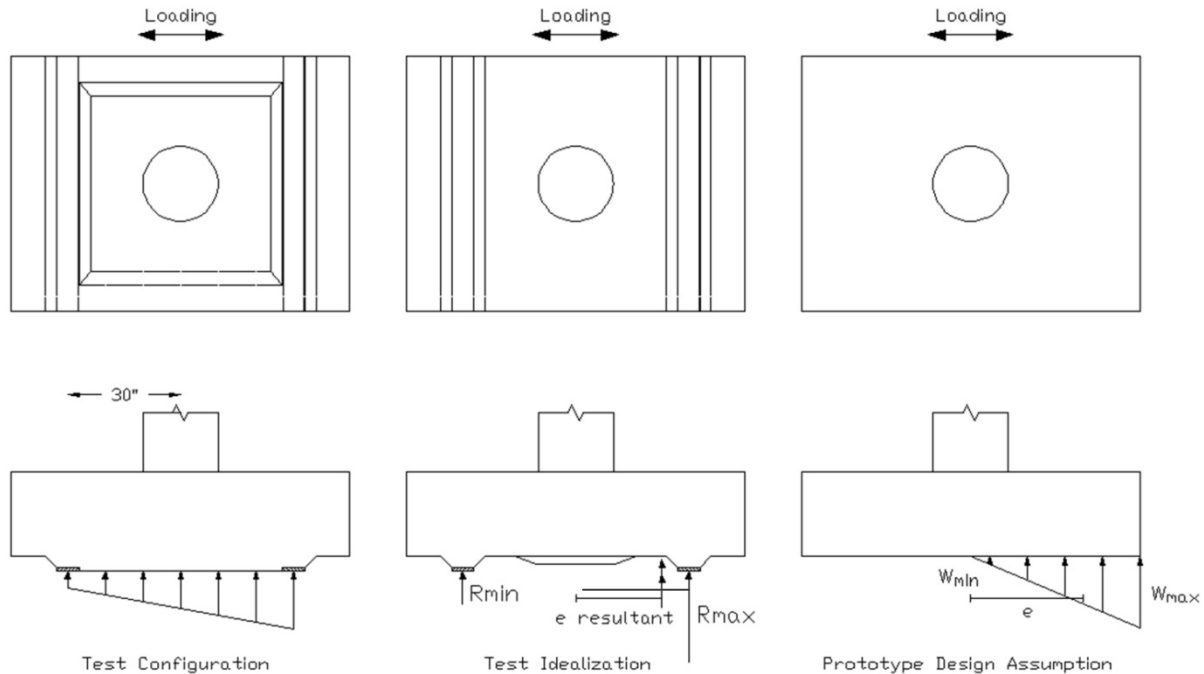


Figure 64. Diagram. Support conditions.

If the columns had been stronger than expected, the footing could have lifted off the supporting blocks and rocked about one of the line supports. This behavior would have limited the applied load and prevented the test from proceeding. To prevent this behavior, rods were placed on each side of the column to hold down the footing, and load cells were installed to detect any forces that might have restrained overturning. Each rod was located 31 inches from the column centerline in the direction of loading. A slack of 1/16 inch was provided at the start of the test between the load cell and the nut above it, so that in the absence of lift-off, the bolts and load cells would remain inactive but they would engage almost immediately after any lift-off started. In the tests, lift-off never occurred, and the load cells read zero at all times.

The test specimens were analyzed assuming that the support was provided by two line loads alone, ignoring any additional upwards pressure from the side strips. That arrangement was statically determinate, so the reactions could be computed from the measured loads and the resulting eccentricity could be computed and used as the measure of how close the footing was to violating the AASHTO Seismic Guide Specifications requirements.

Table 12 summarizes the maximum and minimum reactions and reports the resulting reaction force eccentricities.

Table 12. External forces, displacements, and estimated reactions.

Specimen	SF-1		SF-2		SF-3	
	North	South	North	South	North	South
<b>Axial Load, <math>P_{total}</math> (kips)</b>	~174		~174		~167	
<b>Maximum Column Base Moment, <math>M_u</math> (kip-in.)</b>	-3,073	3,091	-3,113	3,065	-3,315	3,392
<b>Drift Ratio at Maximum Column Base Moment (percent)</b>	-2.61	1.95	-1.45	1.38	-2.69	2.64
<b>Top Displacement at Maximum Column Moment (60 in above interface) (in.)</b>	-1.57	1.17	-0.87	0.83	-1.61	1.58
<b>Column shear at Maximum Moment, <math>V_u</math> (kips)</b>	-45.6	47.5	-49	48.4	-50.6	52
<b>Eccentricity, <math>e</math> (in.)</b>	23.6	23.9	24.2	23.9	23.5	23.5
<b>Maximum Reaction, <math>R_{max}</math> (kips)</b>	158.1	159.2	160.2	159.2	150.2	151.8
<b>Minimum Reaction, <math>R_{min}</math> (kips)</b>	15.8	14.6	13.6	14.7	16.5	14.9

The eccentricities under load remained below the AASHTO Seismic Guide Specifications limits. They were calculated by dividing the moment at the base (due to column moment and shear) by the axial load acting on the specimens, including both the applied axial load and the weight of the column and footing ( $P_{total} = 173.8$  kips for SF-1 and SF-2, and  $P_{total} = 166.8$  kips for SF-3). All specimens had the same 20-inch-diameter circular columns with a shear span ratio of 3. Specimens SF-1 and SF-2 shared the same footing geometry of 68 inches by 90 inches by 22.5 inches, but the depth of specimen SF-3 was shallower (10 inches). The heights of the four edges that supported the specimens were 3.75 inches, but their weight (about ~1 kip) was not included in this analysis.

The table shows that both reaction strips remained in compression during the tests, indicating that there was no lift-off. For specimens SF-1 and SF-2, the maximum estimated upward reaction at a support was about 160 kips, and the minimum was about 14 kips. The corresponding values for specimen SF-3 were 152 kips and 15 kips.

These reactions forces are used to estimate the demands on the footings.

## FOOTING RESPONSE

### Footing Flexural Strength

The footing flexural strength was evaluated following the recommendations of the AASHTO LRFD and the AASHTO Seismic Guide Specifications.<sup>(14,15)</sup> The test specimens were reinforced as shown in chapter 2. The nominal flexural capacity was calculated at the column face and was based on the bars within an effective width. For flexural strength and beam shear calculations, the effective width of the footing,  $b_{eff}$ , is defined as the sum of the column diameter and two times the spread footing depth ( $b_{eff} = D_c + 2H_f$ ). Here,  $b_{eff} = 65$  inches for specimens SF-1 and SF-2, and 40 inches for specimen SF-3.

In contrast, AASHTO LRFD recommends that the cracking moment be calculated using the whole width of the footing ( $b_{eff} = 68$  inches). This assumption implies that the moment distribution is constant across the width because, if it were not so, the stress would be higher than the average and cracking would initiate earlier at the point of peak moment. The AASHTO LRFD does not account for any differences between precast and cast-in-place behavior. In this study, the cracking moment of the test specimens was calculated using the whole width.

Table 13 summarizes the demands and computed capacities at the face of the columns. The moment demands in the footings at the column face were calculated using the computed reactions in table 12. The strengths reported in table 13 were calculated using both the specified and measured strengths of the materials.

Table 13. Footing flexural capacities and demands.

Specimen	SF-1		SF-2		SF-3	
	Specified Properties	Measured Properties	Specified Properties	Measured Properties	Specified Properties	Measured Properties
Capacity Values Input						
Measured $M_u$ (kips-in)	3,184		3,204		3,036	
$M_{cr}$ (kips-in.)	2,754	3,512	2,754	3,581	544	765
$M_{cr}/M_u$	0.86	1.10	0.86	1.12	0.18	0.25
Calculated $M_n$ (kips-in.)	5,254	5,569	5,254	5,622	3,419	4,033
$M_u/M_n$	0.61	0.57	0.61	0.57	0.89	0.75

In the SF-1 and SF-2 specimens, the flexural demand at the column face slightly exceeded the cracking moment calculated based on the specified material properties. However, the concrete strength was higher than assumed in design, so the demand at the column face was slightly lower than the cracking moment calculated using measured material properties for SF-1 and SF-2. This calculation is consistent with the fact that footing cracking was not observed during the tests of

specimens SF-1 and SF-2. For SF-3, the moment demand greatly exceeded the cracking capacity calculated using either the specified or measured materials properties.

The nominal moment capacity of the spread footings exceeded the moment induced in the footings by the columns. Using the measured properties, the moment demand-to-capacity ratios ranged from 0.57 to 0.75.

For specimens SF-1 and SF-2, the strains measured in the bottom mats show that the moment was not distributed evenly across the footing width; rather, the moment decreased with distance from the column. This general pattern is as expected, but some doubt exists about the exact values of the strains because of the need to correct the raw, measured strains for thermal effects. The thermal effects were potentially 2 to 3 times the mechanical strains. Furthermore, the footings in the tests were uncracked, whereas the AASHTO Seismic Guide Specifications equation for  $b_{eff}$  is based on the assumption that the footing is cracked, and cracking may affect  $b_{eff}$ . Because of these considerations, the data from specimens SF-1 and SF-2 do not provide a reliable basis for evaluating the AASHTO Seismic Guide Specifications definition of effective width.

In the thin footing specimen (SF-3), the concrete was cracked, the mechanical strains were much larger, and there was no need to correct for thermal effects because temperature-compensated (three-wire) gauges were used. The data from specimen SF-3 should therefore have been useful for evaluating the AASHTO Seismic Guide Specifications  $b_{eff}$  model. However, the measured bar strains increased with distance from the column. This result was unexpected, and the reasons for it are unknown. For example, there was no indication that the gauges malfunctioned. These results suggest that the steel outside the effective width is the primary contributor to the flexural strength. This is both irrational and the opposite of what the AASHTO Seismic Guide Specifications model states, so the footing steel strain data from specimen SF-3 were ignored.

### **Footing One-Way Shear Strength**

The AASHTO Seismic Guide Specifications require that the one-way shear strength to be calculated at the column face using the effective width,  $b_{eff}$ . The current WSDOT philosophy is to make the footing thick enough such that the concrete strength alone can resist all of the shear, and to place only the prescriptive transverse reinforcement recommended in the Caltrans SDC.<sup>(16)</sup> Specimens SF-1 and SF-2 were constructed with footings deep enough for the concrete alone to resist the shear ( $D_c/h_f = 1.125$ ).

The current edition of the AASHTO Seismic Guide Specifications was based on the Caltrans SDC. However, the Caltrans SDC requirement for prescriptive ties was not included in the AASHTO Seismic Guide Specifications. The requirement for these prescriptive ties will be included in the next edition. Thus, to be in keeping with the intent of the AASHTO Seismic Guide Specifications, the full Caltrans SDC prescriptive ties were included in specimen SF-1. For the prototype, the requirement results in No. 5 ties at 12-inch spacing, which results in a nominal shear stress capacity,  $v_s$ , of 129 psi. For 4,000 psi concrete, this represents about  $2\sqrt{f'_c}$  and is comparable in magnitude to the concrete contribution of  $v_c = 2\sqrt{f'_c}$ . In specimen SF-2, the stirrups were arbitrarily reduced by a factor of one-half (from the Caltrans SDC requirement), because placing stirrups in a spread footing on-site slows down construction, and they were believed to be unnecessary when the columns reinforcement is anchored with headed bars.

To force failure out of the column and into the connection region, the footing depth in specimen SF-3 was reduced to half of the column diameter ( $D_c/h_f = 0.5$ ). Without transverse reinforcement, this thin footing would be susceptible to one-way shear failure, so ties were included in the footing. They were placed so that they would help to resist one-way (“beam”) shear but would not affect two-way (“punching”) shear.

Table 14 summarizes the computed one-way shear demands and strengths of the spread footings. Values are given for both the specified and measured strengths of the concrete and the steel (specified  $f_y = 70$  ksi, since the smooth wire was used). The shear force demand,  $V_u$ , was obtained from the measured loads and the known specimen weight.

Table 14. Footing one-way strength capacities and demands.

Specimen	SF-1		SF-2		SF-3	
Capacity Values Input	Specified Properties	Measured Properties	Specified Properties	Measured Properties	Specified Properties	Measured Properties
$V_c$ (kips)	153	195	153	198	37	52
$V_s$ (kips)	178	161	89	81	144	150
Calculated $V_n$ (kips)	331	356	242	279	181	202
Measured $V_u$ (kips)	154		155		151	
Measured $V_u/V_n$	0.47	0.43	0.64	0.56	0.83	0.75

The values presented show that failure in beam shear was improbable because the ratio  $V_u/V_n$  (demand/capacity for measured material properties) was never greater than 0.75. That is consistent with the fact that there was no indication of one-way shear failure in any of the tests.

### Combined Punching Shear and Moment Transfer

The transfer of moment from the column to the footing induces demands in the connection region that must be added to the two-way shear demands induced by the vertical load on the column. The AASHTO LRFD does not account for this moment transfer. Thus, the method from ACI 318-08, section 11.11.7, was used to estimate the combined shear stresses. Although punching shear failure is really manifested as a tension failure on a conical surface, the ACI procedure for both punching shear alone and for combined punching and moment transfer consists of computing shear stresses on a notional cylindrical failure surface, assuming elastic behavior. Furthermore, the amount of moment being transferred by shear stresses is only a fraction,  $\gamma_v$ , of the total moment. The remainder is assumed to be transferred by flexure; that is, by means of a couple consisting of a pair of horizontal forces. According to ACI 318-08, the combined shear stress is calculated using the equation in figure 65.

$$v_u = \frac{V_u}{b_0 d} \mp \frac{\gamma_v M_{unbal} c}{J_c}$$

Figure 65. Equation. Shear stress demand.

In this equation,  $d$  is the effective shear depth,  $\gamma_v$  is the fraction of the moment carried in shear,  $J_c$  is the moment of inertia of the critical perimeter line about the axis of bending, and  $c$  is the distance from the centroid of the critical-shear perimeter to the edge where the stress is being calculated.

According to ACI 318-08, the calculated maximum shear stress should not exceed the limiting value of the equation shown in figure 66.

$$v_n = (V_c + V_s)/b_0 d$$

Figure 66. Equation. Nominal shear capacity.

The concrete contribution is taken not to be higher than  $2\sqrt{f'_c}b_0d$  ( $f'_c$  is in psi) if shear reinforcement is used. Specimens SF-1 and SF-2 included stirrups within the critical perimeter, whereas specimen SF-3 did not. Table 15 summarizes the combined punching shear and moment transfer strengths and demands on the connection.

Table 15. Combined punching shear and moment transfer capacities and demands.

Specimen	SF-1		SF-2		SF-3	
	Specified Properties	Measured Properties	Specified Properties	Measured Properties	Specified Properties	Measured Properties
$v_c$ (ksi)	0.126	0.161	0.126	0.164	0.253	0.356
$v_s$ (ksi)	0.147	0.133	0.084	0.076	0	0
Calculated $v_n$ (ksi)	0.274	0.295	0.211	0.241	0.253	0.356
Measured $v_u$ (ksi)	0.060		0.060		0.452	
$v_u/v_n$	0.22	0.20	0.28	0.25	1.79	1.27

Calculations were based on an equivalent square of a circular column. ACI-ASCE (American Society of Civil Engineers) Committee 426 recommends that combined punching shear and moment transfer for circular columns be calculated with an equivalent square. The base of the precast column was an octagon inscribed in a 20-inch-diameter circle. This approximation was considered sufficient since the perimeter of an inscribed octagon is only 2.6 percent less than that of a circle.

Table 15 shows that calculated capacities (for measured material properties) of specimens SF-1 and SF-2 exceeded the calculated demands by at least a factor of four. Consistent with this

calculation, no sign of this failure mode was detected during testing of specimens SF-1 and SF-2. The depths of those specimens were roughly two times greater than the depth at which the combined punching shear and moment transfer would become a problem, according to the ACI 318 provisions.

In contrast, the demand was 27 percent larger than the calculated capacity for specimen SF-3. That results is consistent with what was observed during the test, in which the specimen ultimately failed (in the desired failure mode) in the combined punching shear and moment transfer during its last cycle (at a drift ratio exceeding 10 percent).

### Footing Punching Shear Strength

The AASHTO LRFD recommends two equations to calculate the punching shear-strength capacity, one including and one excluding transverse steel. The equations were used to evaluate the performance in pure punching shear when the columns were loaded only with a large vertical load.

The prototype spread footing was originally designed to have the minimum transverse reinforcement according to the Caltrans SDC; the same was true for specimen SF-1. In specimen SF-2, the proportion of transverse reinforcement in the spread footing was reduced to half of the minimum required by Caltrans. Specimen SF-3 had stirrups, too, but they were placed so they would not increase the punching shear capacity.

Table 16 summarizes the punching shear capacities using the specified and measured strengths of the concrete and reinforcement.

Table 16. Punching shear capacities and demands.

Specimen	SF-1		SF-2		SF-3	
	Specified Properties	Measured Properties	Specified Properties	Measured Properties	Specified Properties	Measured Properties
$V_c$ , Eq. 6-3 (kips)	292	372	292	380	133	188
$V_c$ , Eq. 6-4 (kips)	582	742	582	757	N/A	N/A
$V_s$ (kips)	441	399	253	229	0	0
Calculated $V_n$ (kips)	733	771	545	608	133	188
Maximum axial load $V_u$ (kips)	918		820		342	
$V_u/V_n$	1.25	1.19	1.50	1.35	2.57	1.82

Figure 67 (AASHTO LRFD equation 5.13.3.6.3-3), which takes into account that shear reinforcement is present in the footing, was used for specimens SF-1 and SF-2.

$$V_n = V_c + V_s \leq 0.192\sqrt{f'_c}b_o d_v$$

Figure 67. Equation. Nominal punching shear capacity including transverse steel.

In this equation,  $V_c = 0.0632\sqrt{f'_c}b_o d_v$ , and  $V_s = A_v f_y d_v / s$ . Here,  $f'_c$  is the unconfined concrete strength (in ksi),  $b_o$  is the perimeter of the critical section,  $d_v$  is the effective shear depth,  $A_v$  is the area of ties crossing within  $d_v$  from the column,  $f_y$  is the yield strength of the ties, and  $s$  is the spacing between ties.

Table 16 also shows the punching shear capacity calculated with AASHTO LRFD equation 5.13.3.6.3-1, which excludes any transverse steel.

$$V_n = \left(0.063 + 0.126/\beta_c\right) \sqrt{f'_c}b_o d_v \leq 0.126\sqrt{f'_c}b_o d_v$$

Figure 68. Equation. Nominal punching shear capacity excluding transverse steel.

In figure 68,  $\beta_c$  is the ratio of long side to short side of the rectangle and other values are as defined for figure 67.

Because the stirrups did not cross the crack plane for specimen SF-3, only the equation in figure 68 was used for that specimen. For square critical sections, this equation increases the concrete contribution by approximately a factor of two, compared to the equation in figure 67.

After the cyclic tests were finished, specimens SF-1 and SF-2 were loaded axially until either the column punched through the footing or the (already damaged) column failed. The value measured for specimen SF-1 (842 kips) is not reported because it was loaded higher in the beginning to 918 kips. For reference, the maximum factored axial load on the prototype was  $P_u = 1.25DL + 1.75LL = 1382$  kips, which corresponded to 240 kips at laboratory scale. In both specimens, the axial load reached exceeded the nominal capacity and there was no indication of punching shear failure when the column failed in the previously damaged plastic hinge zone. By contrast, specimen SF-3 punched through the footing in combined punching shear and moment transfer so a pure axial test could not be conducted. However, the specimen was loaded successfully up to 342 kips prior to the lateral-load testing (see chapter 4), which was nearly twice the calculated capacity.

In all cases, even when the footing had been previously damaged by combined bending and axial load, the demand exceeded the nominal capacity, in some cases by a large margin. The implication is that the AASHTO procedure for computing punching shear strength is safe and may be quite conservative. The tests also show that, if the footing has already been damaged, the punching strength drops. For example, at zero drift (and approximately zero moment) after reaching a previous peak drift ratio of 9 percent, specimen SF-3 was unable to sustain an axial load of 159 kips, even though the nominal punching shear capacity was 188 kips, using

measured material strengths. The drop in axial capacity that is caused by this level of damage is not surprising. AASHTO LRFD does not have a procedure for estimating strength under combined static axial load and moment, much less under cyclic moment. ACI 318-08 section 21.13.6 contains provisions for such cyclic loading, and the nominal strength is less than under static loading.

### Footing Shear-Friction Strength

Loads were carried from the precast column to the cast-in-place spread footing by shear and normal stresses across the interface. The capacity of the “socket” was evaluated using the shear-friction calculation procedure in section 5.8.4 of the AASHTO LRFD. The nominal shear resistance was calculated using equation 5.8.4.1-3 in the AASHTO LRFD, shown here in figure 69.

$$V_n = cA_{cv} + \mu(A_{vf}f_y + P_c)$$

Figure 69. Equation. Nominal shear friction resistance.

In this equation,  $V_n \leq \min(K_1f'_cA_{cv}, K_2A_{cv})$ . Here,  $c$  is the cohesive shear stress,  $A_{cv}$  is the area of concrete considered in an interface shear transfer,  $\mu$  is the coefficient of friction,  $f_y$  is the yield stress of the reinforcement crossing the interface,  $P_c$  is the net compressive force normal to the shear plane,  $P_c$  was assumed to be zero in this case,  $K_1$  is the fraction of concrete strength available to resist interface shear, and  $K_2$  is the limiting interface shear resistant.

The precast test columns were roughened with the same roughness detail as required in the WSDOT BDM for the ends of prestressed girders.<sup>(17)</sup> This roughness detail satisfied the AASHTO LRFD specifications in terms of minimum amplitude and minimum spacing between ridges. For a normal-weight concrete placed against an intentionally hardened concrete surface with an amplitude of 0.25 inches, the AASHTO LRFD proposes the following to be used in shear-friction design:  $c = 0.24$  ksi,  $\mu = 1.0$ ,  $K_1 = 0.25$ ,  $K_2 = 1.5$  ksi.

Figure 69 has two components that contribute to shear-friction: cohesion and friction. In the design of the prototype connection and for the test specimens, the cohesion component was ignored.

A question arises over the use of the main tension steel in the footing for resisting shear friction. The horizontal tension force is equilibrated by a horizontal compression force between the top of the footing and the column, which therefore provides friction capacity. While this argument is rational, and is based on equilibrium alone, the AASHTO specifications give no guidance on the use of flexural steel to also serve as shear friction steel. Therefore, in specimen SF-1 separate shear friction steel was designed to resist the entire vertical shear force.

The calculated amount of reinforcement needed to cross the interface ( $A_{cv}$ , 12 No. 4 bars) was stacked on the bottom mat around the column base to provide more confinement around the roughened base. These bars were placed diagonally and stacked in four layers for specimen SF-1. The amount was reduced by a factor of three, to four No. 4 bars for specimen SF-2, in an attempt to find out whether the main tension steel alone would provide sufficient shear friction capacity.

However, one set (four bars) of diagonal steel was retained to act as trimming steel in the corners, since the column was octagonal but the opening in the mat of main steel was square. Discussions with WSDOT designers confirmed that they would require such trimming steel in the prototype.

For specimen SF-3, the required friction strength was the same as in specimen SF-1. However, when specimen SF-3 was designed, the results of the tests on specimens SF-1 and SF-2 were available, and in particular it was known that the diagonal steel had experienced low stresses and had contributed little to shear friction resistance. Thus, it was concluded that the main tension steel does indeed contribute towards shear friction resistance, and in specimen SF-3, which had a shallower footing and consequently less space for placing diagonal bars, the bottom mat flexural reinforcement was counted as part of the “shear friction” steel. The required total was made up by adding four No. 5 diagonal bars.

This argument could be further refined to show that not only the longitudinal bottom steel but also the transverse tension steel contributes to shear friction resistance. Consider a square footing subjected to north-south earthquake motion. Because the main bars are placed at the side of the column, rather than beneath it, a strut-and-tie model of the footing would contain struts that are oriented at a compound angle; that is, they would be diagonal when viewed in in both plan and section. The compressive force between the footing and column concrete would then be larger than the force from the north-south tension steel alone, and it is the normal force that determines the friction resistance. In this case the normal force is given by the vector sum of the tension strengths of the bottom tension steel in the two directions. Thus, even using the longitudinal tension steel to provide shear friction reinforcement is conservative.

It should be noted that AASHTO LRFD takes a different approach to shear friction than both ACI 318-08 and the Precast/Prestressed Concrete Institute (PCI) Design Handbook.<sup>(23)</sup> The latter two specifications contain no contribution from cohesion, but the AASHTO LRFD does. During design, the cohesion component was ignored in the interest of safety and conservatism.

Table 17 lists the shear-friction capacities calculated using the equation in figure 69 for the socket connection. Note that the cohesive component has been included for the comparison with the maximum applied, post-lateral axial demand.

The table shows that AASHTO’s cohesive component alone was enough the resist the maximum factored load of 240 kips for specimens SF-1 and SF-2. In contrast, the cohesive component in the thin footing in specimen SF-3 was not enough to resist the maximum axial load. There was no indication of sliding shear failure in any of the three test specimens at the interface between the column and the footing during the application of the maximum axial load.

Table 17. Footing shear-friction capacities and demands.

Specimen	SF-1		SF-2		SF-3	
	Specified Properties	Measured Properties	Specified Properties	Measured Properties	Specified Properties	Measured Properties
Capacity Values Input						
Calculated Cohesive Component (kip)	330	330	330	330	147	147
Calculated Friction Component (kip)	288 <sup>1</sup>	306 <sup>1</sup>	96 <sup>1</sup>	102 <sup>1</sup>	288 <sup>2</sup>	318 <sup>2</sup>
Calculated $V_n$ (kip)	618	636	426	432	435	465
Measured $V_u$ (kip)	918		820		342	
$V_u/V_n$	1.49	1.44	1.92	1.90	0.79	0.74

<sup>1</sup>Including diagonal steel, which does not cross the interface between the precast and cast-in-place elements.

<sup>2</sup>Including diagonal steel and bottom mat of flexural reinforcement.

### Footing Joint Shear

The joint shear stress was evaluated by using a procedure recommended in section 6.4.5 in the AASHTO Seismic Guide Specifications.<sup>(15)</sup> The column-to-footing joint principal stresses have to satisfy the equations shown in figures 70 and 71.

$$p_c \leq 0.25f'_c$$

Figure 70. Equation. Maximum principal compressive stress.

$$\text{abs}(p_t) \leq 0.38\sqrt{f'_c}$$

Figure 71. Equation. Maximum principal tensile stress.

$f'_c$  is in ksi, and  $p_c$  and  $p_t$  are calculated using the equations in figure 72 and 73.

$$p_t = \frac{f_v}{2} - \sqrt{\left(\frac{f_v}{2}\right)^2 + v_{jv}^2}$$

Figure 72. Equation. Principal tensile stress.

$$p_c = \frac{f_v}{2} + \sqrt{\left(\frac{f_v}{2}\right)^2 + v_{jv}^2}$$

Figure 73. Equation. Principal compressive stress.

In these equations,  $v_{jv} = \frac{T_{jv}}{(B_{eff}^{ftg} D_{ftg})}$  and  $f_v = \frac{P_{col}}{A_{jh}^{ftg}}$ . Here,  $T_{jv}$  is the sum of the tensile forces in the column reinforcement,  $B_{eff}^{ftg}$  is the effective width of the footing,  $D_{ftg}$  is the depth of the footing,  $P_{col}$  is the axial force acting on the column and included overturning, and  $A_{jh}^{ftg}$  is the effective horizontal area at mid-depth of the footing assuming 45 degrees spread away from the boundary of the column.

The design overstrength moment ( $M_{po} = 3,081$  kip-in.,  $P = 159$  kips) and the total column tensile force associated with it ( $T = 154$  kips) were obtained from a moment-curvature program in OpenSees. Table 18 summarizes the results using specified and measured material properties. Demands in the connection of specimens SF-1 and SF-2 did not come close to the nominal stress limits given in the same table. The demands increased in specimen SF-3, which had a shallower foundation, as was expected, but did not exceed limits. There were no signs of joint shear failure of any kind in any of the tests.

Table 18. Footing joint shear stress capacities and demands.

Specimen	SF-1		SF-2		SF-3	
	Specified Properties	Measured Properties	Specified Properties	Measured Properties	Specified Properties	Measured Properties
Compressive Limit Stress $p_c^{limit}$ (ksi)	1.00	1.25	1.00	1.37	1.00	1.98
Tensile Limit Stress $p_t^{limit}$ (ksi)	0.76	0.85	0.76	0.89	0.76	1.07
Compressive Demand Stress $p_c^{calc}$ (ksi)	0.29		0.29		0.64	
Tensile Demand Stress $p_t^{calc}$ (ksi)	0.2		0.2		0.47	
$p_c^{calc}/p_c^{limit}$	0.29	0.23	0.29	0.21	0.64	0.32
$p_t^{calc}/p_t^{limit}$	0.26	0.24	0.26	0.22	0.62	0.44

The applicability of these joint shear stress equations for socket connections, where the column longitudinal bars are terminated with anchors instead of being bent out into the foundation, is debatable. A strut-and-tie model of the joint, such as the one shown in figure 74, suggests that, after the joint cracks, the shear forces in it are carried by a diagonal strut. If the vertical column bars are bent outwards into the footing, the load transfer between strut and bar at the node has to be achieved by bond stress, because the direction of the force is parallel the bar axis. That load transfer mechanism has a low capacity, and the AASHTO limits on joint shear stress serve to keep the load in the strut down to a level at which the force can be transferred at the node without failure. However, if straight bars with anchor heads are used, the load transfer from the strut is achieved by bearing on the head, and not by bond. That mechanism has a high capacity, so much higher joint shear stresses should be permitted, in which case the need for ties is reduced or may be eliminated.

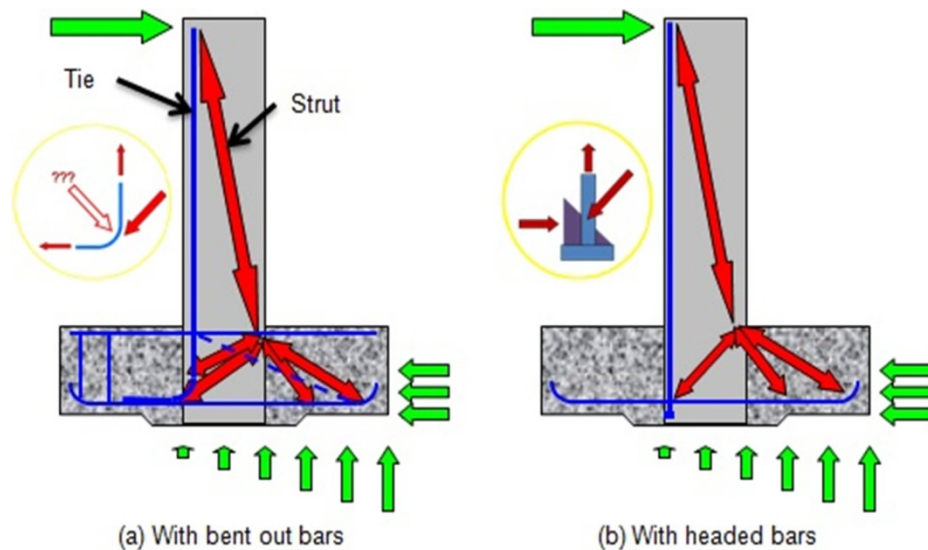


Figure 74. Diagrams. Strut and tie models for bent-out bars (left) and headed bars (right).

The test specimens all used headed bars, and the joint shear stresses were well below even the AASHTO limits, so it was not surprising that there were no signs of joint shear failure. Even in specimens SF-3, where the joint was smallest and the joint shear stress was highest, there were no signs of joint shear failure. As shown in figure 75, the base of the column, which constitutes the joint region, was still intact at the end of testing, and the concrete behind the anchor heads was still in place.



Figure 75. Photo. Joint region of specimen SF-3 after failure.

## COLUMN RESPONSE

### Column Axial-Load Capacity

The column needs to be able to resist the expected maximum axial load. The largest factored axial load for the prototype column was 1,382 kips, or 240 kips at specimen scale.

The test program for all three specimens started with a pure axial load test to verify that the connection could resist at least the factored load. Once cyclic lateral loading was complete, the columns of SF-1 and SF-2 were again loaded axially until the column failed in the column hinge region, which had formed during the lateral-load tests. The axial-load capacity of the column was calculated using equation 5.7.4.4-2 in the AASHTO LRFD.<sup>(14)</sup> Figure 76 shows the AASHTO LRFD, excluding the prestressing terms.

$$P_n = 0.85(0.85f'_c(A_g - A_{st}) + f_y A_{st})$$

Figure 76. Equation. Nominal axial-load capacity of the column.

Table 19 summarizes the nominal and measured axial capacities for the test columns. The capacities were calculated based on both the specified and measured material properties.

Table 19. Column axial-load capacities and demands.

Specimen	SF-1		SF-2		SF-3	
Capacity Values Input	Specified Properties	Measured Properties	Specified Properties	Measured Properties	Specified Properties	Measured Properties
Calculated $P_n$ (kips)	1077	1301	1077	1413	1077	1960
Measured $P_u$ (kips)	918		820		342	
$P_u/P_n$	0.85	0.71	0.76	0.58	0.32	.17

During the lateral-load tests of specimens SF-1 and SF-2, there was no indication of loss of axial-load capacity in the columns. In the axial-load tests performed after completing those lateral load-tests, more than 58 percent of the nominal axial capacity of the column remained, even though the columns had hinged, and the spiral and some bars had fractured. The axial-load capacity of specimen SF-3 dropped when the column failed in combined moment transfer and punching shear under an axial load of 159 kips, which corresponded to 8 percent of the nominal column axial-load capacity calculated with the measured material properties.

### Column Flexural Strength

The column flexural strength was computed following the recommendations given by the AASHTO LRFD and the AASHTO Seismic Guide Specifications.<sup>(14,15)</sup> The nominal capacity,  $M_n$ , of the column was calculated according to AASHTO LRFD specifications using the specified material properties.

In design, the overstrength demand on the spread footing comes mainly from the plastic capacity of the columns, computed for expected materials properties. The expected concrete compressive strength was 5.2 ksi for a specified strength of 4.0 ksi. This assumption was approximately correct for SF-1 and SF-2, but it underestimated the compressive strength of the concrete in SF-3 (8.0 ksi). The AASHTO expected tensile yield stress for the reinforcement was 68 ksi for a specified yield stress of 60 ksi. This assumption overestimated the yield stress in the actual reinforcement.

The AASHTO Seismic Guide Specifications recommends that the  $M-\phi$  relationship be idealized as elastic perfectly plastic, in which the idealized curve passes through the point of first yield in the reinforcement (see figure 77). The idealized plastic moment capacity,  $M_p$ , was obtained by equating the areas between the idealized and the actual curves. The ultimate curvature,  $\phi_u$ , was determined as the smaller of:

- The ultimate confined concrete compressive strain,  $\epsilon_{cu} = 0.016$ , divided by the distance from the plastic neutral axis to the extreme fiber of the confined concrete.
- The reduced ultimate tensile strain,  $\epsilon_{su}^R = 0.09$  (A706 No.6), of the steel divided by the distance from the plastic neutral axis to the extreme tension fiber of the longitudinal reinforcement.

The overstrength plastic moment capacity was obtained by multiplying  $M_p$  by an overstrength magnifier,  $\lambda_{mo}$ , which takes into account variations in material strengths. For ASTM A706 reinforcement, this magnifier is 1.2.

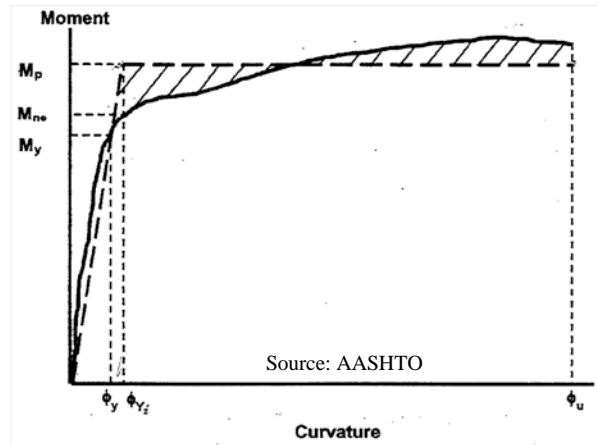


Figure 77. Graph. Moment-curvature model.<sup>(15)</sup>

To compute the flexural strengths according to the AASHTO Seismic Guide Specifications recommendations, moment-curvature analyses were performed using the software Xtract. That program uses Mander’s confined concrete model and the AASHTO Seismic Guide Specification’s strain-hardening steel model.<sup>(15,19)</sup> Table 20 summarizes the moment-curvature analysis performed for an axial force of 159 kips for the specified and measured material properties. For the analyses using the measured material properties, a factor of 1.2 was not applied to the calculated plastic moments.

The actual moment capacity exceeded the nominal moment capacity (using measured properties) according to AASHTO LRFD by about 20 percent. That discrepancy was expected, because the AASHTO nominal moment capacity does not account for strain-hardening in the reinforcement nor for differences between specified and actual material properties. The maximum moments measured in the tests were nearly identical to the overstrength plastic moment predicted with the AASHTO procedure for the specified material properties.

Table 20. Column flexural capacities and demands.

Specimen	SF-1		SF-2		SF-3	
	Specified Properties	Measured Properties	Specified Properties	Measured Properties	Specified Properties	Measured Properties
Nominal Moment $M_n^{AASHTO LRFD}$ (kips-in.)	2,711	2,576	2,711	2,613	2,711	2,774
Plastic Moment Capacity $M_p$ (kips-in.)	2,671	2,487	2,671	2,505	2,671	2,672
Overstrength Moment $M_{po}^{AASHTO GS}$ (kips-in.)	3205	2,984	3205	3,006	3205	3,206
Largest Measured Moment $M_u$ (kips-in.)	3,091		3,113		3,392	
$M_u/M_{po}^{AASHTO GS}$	0.96	1.04	0.97	1.04	1.06	1.06

### Column Shear Strength

The AASHTO Seismic Guide Specifications require that the shear demand,  $V_{po}$ , be calculated corresponding to the overstrength plastic moment,  $M_{po}$ . That demand was calculated using the equation shown in figure 78.

$$V_{po} = \frac{M_{po}}{L}$$

Figure 78. Equation. Plastic overstrength shear demand.

In this equation,  $L$  is the total height between the footing surface and the line of action of the lateral load. For specimens SF-1, SF-2, and SF-3, the actual shear demands were calculated to be 47.5, 49, and 52, respectively.

The nominal shear resistance was calculated according section 8.6.1 in the AASHTO Seismic Guide Specifications (see figure 79).

$$V_n = V_c + V_s$$

Figure 79. Equation. Nominal shear resistance.

This procedure takes into account the contributions of both the concrete and the transverse reinforcement. The concrete contribution is calculated using the equations in figure 80 and 81.

$$V_c = 0.8A_{\text{gross}}v_c$$

Figure 80. Equation. Component of total shear resistance due to concrete strength.

$$v_c = 0.032\alpha' \left( 1 + \frac{P_u}{2A_{\text{gross}}} \right) \sqrt{f'_c} \leq \min (0.11\sqrt{f'_c}, 0.047\alpha'\sqrt{f'_c})$$

Figure 81. Equation. Concrete shear resistance.

Here,  $f'_c$  is in ksi;  $\alpha'$  (here, 3) was determined from an equation that takes into account volumetric transverse reinforcement ratio, yield stress of the spiral, and a ductility ratio; and  $P_u$  is the ultimate compressive force acting on a section.

The reinforcement contribution was determined using the equation in figure 82.

$$V_s = \frac{\pi}{2} \left( \frac{nA_{sp}f_{yh}D'}{s} \right)$$

Figure 82. Equation. Contribution of total shear resistance due to transverse steel strength.

Values of demand and capacity using both the specified and the measured material properties are given in table 21. There was no sign of shear failure in the columns during tests.

Table 21. Column shear capacities and demands.

Specimen	SF-1		SF-2		SF-3	
	Specified Properties	Measured Properties	Specified Properties	Measured Properties	Specified Properties	Measured Properties
$V_c^{AASHTO GS}$ (kips)	55	62	55	65	55	78
$V_s^{AASHTO GS}$ (kips)	70	59	70	59	70	59
$V_n^{AASHTO GS}$ (kips)	125	121	125	124	125	137
Measured Shear Demand, $V_u$ (kips)	47.5		49		52	
$V_u/V_n^{AASHTO GS}$	0.38	0.39	0.39	0.40	0.42	0.38

For specimen SF-1 and SF-2, the capacity decreased when calculated with measured material properties. That occurred because the yield strength of the 2-gauge spiral was lower than specified by ASTM A82, which is 70 ksi. A possible explanation for this discrepancy was that the spiral had to be straightened out for tensile testing. The increase in concrete strength for specimen SF-3 was large enough to counteract the loss of strength in the spiral. In all tests, column shear failure was improbable because the shear demands placed on the columns were well below the calculated shear capacity for all three specimens.

### Column Splice in Specimens SF-1 and SF-2

Specimens SF-1 and SF-2 both had segmental columns with splices located 20 inches above the surface of the spread footings. Section 4.11.7 in the AASHTO Seismic Guide Specifications recommends that the plastic-hinge length,  $L_{pr}$ , be taken as the larger of 1.5 times the gross sectional diameter, the region where 75 percent of the overstrength moment occurs, or the analytical plastic-hinge length.  $L_{pr}$  is calculated using the equation in figure 83.

$$L_{pr} = \max \left\{ \begin{array}{l} 1.5D_c \\ \text{where } 0.75M_{po} \\ 0.08L + 0.15f_{ye} d_{bl} \geq 0.3f_{ye} d_{bl} \end{array} \right.$$

Figure 83. Equation. Analytical plastic hinge length.

To increase the demands on the splices, they were placed based on the moment diagram only, instead of placing the splice at the top of the plastic hinge region, as determined above. The base moment was assumed to have the computed overstrength value, and a straight-line diagram was constructed, dropping to zero at the level of the lateral load. The elevation at which the moment diagram corresponded to the first yield moment was approximately 18 inches above footing surface, and strain gauges were mounted on the column longitudinal bars at that location.

The bars yielded considerably, 2 inches below the splice. Potentiometers bridging the splice recorded crack opening displacements of about 0.045 inches. No grout damage was observed in spite of the initiation of yielding at the splice location. In both specimens, the splices performed well in flexure.

Each splice was built with a shear key at the center of the column, which was grouted. No shear slip was detected in either case. It is likely that the shear key was unnecessary. The peak shear force was approximately 53 kips, while the axial load was 159 kips. Thus, to prevent slip, and in the absence of additional forces from the bars, a coefficient of friction of  $53/159 = 0.333$  was needed. The effect of the bar forces on slip could also be taken into account. The total bar force is likely to be tensile because the distance from the neutral axis to the compression face is likely to be less than  $0.5D_{col}$  as a result of the relatively low axial load. That implies that additional compression exists between the two concrete faces of the splice, so the normal force available for creating friction is greater than the 159 kip axial load and the friction coefficient needed to prevent slip is less than 0.333. Friction between precast elements and the adjacent grout layer has been measured at approximately 0.6. It is thus likely that slip would not have occurred even if the shear key had been omitted.

## DAMAGE PROGRESSION MODELS

Berry and Eberhard proposed damage models to predict the onset of spalling, bar buckling, and bar fracture.<sup>(24,25)</sup> The three relevant equations for spiral reinforced columns are shown in figures 84 through 86.

$$\frac{\Delta_{sp}^{calc}}{L} \text{ (percent)} = 1.6 \left(1 - \frac{P}{A_g f'_c}\right) \left(1 + \frac{L}{10D}\right)$$

Figure 84. Equation. Damage model for spalling.

$$\frac{\Delta_{bb}^{calc}}{L} \text{ (percent)} = 3.25 \left(1 + 150\rho_{eff} \frac{d_b}{D}\right) \left(1 - \frac{P}{A_g f'_c}\right) \left(1 + \frac{L}{10D}\right)$$

Figure 85. Equation. Damage model for bar buckling.

$$\frac{\Delta_{bf}^{calc}}{L} \text{ (percent)} = 3.5 \left(1 + 150\rho_{eff} \frac{d_b}{D}\right) \left(1 - \frac{P}{A_g f'_c}\right) \left(1 + \frac{L}{10D}\right)$$

Figure 86. Equation. Damage model for bar fracture.

In these equations,  $P$  is the axial load applied,  $L$  is the distance to the point of contraflexure (here, 60 inches),  $D$  is the column depth (here, 20 inches),  $A_g$  is the column gross-sectional area,  $d_b$  is the longitudinal reinforcement diameter,  $f'_c$  is the concrete compressive strength, and  $\rho_{eff} = \rho_s f_{ys} / f'_c$ , where  $\rho_s$  is the transverse volumetric ratio and  $f_{ys}$  is the transverse reinforcement yield strength.

Table 22 shows a comparison of the results from the models, using measured material properties, with the observed behaviors from the tests.

Table 22. Comparison of damage model predictions and observed occurrences.

Specimen	Drift ratio at onset of spalling			Drift ratio at onset of bar buckling			Drift ratio at onset of bar fracture		
	Pred.	Obs.	Obs./Pred.	Pred.	Obs.	Obs./Pred.	Pred.	Obs.	Obs./Pred.
<b>SF-1</b>	1.87	1.07	0.57	6.03	7.09	1.18	6.50	10.61	1.63
<b>SF-2</b>	1.89	1.10	0.58	5.89	7.19	1.22	6.34	10.65	1.68
<b>SF-3</b>	1.94	1.41	0.73	5.50	7.15	1.30	5.92	N/A	N/A
<b>Mean</b>	1.90	1.19	0.63	5.81	7.14	1.23	6.25	10.63	1.66

The onset of spalling occurred much earlier than predicted by the equation in figure 84. The drift ratio at the onset of bar buckling was predicted more accurately. Bar fracture occurred much later than predicted by the equation in figure 86.

### EFFECTIVE STIFFNESS MODEL

The measured effective moduli of rigidity ( $EI$ ) of the test specimens were compared with a model proposed by Elwood and Eberhard that takes into account for deformations due to flexure, shear and anchorage-slip.<sup>(26)</sup> The effective modulus of rigidity is calculated using the equation in figure 87.

$$\frac{EI_{\text{eff calc}}}{EI_g} = \frac{0.45 + 2.5P/A_g f'_c}{1 + 110 \left(\frac{d_b}{D}\right) \left(\frac{D}{a}\right)}$$

Figure 87. Equation. Effective modulus of rigidity.

In this equation,  $EI_g$  is gross modulus of rigidity,  $P$  is the axial load applied on the test specimen,  $A_g$  is the gross-sectional area of the column,  $f'_c$  is the unconfined concrete strength,  $d_b$  is the longitudinal bar diameter,  $D$  is the column diameter, and  $a$  is the cantilever length.

Table 23 summarizes the measured and the predicted values using the measured concrete strength. The measured and predicted effective modulus of rigidities compared well, with an average error of 10 percent.

Table 23. Comparison of model prediction and measured effective modulus of rigidity.

Specimen	Gross Section Modulus of Rigidity (kip-in <sup>2</sup> )	Normalized Effective Modulus of Rigidity ( $EI_{\text{eff}}/EI_g$ )		
		Pred.	Obs.	Obs./Pred.
SF-1	31,639,709	0.30	0.26	0.87
SF-2	33,188,536	0.29	0.28	0.97
SF-3	39,878,444	0.26	0.22	0.85
Mean	34,902,230	0.85	0.25	0.90

### NORMALIZED MOMENT-DRIFT RESPONSE

The normalized moments for the three socket connection specimens are plotted versus drift ratio in figure 88. The measured moments were normalized with their corresponding values of  $M_n$  using measured properties. A typical cast-in-place column is shown for comparison. This reference specimen (DB5-RE) was also used for comparison with the “large-bar” column-to-cap beam connection tests, in research conducted by Pang et al. at the University of Washington.<sup>(7)</sup> In traditional cast-in-place construction, the construction procedure is similar for the column-to-cap beam connection and the column-to-footing connection. In the former, the longitudinal bars

protrude up from the column to be cast with the cap-beam. In the latter, the procedure is the same, except that the bars protrude from the footing and are cast entirely within the column. In both connections, a horizontal cold joint is constructed between the elements.

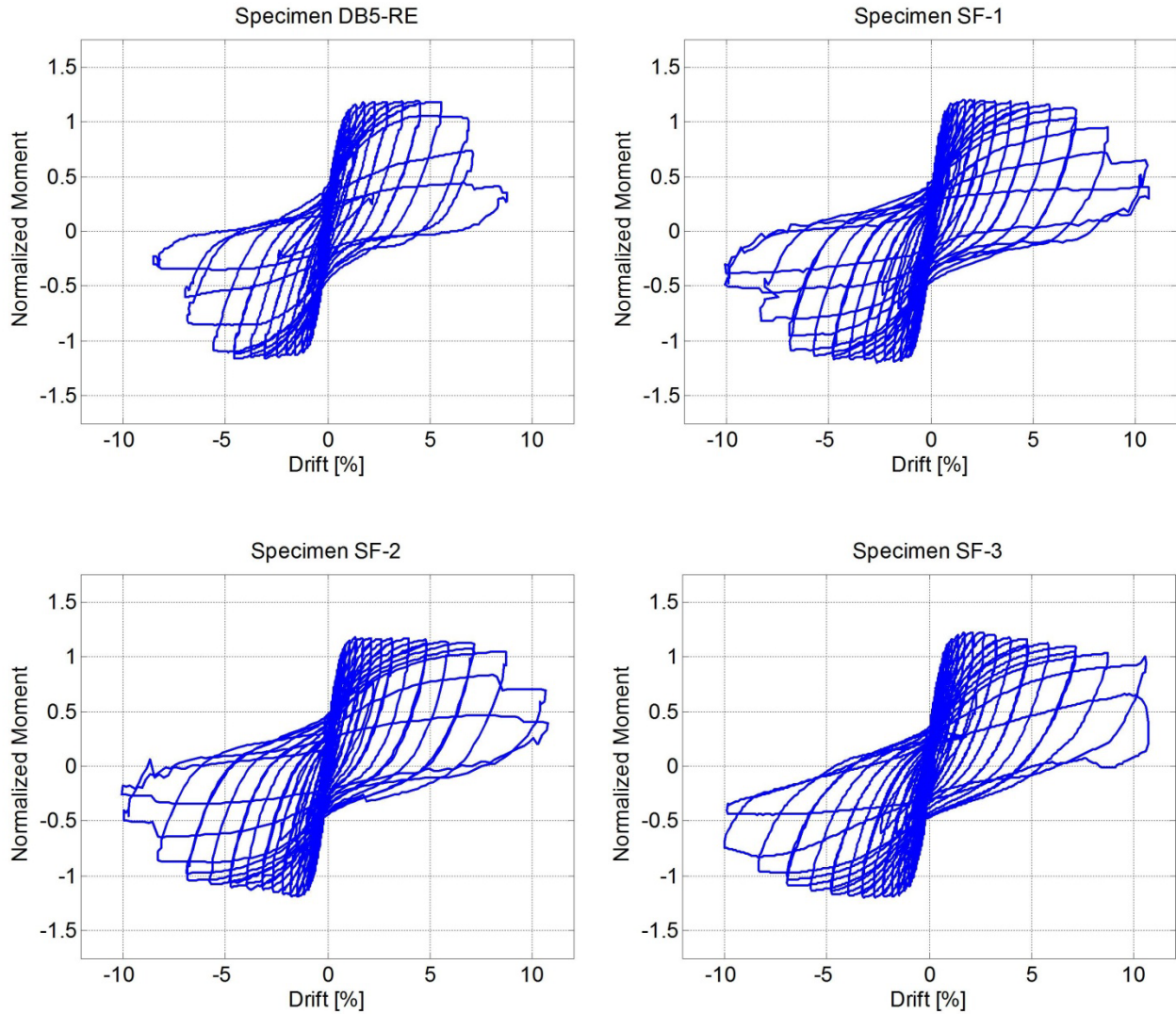


Figure 88. Graphs. Normalized equivalent moment-drift response.

The reference column shared the same geometry as specimens SF-, SF-2, and SF-3, but it had more longitudinal reinforcement (longitudinal ratio of 1.6 percent, 16 No. 5 bars, instead of 1 percent). The concrete specified strength differed as well (5,000 psi instead of 4,000 psi). The nominal moment strength of specimen DB5-RE was determined to be 3,815 kips-in.<sup>(7)</sup>

The socket specimens behaved similar to the cast-in-place reference specimen. In all specimens, the overstrength moment exceeded the nominal moment strength, as expected. The difference was about 15 to 20 percent for all specimens. The peak strength was reached at 2 percent drift, and the moment was constant up to about 6 percent drift, with the exception of specimen SF-3,

whose strength gradually decreased after 2.5 percent drift. As the specimens were cycled, the longitudinal bars buckled and later fractured. Specimen SF-3 failed in combined punching shear and moment transfer before any bar could fracture.

## STRENGTH DEGRADATION

Figure 89 compares the effective force versus drift ratio for the three specimens, which shows that the specimens performed similarly. The maximum effective force was approximately 51 kips for both specimens SF-1 and SF-2, whereas the peak was about 55 kips for specimen SF-3. The peak was reached at about 2 percent drift for all specimens. The load capacity remained almost constant up to 6 percent drift for specimens SF-1 and SF-2, after which both specimens lost strength at the same drift and degraded at the same rate. Specimen SF-3 proved to be about 7 to 10 percent stronger than specimens SF-1 and SF-2 and decayed more gradually, starting at 2.5 percent drift.

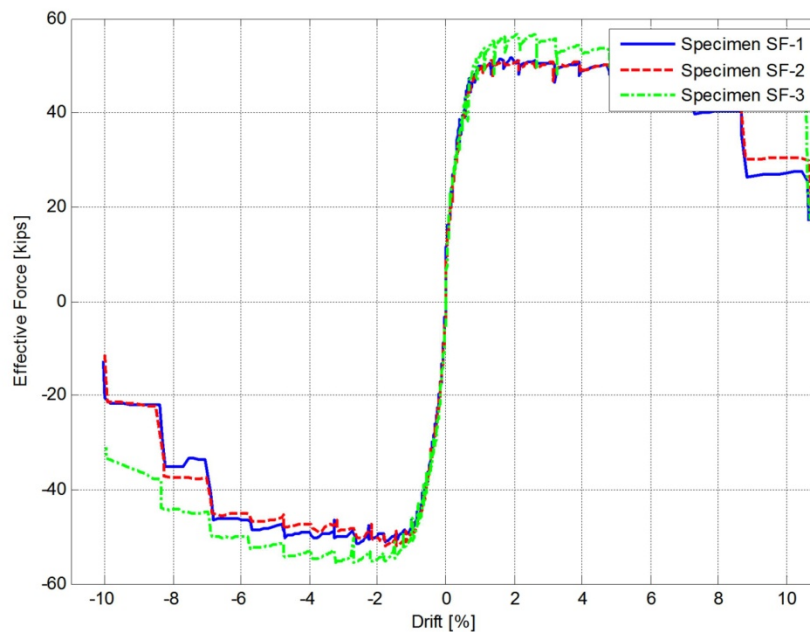


Figure 89. Graph. Comparison of effective force vs. drift.

## ENERGY DISSIPATION

The energy dissipation is the area inside the force-displacement curve and is a measure of how much damping the system can provide during an earthquake. It was calculated in this research using the trapezoidal integration procedure shown in figure 90.

$$E_{\text{cycle}} = \sum_i \frac{F_{i+1} + F_i}{2} (\Delta_{i+1} - \Delta_i)$$

Figure 90. Equation. Energy dissipation.

Figure 91 shows both the energy dissipated per cycle and the cumulative energy dissipation for the three specimens. To facilitate reading of the plots, the cycles are numbered continuously from the beginning. The tests consisted of sets of four cycles in which the peak amplitudes were 1.2A, 1.4A, 1.4A, and 0.33A, where A is the peak amplitude of the previous cycle set. The sets are visible as “humps” in the figure.

Figure 91 shows that the energy dissipation is almost the same in all specimens up to cycle 36 (cycle 9-4). However, in the last set of cycles there are slight differences between them, because buckling of the longitudinal reinforcement and first transverse reinforcement fracture were observed earlier in specimen SF-1 than in specimens SF-2 and SF-3. The transverse reinforcement in SF-1 fractured in cycle 34 (-6.88 percent drift), whereas the transverse reinforcement in SF-2 and SF-3 fractured in cycle 37 (-8.29 percent and +8.72 percent drift respectively). In cycle 38 (~10.6 percent drift), both specimen SF-1 and SF-2 fractured longitudinal bars for the first time. After the last cycle, SF-1 had fractured three bars and SF-2 had fractured four bars. Specimen SF-3 did not fracture any longitudinal bars.

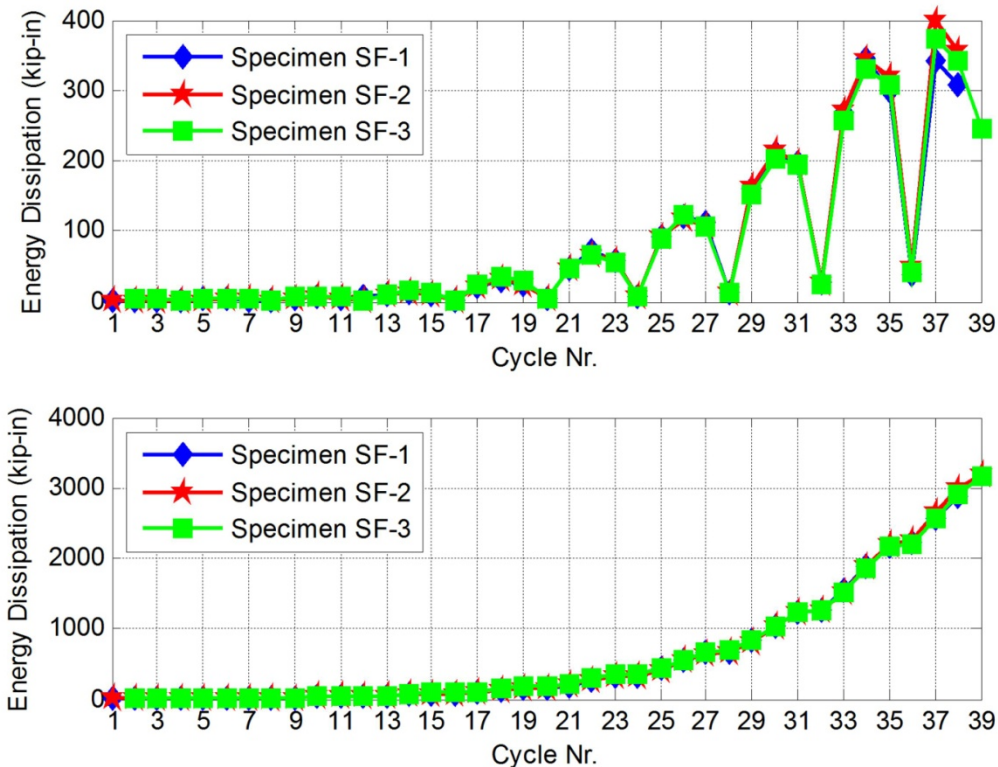


Figure 91. Graphs. Calculated energy dissipation per cycle (top), and calculated cumulative energy dissipation (bottom).

Figure 92 shows the calculated equivalent viscous damping ratio versus every fourth cycle. Equivalent viscous damping was calculated using the equation in figure 93, where  $A_{loop}$  is the cycle energy and  $A_{rectangle}$  is the area of a rectangle circumscribing the loop.

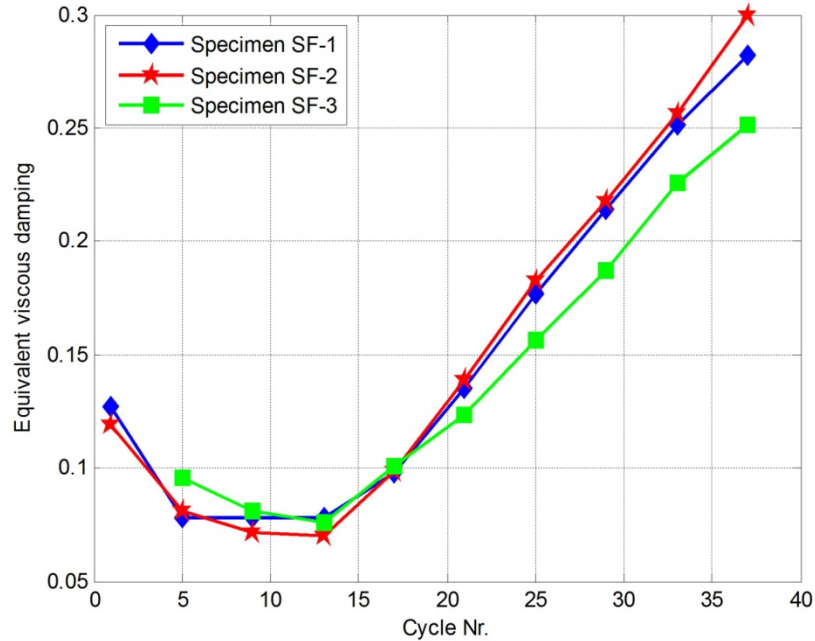


Figure 92. Graph. Equivalent viscous damping calculated per cycle.

$$\zeta_{eq} = \frac{2}{\pi} \left( \frac{A_{loop}}{A_{rectangle}} \right)$$

Figure 93. Equation. Equivalent viscous damping.

The same information is shown in figure 94, in which the equivalent viscous damping ratio is plotted against the average drift ratio for the same cycles.

Damping was similar but not identical for the three specimens. All tests showed higher damping in the beginning of tests. With increasing drift the systems were dissipating more energy. The responses of specimens SF-1 and SF-2 were almost identical, but specimen SF-3 was consistently lower after 1 percent drift. Specimen SF-3 proved to be little bit stronger than the other two specimens, which resulted in lower damping values ( $A_{rectangle}$  is bigger in SF-3).

In all three specimens, the damping values at small drifts were quite large. This is believed to be a consequence of the process used to correct for the friction in the sliding channel in the Baldwin Universal Testing Machine. The friction was approximately constant throughout the test but, at low drifts, the amount of energy dissipated by the column was small. The result is that the relative error (caused by imperfect estimation of the true friction) was greatest at small drift ratios, and reliance should not be placed on those values.

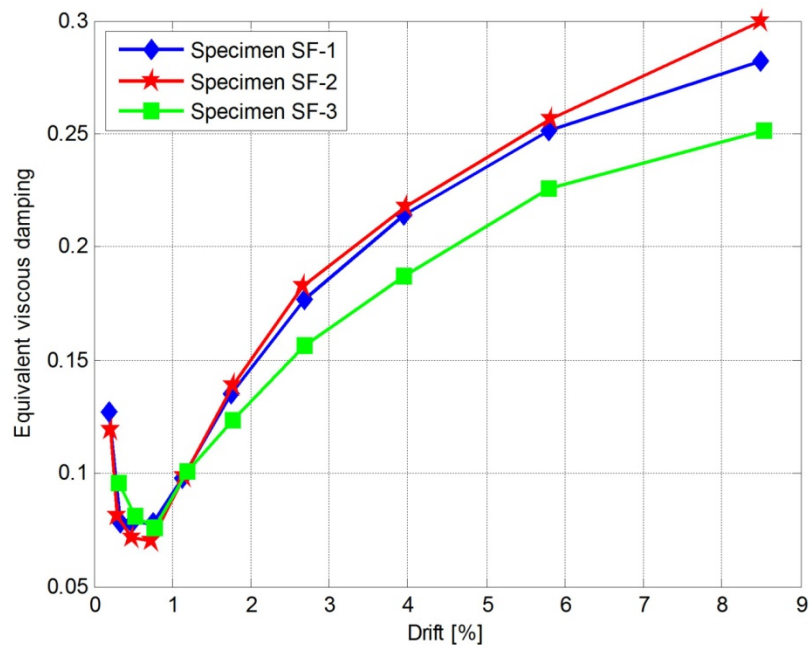


Figure 94. Graph. Equivalent viscous damping vs. drift.

Despite the fact that specimen SF-3 had a configuration that was very different from those of specimens SF-1 and SF-2, the energy dissipation behavior of all three was remarkably similar. Photographic evidence from the tests also shows extensive damage to the columns in all three specimens. Damage to the footing in specimen SF-3 only became visible starting at about 9 percent drift ratio. The observation suggests that specimen SF-3 was very close to being governed by column strength rather than footing connection strength. That, in turn, suggests that only a small increase in footing depth or connection reinforcement would be needed to make it behave like a conventional cast-in-place system.



## CHAPTER 7. SUMMARY AND CONCLUSIONS

### SUMMARY

#### System Concept

A new column-to-footing “socket” connection suitable for use with spread footings was developed and tested at the University of Washington. The connection concept is intended to accelerate the construction of bridge piers and to provide excellent seismic performance.

First, a column is precast with the intentional surface roughening around the base. Then the column is set in the excavation, plumbed, leveled, and braced. Finally, the footing reinforcement is tied around the column, and the foundation is cast.

The column longitudinal bars are straight and are terminated with mechanical anchors instead of being bent outwards into the footing. This configuration has several advantages. It avoids fit-up of bars in ducts at the base of the column, the column detailing can be almost identical to that of a cast-in-place column, and no grouting is needed. Other advantages include better seismic performance, because the force transfer between the column and the footing is more direct, as suggested with strut-and-tie modeling. This use of headed bars also makes fabrication, transportation, and erection safer, easier, and quicker.

#### Design of Test Specimens

WSDOT selected a prototype bridge to demonstrate the implementation of the proposed rapid construction technology. The laboratory specimens represented the essential details of the bridge footings at 42 percent scale. The tests provided proof of concept for the seismic performance of the system, and the bridge construction was used for field verification of the system’s constructability.

Three cantilever-footing specimens were constructed. Specimens SF-1 and SF-2, illustrated in figure 95, were designed and tested before starting the construction of the prototype bridge. Specimen SF-1 was designed to satisfy the conventional cast-in-place requirements of the AASHTO Seismic Guide Specifications, with minor modifications. Slots in each direction were created at the base of the precast column to allow some of the bottom footing reinforcement to pass through the slots.

Specimen SF-2 was similar to SF-1 but simpler and more economical to construct. It did not have slots at the base of the column, and it contained less reinforcement, so it was inherently less conservative. Some classes of reinforcement (such as footing ties) were reduced below the level specified in the Caltrans SDC to determine whether they were needed. In both specimens, the column was segmental and spliced at the top of the anticipated plastic hinge. The segments were included to test the seismic performance of such a splice, because splices were included in the prototype to investigate their constructability.



Figure 95. Photos. Specimen SF-1 (left) and specimen SF-2 (right).

Specimens SF-1 and SF-2 failed in column flexure and so revealed little about the strength of the footing connection. To investigate the connection behavior, specimen SF-3 was designed to fail in the connection region. This goal was achieved by reducing the footing depth and adding steel to suppress unwanted modes of failure, such as footing flexure and one-way shear.

### **Experimental Testing**

Each specimen was subjected to the following series of tests:

- First, each specimen was subjected to an axial load of at least 240 kips, which is the largest factored load expected to act on the connection after reduction to laboratory scale. Specimen SF-3 was loaded to an even higher axial load (342 kips).
- Second, the vertical load was reduced to 159 kips, which represented the service dead load plus vertical (overturning) load resulting from horizontal earthquake motion, and cyclic horizontal loading was applied to the column using a displacement controlled actuator.
- Third, after the cyclic loading was complete, specimens SF-1 and SF-2 were subjected to a pure axial-load test to failure to investigate the resistance of the footing to push-through of the column. Such loading was not possible in specimen SF-3, because the footing had already failed in punching shear.

In specimens SF-1 and SF-2, which had the thicker footings, the damage due to lateral loading was concentrated at the base of the columns, and the connections were nearly undamaged. Column flexural failure was initiated by buckling of the longitudinal bars (at drift ratios of about 7 percent) and was completed by fracture of those bars as they straightened during the subsequent tension part of the loading cycle. This behavior has been observed in many cast-in-place columns tested at the University of Washington and elsewhere. The failure of these specimens under pure axial load, in the third phase of testing, was due to crushing of the concrete within the hinging region. When that load was applied, the spiral had already failed during the lateral load tests.

Specimen SF-3, which had a much thinner footing, experienced much more damage in connection region. Nonetheless, the specimen carried the axial load to a drift ratio of 10 percent

before the precast column punched through the supporting footing in a failure mode caused by combined punching shear and moment transfer.

### Experimental Analysis

The measured responses of the test specimens were compared with the results of analytical models for both the spread footing and column. Table 24 summarizes the ratios of the demands on the footings to the nominal calculated capacities using the measured material properties.

Table 24. Summary of ratios of footing demands to calculated capacities.

<b>Design Criteria</b>	<b>SF-1</b>	<b>SF-2</b>	<b>SF-3</b>
<b>Footing cracking, <math>M_u/M_{cr}</math></b>	0.91	0.89	3.97
<b>Footing flexural strength, <math>M_u/M_n</math></b>	0.57	0.57	0.75
<b>Footing one-way shear strength, <math>V_u/V_n</math></b>	0.43	0.56	0.75
<b>Connection combined punching shear and moment transfer under cyclic loading, <math>v_u/v_n</math></b>	0.20	0.25	1.27
<b>Punching shear strength under pure axial load, <math>V_u/V_n</math></b>	1.19	1.35	1.82
<b>Shear-friction push-through strength under pure axial load, <math>V_u/V_n</math></b>	1.44	1.90	0.74
<b>Joint shear (compressive), <math>p_c^{calc}/p_c^{limit}</math></b>	0.23	0.21	0.32
<b>Joint shear (tensile), <math>p_t^{calc}/p_t^{limit}</math></b>	0.24	0.22	0.44

The flexural demands in the footings were approximately 10 percent below the calculated cracking capacities for the two thick footings (SF-1 and SF-2), but the demands greatly exceeded the nominal cracking moment for the thin footing (SF-3). These findings are consistent with the observed damage patterns.

The footing and connection demands for specimens SF-1 and SF-2 were well below the calculated capacities for footing flexural strength, footing one-way shear, combined punching shear and moment transfer, and joint shear. These calculations are also consistent with the observed damage patterns. The demands exceeded the calculated capacities for punching shear

under pure axial load and for shear friction. Neither specimen SF-1 nor specimen SF-2 failed in these manners.

The demands on the thin footing in SF-3 were lower than the nominal capacities for footing one-way shear, shear friction, and joint shear. The specimen did not fail in any of these modes. The demands were greater than the capacities for both punching shear pure axial load and for combined punching shear and moment transfer. Specimen SF-3 successfully withstood the pure axial load and demonstrated that the capacity of the thinner spread footing was sufficient. The load exceeded 140 percent of the maximum axial load expected on the connection. Specimen SF-3 failed in the combined punching shear and moment transfer. The demand exceeded the nominal capacity by 27 percent.

## CONCLUSIONS

**Connection concept.** The column-to-footing socket connection can be designed to behave at least as well as a comparable cast-in-place column-to-footing connection.

**Behavior of precast columns.** In all three specimens, the response to cyclic lateral loading of the precast columns was essentially identical to that of a cast-in-place column with the same geometry and reinforcement. Such precast columns can be designed following the same design approach used to design cast-in-place columns, including the calculation of displacement capacity.

**Need for mechanical anchors.** In specimens SF-1 and SF-2, the bar stress directly behind the anchors reached values of up to about 3 ksi. The headed anchors were more active in SF-3. These measurements showed that the anchors were providing partial anchorage and should be included in future implementations of the socket connection.

**Design against overturning.** The procedures outlined in the AASHTO Seismic Guide Specifications for determining the expected strength of the column and the size of footing required to prevent overturning proved to be slightly conservative in all three tests.

**Design against footing failure.** The procedures outlined in the AASHTO Seismic Guide Specifications for determining the required flexural strength of the footing were effective in preventing footing failure in all three column tests. In specimens SF-1 and SF-2, with  $h_{footing} = 1.1D_{col}$ , the amount of flexural reinforcement in the footing was controlled by minimum requirements, so the absence of footing failure was expected. In those specimens the footing did not even crack in flexure, and nearly all the moment was carried by the concrete.

In specimen SF-3, with  $h_{footing} = 0.5 D_{col}$ , the footing reinforcement was controlled by strength requirements. The footing cracked, but the stress in the footing steel never rose above 26 ksi. Failure was controlled by shear stress in the connection caused by loading in combined shear and moment transfer. For thinner footings, it is advisable to include a check for a potential failure in a combined punching shear and moment transfer, using the procedure outlined in ACI 318-08. The AASHTO LRFD Design Specifications contain no provisions for this potential failure mode, despite the fact that it proved critical here.

**Vertical ties in the footing.** When the column steel consists of straight bars equipped with headed anchors, rather than the conventional bent-out bars, the prescriptive vertical footing ties specified by the AASHTO Seismic Guide Specifications perform no useful function and can be omitted. This conclusion applies only to the prescriptive ties, and not to ties that are needed to supply shear resistance required to resist computed shear demands.

**Shear-friction push-through resistance of connection.** The shear friction strength of the connection between column and footing was sufficient to prevent any slip, much less sliding failure, in any of the three test specimens. In specimens SF-1 and SF-2, in which the footing was essentially undamaged, the connection interface withstood a shear stress of 611 psi with no sign of damage even after the specimens had been subjected to large lateral deformations.

**Shear-friction reinforcement.** The bottom diagonal bars included in the thick footing test specimens (SF-1 and SF-2) experienced little stress during the factored axial-load test and during the cyclic lateral-load tests and, therefore, proved unnecessary for resisting shear friction. During these tests, the footing remained essentially elastic. If the column is circular or octagonal and the opening in the main footing reinforcement is square, it is recommended that at least one set of diagonal bars be included in the top and bottom mat to avoid the existence of unreinforced concrete in the corners.

**Joint shear stress.** Analysis showed that the permissible tensile and compressive stresses due to joint shear were not exceeded in any of the specimens, and that is in agreement with the observed lack of cracking. The largest joint shear demands were in specimen SF-3.

**Column splice location.** Any splice in the column should be located outside the plastic hinge length, as defined by the AASHTO Seismic Guide Specifications. The splices in specimens SF-1 and SF-2 were located exactly where yielding would be first expected when the column moment at the base reached its full plastic value ( $M_{po}$ ), but they were closer to the base than the prescriptive  $1.5D_{col}$  value included in the AASHTO Seismic Guide Specifications criteria for plastic hinge length. The longitudinal reinforcement just yielded there, but the joints did not suffer damage or display any residual crack opening.

**Column splice design.** The splice length in specimens SF-1 and SF-2 was controlled by the length required to splice the confined column bars outside the ducts. The development length used in design should take into account any top bar effects that arise from casting in a particular direction (i.e., horizontally or vertically).

**Column shear resistance at the splice.** No shear slip or damage occurred at the splice in either of the two specimens that included a splice (SF-1 and SF-2). Each splice was made with a circular key at the column center. The average shear stress on the gross column section reached a maximum of 156 psi.

## RECOMMENDATIONS

The proposed system is ready for implementation in the field in cases where the configuration and geometry are similar to those used in the tests. The tests showed excellent seismic performance, and the construction of the prototype demonstrated the system's constructability.

These three tests begin to form the data set needed for design. More data on the behavior of socket connections are still needed to allow design in wider range of configurations. The wooden strips used here provided sufficient roughness for the column surface, but less labor intensive methods of creating the roughened surface should be investigated as well.

Finite element analysis of the connection should be conducted to investigate numerically the distribution of stress in the connection region and to allow extrapolation of these test results to other situations.

## REFERENCES

1. FHWA. (2008). "2008 Condition and Performance Report." U.S. Department of Transportation, Federal Highway Administration, McLean, VA.
2. Matsumoto, E., Waggoner, M., Sumen, G., Kreger, M., Wood, S., and Breen, J. (2001). *Development of a Precast Bent Cap System*, Center for Transportation Research, Research Project 0-1748, University of Texas at Austin.
3. Matsumoto, E., Waggoner, M., Kreger, M., Vogel, J., and Wolf, L. (2008). "Development of a Precast Concrete Bent-Cap System." *PCI Journal*, vol. 53, no. 3, pp. 74-99.
4. Hieber, D., Wacker, J., Eberhard, M.O., and Stanton, J.F. (2005). *State of the Art Report on Precast Concrete Systems for Rapid Construction of Bridges*. Report No. WA-RD-549.1, Washington State Department of Transportation, Olympia, WA.
5. Wacker, J., Hieber, D., Eberhard, M., and Stanton, J. (2005). *Design of Precast Concrete Piers for Rapid Construction of Bridges in Seismic Regions*. Report No. WA-RD-629.1, Washington State Department of Transportation, Olympia, WA.
6. Hieber, D., Wacker, J., Eberhard, M.O., and Stanton, J.F. (2005). *Precast Concrete Pier Systems for Rapid Construction of Bridges in Seismic Regions*. Report No. WA-RD-611.1, Washington State Department of Transportation, Olympia, WA.
7. Pang, J.B.K., Steuck, K., Cohagen, L., Stanton, J.F., Eberhard, M.O. (2008). *Rapidly Constructable Large-Bar Precast Bridge-Bent Seismic Connection*. Washington State Transportation Center Report No. WA-RD 684.2, Seattle, WA.
8. Pang, J.B.K., Eberhard, M.O., and Stanton, J.F. (2010). "Large-Bar Connection for Precast Bridge Bents in Seismic Regions." *Journal of Bridge Engineering, ASCE*, vol. 15, no. 3, May-June, pp. 231-239.
9. Steuck, K., Pang, J.B.K., Stanton, J.F. and Eberhard, M.O. (2007) *Anchorage of Large Bars in Grouted Ducts*. Washington State Transportation Center Report WA-RD 684.1, Seattle, WA.
10. Steuck, K., Stanton, J.F. and Eberhard, M.O. (2009) "Anchorage of Large-Diameter Reinforcing Bars in Ducts." *ACI Structural Journal*, vol. 106, no. 4, July-August, pp. 506-513.
11. Cohagen, L.S., Pang, J.B.K., Eberhard, M.O., and Stanton, J.F. (2008). *A Precast Concrete Bridge Bent Designed to Re-center after an Earthquake*. Report No. WA-RD 684.3, Washington State Department of Transportation, Olympia, WA.
12. Haraldsson, O.S. (2011). "Spread Footing Socket Connections for Precast Columns." MSCE Thesis. University of Washington, Seattle, WA.
13. Janes, T.M. (2011). "Precast Column Socket Connections for Thin Spread Footings." MSCE Thesis. University of Washington, Seattle, WA.
14. American Association of State Highway and Transportation Officials (AASHTO) (2009). *AASHTO LRFD Bridge Design Specifications*. 4th ed., with 2009 Interim Revisions. American Association of State Highway and Transportation Officials, Washington, DC.

15. AASHTO (2009). *AASHTO Guide Specification for LRFD Seismic Bridge Design*. 1st ed. American Association of State Highway and Transportation Officials, Washington DC.
16. California Department of Transportation (Caltrans). (2006). *Seismic Design Criteria Version 1.4*. Caltrans, Sacramento, CA.
17. Washington State Department of Transportation (WSDOT). (2008). *Bridge Design Manual Version M23-50.02*. Washington State Department of Transportation, Olympia, WA.
18. American Concrete Institute (ACI) Committee 318. (2008). *Building Code Requirements for Structural Concrete and Commentary*. ACI 318-08, American Concrete Institute, Farming Hills, MI.
19. Mander, J. Priestley, M., and Park, R. (1998). "Theoretical Stress-Strain Model for Confined Concrete." *Journal of the Structural Division ASCE*, vol. 114, no. 8, pp. 1804-1826.
20. Building Seismic Safety Council. (2003). "NEHRP Recommended Provisions for Seismic Regulations for New Buildings and Other Structures (FEMA 450)." *National Earthquake Hazards Reduction Program*, National Institute of Building Sciences, Washington, D.C.
21. Berry, M.P., and Eberhard, M.O. (2004). "PEER Structural Performance Database User's Manual." *Pacific Earthquake Engineering Research Center Report 2004*, <www.ce.washington.edu/~peeral>, University of California, Berkeley.
22. Brown, W. (2008). "Bar Buckling in Reinforced Concrete Bridge Columns." MSCE Thesis, University of Washington, Seattle, WA.
23. Precast/Prestressed Concrete Institute (2004). *PCI Design Handbook*. 6th ed. PCI, Chicago, IL.
24. Berry, M.P., and Eberhard, M.O. (2003). "Performance Models for Flexural Damage in Reinforced Concrete Columns." *Pacific Earthquake Engineering Research Center Report 2003*, University of California, Berkeley.
25. Berry, M.P. and Eberhard, M.O. (2005). "A Practical Performance Model for Bar Buckling," *Journal of Structural Engineering*, ASCE, Vol. 131, No. 7, pp. 1060-1070.
26. Elwood, K.J., and Eberhard, M.O. (2009). "Effective Stiffness of Reinforced Concrete Columns." *ACI Structural Journal*, vol. 106, no. 4, July-August, pp. 476-484.

# APPENDIX A: SPECIMEN CONSTRUCTION DRAWINGS

## SPECIMEN SF-1

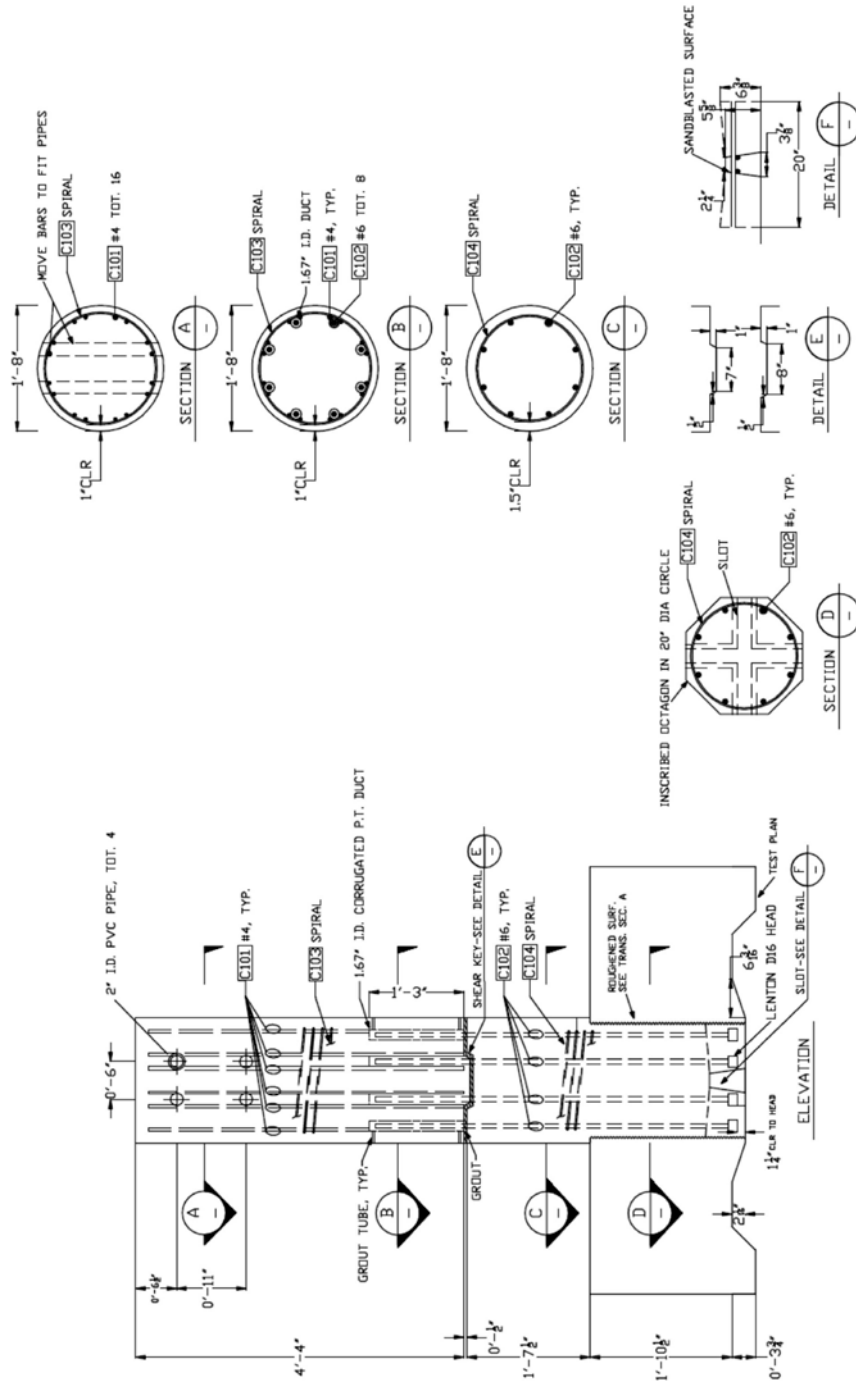


Figure 96. Diagram. Specimen SF-1 column elevation and sections.

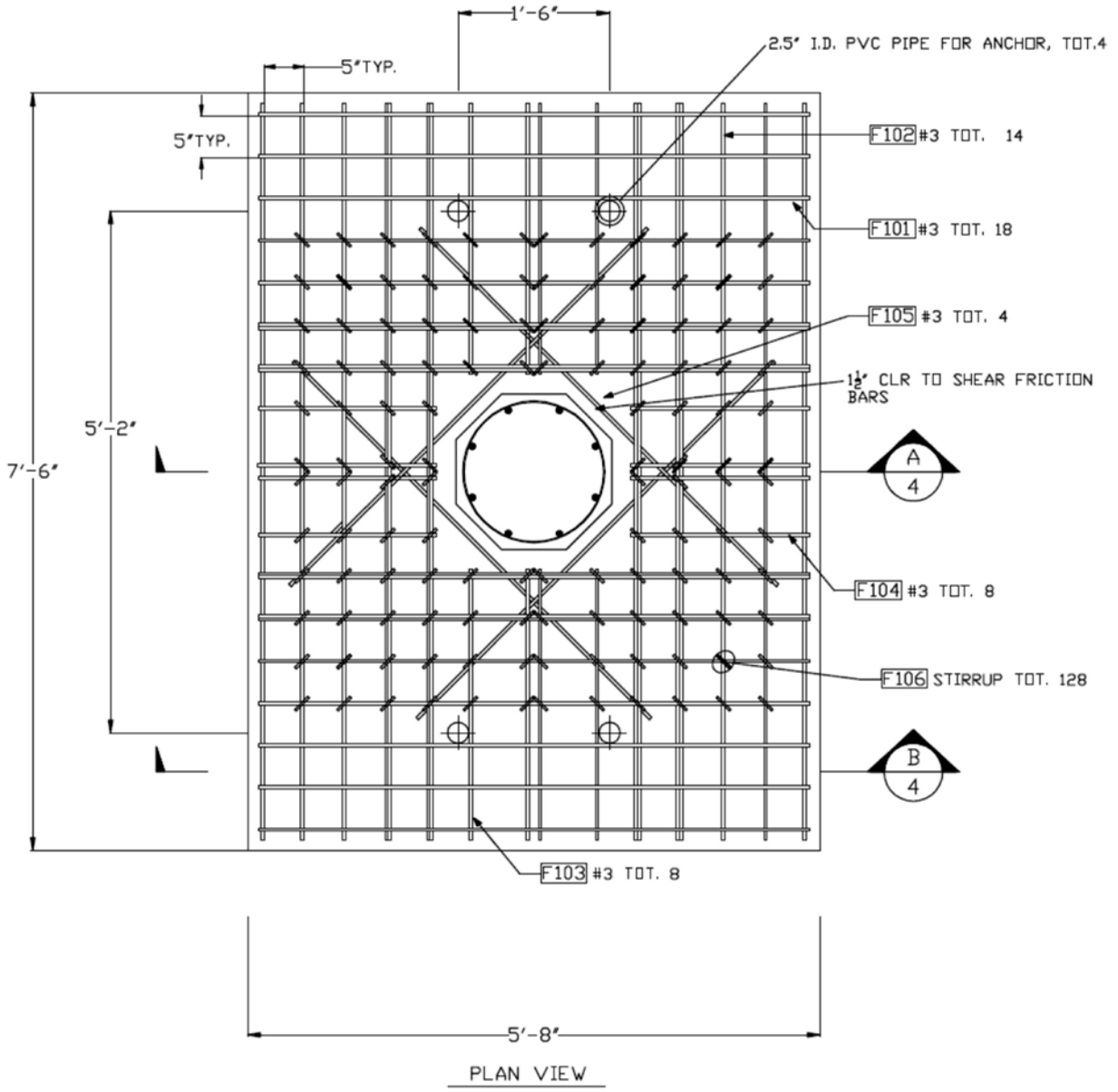


Figure 97. Diagram. Specimen SF-1 top mat plan view.

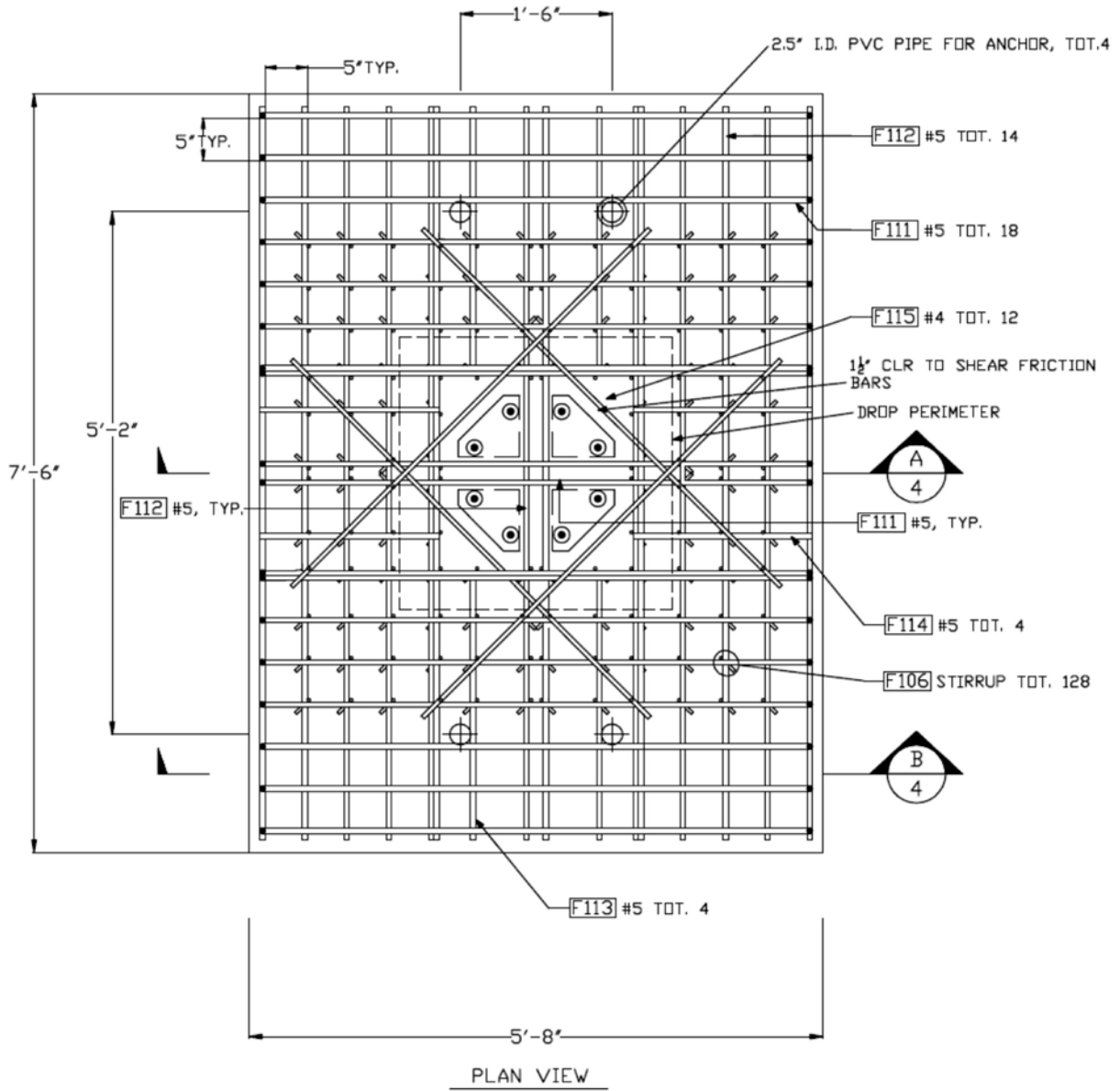
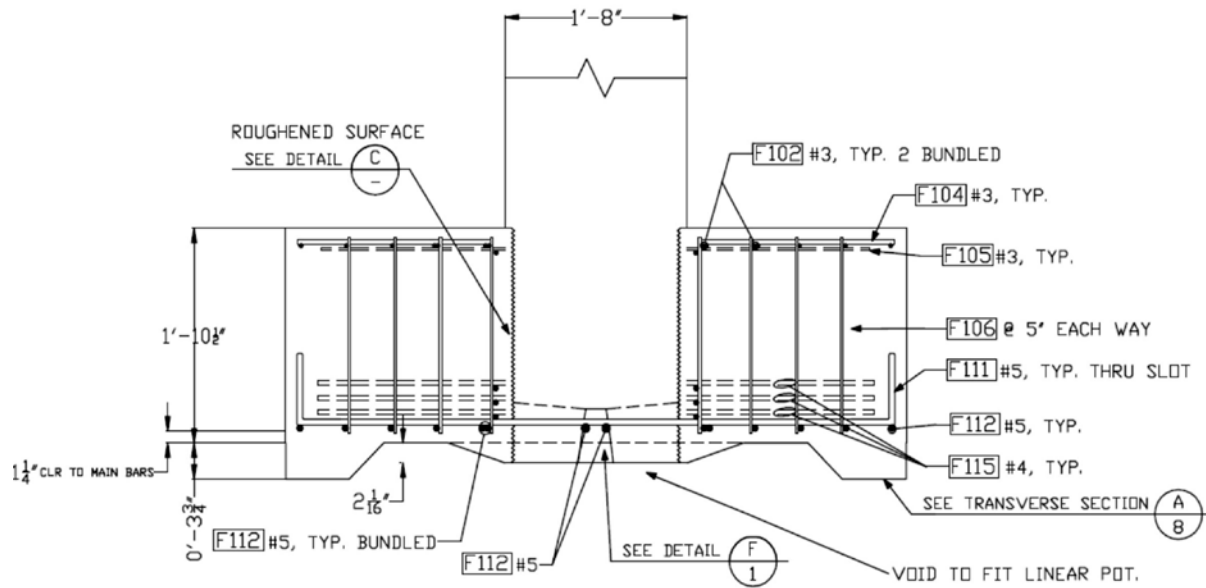
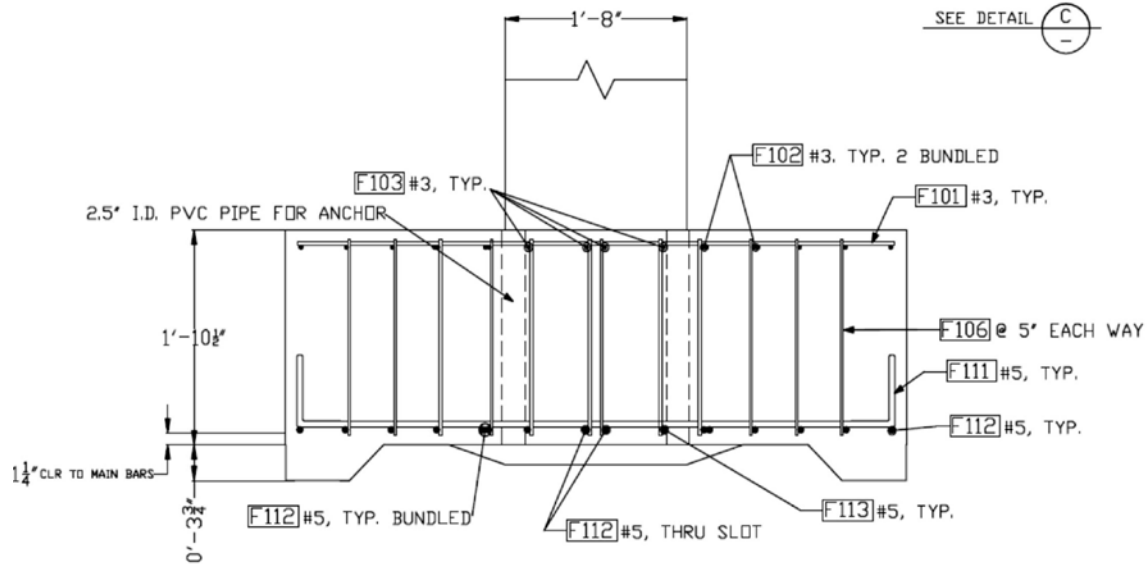
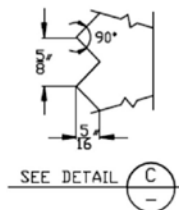


Figure 98. Diagram. Specimen SF-1 bottom mat plan view.



TRANSVERSE SECTION (A) 2



TRANSVERSE SECTION (B) 2

Figure 99. Diagram. Specimen SF-1 sections.

**SPECIMEN SF-2**

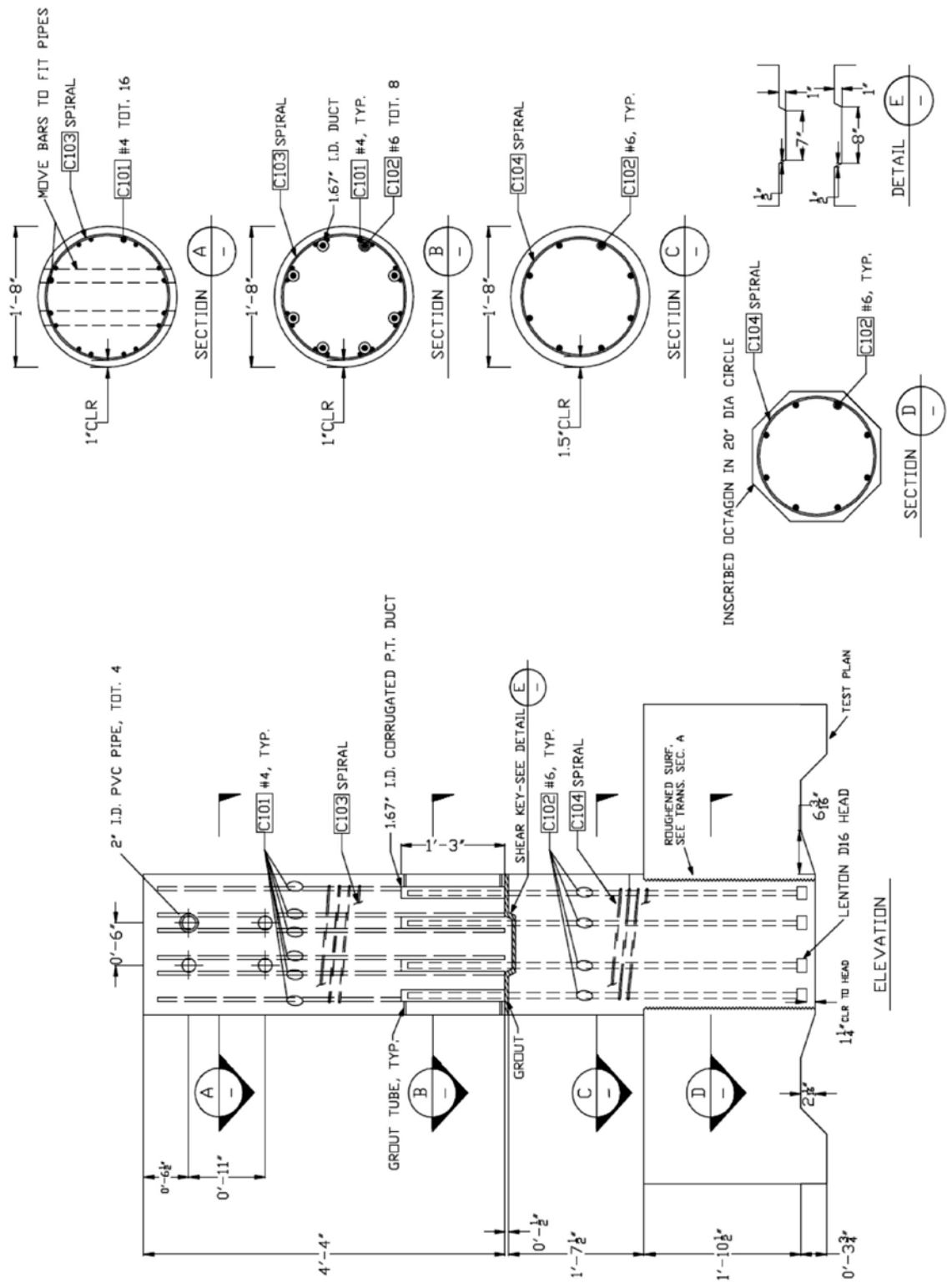


Figure 100. Diagram. Specimen SF-2 column elevation and sections.

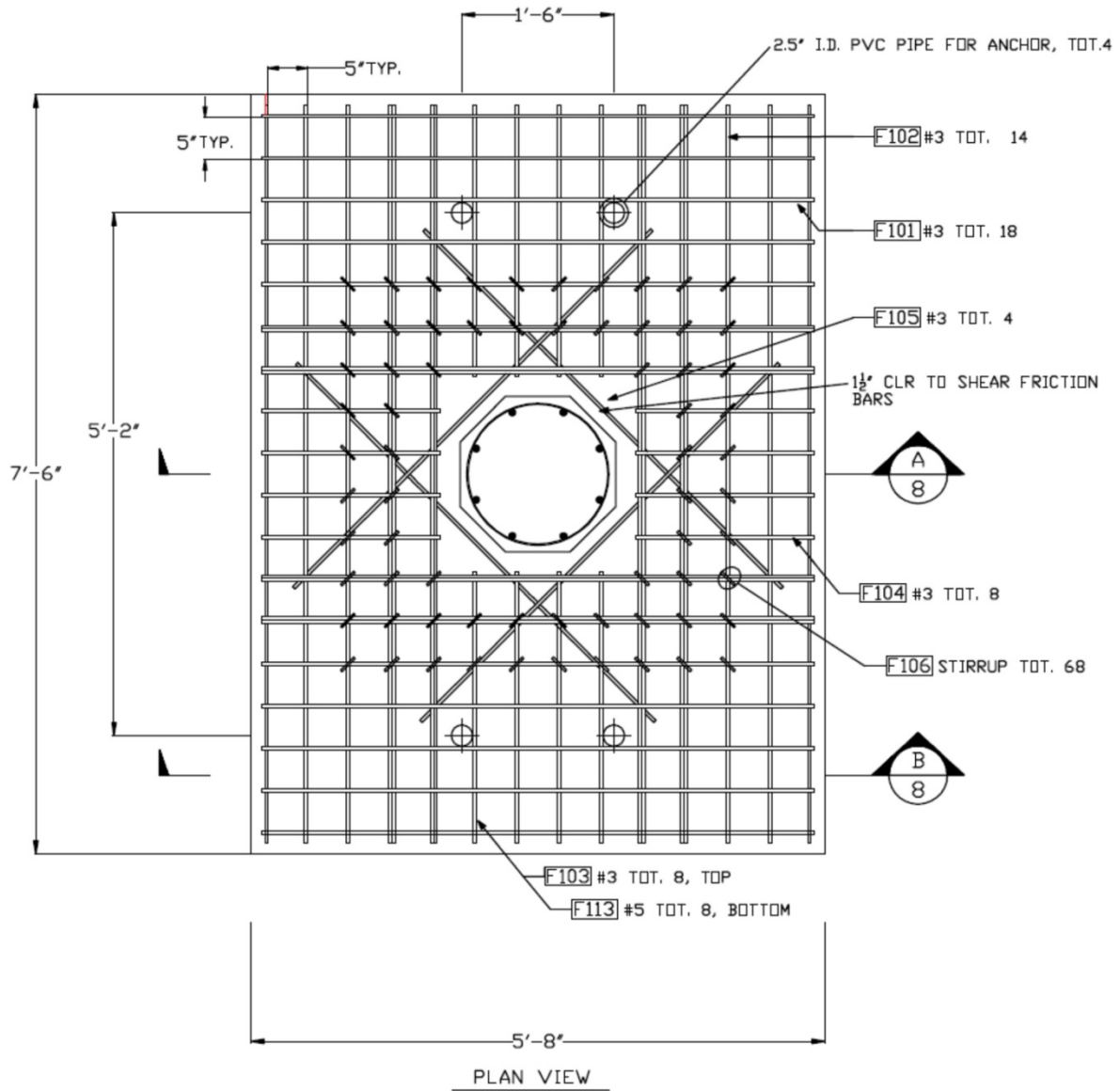


Figure 101. Diagram. Specimen SF-2 top mat plan view.

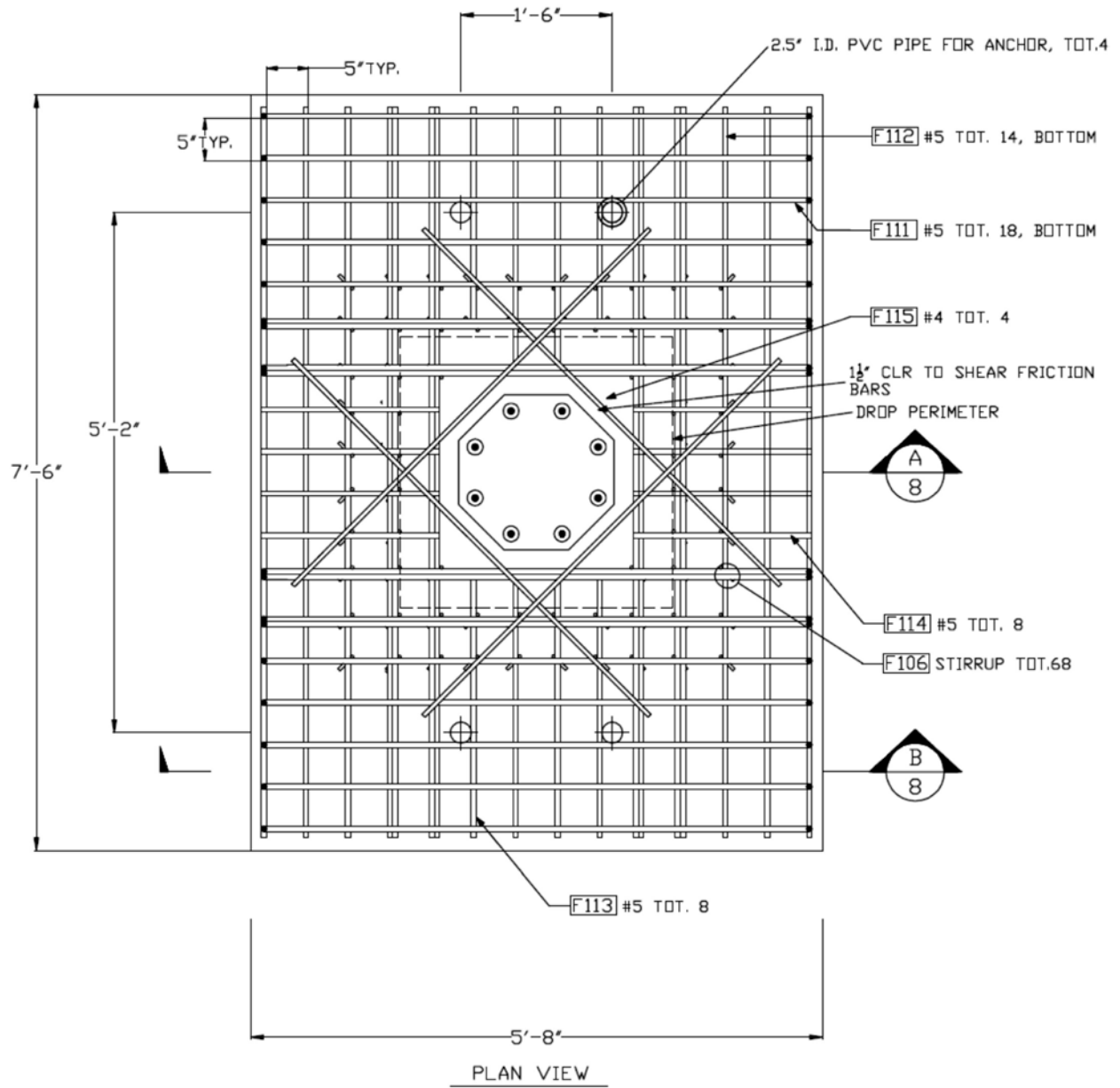
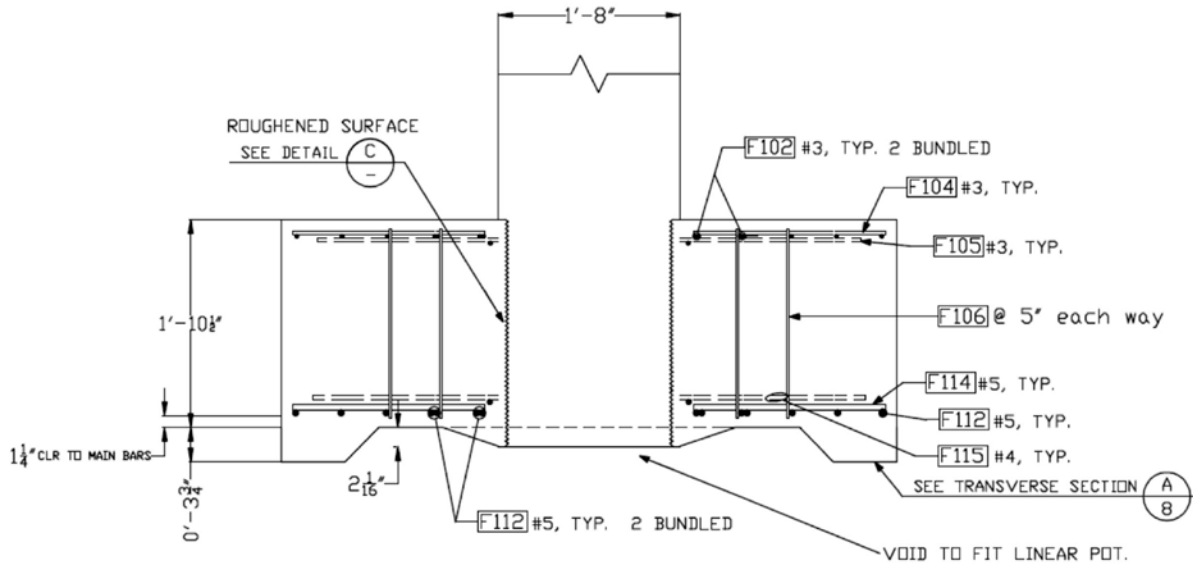
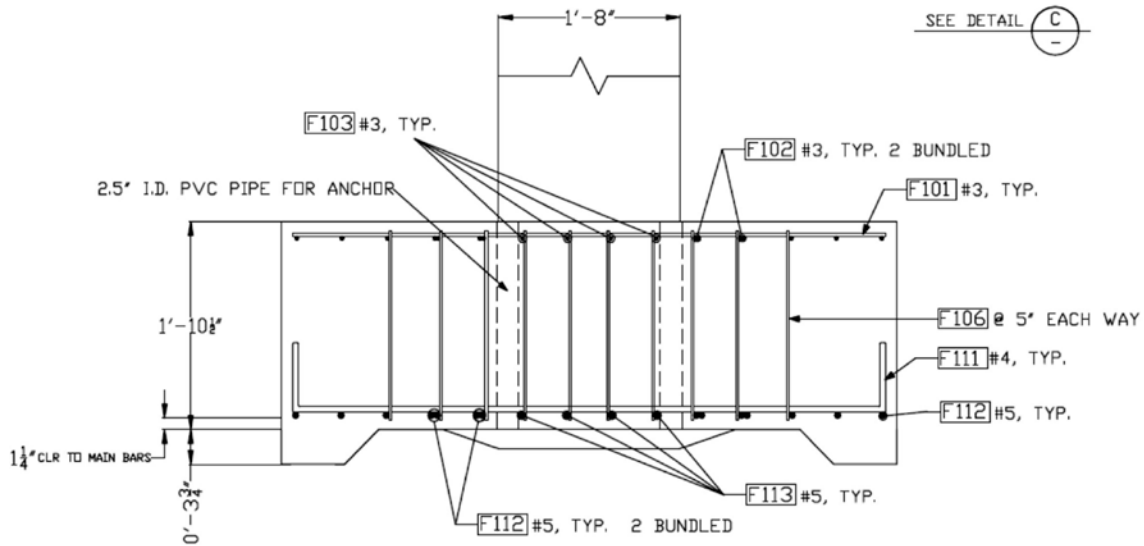
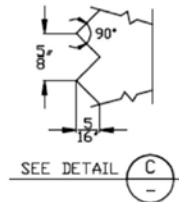


Figure 102. Diagram. Specimen SF-2 bottom mat plan view.



TRANSVERSE SECTION (A/6)



TRANSVERSE SECTION (B/6)

Figure 103. Diagram. Specimen SF-2 sections.

**SPECIMEN SF-3**

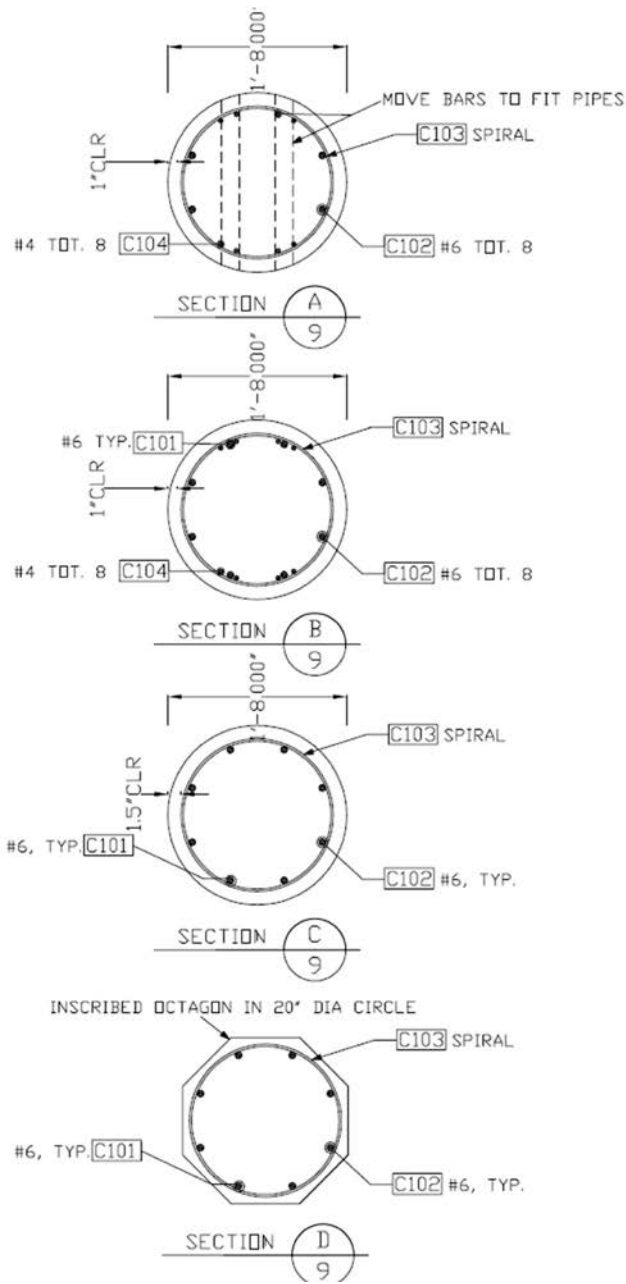


Figure 104. Diagram. Specimen SF-3 column sections.



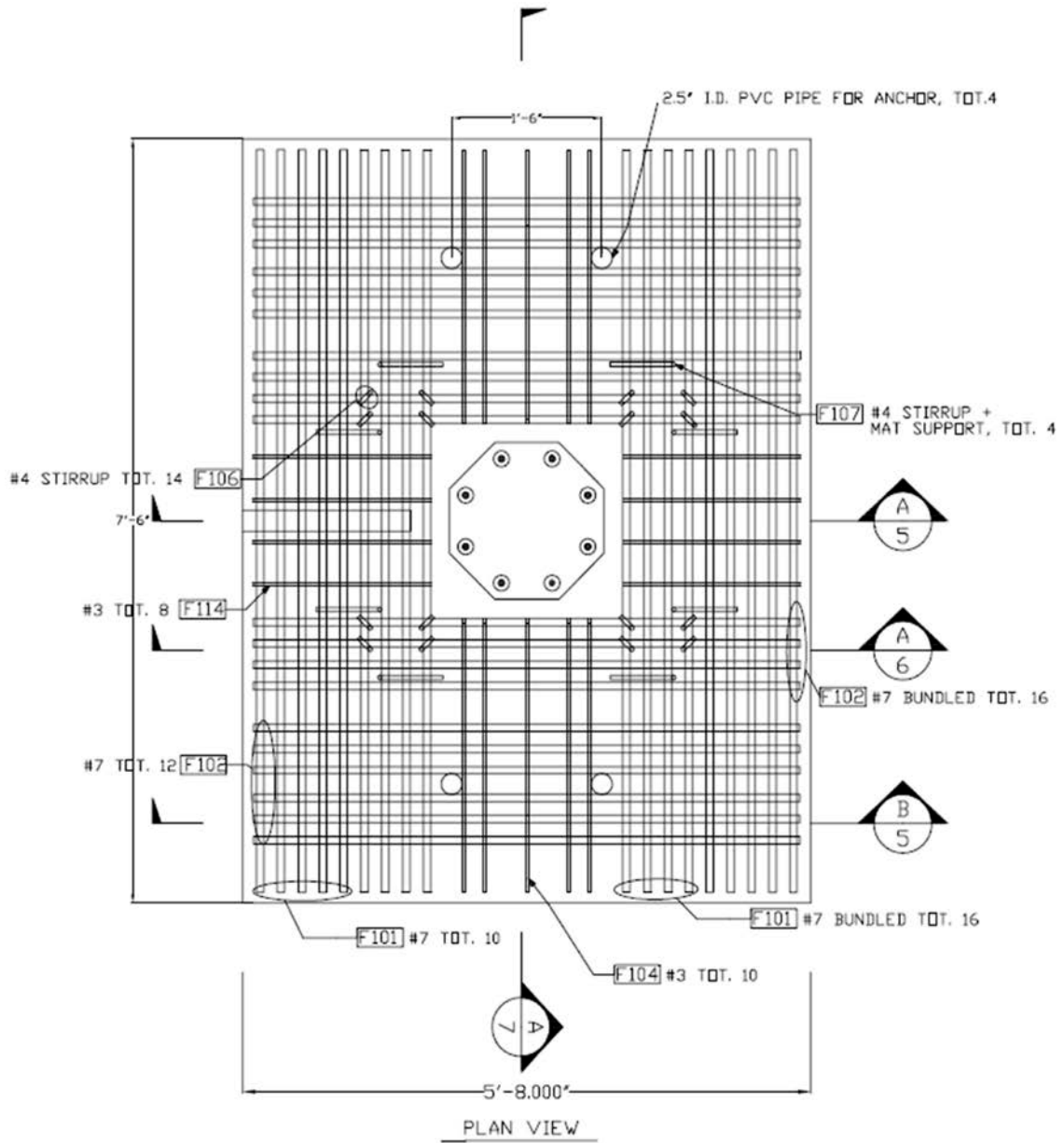


Figure 106. Diagram. Specimen SF-3 bottom mat plan view.

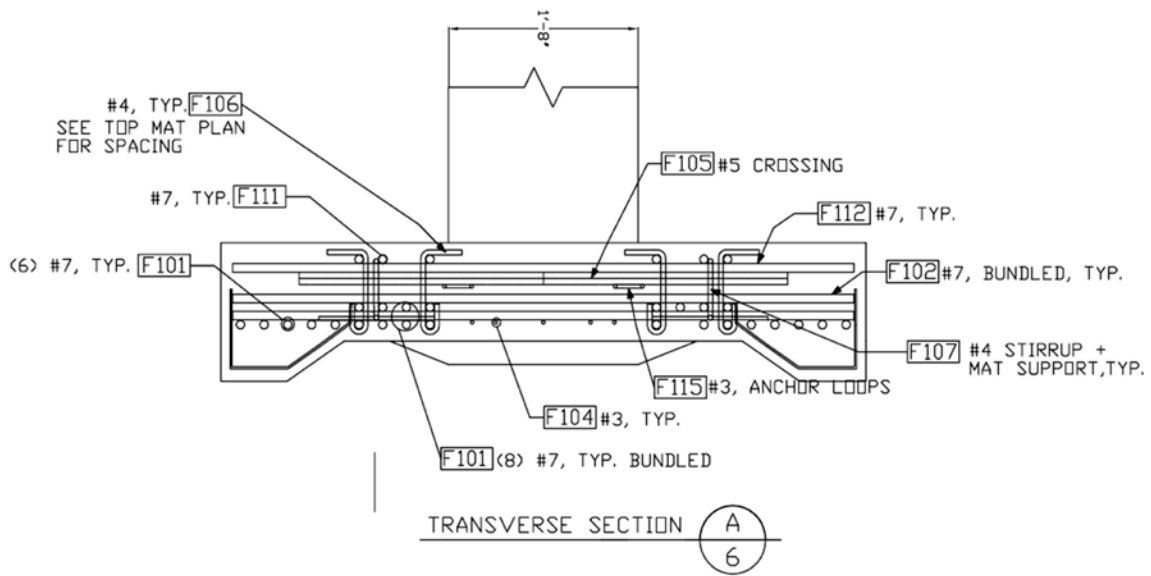
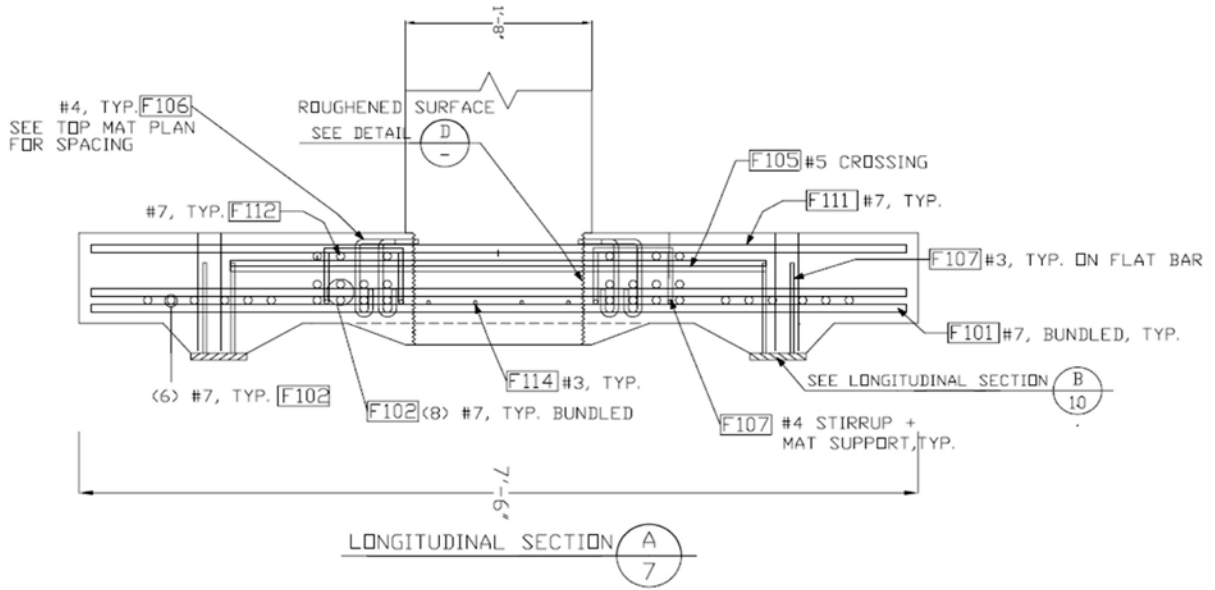


Figure 107. Diagram. Specimen SF-3 footing sections A7 and A6.

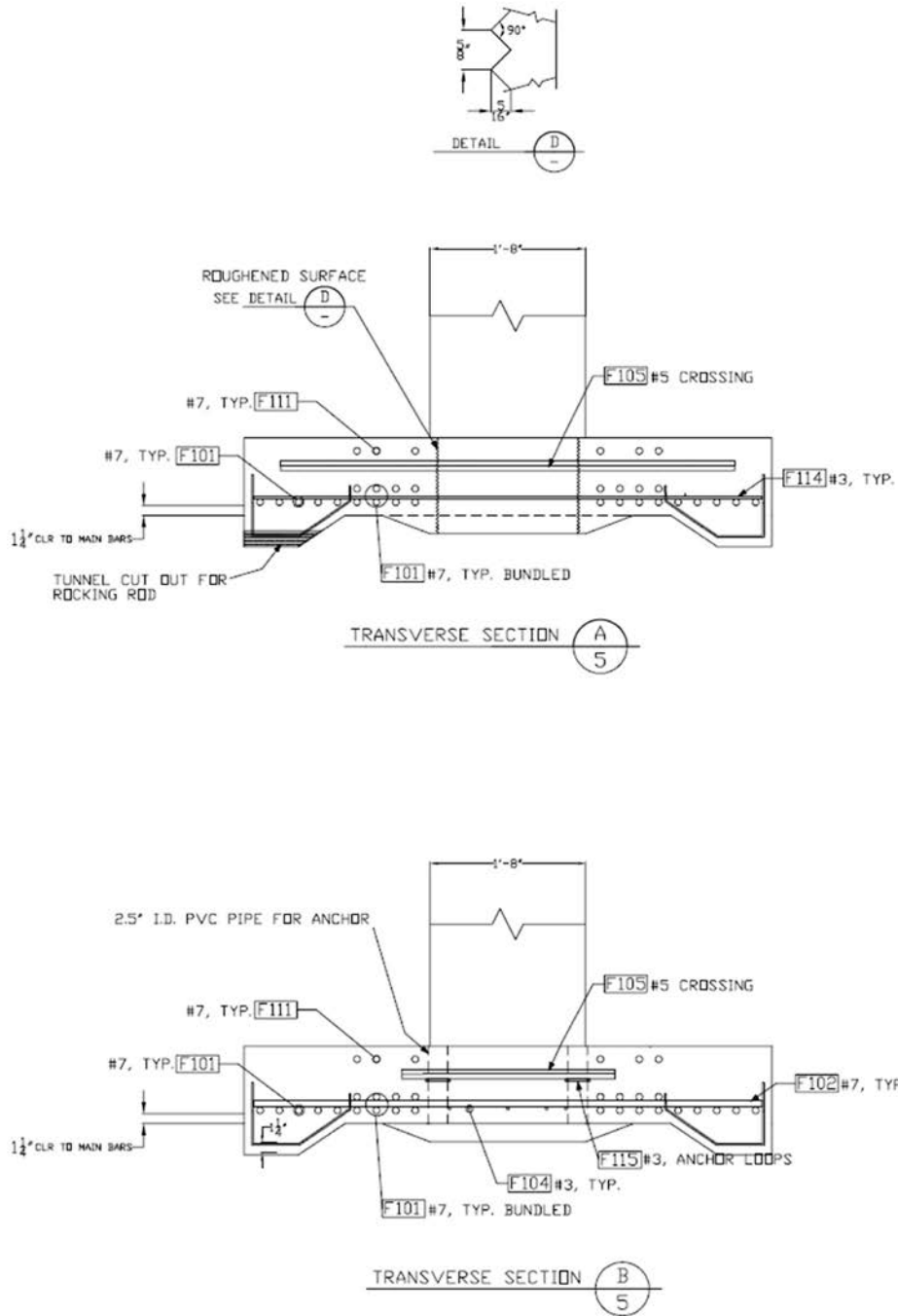


Figure 108. Diagram. Specimen SF-3 footing sections A5 and B5.



## APPENDIX B: MATERIAL TESTS

### CONCRETE STRENGTH

The design compressive strength of both the precast columns and the cast-in-place spread footings was 4,000 psi. The coarse aggregate used was 3/8-inches, and the specified slump was 5 inches. Air-entrainment was used in the precast columns to simulate practice conditions in the Pacific Northwest. The cast-in-place footings were not intended to be air-entrained, but it was necessary since the fabricator was not able to provide a batch without air-entrainment for a 3/8-inch aggregate mix. Bigger aggregates increase shear strength, so the column mix was used for the footings as well.

For every casting operation the slump and air content were measured. The slump test was conducted according to ASTM C143, and the air content according to ASTM C231. The results of those measurements are summarized in table 25.

Table 25. Slump and air content test results.

<b>Specimen</b>	<b>Batch</b>	<b>Slump (in.)</b>	<b>Air Content ( percent)</b>
<b>SF-1/SF-2</b>	Column	5.4	7
	Footing	5	5.7
<b>SF-3</b>	Column	N/A	N/A
	Footing	N/A	N/A

The precast column segments for specimen SF-1 and SF-2 were constructed by a contractor at a construction site in the City of Redmond. The segments cured outdoors for the first 16 days before they were transferred into the University of Washington Structural Laboratory, where footings were fabricated. In contrast to specimen SF-1 and SF-2, specimen SF-3 was constructed entirely at the Structural Laboratory.

For all specimens, cylinders for both batches (column and footing) were fabricated according to ASTM C31 (4-inch by 8-inch cylinders for SF-1 and SF-2, 6-inch by 12-inch cylinders for SF-3). For specimens SF-1 and SF-2, the cylinders were kept adjacent to the specimens to capture their compressive strength. Concrete cylinders for specimen SF-3 were stored in a fog room. The number of column cylinders was limited, so strength tests at 7 days and 14 days were skipped for specimen SF-1 and SF-2. Split cylinder tests were conducted according to ASTM C496. Test results are presented in tables 26 through 28.

Table 26. Concrete compressive strengths up to 28 days.

<b>Specimen</b>	<b>Cylinder Sample</b>	<b>Test Cylinder No.</b>	<b>7 Day (psi)</b>	<b>14 Day (psi)</b>	<b>28 Day (psi)</b>
<b>SF-1/SF-2</b>	<b>Column</b>	1	N/A	N/A	4,791
		2	N/A	N/A	4,717
	<b>Footing</b>	1	N/A	N/A	6,077
		2	N/A	N/A	5,998
<b>SF-3</b>	<b>Column</b>	1	5,282	5,920	6,384
		2	5,615	5,836	7,088
	<b>Footing</b>	1	5,069	5,609	6,212
		2	5,252	5,823	6,854

Table 27. Concrete compressive strengths on test day.

<b>Specimen</b>	<b>Cylinder Sample</b>	<b>Test Cylinder No.</b>	<b>Days</b>	<b>Day of Test (psi)</b>
<b>SF-1</b>	<b>Column</b>	1	113	4,660
		2		5,330
	<b>Footing</b>	1	91	6,680
		2		6,330
<b>SF-2</b>	<b>Column</b>	1	129	5,401
		2		5,591
	<b>Footing</b>	1	107	6,723
		2		6,805
<b>SF-3</b>	<b>Column</b>	1	120	8,190
		2		7,679
	<b>Footing</b>	1	113	7,693
		2		8,117

Table 28. Concrete split cylinder strengths on test day.<sup>1</sup>

Specimen	Cylinder Sample	Test Cylinder No.	Days	Day of Test (psi)
SF-1	Column	1	113	511
		2		-
	Footing	1	91	596
		2		-
SF-2	Column	1	129	613
		2		-
	Footing	1	107	653
		2		-
SF-3	Column	1	120	718
		2		644
	Footing	1	113	596
		2		599

<sup>1</sup>Two 28<sup>th</sup> day split cylinder tests (No. 1: 553 psi, No. 2: 592 psi) were performed on footing cylinders for specimens SF-1 and SF-2.

## GROUT STRENGTH

The precast columns for specimens SF-1 and SF-2 were segmentally constructed. In both specimens, the splice was located 20 inches above the spread footing. Bars protruded up from the base segment of the column to be spliced into ducts in the top segment. The grouting operation for the specimens was performed in two steps. First, the precast column segments were leveled and shimmed. The interface between the segments was grouted. Once the interface grout had hardened, the corrugated metal ducts were injected with grout to anchor the bars in them.

A commercially available packaged grout (1118 Grout-Unsanded Silicon Fume Grout) was used for both grouting operations. The grout is designed to be used as a flowable grout. The procedure

was to mix together the dry grout ingredients and clean water at a temperature between 50 and 64 degrees Fahrenheit, to mix continuously for at least 5 minutes, and then place the grout using a hand pump and plastic tubes. In each grouting operation, four standard 2-inch testing cubes were made, and two cubes were tested according to ASTM C109 on each subassembly's test day. Table 29 summarizes the results of the grout on test day. Test cubes for the ducts in specimen SF-2 measured lower strength because they were accidentally mishandled.

Table 29. Grout cube strength on test day.

<b>Specimen</b>	<b>Cube Sample</b>	<b>Test Cylinder No.</b>	<b>Days</b>	<b>Day of Test (psi)</b>
<b>SF-1</b>	<b>Interface</b>	1	60	13,100
		2		13,050
	<b>Ducts</b>	1	56	12,850
		2		12,150
<b>SF-2</b>	<b>Interface</b>	1	73	12,700
		2		13,350
	<b>Ducts</b>	1	77	9,950
		2		12,400

## **REINFORCEMENT**

Prototype design reinforcement conformed to ASTM Standard A706. All main reinforcement steel was scaled down appropriately (42 percent). Scaling down the transverse reinforcement in the column and the ties in the spread footing was difficult (No. 5) since the smallest reinforcement available conforming to A706 is No. 3 bars. Smooth wires conforming to ASTM A82 were used instead, with 3-gauge wire (0.244-inch diameter) for the spiral and 2-gauge wire (0.263-inch diameter) for both the footing ties. A laser extensometer with 1-inch gauge length was used to calculate strain. In contrast to specimens SF-1 and SF-2, the tension tests for specimen SF-3 were performed using an 8-inch gauge length extensometer. The coupons were loaded until the steel began to yield and the load dropped. The extensometer was then removed to prevent damage to the equipment. The coupon was then loaded till failure, after which the length was measured to obtain a strain at failure. Therefore, the line from yield to failure shown in the plots does not represent an actual measure response, but rather is there to provide a visual connection between the yield and failure point.

Table 30 shows the measured mild reinforcement properties, and the results from the tension tests are presented in figures 110 through 120. ASTM A82 requires 70 ksi minimum yield strength and a minimum tensile strength of 80 ksi. The test results for the spirals and the stirrups showed lower values because the wires were supplied bent into a coil and needed to be straightened out before testing. To be consistent with previous tests, the yield strain was taken as 0.35 percent strain to avoid any subjectivity into the test results.

For each bar size, the yield strain was calculated using the equation in figure 109, where E = 29,000 ksi.

$$\epsilon_y = \sigma_y / E$$

Figure 109. Equation. Calculating yield strain.

Table 30. Measured mild reinforcement properties.

Bar	A <sub>nominal</sub> (in <sup>2</sup> )	Specimens SF-1 and SF-2		Specimen SF-3	
		f <sub>y</sub> (ksi)	f <sub>u</sub> (ksi)	f <sub>y</sub> (ksi)	f <sub>u</sub> (ksi)
No. 7	0.60	N/A	N/A	66.2	95
No. 6	0.44	61.6	86.1	59.2	88.2
No. 5	0.31	63.3	91.4	66.1	108
No. 4	0.20	63.7	90.4	65.9	91.6
No. 3	0.11	65.2	94.5	62.4	99.9
2-gauge wire	0.054	63.4	86.4	N/A	N/A
3-gauge wire	0.047	59.4	73.6	N/A	N/A

### Stress-Strain Plots for Specimens SF-1 and SF-2

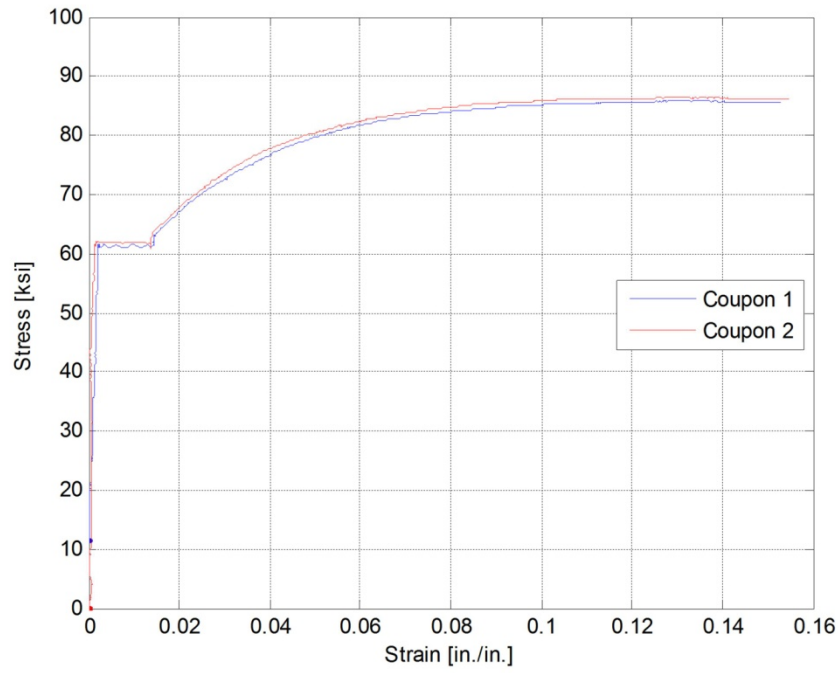


Figure 110. Graph. Specimens SF-1/SF-2 stress-strain curves for No. 6 bars.

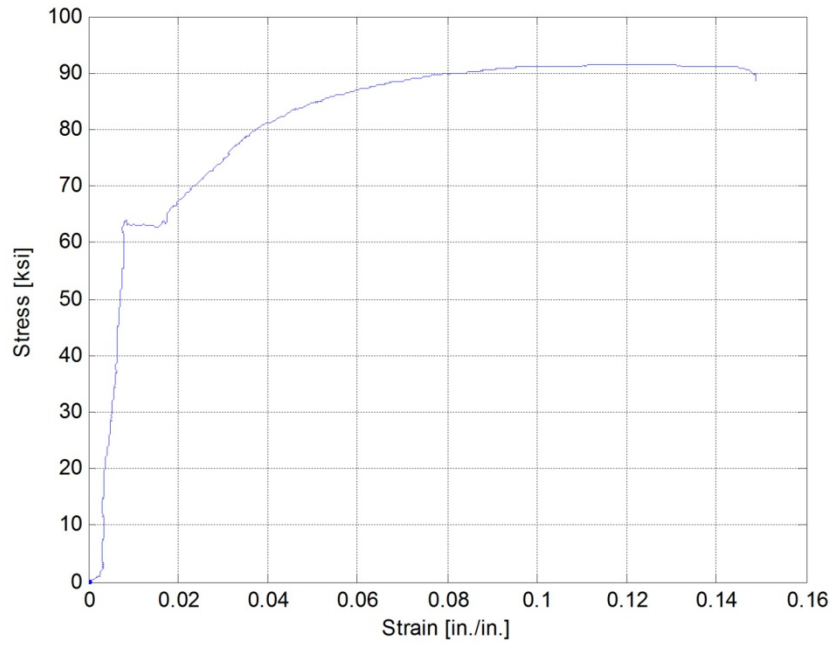


Figure 111. Graph. Specimens SF-1/SF-2 stress-strain curve for No. 5 bar.

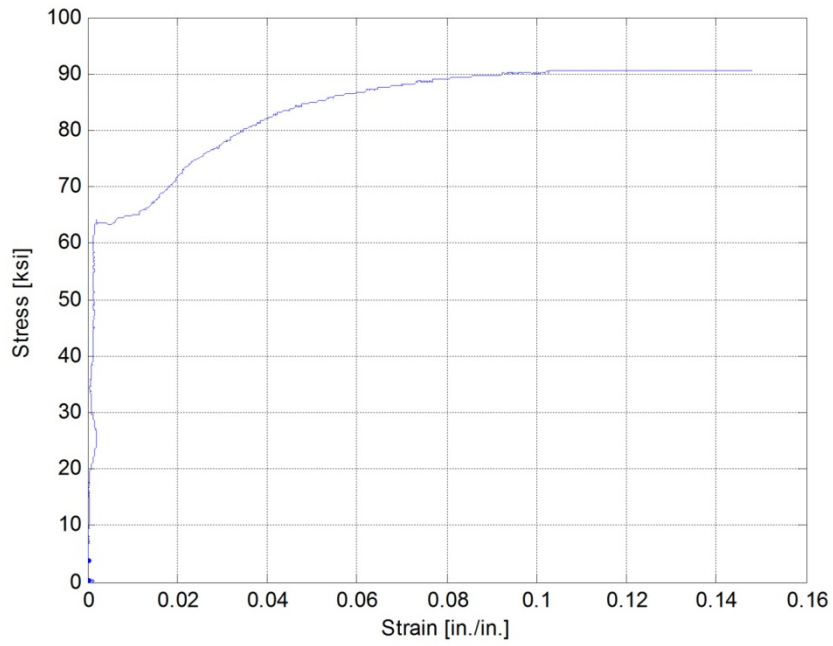


Figure 112. Graph. Specimens SF-1/SF-2 stress-strain curve for No. 4 bar.

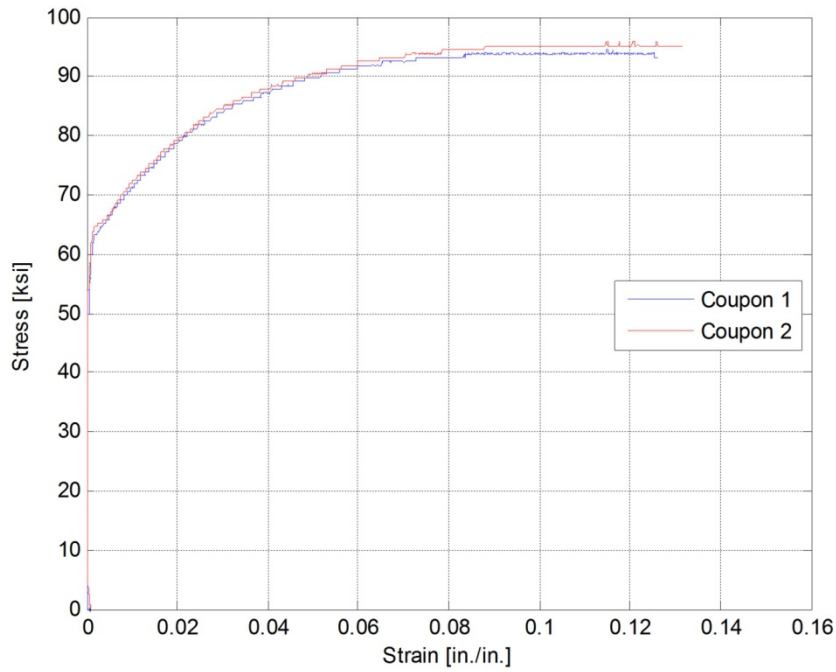


Figure 113. Graph. Specimens SF-1/SF-2 stress-strain curves for No. 3 bar.

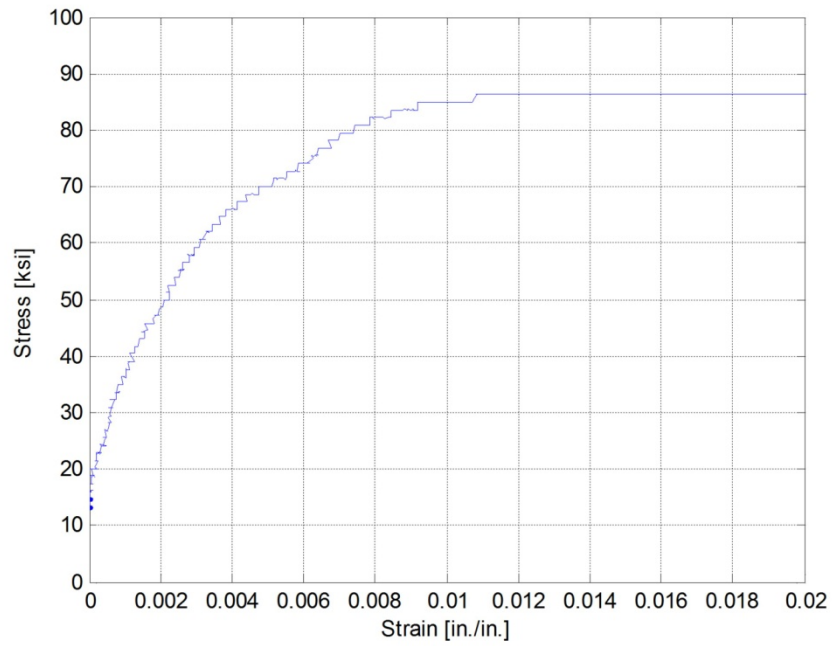


Figure 114. Graph. Specimens SF-1/SF-2 stress-strain curves for stirrups (2-gauge wire).

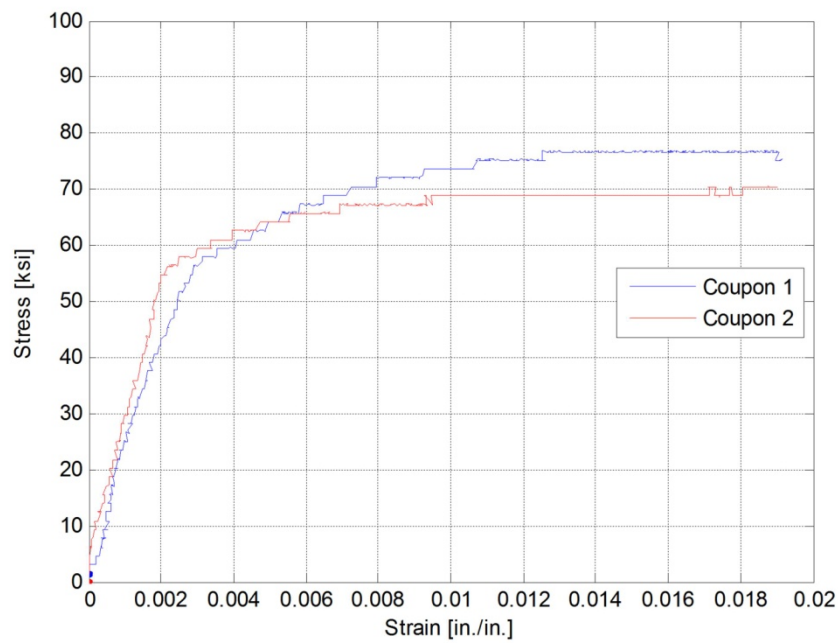


Figure 115. Graph. Specimens SF-1/SF-2 stress-strain curves for spiral reinforcement (3-gauge wire).

**Stress-Strain Plots for Specimen SF-3**

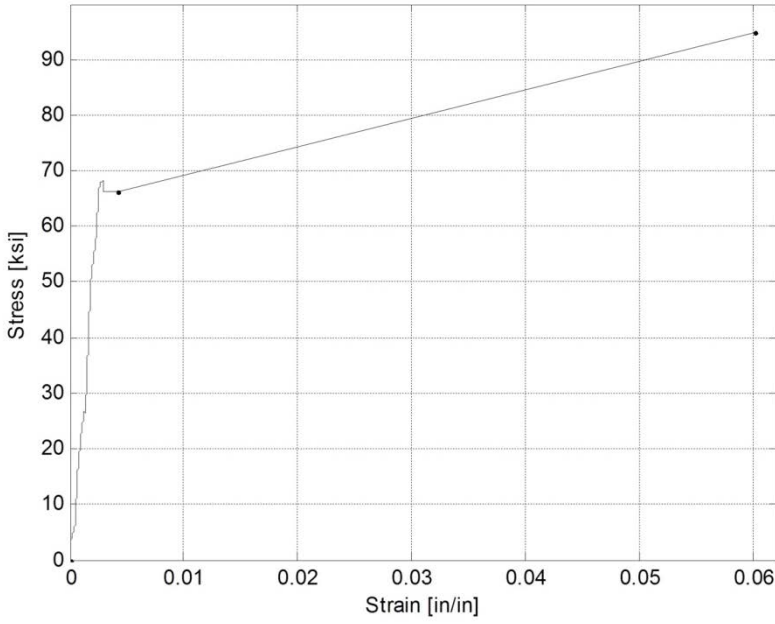


Figure 116. Graph. Specimen SF-3 stress-strain curve for No. 7 bar.

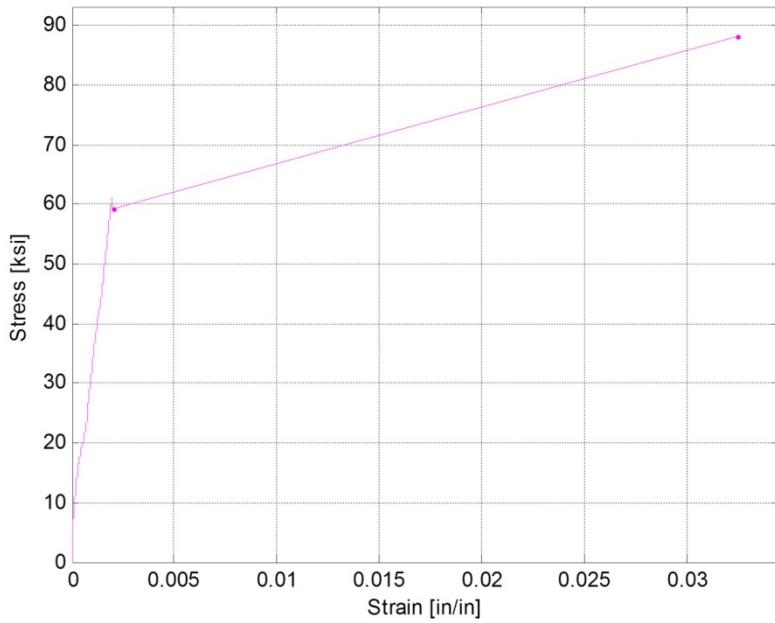


Figure 117. Graph. Specimen SF-3 stress-strain curve for No. 6 bar.

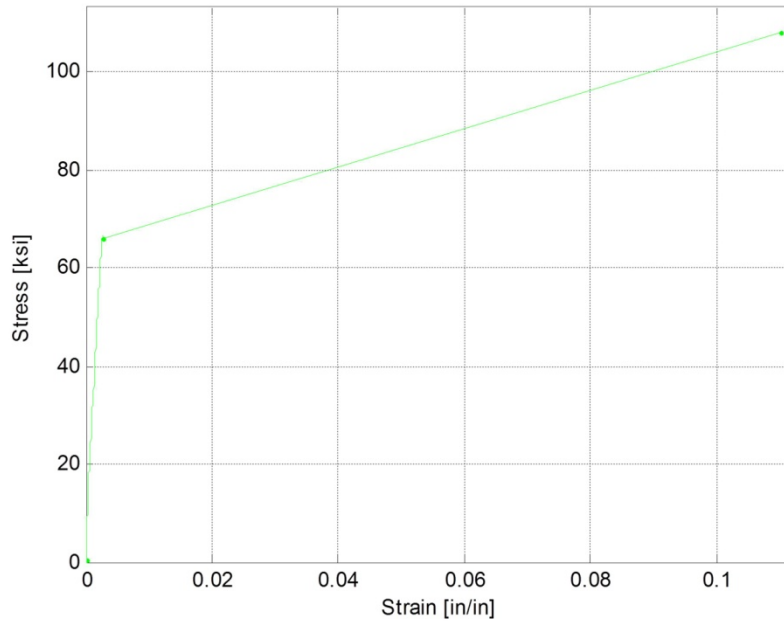


Figure 118. Graph. Specimen SF-3 stress-strain curve for No. 5 bar.

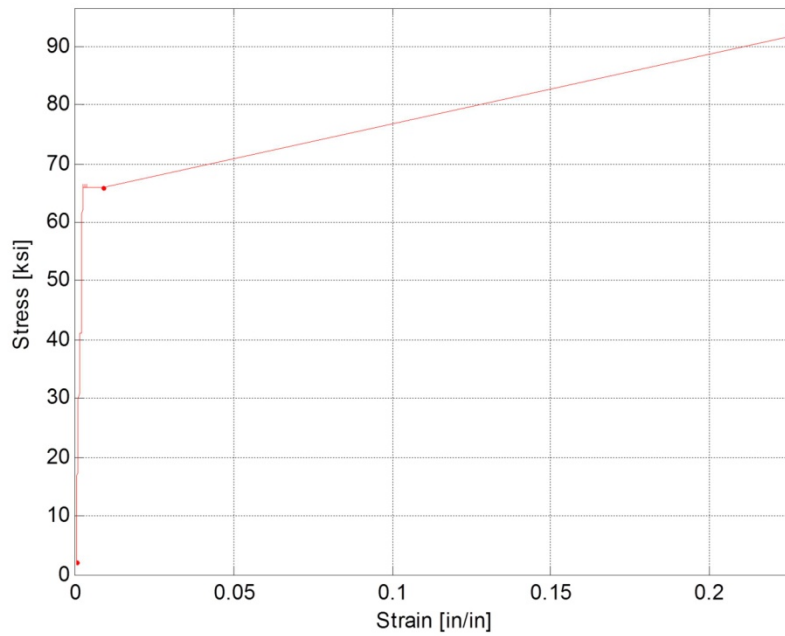


Figure 119. Graph. Specimen SF-3 stress-strain curve for No. 4 bar.

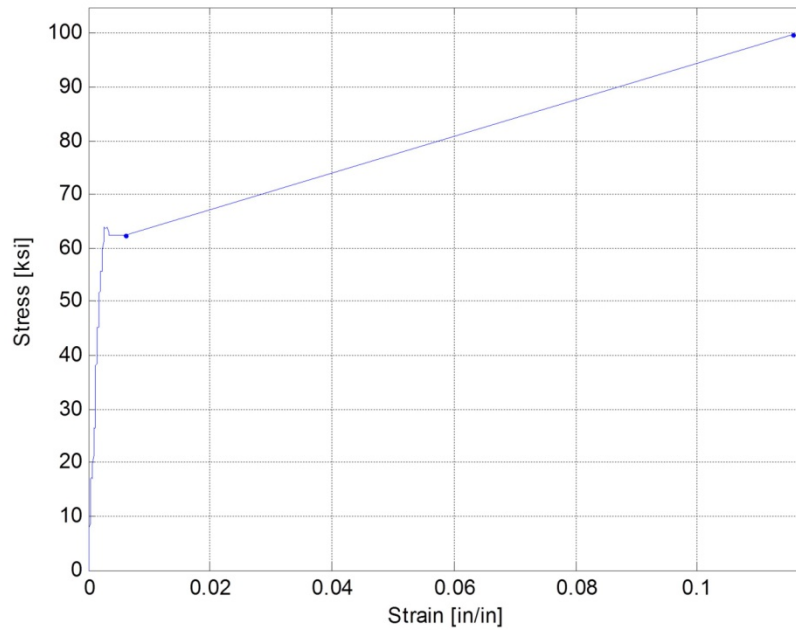


Figure 120. Graph. Specimen SF-3 stress-strain curve for No. 3 bar.

### **CORRUGATED METAL DUCTS**

The corrugated post-tensioning ducts used to splice together the column segments in specimens SF-1 and SF-2 had an inside diameter of 1.67 inches. They were 26-gauge thick and conformed to ASTM A653. See figure 121.



Figure 121. Photo. Corrugated metal duct used in test specimens.

## APPENDIX C: DAMAGE PROGRESSION

### SPECIMEN SF-1



Figure 122. Photo. Specimen SF-1 flexural cracks after cycle 4-1 (+1.00/-1.00 target drift ratio).



Figure 123. Photo. Specimen SF-1: first significant spalling at cycle 6-2 (+2.48/-2.48 target drift ratio).



Figure 124. Photo. Specimen SF-1: plastic hinge became more pronounced in subsequent cycles. Photo taken during cycle 8-1 (+4.28/-4.28 target drift ratio).



Figure 125. Photo. Specimen SF-1: first noticeable bar buckling was the N-NW bar in cycle 9-2 (+7.40/-7.40 target drift ratio).



Figure 126. Photo. Specimen SF-1: N-NE bar fractured first when the column was loaded to peak in cycle 10-2 (+10.65/-10.65 target drift ratio).



Figure 127. Photo. Specimen SF-1: damage after the cyclic testing.

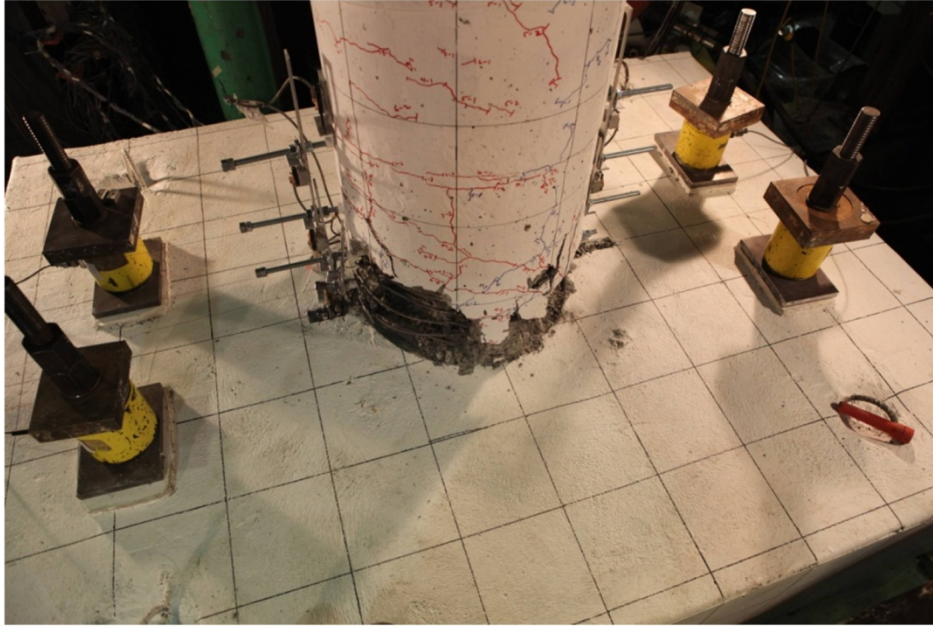


Figure 128. Photo. Specimen SF-1: no damage to the footing was observed after the cyclic testing.

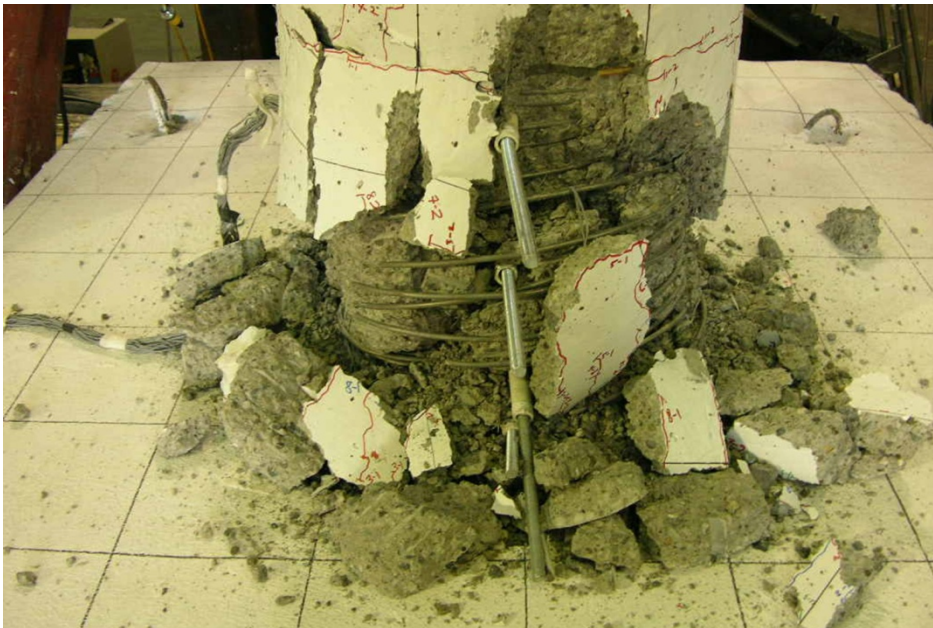


Figure 129. Photo. Specimen SF-1: damage the end of testing. The column crushed after application of vertical load of 842 kips.

## SPECIMEN SF-2



Figure 130. Photo. Specimen SF-2: flexural cracks after cycle 3-2 (+0.83/-0.83 target drift ratio).



Figure 131. Photo. Specimen SF-2: first significant spalling at cycle 7-1 (+2.97/-2.97 target drift ratio).

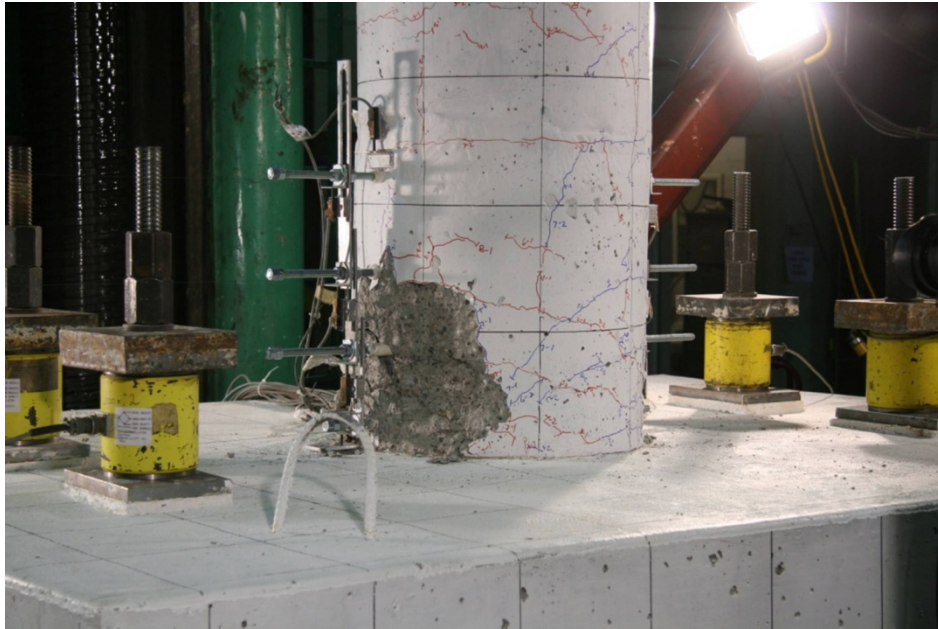


Figure 132. Photo. Specimen SF-2: the column fully spalled after cycle 8-1 (+4.28/-4.28 target drift ratio).



Figure 133. Photo. Specimen SF-2: first noticeable bar buckling was the N-NW bar in cycle 9-3 (+7.40/-7.40 target drift ratio).

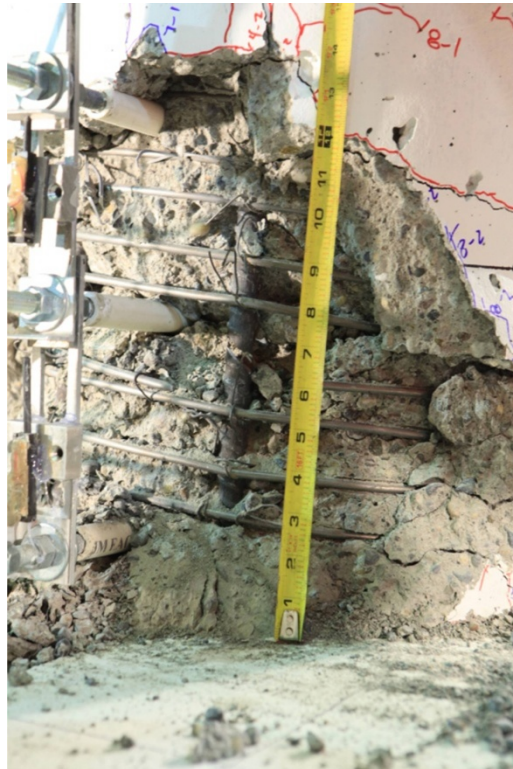


Figure 134. Photo. Specimen SF-2: N-NW bar fractured first when the column was being loaded to peak in cycle 10-2 (+10.65/-10.65 target drift ratio).



Figure 135. Photo. Specimen SF-2: damage after the cyclic testing.



Figure 136. Photo. Specimen SF-2: no damage to the footing was observed after the cyclic testing.



Figure 137. Photo. Specimen SF-2: damage the end of testing. The column crushed after application of vertical load of 819.5 kips.

## SPECIMEN SF-3

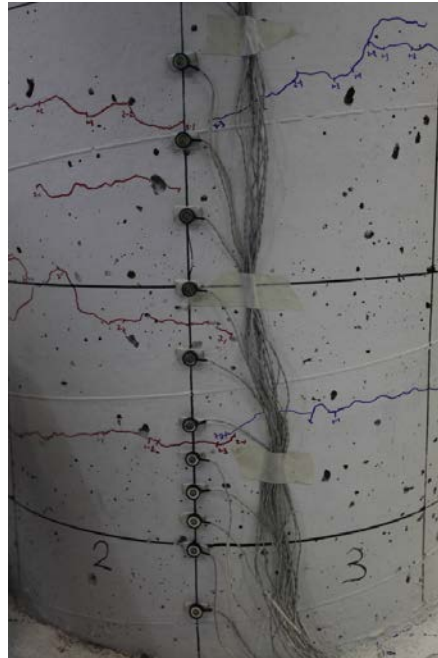


Figure 138. Photo. Specimen SF-3: significant horizontal crack in cycle 3-1 (+0.69/-0.69 target drift ratio).



Figure 139. Photo. Specimen SF-3: separation at column-footing interface in cycle 5-3 (+1.72/-1.72 target drift ratio).



Figure 140. Photo. Specimen SF-3: first diagonal cracking in cycle 6-1 (+2.06/-2.06 target drift ratio).



Figure 141. Photo. Specimen SF-3: first column spalling in cycle 6-2 (+2.48/-2.48 target drift ratio).



Figure 142. Photo. Specimen SF-3: radial footing crack propagation in cycle 6-2 (+2.48/-2.48 target drift ratio).



Figure 143. Photo. Specimen SF-3: large horizontal crack in cycle 6-2 (+2.48/-2.48 target drift ratio).



Figure 144. Photo. Specimen SF-3: large column flexural cracks occurring in cycle 7-2 (+3.57/-3.57 target drift ratio).



Figure 145. Photo. Specimen SF-3: full column spalling in cycle 9-1 (+6.16/-6.16 target drift ratio).



Figure 146. Photo. Specimen SF-3: first footing spalling in cycle 9-2 (+7.40/-7.40 target drift ratio).



Figure 147. Photo. Specimen SF-3: transverse steel exposed in cycle 9-3 (+7.40/-7.40 target drift ratio).

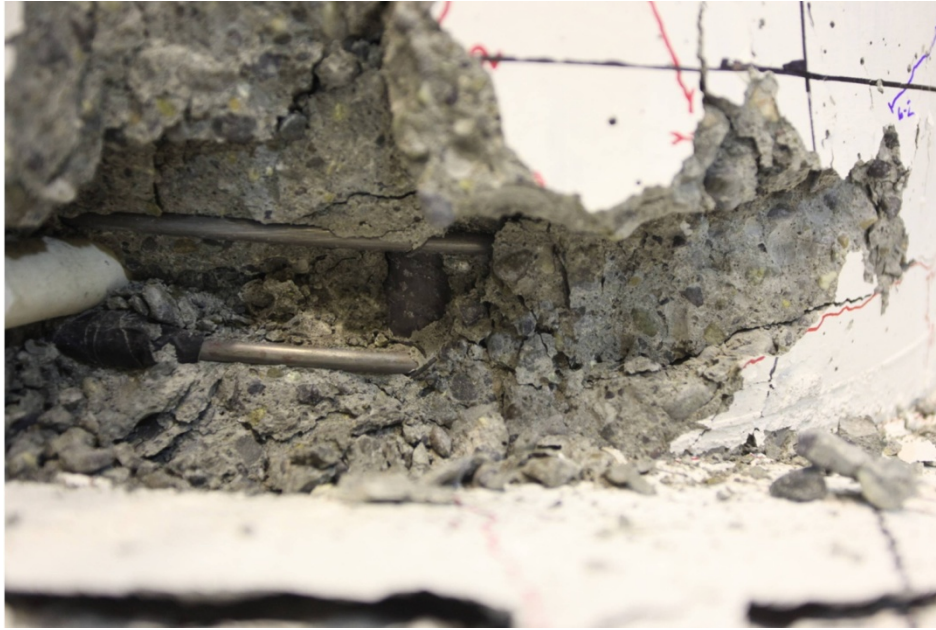


Figure 148. Photo. Specimen SF-3: first exposure of longitudinal reinforcement in cycle 9-3 (+7.40/-7.40 target drift ratio).



Figure 149. Photo. Specimen SF-3: fracture of transverse reinforcement in cycle 10-1 (+8.87/-8.87 target drift ratio).



Figure 150. Photo. Specimen SF-3: major footing spalling occurring in cycle 10-1 (+8.87/-8.87 target drift ratio).



Figure 151. Photo. Specimen SF-3: major cracks in the concrete core in cycle 10-2 (+10.65/-10.65 target drift ratio).



Figure 152. Photo. Specimen SF-3: condition of specimen just before last cycle.



Figure 153. Photo. Specimen SF-3: column after punching through in last cycle (cycle 10-3, +10.65/-10.65 target drift ratio).



Figure 154. Photo. Specimen SF-3: column after punching through in last cycle (cycle 10-3, +10.65/-10.65 target drift ratio).



## APPENDIX D: CONSTRUCTION SEQUENCE

All specimens were constructed in the same manner. Specimen SF-3 differed from specimens SF-1 and SF-2 because it had a shallower spread footing and did not include a column splice. The basic construction sequence was to precast the column, place it in the prepared footing, and then pour the footing around the column. The construction sequence and details are provided in this appendix.

### SPECIMEN CONSTRUCTION SEQUENCE

The column was constructed using a circular, Sonotube form for the portion of the column above the footing. This form was connected to a custom-built octagonal piece which had a roughened surface. The roughened surface was formed by nailing on wooden strips. After the cage was placed in the formwork, PVC pipes to allow for the actuator bolts and the curvature rods were inserted into the formwork. The PVC pipe and curvature rods (for mounting instruments) also served to secure the cage in the formwork. The precast column segments for specimens SF-1 and SF-2 were fabricated in the City of Redmond. Specimen SF-3 was fabricated entirely in the Structural Laboratory at the University of Washington. Figures 155 through 158 show the column fabrication and formwork.



Figure 155. Photo. Column segments for specimens SF-1 and SF-2 were match-tied at a bridge construction site in the City of Redmond.



Figure 156. Photo. Roughened surface of octagonal, bottom portion of column.



Figure 157. Photo. Specimens SF-1 and SF-2, column segments formed and ready to be cast.



Figure 158. Photo. Specimen SF-3, column formed and ready to be cast.

The column segments for specimens SF-1 and SF-2 were low enough to be cast directly from a concrete truck. The precast column for specimen SF-3 was twice as high as each segment of specimens SF-1 and SF-2, and it was located inside the Structural Laboratory. Because of space limitations, a clamshell bucket was used to deposit the concrete. In all specimens, concrete was poured in lifts of approximately 2 to 3 feet each. To avoid segregation problems for specimen SF-3, a tremie tube was connected to the bucket to deliver the concrete to the bottom of the form.

The footing formwork for specimens SF-1 and SF-2 was constructed in the Structural Laboratory while the column segments cured outside. In both specimens, the bottom mat was placed in the footing forms, the column base segment was lifted in and braced, and the top mat and the ties were placed. Specimen SF-3 had a thin footing, so all of these steps were completed before the column was inserted into the forms. In all specimens, PVC pipes were included to allow for hold-down rods, and lifting loops were placed to maneuver the specimen. Finally, the footing was cast. Figures 159 to 161 show the footing formwork and reinforcement, and figure 162 shows the footing cast with concrete.

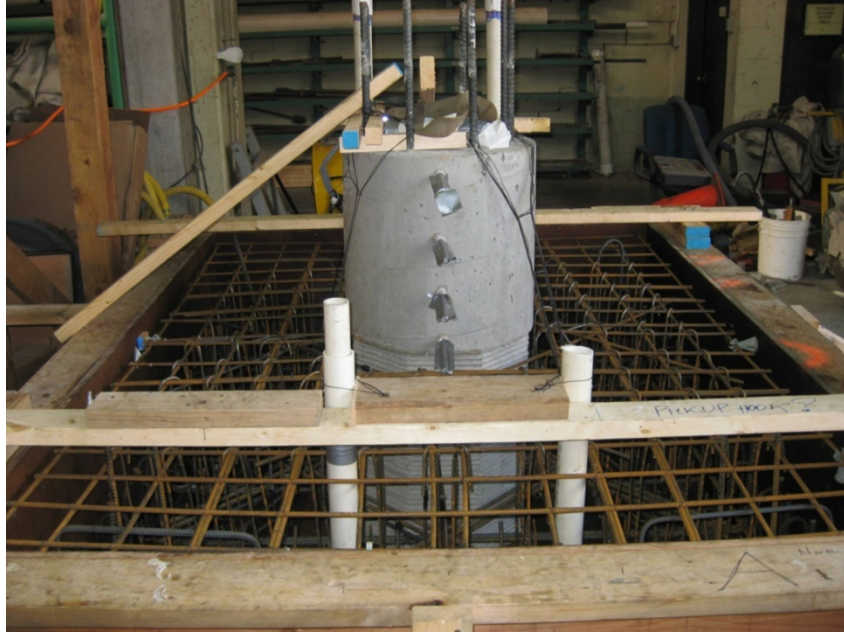


Figure 159. Photo. Specimen SF-1 footing ready to be cast.

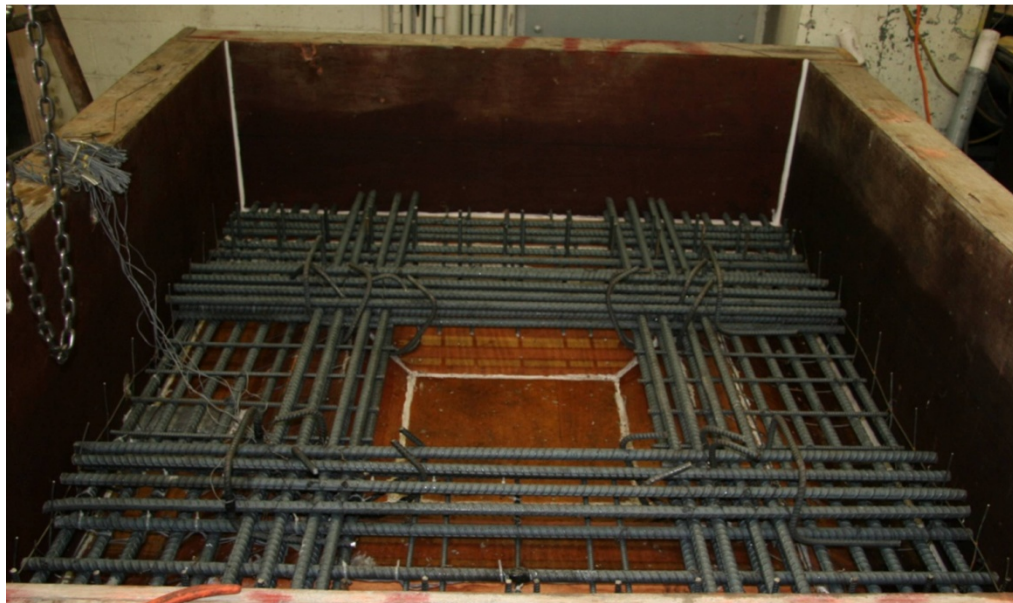


Figure 160. Photo. Specimen SF-3 footing formwork and reinforcement.



Figure 161. Photo. Specimen SF-3 column inserted into footing that is ready to cast.



Figure 162. Photo. Specimen SF-3: finishing the footing surface.



## APPENDIX E: DESIGN CONCEPTS

This appendix describes four concepts for connecting a precast concrete bridge column to a cast-in-place foundation. These concepts arose while the research team was preparing the proposal for this Highways for LIFE project. The purpose was to permit participants in the WSDOT ABC group to see the concepts prior to a meeting on July 30, 2009. It was hoped that, at that meeting, one concept could be selected for use in the Grand Mound Bridge, and that preparations for testing it at the University of Washington could begin. The Highways for LIFE schedule required testing to start that summer.

The goal of these four design concepts was to develop a footing-to-column connection that combines good constructability and seismic performance. The concepts use a small number of large bars in the column, so that they will be compatible with the cap-beam connection shown on the plans.

These concepts constituted a basis for discussion and were not finished designs. The discussion that follows explains the rationale behind their development. The concepts were divided into two groups. In group 1, the bars project below the bottom of the precast concrete and are used for supporting the column while the footing is cast. In group 2, the precast concrete extends below the bottom of the bars and is used to support the column's weight.

The drawings show circular columns, but the same concepts could be used with rectangular columns.

### COLUMNS WITH PROJECTING BARS

Figure 163 shows a detail similar to the one presented on the WSDOT preliminary plans in early summer 2009 that includes a steel ring attached to the bottom of the main column bars. However, the construction sequence for the detail on the plans was not clear. The detail shown here was intended to be used in a construction sequence in which the ring is used both as a temporary locating device during construction and as end anchorage for the main column bars under seismic loading.

The main bars have threaded ends and project from the bottom of the column. A light ring template is attached (with two nuts per bar) to hold the bars in exactly the right location when the column is (pre-)cast. The ring is removed after casting, but one nut remains on each bar. On-site, a similar (but maybe heavier) ring is set and secured in position, and it acts as a location device for the column. The bottom mat is placed on top of the ring. The column is brought in and set with the bars projecting through the holes in the ring. The ring ensures that the column base is located correctly. By careful pre-placement of the nuts on the bars (jam-nutted, if desired, to prevent movement), the column alignment and plumb should also be very close to true. Adjustments can be made as needed by turning the nuts. When the column is plumb, a second nut is screwed onto the end of the bar below the ring, thereby securing the ring to the bar for anchorage.

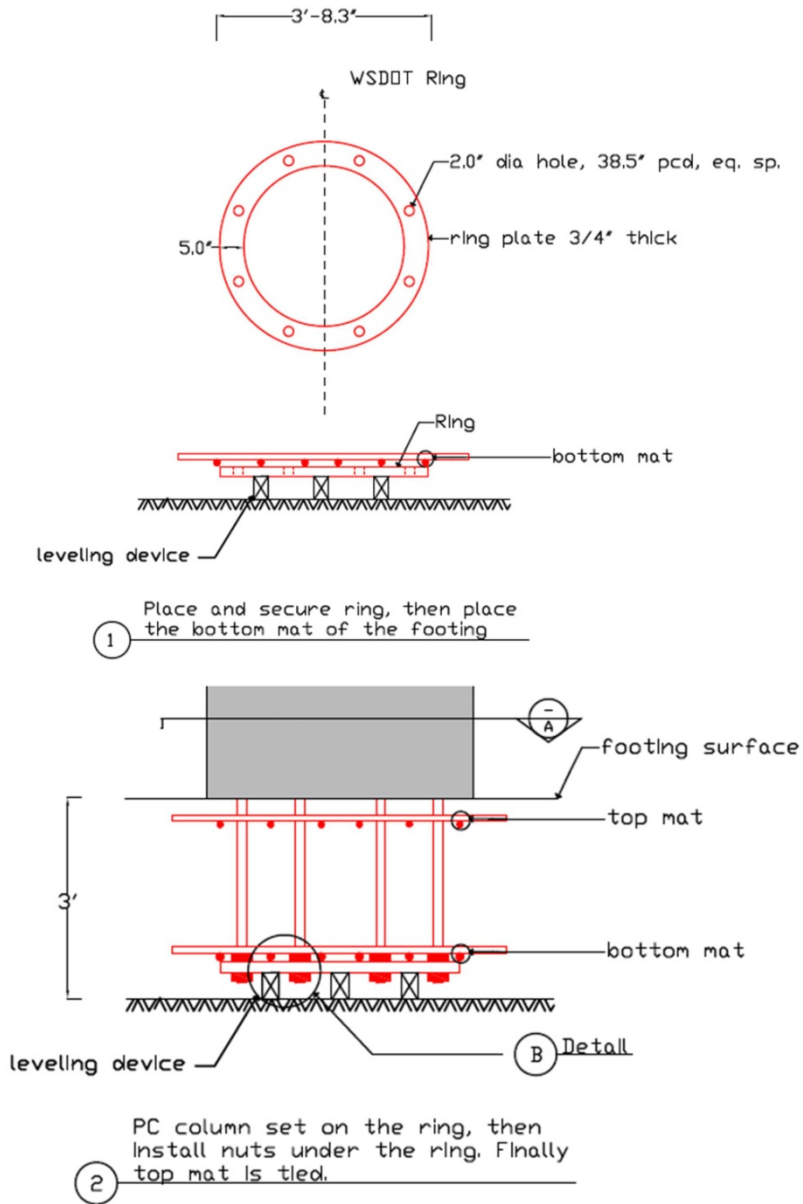


Figure 163. Diagram. Column detail with projecting bars.

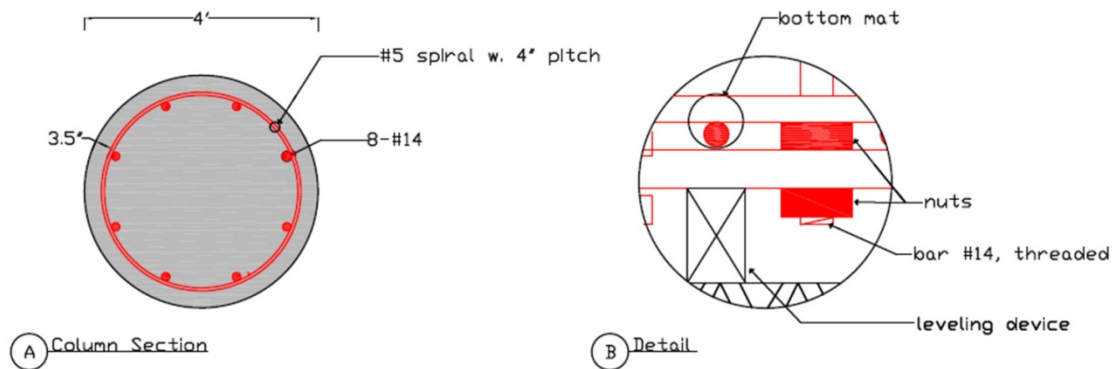


Figure 163. Diagram. Column detail with projecting bars (continued).

The proposed construction sequence was:

1. Fix the light ring template to the threaded bars. Place it the form.
2. Precast the column.
3. Remove the template. Leave one nut on each bar.
4. On-site, place and secure the heavy ring.
5. Place the bottom mat of the footing steel.
6. Set the precast column on the heavy ring. Adjust for level and plumb as needed using nuts on bars.
7. Place and tighten a nut on each bar beneath the ring.
8. Install and tie the top mat. Pass top bars through the spiral and column bars as needed.
9. Cast the footing.

## COLUMNS WITHOUT PROJECTING BARS

Three details were shown in this group—socket columns, long struts, and short struts. In each case, the goal was to have no bars projecting below the bottom of the concrete, thereby making the system more robust for transportation and handling.

### Socket Columns

The socket column was the simplest connection to erect. This concept formed the basis of the socket connection that was tested in the program. Its advantages were:

- Robust for handling and transportation.
- Connection is simple. No steel to connect on site.

Disadvantages were that the footing may have to be deeper, to handle the joint shear forces.

The proposed construction sequence was:

1. Precast the column.
2. Place the bottom mat of the footing steel.

3. Set the precast column, level (using shims or other devices), and brace it.
4. Install and tie the top mat.
5. Cast the footing.

Notes on this connection:

- Figure 164 shows a notch in the bottom of the column in each direction. This was to permit some bottom bars of the footing to pass under the column, where they are most useful. Note that these bars will not engage directly with the vertical column steel. The couple that resists the column moment will therefore consist of horizontal forces at the top and bottom of the footing.
- From a construction viewpoint, it would be slightly easier to place no bars under the column, and to distribute them all uniformly either side of the column. However, this might be less satisfactory from a structural viewpoint.
- The top mat will either have to be placed with no bars passing through the column, or (straight) bars will have to be placed in ducts through the column. Under seismic load, the negative cantilever moment on the uplift side of the footing is much smaller than the positive moment on the high soil pressure side, because it is caused only by the self-weight of the footing. Therefore, the top steel plays a much less significant role than the bottom steel, and a top mat that requires no steel to pass through the column may be feasible.
- The column must resist vertical punching shear. Two critical perimeters should be checked: the usual one, forming a cone through the footing, and a second, cylindrical one at the interface between the precast column and the cast-in-place footing. However, the shear stress on the latter is on the order of 100 psi in the Grand Mound Bridge, and that stress can easily be handled by roughening the surface of the precast column directly or by casting a corrugated steel tube around the part of it that is to be embedded in the footing.

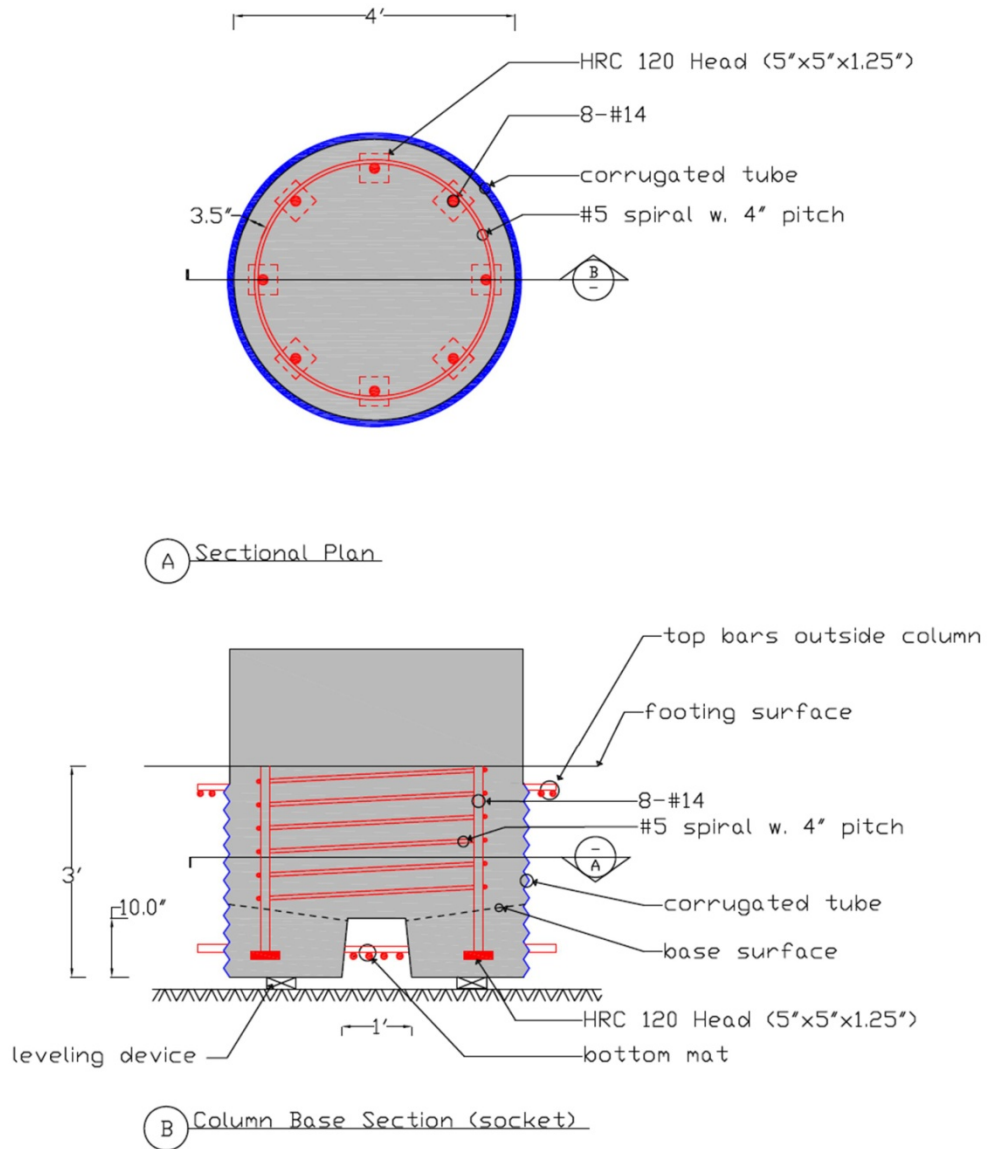


Figure 164. Diagram. Socket column concept.

### Long Struts

The goal of this detail was to enable the column to be supported on concrete components, rather than resting on projecting bars, while the footing is cast. Details are shown in figure 165. The column bars are not fully encased in the precast concrete, and their end anchors are embedded in the cast-in-place concrete of the footing. This achieves better engagement between the footing steel and the column steel than would be the case with a socket column.

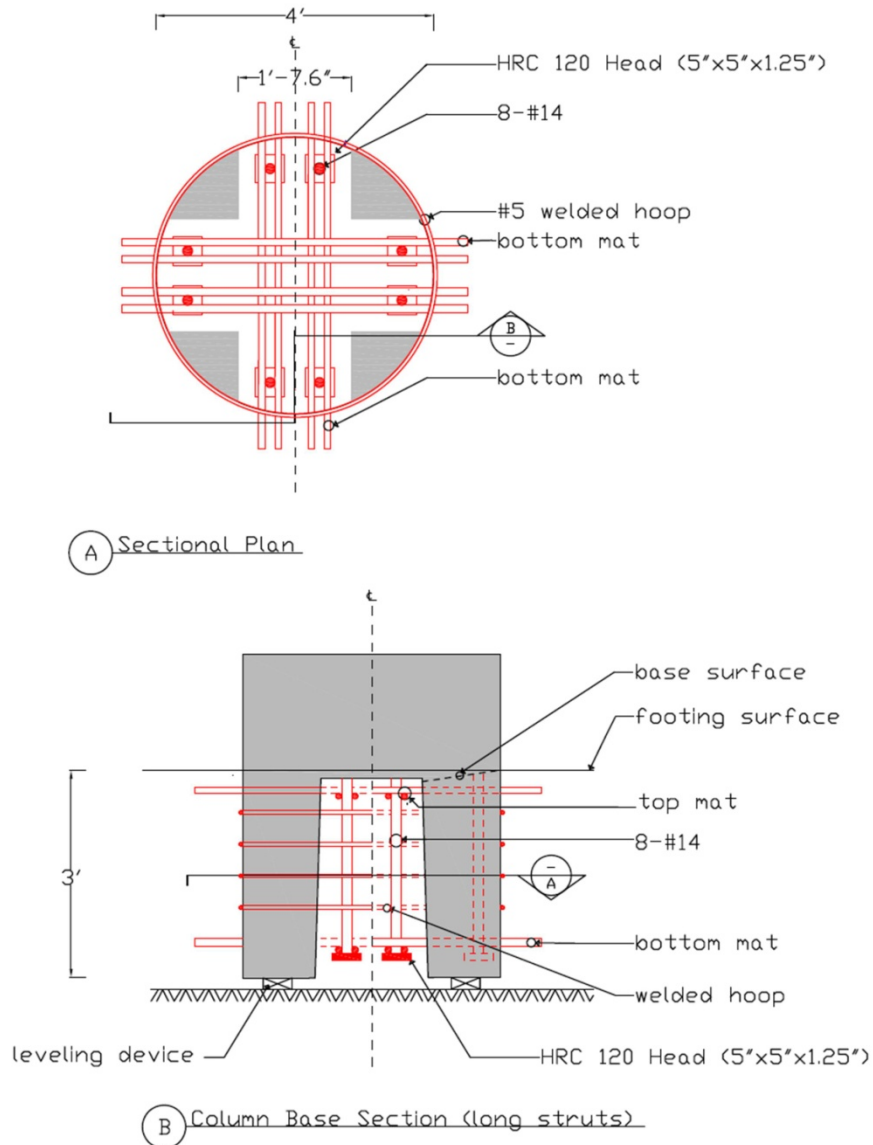


Figure 165. Diagram. Long struts concept.

The column is cast with a cruciform blockout at the bottom. The blockout depth is approximately the same as the footing depth and has a slight taper on it to facilitate removal of the blockout formwork. The four concrete struts, or legs, projecting from the bottom of the solid part of the column support the weight of the column while the footing is cast in place round it. Within the footing depth, the column spiral is shown at the outer face of the column, with no cover. This arrangement has several consequences:

- It allows the blockout to be formed and removed more easily than if the spiral were placed 3 inches in from the curved surface.
- It creates a rough surface at the outer face of the precast concrete, to improve bond.
- It provides some support for the struts during handling.
- It provides a mechanism for joint shear resistance within the column core.

The proposed construction sequence was:

1. Precast the column.
2. Place the bottom mat of the footing. Leave the center four bars each way under the column loose.
3. Set the precast column, level (using shims or other devices), and brace it.
4. Move the four center bars in each direction of the footing mat so they lie on top of the column bar terminators. Tie the bars.
5. Install and tie the top mat. This requires passing some of the bars through the cruciform breakout space in the column. (Those bars will have to be straight.)
6. Cast the footing.

Notes on this connection:

- The top of the breakout has a slope to facilitate compaction of the cast-in-place concrete and to avoid air pockets.
- Leveling may be done using shims or other leveling devices.
- A “rat slab” may be cast under the column (or precast) if the ground will be unable to support the local contact pressure caused by the leveling devices. (The column segment in the Grand Mound bridge weighs less than 8 kips.)
- The bottom mat bars will probably have hooks. Therefore, they cannot be installed after the column is set.
- The plan is to lift the loose bars of the bottom mat over the T-heads of the main column bars, once the precast column is in place. This is straightforward for the top layer of steel in the bottom mat, but the bottom layer creates some challenges. That issue needs to be studied and resolved.
- The column spiral is cast with the precast column and is to be exposed to provide a rough surface. The intent is to avoid placing a corrugated tube there, because the tube would have to be cut extensively at the breakouts, thereby causing additional work and reducing the tube’s effectiveness for shear resistance and confinement.
- Some vertical steel is needed in the long struts to prevent bending failure during handling. If it extends past the top of the footing, it provides additional flexural strength at the column-footing interface. There is nothing inherently bad about this, but it would be necessary to check that the increased flexural strength does not cause problems elsewhere (such as at the partial-height column splice).
- The concrete surfaces at the breakout should be roughened to optimize transfer of shear across the interface between the precast column and the cast-in-place footing. Roughening could be achieved by use of a retarder on the breakout form.

### **Short Struts**

This detail, illustrated in figure 166, was intended to overcome one of the potential weaknesses of the “long struts” system, namely the fact that the struts are quite slender and therefore vulnerable to damage during handling. The detail was in most ways identical to the “long struts” system, but the struts are made shorter. This means that the top mat bars cannot be passed through the breakout and will have to be placed in the footing outside the column. For the socket column detail, it was argued that this may be acceptable. The same argument holds here. If not,

horizontal ducts could be placed in the column to accommodate these top mat bars, but they represent additional complexity and congestion, and they create a weak plane for horizontal shear, so they were undesirable.

The main potential disadvantage of the short struts system lies in the configuration of the strut-and-tie system in the footing. The primary struts (of the strut-and-tie model) may have to pass through the cast-in-place footing and precast concrete, with the associated interfaces between. The precast concrete will be roughened at the interfaces, but if the shear capacity there is inadequate it may compromise the ability of the struts to carry their full load. As with the long strut detail, the spiral should be placed at the outer cylindrical surface to simplify the breakout formwork and to create a rough surface there.

The conservative version tested in this research (specimen SF-1) was a modified version of the short strut concept.

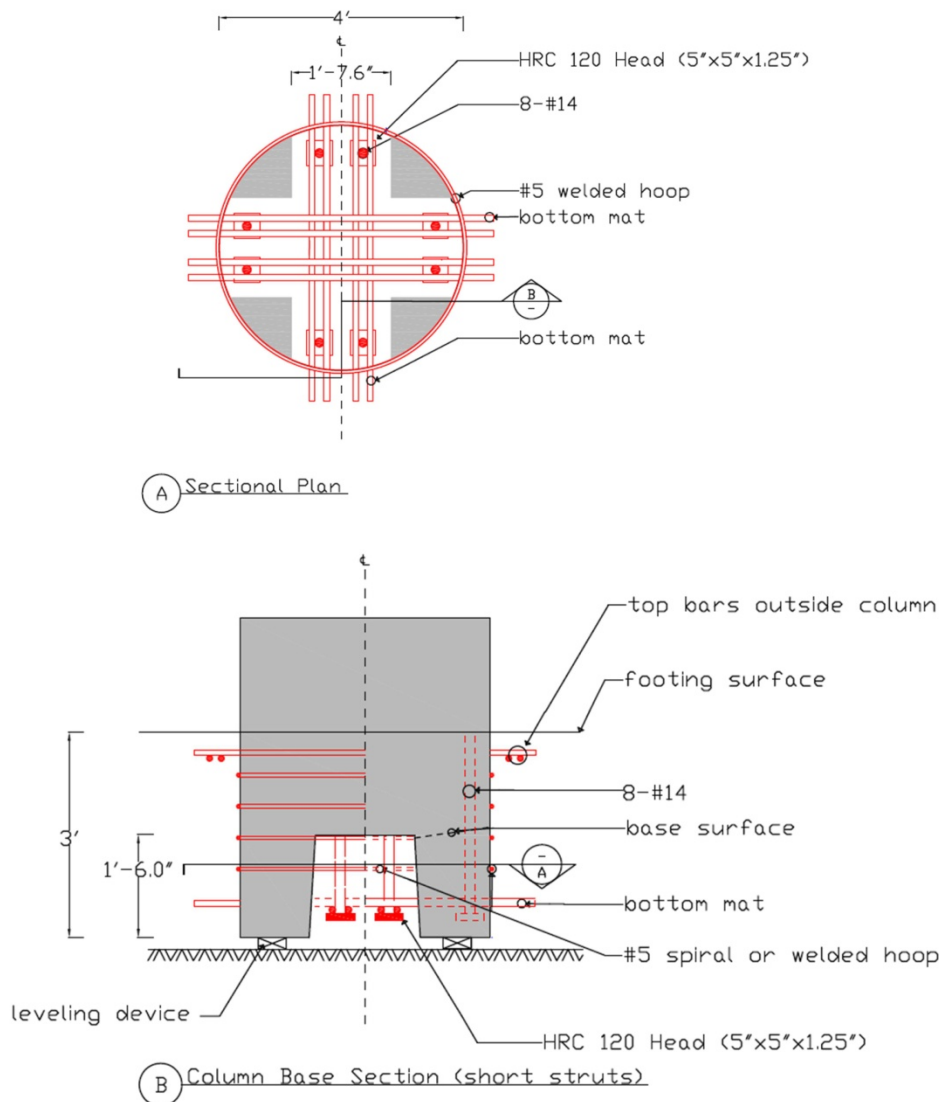


Figure 166. Diagram. Short struts concept.